FEEDBACK INTERCONNECTION BASED INPUT-OUTPUT ANALYSIS OF SPATIO-TEMPORAL RESPONSE IN WALL-BOUNDED SHEAR FLOWS

by

Chang Liu

A dissertation submitted to Johns Hopkins University

in conformity with the requirements for the degree of

Doctor of Philosophy

Baltimore, Maryland

July, 2021

Abstract

This work investigates the characteristic length, time, and velocity scales in canonical wall-bounded shear flows through analysis of their spatio-temporal frequency response operators. First, we employ input-output analysis to analyze convective velocity in turbulent channel flows in regions of high shear. This framework is exploited to isolate different mechanisms contributing to the breakdown of Taylor's hypothesis. The insights gained are used to develop a viscous correction to Taylor's hypothesis to capture the near-wall convective velocity. We then apply spatial input-output analysis to overcome the ambiguity imposed in specifying streamwise wavenumber associated with a spatially localized actuation signal. This framework embeds a wall-normal dependent convective velocity that allows us to analyze the downstream evolution of actuated flow structures.

This dissertation then systematically models the effect of nonlinearity within computationally tractable linear frameworks and provides a suite of new analysis tools to understand wall-bounded shear flows. We build upon the traditional input-output approach by introducing a feedback interconnection between a modified linear operator and a structured input-output model of the nonlinearity. The associated amplification is quantified by structured singular value. This structured input-output analysis predicts the horizontal wavelengths of transition-inducing perturbations in plane Couette flow (PCF) and plane Poiseuille flow (PPF). The results closely match those obtained from direct numerical simulation and nonlinear optimal perturbation analysis, which differ from the results of traditional input-output analysis. We then show that structured input-output analysis also predicts dominant flow structures in stratified PCF and uncovers the parameter dependence associated with the dominance of different types of flow

structures. Structured input-output analysis is also employed to explore the range of validity of a previously proposed mathematical equivalence between rotating PCF and stratified PCF. The results of these studies suggest that structured input-output analysis forms a unified framework to predict the prevalence of oblique turbulent bands in the intermittent regime of PCF, PPF, stratified PCF, and rotating PCF.

Finally, we propose alternate approach to include the effect of nonlinearity and certify permissible perturbation amplitudes in a range of transitional shear flow models. This linear matrix inequality based approach is more computationally efficient than prevailing nonlinear analysis tools.

Primary reader and advisor: Dennice F. Gayme

Secondary reader: Colm-cille P. Caulfield and Charles Meneveau

Acknowledgments

First of all, I would gratefully acknowledge my advisor Dennice F. Gayme for her support, encouragement, and great freedom of my research. This dissertation would not be possible without her insight into both wall-bounded shear flows and control theory. She also taught me a lot of important lessons on personal and professional developments. I would like to also acknowledge Colm-cille P. Caulfield in collaboration with the stratified flow and serving as my dissertation reader. I should also thank a lot of insightful feedback from Charles Meneveau in the weekly group meeting and thank his kindness in serving as my dissertation reader.

I would like to also acknowledge the collaboration on actuated turbulent boundary layer with Igal Gluzman, and the experimental group from the University of Notre Dame: Stanislav Gordeyev, Flint O. Thomas, Mitchell Lozier, and Samaresh Midya.

I would like to acknowledge the instructors who have taught me numerous knowledge, served as my DQE committee, and GBO committee, including Department of Mechanical Engineering: Dennice F. Gayme, Charles Meneveau, Tamer Zaki, Rajat Mittal, Jung-Hee Seo, Gretar Tryggvason; Department of Electrical & Computer Engineering: Enrique Mallada, Pablo A. Iglesias; Department of Applied Mathematics and Statistics: Gregory Eyink, Donniell Fishkind, Antwan C. Clark, James C. Spall, Soledad Villar, Nicolas Charon, James A. Fill; Department of Earth & Planetary Sciences: Thomas Haine, Darryn Waugh.

I would like to also acknowledge the discussion with group members: Ismail Hameduddin, Joel Bretheim, Carl Shapiro, Igal Gluzman, Xiaowei Zhu, Mingwei Ge, Benjamin A. Minnick, Genevieve Starke, Ghanesh Narasimhan, Pengcheng You, Chengda Ji, Rajni Kant Bansal, Manuel

Ayala, Aishwarya Rath, and Yu Shuai. I would like to also acknowledge discussion with members in the group of Professor Meneveau: Wen Wu, Zhao Wu, Patricio Clark Di Leoni, Mostafa Aghaei Jouybari, Ruifeng Hu, Jia Deng, Kristofer Womack, Aditya Aiyer, Samvit Kumar, Mitchell Fowler, and Yue Hao. I also enjoy talking with my friends: Yifan Du, Xianyang Chen, Mengze Wang, Qi Wang, Yinghe Qi, Shiyong Tan, Xu Xu, Chuanxin Ni, Zeng Zhang, Karthik Menon, Shantanu Bailoor, Alberto Roman-Afanador, Xuebo Zheng, Guangpu Zhu, Zhiping Yuan, Wen Liu, Yan Jiang, Tianqi Zheng, Hancheng Min, Peng Zheng, Le Liang, Zhidong Zhang, and Tianqi Cui.

I would like to thank the communication with Edgar Knobloch and Keith Julien, which motivated the author to study stratified and rotating flows.

I would like to also acknowledge my undergraduate advisor Professor Shixiao Fu in Shanghai Jiao Tong University and group members Mengmeng Zhang, Haojie Ren, Yuwang Xu, Leijian Song, Jungao Wang, Ziqi Lu, Yadong Zeng for the collaboration and discussion.

I would like to thank Denise Link-Farajali in the Center of Leadership Education offering English Second Language (ESL) Consulting, who significantly improved my English writing and speaking.

I would like to acknowledge numerous publicly available videos in the Institute for Pure & Applied Mathematics (IPAM) at the University of California, Los Angeles, and the Kavli Institute for Theoretical Physics (KITP) at the University of California, Santa Barbara, where a large part of this work is significantly benefited from.

I would like to gratefully acknowledge support from the US National Science Foundation (NSF) through grant number CBET 1652244, the Office of Naval Research (ONR) through grant number N00014-18-1-2534, and the Chinese Scholarship Council.

Last but not the least, I would like to acknowledge the encouragement and support from my parents Aixia Han, Yanli Dong, Yinghui Zhou, Baojun Liu. This dissertation is dedicated to my wife Lu Dong for her love.

Table of Contents

List of Tables

List of Figures

Chapter 1

Introduction

"...big whirls have little whirls that feed on their velocity, and little whirls have lesser whirls and so on to viscosity..."

Lewis F. Richardson[1], 1922

1.1 Wall-bounded shear flows

Wall-bounded shear flows are widely observed in transport applications, including flow over air, road, surface, and underwater vehicles. They are also prevalent in internal flows such as pipelines transporting oil (McKeon, 2010) and energy systems such as turbomachinery and wind farms (Veers *et al.*, 2019). The atmospheric boundary layer (Mahrt, 2014) and oceanic bottom boundary layer (Weatherly & Martin, 1978) provide additional examples of wall-bounded shear flows. Flow in the cardiovascular system (Taylor & Draney, 2004) and microfluidics for digital manufacturing (Naderi *et al.*, 2019) can be also modeled as wall-bounded shear flows. Although the underlying properties of these flows vary widely, in all cases the spatio-temporal scales of interest remain fundamental to understanding the underlying phenomena. Predicting and analyzing the characteristic length, time, and velocity scales can be achieved by simulations or experiments, but developing a full characterization through these methods pose several challenges. For example, the smallest length scale is restricted by limitations on the spatial resolution that can be achieved, while resolving the largest length scale requires a

[1](Richardson, 2007, p. 66)

very large domain, which leads to competing priorities. Similar challenges remain in studying the characteristic time scale, particularly, in applications where the flow is under strong stratification or rapid rotation that introduces a fast time scale associated with the frequency of internal gravity waves or inertial waves. Resolving this time scale imposes challenges in temporal resolution. Both of these challenges are particularly acute in applications involving atmospheric and oceanic motion, where the length scale can vary from 1 cm of microturbulence to a global scale governing climate variation, and the time scale can vary from a few seconds to decades (Cushman-Roisin & Beckers, 2011, table 1.2). Studying the characteristic velocity certainly require measurements resolved in both space and time. Data-driven methods provide new possibilities for filling in missing information, but the aforementioned challenges for simulations or experiments remain in generating the required training data. Analytical tools that can isolate and analyze the characteristic length, time, and velocity scales can therefore provide important complements to numerical and experimental approaches in developing a full understanding of the flow physics.

1.2 Input-output and feedback interconnection based analyses

The frequency-domain analysis is widely applied in control theory for obtaining an input-output relation, which can be described by a transfer function through a Laplace transform of linearized dynamics. The spatio-temporal frequency response operator instead comprises a spatio-temporal Fourier transformed operator with real spatial and temporal frequency variables. The linearity of the Fourier transform enables a decomposition of the response into contributions from different spatial and temporal frequency triplets that can be used to isolate and analyze the aforementioned characteristic length, time, and velocity scales in wall-bounded shear flows. This spatio-temporal frequency domain analysis therefore provides a natural framework for analyzing the question of a characteristic length, time, and velocity scales.

Nonlinearity can be also incorporated into this type of frequency domain analysis; see e.g., (Khalil, 2002, chapter 7). This is typically done by partitioning dynamics into a feedback interconnection between the linear and nonlinear components (this partition is referred to as the Luré

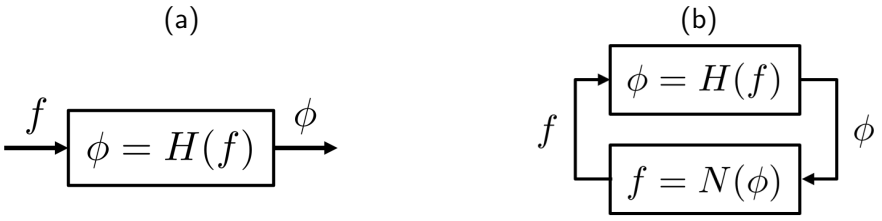

Figure 1.1: Illustration of analysis based on (a) input-output and (b) feedback interconnection.

system (Kalman, 1963)), and the stability of the overall system is sometimes referred to as 'absolute stability'[1] (Khalil, 2002, chapter 7). A natural way to characterize the nonlinearity within this setting is through input-output relations that allow the overall system to be represented in terms of input-output, or transfer function type relations. One widely employed method to characterize the nonlinearity is through a sector bounding approach (see e.g., (Zames, 1966; Khalil, 2002, chapter 6)), which can be achieved in systems wherein the nonlinear map of the state $N(\phi)$ is constrained within a sector in the $(\phi, N(\phi))$ plane. A special case of sector bounded systems is passive systems (see e.g., (Khalil, 2002, definitions 6.1 and 6.2)). Passivity has a close relationship with the energy-conserving property of the nonlinearity in Navier-Stokes equations and energy stability method (Joseph, 2013; Straughan, 2013). Another important application of this type of feedback interconnection is robust stability and performance analysis (Zhou *et al.*, 1996), where the problem setup is typically the feedback interconnection between a nominal system and the model uncertainty. In wall-bounded shear flow applications, this approach can be implemented by describing the nominal system in terms of some linear or linearized dynamics with the nonlinearity modeled as the uncertainty.

The main difference between traditional applications of input-output analysis of the spatio-temporal frequency response operator of the "linear dynamics" and feedback interconnection based analyses is that the prior can be considered as an open-loop system. Instead, the latter involves a closed-loop interconnection as shown in figure 1.1. More precisely, the input f in the input-output analysis of figure 1.1(a) does not provide a direct model of the nonlinear interactions and its form is typically chosen based on the problem of interest including Gaussian

[1] Note that this is different from the notion of absolute stability employed to study spatial developing flow (Huerre & Monkewitz, 1985).

noise (meant to excite all frequencies) (Jovanović & Bamieh, 2005), colored noise (Zare *et al.*, 2017) as well as harmonic (Jovanović, 2004), impulsive (Jovanovic & Bamieh, 2001; Vadarevu *et al.*, 2019), step functions excitations. These types of input can be used to model the effect of nonlinearity (Chevalier *et al.*, 2006; Zare *et al.*, 2017), the system disturbance (e.g., free-stream turbulence) (Ran *et al.*, 2019), and actuation (Jovanovic & Bamieh, 2001). The output can be defined in terms of velocity, vorticity, or wall pressure, etc. Then, the problem of interest is to analyze the output due to a given input which is determined through an input-output mapping $\phi = H(f)$. In the feedback interconnection of figure 1.1(b), the input is instead correlated to the output by a feedback loop $f = N(\phi)$ that can be defined in terms of e.g., another transfer function, system uncertainty, or nonlinear function. One of the main focuses of the thesis is the definition of this feedback pathway in a manner that augments linear analysis techniques with information about the nonlinear interactions in order to provide additional physical insights.

1.3 Organization and contributions

A schematic describing contributions and analysis techniques applied in this dissertation is summarized in figure 1.2 where the horizontal axis represents to what extent nonlinear interactions are modeled within the techniques applied while the vertical axis defines the relative complexity of the dynamics of the different flow configurations analyzed in particular chapter.

Chapter 2 provides the unifying analysis framework by introducing the spatio-temportal response operators along with the associated input-output and feedback interconnection based analysis techniques that will be employed throughout the dissertation. In order to illustrate the theory, this chapter also presents examples in which the analysis tools are applied to low-dimensional shear flow models. As shown in figure 1.2, remaining chapters are organized based on the primary analysis techniques that are applied and the flow configurations of interest. We now briefly summarize the contributions of each chapter.

Chapter 3 describes the application of traditional (open-loop) input-output analysis to the determination and analysis of convective velocity across a range of flow scales in turbulent

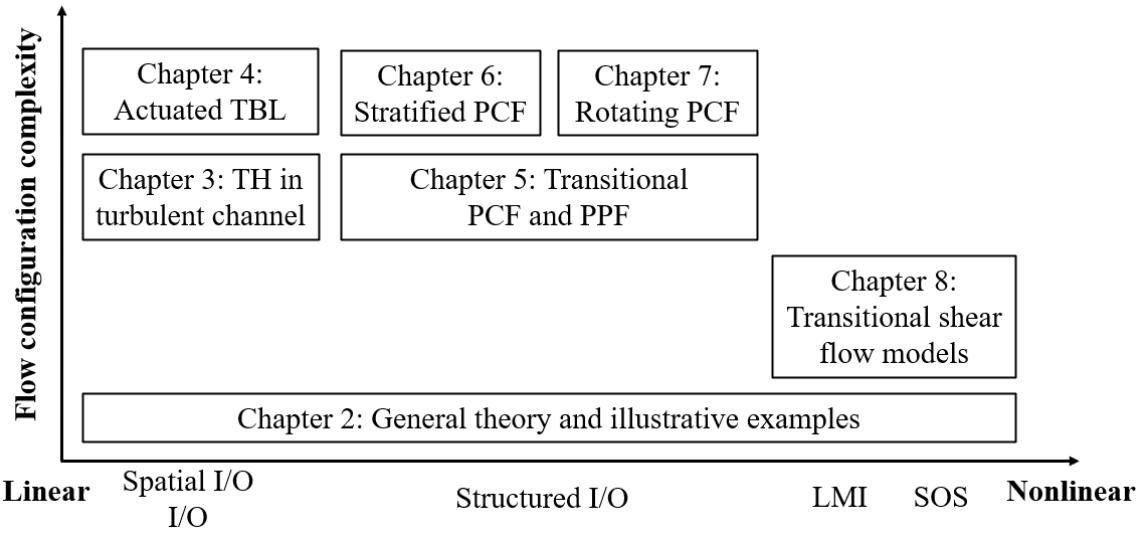

Figure 1.2: Organization of this dissertation. Acronym: I/O: input-output; TH: Taylor's hypothesis; TBL: turbulent boundary layer; PCF: plane Couette flow; PPF: plane Poiseuille flow; LMI: linear matrix inequalities; SOS: sum-of-squares.

channel flows with particular emphasis on the mechanism underlying the breakdown of Taylor's hypothesis in the near-wall region. The convective velocity for a fluctuating quantity associated with streamwise–spanwise wavelength pairs at each wall-normal location is obtained through the maximization of the power spectral density associated with the spatio-temporal response operator associated with the linear part of the Navier-Stokes equations with a turbulent mean profile. Delta-correlated Gaussian forcing provides the input forcing and the output is chosen as each velocity and vorticity components. We first demonstrate that the mean convective velocities computed in this manner agree well with those reported previously in the literature. We then exploit the analytical framework to probe the underlying mechanisms contributing to the local convective velocity at different wall-normal locations by isolating the contributions of each streamwise–spanwise wavelength pair (wall-parallel flow scale). The resulting analysis suggests that the behavior of the convective velocity in the near-wall region is influenced by large-scale structures further away from the wall. We then investigate the role of each linear term in the momentum equation to isolate the contribution of the pressure, mean shear, and viscous effects to the deviation of the convective velocity from the mean at each flow scale. Our analysis highlights the role of the viscous effects, particularly in regards to large channel

spanning structures whose influence extends to the near-wall region. We leverage these findings to provide a viscous correction to Taylor's hypothesis that greatly improves its accuracy in predicting the convective velocity of both the velocity and vorticity components in the near wall region. The results in this chapter have been published in the Journal of Fluid Mechanics (vol. 888, A32) (Liu & Gayme, 2020*a*) and Proceedings of the Eleventh International Symposium on Turbulence and Shear Flow Phenomenon (TSFP) 2019 (Liu & Gayme, 2019) and presented in the 71st Annual Meeting of the APS Division of Fluid Dynamics (vol. 65, 13) in 2018 (Liu & Gayme, 2018).

Chapter 4 employs the recently proposed one-way spatial integration technique (Towne & Colonius, 2015) to perform the spatial input-output analysis to model the streamwise propagation of large-scale structures in an actuated turbulent boundary layer. The transformation of the dynamics to reflect the spatial evolution of the flow field eliminates the ambiguity associated with the need to specify streamwise wavenumber in input–output (resolvent) analysis. This downstream marching also embeds a wall-normal dependent convective velocity for flow structures associated with a dominant temporal frequency. The application of interest is a turbulent boundary layer with a fixed frequency actuation signal applied in the outer layer to generate synthetic large-scale structures. The effect of the actuator on the flow is modeled as a body force associated with a dominant temporal frequency comprised of a Dirac delta function in the streamwise direction, a Gaussian function in the wall-normal direction that is uniform in the spanwise direction. The results are compared with the evolution of large-scale structures experimentally generated through dielectric barrier discharge plasma actuator attached to a plate mounted in the outer region of the flow. Large-scale structures obtained from this spatial input–output analysis show qualitative agreements with measurements from hot-wire measurements and a phase-locked analysis. These differences in convective velocity as a function of wall normal height lead to increasing inclination angle as the induced structures travel downstream. The ability of the framework to capture this demonstrates its benefit over the use of the traditional operator as that type of analysis has been shown to produce a single convective velocity over

wall-normal height given a single streamwise wavenumber and actuation frequency pair. The detailed velocity field enables us to perform a quadrant trajectory analysis to assess the similarity between these actuated large-scale structures and the large-scale structures naturally occurring in a canonical wall-bounded turbulent flow. This observation highlights the promise of a spatial framework in modeling and analyzing large-scale structures in turbulent boundary layers through a spatially localized perturbation with a dominant temporal frequency. These results are going to appear as a conference proceeding at American Institute of Aeronautics and Astronautics (AIAA) Aviation 2021 Forum (p. 2873) (Liu *et al.*, 2021).

Chapters 5-7 focus on transitional or intermittent flow regimes. In the analyses of these flows, we employ the notion of feedback interconnection discussed above to incorporate properties of the nonlinearity into the spatio-temporal frequency response analysis paradigm. In particular, these chapters highlight the benefit of such an analytical technique in analyzing the wall-parallel length scales associated with the recently observed oblique turbulent bands in very large channel DNS or experiments in the transitional or intermittent regime of plane Couette flow, plane Poiseuille flow, vertically stratified plane Couette flow, and spanwise rotating plane Couette flow.

Chapter 5 introduces structured input-output analysis, which develops a feedback interconnection between the linearized operator and a structured input-output gain operator to include the effect of nonlinearity. This framework employs a *structured* singular value-based approach that preserves certain input–output properties of the nonlinear forcing function in an effort to recover the larger range of key flow features identified through nonlinear analysis, experiments, and direct numerical simulation (DNS) of transitional channel flows. Application of this method to transitional plane Couette and plane Poiseuille flows leads to the identification of not only the streamwise coherent structures predicted through traditional input–output approaches but also characterization of the oblique flow structures as those requiring the least energy to induce transition in agreement with DNS studies, and nonlinear optimal perturbation analysis. The proposed approach also captures the recently observed oblique turbulent bands that have been

linked to transition in experiments and DNS with very large channel size. The ability to identify the larger amplification of the streamwise varying structures predicted from DNS and nonlinear analysis in both flow regimes suggests that the lift-up mechanism, which is known to dominate the linear operator, is weakened by the componentwise structure of nonlinearity maintained within structured approach. Capturing this key nonlinear mechanism enables the prediction of the wider range of known transitional flow structures within the analytical input–output modeling paradigm. The manuscript reporting this framework has been submitted for publication. A preprint version is available at (arXiv:2104.00062) (Liu & Gayme, 2021*a*). This work will also be presented at the AIAA Aviation 2021 Forum (Liu & Gayme, 2021*b*)

Chapter 6 then extends the structured input-output analysis to include density stratification and employs it to analyze the characteristic horizontal length scales of flow structures in stratified plane Couette flow. This approach predicts high amplification associated with wavelengths of oblique turbulent bands observed in a very large channel with extents $\sim O(100)$ times of channel half-height at the low-Reynolds number (Re) low-bulk Richardson number (Ri_b) intermittent regime. At high-Re high-Ri_b intermittent regime, this approach also identifies quasi-horizontal flow structures resembling turbulent-laminar layers that are associated with amplification close to oblique turbulent bands. This approach further suggests the threshold value of the Miles-Howard theorem ($Ri_b > 0.25$) is associated with suppressing the amplification of streamwise dependent flow structures at the Prandtl number close to one ($Pr \approx 1$) and this behavior is robust against a wide range of Re. At $Pr \ll 1$, the amplification is determined by $PrRi_b$, and a larger Ri_b is required to suppress the prevalence of streamwise dependent flow structures than $Pr \approx 1$. At $Pr \gg 1$, this approach identifies another quasi-horizontal flow structure independent of Ri_b. By decomposing input-output pathways into each velocity and density component, we show these quasi-horizontal flow structures at $Pr \gg 1$ are associated with density. The importance of this density-associated flow structure at $Pr \gg 1$ is further demonstrated by the analytical scaling of amplification over Re and Pr under the passive scalar and streamwise constant assumptions.

Chapter 7 then employs structured input-output analysis to examine a mathematical analogy between rotating plane Couette flow and stratified plane Couette flow. In particular, we focuses on a mathematical equivalence between two-dimensional three-component (2D/3C, no streamwise variation) spanwise rotating PCF and two-dimensional (2D, no streamwise variation and no streamwise velocity) vertically stratified PCF. At relatively slow rotation, the structured input-output analysis captures the streamwise and spanwise wavelengths of the oblique turbulent bands in rotating PCF similar to the observation in the stratified PCF. Increasing the stabilizing effect of rotation and stratification associated with the mathematical equivalence, this approach quantifies that stratification is suppressing the amplification of streamwise dependent flow structures faster than rotation. The largest amplification of streamwise constant (2D/3C) flow structures in rotating PCF is not influenced by the rotation number, which suggests additional mathematical equivalence. We then extend (2D/3C-R=2D-S) to a mathematical equivalence between stratified and rotating PCF 2D/3C rotating PCF. We illustrate one additional mathematical equivalence between 2D/3C rotating PCF with passive scalar and 2D/3C stratified PCF and demonstrate the validity of this theoretical behavior using structured input-output analysis.

Chapter 8 proposes a linear matrix inequality based method to provide a provable Reynolds number-dependent bound on the amplitude of perturbations a flow can sustain while maintaining the laminar state. We construct quadratic constraints of the nonlinear term that is restricted by system physics to be energy-conserving (lossless) and to have bounded input–output energy. The problem of computing the region of attraction of the laminar state (set of safe perturbations) and permissible perturbation amplitude are then reformulated as Linear Matrix Inequalities (LMI), which provide a more computationally efficient solution than prevailing nonlinear approaches based on the sum of squares programming. We apply our approach to low-dimensional nonlinear shear flow models for a range of Reynolds numbers. The results from our analytically derived bounds are consistent with the bounds identified through exhaustive simulations. However, they have the added benefit of being achieved at a much lower computational cost and providing a provable guarantee that a certain level of perturbation is permissible. These results have been

published in Physical Review E (vol. 102, 063108) (Liu & Gayme, 2020*b*) and presented in the 73rd Annual Meeting of the APS Division of Fluid Dynamics in 2020 (vol. 65, 13) (Liu & Gayme, 2020*c*).

This dissertation is concluded in chapter 9, where future work directions are also discussed. The notations in each chapter are independent and self-consistent.

Chapter 2

Input-output and feedback interconnection based analyses

> "I couldn't reduce it to the freshman level. That means we don't really understand it."
>
> Richard Feynman[1]

This chapter introduces the basic concept and analysis tools based on input-output and feedback interconnection. Section 2.1 describes the input-output analysis that is used in chapters 3-4. Then we describe the feedback interconnection and structured singular value in section 2.2 that is used in chapters 5-7. Then, we apply these tools to an illustrative low-dimensional shear flow model in section 2.3. The following sections demonstrate tools employed in chapter 8 that includes the linear matrix inequality in § 2.4 and the unified idea to characterize nonlinearity using input-output relationship in § 2.5

2.1 Input-output analysis based on frequency response operator

In this section, we will introduce the input-output analysis and spatio-temporal frequency response operator that will be analyzed in chapters 3 and 4 in wall-bounded turbulent flows through different realizations and their associated input-output pairs.

[1](Goodstein, 1989, p. 75)

Here, we start from a generalized (or descriptor) state-space model:

$$E\frac{d}{dt}\psi = A\psi + Bf, \tag{2.1}$$

$$\phi = C\psi. \tag{2.2}$$

Here, ψ is the state vector, f is the input vector, and ϕ is the output vector. The state ψ, input f, and output ϕ are chosen based on the problem of interest, and one example is to choose state ψ as wall-normal velocity and vorticity, input f as the body force applied in the momentum equation and output ϕ as the velocity. These vectors can depend on space and time variables (x, y, z, t). The matrices A, B, C, E are state-space matrices that express the system dynamics. These matrices can be obtained by Navier-Stokes equations linearized around a base flow, and they typically depend on the flow configuration, such as the background mean shear and the Reynolds number. In the formulation using the primitive variables with velocity and pressure, E matrix is not equal to the identity matrix I and it is singular. Instead, the formulation using wall-normal velocity and vorticity will eliminate the pressure and enforce the divergence-free constraint on velocity, which directly ends up $E = I$. The precise formulation will be detailed in the following chapters for each flow configuration. These matrices A, B, C, E can contain operators in the spatial domain (x, y, z) and typically they are not dependent on t.

For certain spatial directions, such as the wall-parallel directions (x and z) in channel flow configurations, we can exploit shift-invariance in these two directions. We can also sometimes assume temporal shift invariance, which allows us to define the spatio-temporal Fourier transform in x, z, and t domains:

$$\widehat{\psi}(y; k_x, k_z, \omega) := \int_{-\infty}^{\infty}\int_{-\infty}^{\infty}\int_{-\infty}^{\infty} \psi(x, y, z, t) e^{-\mathrm{i}(k_x x + k_z z + \omega t)}\, dx\, dz\, dt. \tag{2.3}$$

Here, $\mathrm{i} = \sqrt{-1}$ is the imaginary unit. k_x and k_z are respectively wavenumber (spatial frequency) in the spatial domain x and z. ω is temporal frequency. The shift-invariance in the temporal

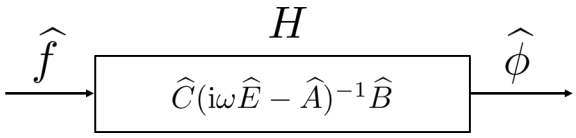

Figure 2.1: Spatio-temporal frequency response operator that maps input $\widehat{f}$ to output $\widehat{\phi}$.

domain can be justified in the following two manners. We can assume that the harmonic input is applied in $-\infty < t < \infty$ and then the initial condition does not play a role. In another way, we can also assume the forcing is applied in $0 \leq t < \infty$ with zero initial states, $\psi(t=0) = 0$, and the transient response dies out as $t \to \infty$ assuming the stability of the operator $\widehat{A}$. We can also replace Fourier transform in the time domain as Laplace transform to relax the shift-invariance in t and analyze the response due to initial conditions.

Here, we can define the spatio-temporal frequency response operator $H(y; k_x, k_z, \omega)$ of the system in equation (2.2) that maps the input forcing $\widehat{f}(y; k_x, k_z, \omega)$ towards the output $\widehat{\phi}(y; k_x, k_z, \omega)$ at the same spatial-temporal wavenumber-frequency triplet; i.e., $\widehat{\phi}(y; k_x, k_z, \omega) = H(y; k_x, k_z, \omega)\widehat{f}(y; k_x, k_z, \omega)$:

$$H(y; k_x, k_z, \omega) = \widehat{C}(y; k_x, k_z)(\mathrm{i}\omega\widehat{E} - \widehat{A}(y; k_x, k_z))^{-1}\widehat{B}(y; k_x, k_z). \tag{2.4}$$

For the spatial direction such as the wall-normal direction that is not suitable to perform such a Fourier transform, we can employ certain numerical discretization to approximate the underlying operators. Then, the dimension of these vectors $\widehat{f}$, $\widehat{\psi}$, and $\widehat{\phi}$ and the size of these $\widehat{A}$, $\widehat{B}$, $\widehat{C}$, $\widehat{E}$ matrices typically depend on the numerical discretization in the wall-normal direction.

2.2 Feedback interconnection and structured singular value

The spatio-temporal frequency response operator described in section 2.1 is able to provide a lot of insight into characteristic length and time scales in wall-bounded shear flows. However, the input forcing that drives the linearized dynamics is typically not explicitly correlated with the output variable. In this subsection, we will describe the feedback interconnection between spatio-temporal frequency response operator introduced in section 2.1 and an uncertainty model

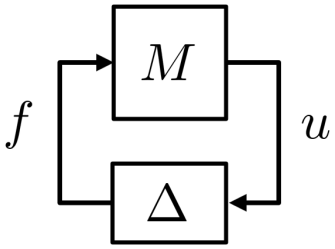

Figure 2.2: Illustration of feedback interconnection between M and Δ. M can also depend on frequency as $M(\mathrm{i}\omega)$.

to account for nonlinearity. In particular, we introduce the stability of feedback interconnection and its analysis based on structured singular value following Packard & Doyle (1993), which will form the basis of structured input-output analysis in chapters 5-7.

We start from a matrix $M \in \mathbb{C}^{n\times n}$ that is feedback interconnected with an uncertain matrix $\Delta \in \underline{\Delta}$ as shown in figure 2.2. The precise form of Δ is typically not known, but we may know a set $\underline{\Delta}$ containing these uncertain matrix. This set depends on the problem of interest and the formulation of M and the M-Δ feedback interconnection. The bottom block Δ can be used to model the system uncertainty, the nonlinearity, or environmental disturbance, and it indicates the relationship $f = \Delta u$. The matrix M here can be considered as $M(\mathrm{i}\omega)$ evaluated at a certain frequency that maps f to u; i.e., $u = Mf$. This feedback interconnection can then be combined as $(I - M\Delta)u = 0$. When $\det(I - M\Delta) = 0$, there exists a non-trivial solution $u \neq 0$ and u can be associated with any magnitude; i.e., u is unbounded. For this case associated with unbounded solutions, we can term that the feedback interconnection between M-Δ as 'unstable'. When $\det(I - M\Delta) \neq 0$, we have $u = 0$ is identically zero, which can be considered as 'stable'.

One important question is to quantify the smallest magnitude $\Delta \in \underline{\Delta}$ that will lead to instability of this M-Δ feedback interconnection. This suggests how far this feedback interconnection is away from instability and will provide insight into reducing the internal or external disturbance level. The smallest destabilizing Δ can be quantified by the structured singular value defined in definition 2.1.

Definition 2.1 *(Packard & Doyle, 1993, definition 3.1) For $M \in \mathbb{C}^{n\times n}$, $\mu_{\underline{\Delta}}(M)$ is defined:*

$$\mu_{\underline{\Delta}}(M) := \frac{1}{min\{\bar{\sigma}[\Delta] \,:\, \Delta \in \underline{\Delta},\, det[I - M\Delta] = 0\}}, \tag{2.5}$$

unless no $\Delta \in \underline{\Delta}$ makes $I - M\Delta$ singular, in which case $\mu_{\underline{\Delta}}(M) := 0$. Here, $\bar{\sigma}[\cdot]$ represents the largest singular value, $det[\cdot]$ is the determinant of the argument, and I is the identity matrix.

The quantity $1/\mu_{\underline{\Delta}}(M)$ in definition 2.1 directly quantifies the smallest Δ within a given uncertainty set $\underline{\Delta}$ that will cause the instability of the M-Δ feedback interconnection; i.e., $\det[I - M\Delta] = 0$.

The structured singular value in definition 2.1 has a close relation with spectral radius and the largest singular value; see e.g, (Packard & Doyle, 1993, p. 73) and (Zhou *et al.*, 1996, p. 269). In particular, if $\underline{\Delta} = \{\delta I_{n\times n} : \delta \in \mathbb{C}\}$, then $\mu_{\underline{\Delta}}(M) = \rho(M)$ with $\rho(\cdot)$ denoting spectral radius. When $\underline{\Delta} = \mathbb{C}^{n\times n}$, then $\mu_{\underline{\Delta}}(M) = \bar{\sigma}(M)$ with $\bar{\sigma}(\cdot)$ denoting the largest singular value. For a general $\underline{\Delta}$ such that $\{\delta I_{n\times n} : \delta \in \mathbb{C}\} \subseteq \underline{\Delta} \subseteq \mathbb{C}^{n\times n}$, we have the inequality

$$\rho(M) \leq \mu_{\underline{\Delta}}(M) \leq \bar{\sigma}(M). \tag{2.6}$$

The inequality in (2.6) directly indicates the importance of structured singular value in studying transitional wall-bounded shear flows. It is known that the linearized operator associated with certain wall-bounded shear flows (e.g., plane Couette flow and plane Poiseuille flow) is *nonnormal* (Trefethen *et al.*, 1993), which results in a gap between the spectral radius and the largest singular value based on the following theorem 2.2 that is an equivalent definition of a normal matrix.

Theorem 2.2 *(Horn & Johnson, 1991, p. 157) The matrix $M \in \mathbb{C}^{n\times n}$ is normal ($M^*M = MM^*$) if and only if $\sigma_i(M) = |\lambda_i(M)|$, $\forall i = 1, ..., n$ where $\sigma_i(M)$ are the singular values with $\sigma_1(M) \geq \cdots \geq \sigma_n(M)$ and $\lambda_i(M)$ are eigenvalues with $|\lambda_1(M)| \geq \ldots |\lambda_n(M)|$.*

This directly indicates that the structured singular value as a quantity between spectral radius and the largest singular value is likely to provide further insight into transitional wall-bounded

shear flows.

Here, we briefly describe the algorithm in computing the upper bound of structured singular value. We introduce a scaling matrix set $\underline{D}$ such that the $D \in \underline{D}$, $D^* = D \succ 0$ commute with $\Delta \in \underline{\Delta}$; i.e., $D\Delta = \Delta D$. After scaling matrix M as DMD^{-1}, the structured singular value does not change based on the following theorem 2.3.

Theorem 2.3 *(Packard & Doyle, 1993, theorem 3.8) Given matrix $M \in \mathbb{C}^{n\times n}$, uncertainty set $\underline{\Delta}$, and scaling matrix set $\underline{D}$ such that the $D \in \underline{D}$ and $D^* = D \succ 0$ commutes with $\Delta \in \underline{\Delta}$; i.e., $D\Delta = \Delta D$. Then, $\mu_{\underline{\Delta}}(M) = \mu_{\underline{\Delta}}(DMD^{-1})$.*

Proof: This can be shown by the property that D and Δ commute and the property of determinant:

$$det(I - M\Delta) = det(I - MD^{-1}\Delta D) \tag{2.7a}$$

$$= det(D^{-1} - MD^{-1}\Delta)det(D) \tag{2.7b}$$

$$= det(D)det(D^{-1} - MD^{-1}\Delta) \tag{2.7c}$$

$$= det(I - DMD^{-1}\Delta) \tag{2.7d}$$

Thus, using the definition 2.1, we have $\mu_{\underline{\Delta}}(M) = \mu_{\underline{\Delta}}(DMD^{-1})$. □

However, scaling the matrix M as DMD^{-1} may change the largest singular value, which gives the following inequality to compute the upper bound of structured singular value (Zhou *et al.*, 1996, equation (11.14)):

$$\mu_{\underline{\Delta}}(M) = \mu_{\underline{\Delta}}(DMD^{-1}) \leq \inf_{D\in\underline{D}} \bar{\sigma}(DMD^{-1}). \tag{2.8}$$

Then, we move further to replace M as a general frequency response operator $M(\mathrm{i}\omega)$ and the stability of the feedback interconnection can be measured by the upper bound of the structured singular value over temporal frequency $\omega \in \mathbb{R}$ based on the small-gain theorem (Zhou *et al.*,

1996, theorem 11.8).

Proposition 2.4 (Small Gain Theorem) *The feedback interconnection $M(i\omega)$-Δ shown in figure 2.2 is stable for all $\Delta \in \underline{\Delta}$ with $\|\Delta\|_\infty := \sup_{\omega\in\mathbb{R}} \bar{\sigma}[\Delta] < \frac{1}{\beta}$ if and only if:*

$$\sup_{\omega\in\mathbb{R}} \mu_{\underline{\Delta}}\left[M(i\omega)\right] \leq \beta. \tag{2.9}$$

2.3 An illustrative example

This section will illustrate analyses based on input-output and feedback interconnections described in § 2.1 and § 2.2. This section will also provide some illustrative examples of their computation with the MATLAB command.

We consider a three-dimensional ODE system previously denoted as (W') in (Baggett & Trefethen, 1997), which is adapted from a four-dimensional model originally proposed by (Waleffe, 1997). We will also study the behavior of this (W') model in chapter 8. The dynamics of this system is described as:

$$\frac{d}{dt}\begin{bmatrix} u \\ v \\ w \end{bmatrix} = \begin{bmatrix} -Re^{-1} & 1 & 0 \\ 0 & -Re^{-1} & 0 \\ 0 & 0 & -Re^{-1} \end{bmatrix}\begin{bmatrix} u \\ v \\ w \end{bmatrix} + \begin{bmatrix} 0 & 0 & -w \\ 0 & 0 & w \\ w & -w & 0 \end{bmatrix}\begin{bmatrix} u \\ v \\ w \end{bmatrix}. \tag{2.10}$$

We consider the origin $[0,0,0]^\mathsf{T}$ that is an equilibrium in (2.10) and then decompose this system as linearized dynamics in state-space and nonlinearity as the input forcing:

$$\frac{d}{dt}\psi = A\psi + Bf, \tag{2.11a}$$

$$\phi = C\psi, \tag{2.11b}$$

where

$$\phi = \psi := \begin{bmatrix} u \\ v \\ w \end{bmatrix}, \quad A := \begin{bmatrix} -Re^{-1} & 1 & 0 \\ 0 & -Re^{-1} & 0 \\ 0 & 0 & -Re^{-1} \end{bmatrix}, \quad f := \begin{bmatrix} 0 & 0 & -w \\ 0 & 0 & w \\ w & -w & 0 \end{bmatrix}\begin{bmatrix} u \\ v \\ w \end{bmatrix} =: \begin{bmatrix} f_x \\ f_y \\ f_z \end{bmatrix}, \tag{2.12a-c}$$

$$B := I_{3\times 3}, \quad C := I_{3\times 3}, \tag{2.12d,e}$$

where I is the identity matrix with size indicated in its subscript.

Here, this model is constructed to have several properties that can reflect the qualitative phenomena of wall-bounded shear flows. The origin is a stable equilibrium for $Re \in \mathbb{R}^+$, which can be viewed from the diagonal term of matrix A. The off-diagonal term in matrix A results in that A is non-normal; i.e., $A^*A \neq AA^*$. The nonlinearity is quadratic and satisfies the energy-conserving property $\phi^{\mathsf{T}} f = 0$, which can be viewed from the skew-symmetric matrix associated with f. This is reminiscent of the energy-conserving property of nonlinearity in the Navier-Stokes equations; e.g., employed in energy stability analysis (Joseph, 2013; Straughan, 2013). For all results in this chapter, we fix the parameter $Re = 100$ the same as (Baggett & Trefethen, 1997) unless otherwise mentioned. All of the sample code implementations in this section is in MATLAB.

2.3.1 Frequency response operator

For this ODE-based model, we only perform the Fourier transform in the temporal domain. We can directly form the frequency response operator as:

$$H(\mathrm{i}\omega) = C(\mathrm{i}\omega I_{3\times 3} - A)^{-1} B, \tag{2.13}$$

which maps the input $\widehat{f}(\omega)$ to the output $\widehat{\phi}(\omega)$ at each frequency. Analyzing this frequency response operator is able to quantify the influence of input forcing at each frequency.

Additional insight can be obtained by modifying the input and output operators B and C to isolate each component of input-output pathways following the procedure of Jovanović & Bamieh (2005). Here, we demonstrate this idea by defining a frequency response operator $H_{ij}(\mathrm{i}\omega)$ that maps the input f_j $(j = x, y, z)$ to the output i $(i = u, v, w)$:

$$H_{ij}(\mathrm{i}\omega) = C_i \left(\mathrm{i}\omega I_{3\times 3} - A\right)^{-1} B_j \tag{2.14}$$

with

$$B_x := \widehat{\mathcal{B}} \begin{bmatrix} 1 & 0 & 0 \end{bmatrix}^{\mathsf{T}}, \quad B_y := B \begin{bmatrix} 0 & 1 & 0 \end{bmatrix}^{\mathsf{T}}, \quad B_z := B \begin{bmatrix} 0 & 0 & 1 \end{bmatrix}^{\mathsf{T}}, \tag{2.15a}$$

$$C_u := \begin{bmatrix} 1 & 0 & 0 \end{bmatrix} C, \quad C_v := \begin{bmatrix} 0 & 1 & 0 \end{bmatrix} C, \quad C_w := \begin{bmatrix} 0 & 0 & 1 \end{bmatrix} C. \tag{2.15b}$$

Then, we compute the $\mathcal{H}_\infty$ norm for each frequency response operator:

$$\|H_{ij}\|_\infty = \sup_{\omega \in \mathbb{R}} \bar{\sigma}[H_{ij}], \tag{2.16}$$

where $\bar{\sigma}$ is the largest singular value and sup represents the supremum (least upper bound) operation. This $\|\cdot\|_\infty$ can be computed by the command `hinfnorm` in the Robust Control Toolbox (Balas *et al.*, 2005). By parsing a state-space model, this command `hinfnorm` will adaptively sample frequency to compute its upper bound. For this model, we can obtain this by the sample code in Example 1:

$$\begin{bmatrix} \|H_{ux}\|_\infty & \|H_{uy}\|_\infty & \|H_{uz}\|_\infty \\ \|H_{vx}\|_\infty & \|H_{vy}\|_\infty & \|H_{vz}\|_\infty \\ \|H_{wx}\|_\infty & \|H_{wy}\|_\infty & \|H_{wz}\|_\infty \end{bmatrix} = \begin{bmatrix} 100 & 10000 & 0 \\ 0 & 100 & 0 \\ 0 & 0 & 100 \end{bmatrix}. \tag{2.17}$$

```
%%Example 1: componentwise input-output analysis
Re=100; %%Reynolds number
%%Form linear system with A, B, and C
A=[-1/Re, 1,0;
    0, -1/Re,0;
    0,0,-1/Re];
B=eye(3,3);
C=eye(3,3);
%%----Componentwise analysis
for i=1:3
    for j=1:3
        sys=ss(A,B(:,j),C(i,:),0); %%Form state-space model H_{ij}
        H_ij_inf(i,j)=hinfnorm(sys);
    end
end
```

This type of componentwise analysis and analytical scaling of frequency response operator will be employed in chapters 5-7.

Actually, for the frequency response operator defined in (2.14), we can also obtain the analytical scaling over Re by firstly writing the componentwise frequency response operator as:

$$\begin{bmatrix} H_{ux} & H_{uy} & H_{uz} \\ H_{vx} & H_{vy} & H_{vz} \\ H_{wx} & H_{wy} & H_{wz} \end{bmatrix} = \begin{bmatrix} Re(\mathrm{i}\omega Re+1)^{-1} & Re^2(\mathrm{i}\omega Re+1)^{-2} & 0 \\ 0 & Re(\mathrm{i}\omega Re+1)^{-1} & 0 \\ 0 & 0 & Re(\mathrm{i}\omega Re+1)^{-1} \end{bmatrix}. \quad (2.18)$$

Then, we note that

$$\sup_{\omega\in\mathbb{R}} \bar{\sigma}[(\mathrm{i}\omega Re+1)^{-1}] = \sup_{\omega\in\mathbb{R}} \frac{1}{\sqrt{\omega^2 Re^2+1}} = 1. \quad (2.19)$$

Similarly, we can also have $\sup_{\omega\in\mathbb{R}} \bar{\sigma}[(\mathrm{i}\omega Re+1)^{-2}] = 1$. Thus, we can obtain:

$$\begin{bmatrix} \|H_{ux}\|_\infty & \|H_{uy}\|_\infty & \|H_{uz}\|_\infty \\ \|H_{vx}\|_\infty & \|H_{vy}\|_\infty & \|H_{vz}\|_\infty \\ \|H_{wx}\|_\infty & \|H_{wy}\|_\infty & \|H_{wz}\|_\infty \end{bmatrix} = \begin{bmatrix} Re & Re^2 & 0 \\ 0 & Re & 0 \\ 0 & 0 & Re \end{bmatrix}, \quad (2.20)$$

which is also consistent with numerical results in (2.17) at $Re = 100$. This analytical scaling law was analogous to (Jovanović, 2004, theorem 11), and we extend this to stratified wall-bounded flow under the passive scalar assumption in theorem 6.2 of chapter 6. We also demonstrate that using an Reynolds number independent operator to modify the output, their Reynolds number scaling remains the same as shown in theorems 5.4 and 6.2.

2.3.2 Structured singular value

We then demonstrate the computation of structured singular value, where we set $M = H(\mathrm{i}\,0) = C(-A)^{-1}B = (-A)^{-1}$ corresponding to the frequency response operator evaluated at $\omega = 0$.

We then define several examples of the set of structured uncertainty and make the connection with spectral radius and the largest singular value. We consider:

$$\underline{\Delta}_1 := \{\delta I_{3\times 3} : \ \delta \in \mathbb{C}\}, \quad (2.21a)$$

$$\underline{\Delta}_2 := \{\mathrm{diag}(\delta_1, \delta_2, \delta_3) : \ \delta_1 \in \mathbb{C}, \ \delta_2 \in \mathbb{C}, \ \delta_3 \in \mathbb{C}\}, \quad (2.21b)$$

$$\underline{\Delta}_3 := \{\Delta : \ \Delta \in \mathbb{C}^{3\times 3}\}. \quad (2.21c)$$

$\rho(M)$	$\mu_{\underline{\Delta}_1}(M)$	$\mu_{\underline{\Delta}_2}(M)$	$\mu_{\underline{\Delta}_3}(M)$	$\bar{\sigma}(M)$
100	100	100	10001	10001

Table 2.1: Values of spectral radius, structured singular value associated with uncertainty set $\underline{\Delta}_1$, $\underline{\Delta}_2$, $\underline{\Delta}_3$, and the largest singular value of matrix M.

The first set $\underline{\Delta}_1$ defines a set of uncertainty that is repeated complex scalar. The structured singular value computed with this set of uncertainty will be the same as the spectral radius. The last set of $\underline{\Delta}_3$ defines a set of uncertainty that is a full block complex matrix, and the obtained structured singular value will equal to the largest singular value. The set of uncertainty $\underline{\Delta}_2$ is three non-repeated complex scalars. This can be viewed as a relaxation of the repeated complex scalar in $\underline{\Delta}_1$; i.e., each component δ_1, δ_2, δ_3 of the perturbation $\Delta_2 \in \underline{\Delta}_2$ does not necessarily repeat). One off-the-shelf tool to compute structured singular values is the `mussv` command in the Robust Control Toolbox (Balas *et al.*, 2005) of MATLAB. The allowed block structure of $\underline{\Delta}$ (`BlockStructure` argument) of the command `mussv` includes the repeated diagonal complex (or real) scalar perturbation and the complex full block perturbation. For the repeated complex full block perturbation, they can be relaxed as the (not necessarily repeated) complex full block perturbation with matched size.

These quantities can be computed using the following commands of MATLAB in Example 2,

```
%%Example 2: structured singular value of a matrix
A=[-1/100,1,0;
     0, -1/100,0;
     0,0,-1/100];
M=inv(-A);
rho=max(abs(eig(M))); %%rho=100
mu1=mussv(M,[3,0]); %%mu1=100
mu2=mussv(M,[1,1;1,1;1,1]); %%mu2=100
mu3=mussv(M,[3,3]); %%mu3=10001
sigma_bar=max(svd(M)); %%sigma_bar=10001
```

The second argument `BlockStructure` of command `mussv` is specifying the set of uncertain $\underline{\Delta}$. This gives results shown in table 2.1.

Scaling matrices corresponding to these three sets of uncertainties can be defined as:

$$\underline{D}_1 := \{D_1 : \quad D_1 \in \mathbb{C}^{3\times 3}, D_1^* = D_1 \succ 0\}, \tag{2.22a}$$

$$\underline{D}_2 := \{\mathrm{diag}[d_1, d_2, d_3] : \ d_i \in \mathbb{R}, \ d_i > 0, \ i = 1, 2, 3\}, \tag{2.22b}$$

$$\underline{D}_3 := \{d\, I_{3\times 3}, \quad d \in \mathbb{R}, \quad d > 0\}. \tag{2.22c}$$

Then, we have:

$$D_i \Delta_i = \Delta_i D_i, \quad i = 1, 2, 3, \quad \forall\, D_i \in \underline{D}_i \ \text{ and } \ \Delta_i \in \underline{\Delta}_i. \tag{2.23}$$

The command `mussvextract` in Robust Control Toolbox (Balas *et al.*, 2005) can also provide the information of D in (2.8) in computing the upper bound of structured singular value.

2.3.3 Structured input-output analysis

We formulate system in (2.10) as the feedback interconnection between the linearized dynamics and nonlinearity as input forcing f, which can be decomposed as:

$$f = \begin{bmatrix} f_x & f_y & f_z \end{bmatrix}^{\mathsf{T}} = diag(w, w, w) M_f \phi, \tag{2.24}$$

where

$$M_f =: \begin{bmatrix} 0 & 0 & -1 \\ 0 & 0 & 1 \\ 1 & -1 & 0 \end{bmatrix}. \tag{2.25}$$

The nonlinearity f is obtained from ϕ by multiplying a matrix M_f and then times the block diagonal matrix formed by w. It is analytically convenient to combine the linear mapping M_f to form a new frequency response operator as the top loop in figure 2.2(b):

$$H_f(\mathrm{i}\omega) = M_f\, H(\mathrm{i}\omega). \tag{2.26}$$

Then in the computation of the structured singular value, the term $\mathrm{diag}(w, w, w)$ is relaxed as $\Delta_w := \mathrm{diag}(w_\xi, w_\xi, w_\xi)$ that is uncoupled from the output (u, v, w), but it still imposes the

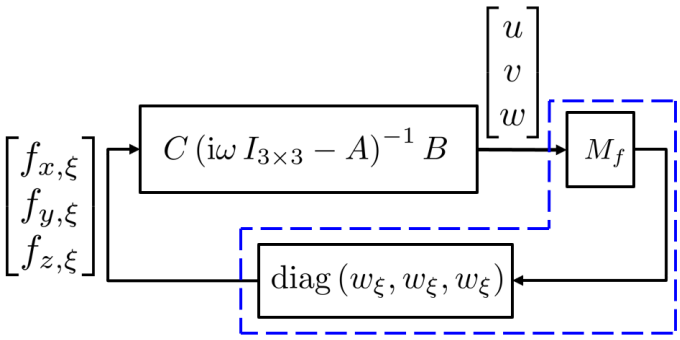

Figure 2.3: Feedback interconnection of the linearized dynamics in (2.11) and model of nonlinearity forcing in (2.27). The blocks inside of the blue dashed lines (– –) maps each component of velocity $[u, v, w]^{\mathsf{T}}$ to each component of modeled forcing $[f_{x,\xi}, f_{y,\xi}, f_{z,\xi}]^{\mathsf{T}}$.

$\sup_{\omega\in\mathbb{R}} \mu_{\underline{\Delta}_1}[H_f]$	$\sup_{\omega\in\mathbb{R}} \mu_{\underline{\Delta}_2}[H_f]$	$\sup_{\omega\in\mathbb{R}} \mu_{\underline{\Delta}_3}[H_f]$	$\sup_{\omega\in\mathbb{R}} \bar{\sigma}[H_f]$
992	1002	9920	9900

Table 2.2: Values of the upper bound of structured and unstructured singular value over frequency.

componentwise structure in the feedback loop. This gives a model of nonlinearity as:

$$f_\xi = \begin{bmatrix} f_{x,\xi} & f_{y,\xi} & f_{z,\xi} \end{bmatrix}^{\mathsf{T}} \tag{2.27a}$$

$$= diag(w_\xi, w_\xi, w_\xi) M_f \phi \tag{2.27b}$$

$$= \Delta_w M_f \phi. \tag{2.27c}$$

This block diagonal structure of uncertainty is shown in the bottom loop of figure 2.2(b). We can also see that Δ_w belongs to the set $\underline{\Delta}_1$ defined before; i.e., $\Delta_w \in \underline{\Delta}_1$.

Table 2.2 then presents results of $\sup_{\omega\in\mathbb{R}} \mu_{\underline{\Delta}_1}[H_f]$, $\sup_{\omega\in\mathbb{R}} \mu_{\underline{\Delta}_2}[H_f]$, $\sup_{\omega\in\mathbb{R}} \mu_{\underline{\Delta}_3}[H_f]$, and $\|H_f\|_\infty$. Here, we parse the state-space model into the command `mussv` and `hinfnorm` both in Robust Control Toolbox (Balas *et al.*, 2005), and they can adaptively sample temporal frequency to compute the upper bound. Here, we similarly observe that $\sup_{\omega\in\mathbb{R}} \mu_{\underline{\Delta}_1}[H_f] \leq \sup_{\omega\in\mathbb{R}} \mu_{\underline{\Delta}_2}[H_f] \leq \sup_{\omega\in\mathbb{R}} \mu_{\underline{\Delta}_3}[H_f]$. Note that from the definition of uncertainty set $\underline{\Delta}_3$, $\sup_{\omega\in\mathbb{R}} \mu_{\underline{\Delta}_3}[H_f]$ is expected to be equal to $\sup_{\omega\in\mathbb{R}} \bar{\sigma}[H_f]$. Their difference in table 2.2 may be attributed to the different upper bound algorithms employed in these two commands, where `mussv` might be slightly conservative.

```
1 %%Example 3: structured singular value of a frequency response
```

```
%%operator expressed by state-space model
Re=100; %%Reynolds number
%%Form linear system with A, B, and C
A=[-1/Re, 1,0;
    0, -1/Re,0;
    0,0,-1/Re];
B=eye(3,3);
C=eye(3,3);
%%matrix M_f
M_f=[0,0,-1;
    0,0,1;
    1,-1,0];

sys=ss(A,B,M_f*C,zeros(3,3));

%%3-by-3 repeated, diagnoal complex scalar perturbation
mu1_freq=mussv(sys,[3,0]);
mu1_freq=max(mu1_freq(1).ResponseData);%%mu1_freq=992

%%3 non-repeated 1-by-1 complex perturbation
mu2_freq=mussv(sys,[1,1; 1,1; 1,1]);
mu2_freq=max(mu2_freq(1).ResponseData);%%mu2_freq=1002

%%3-by-3 complex full block perturbation
mu3_freq=mussv(sys,[3,3]);
mu3_freq=max(mu3_freq(1).ResponseData);%%mu3_freq=9920

H_inf=hinfnorm(sys); %%H_inf=9900
```

2.4 Linear matrix inequality

In this section, we will formulate the linear matrix inequalities (LMI) that can be employed to study the stability, and computing the singular value as well as the structured singular value. Linear matrix inequality is a generalization of linear inequalities such as $Ax \leq b$, where $A \in \mathbb{R}^{n\times n}$, $x \in \mathbb{R}^{n\times 1}$, and $b \in \mathbb{R}^{n\times 1}$. The inequality of a number can be generalized to a symmetric real matrix by examining whether it is positive or negative (semi-)definite. The benefit of employing linear matrix inequality is that it allows a unified framework to analyze the system property and may provide additional insight, but LMI will be typically more computationally expensive than frequency domain analysis that typically has a much faster algorithm. Chapter

8 will employ the LMI based analysis.

We will also focus on the state-space model in (2.11). We employ the notion $M \succeq 0$ and $M \preceq 0$ to respectively represent that M is positive semi-definite and negative semi-definite. The notion $M \succ 0$ and $M \prec 0$ represent that M is positive definite and negative definite, respectively. This section is largely based on Packard & Doyle (1993); Boyd *et al.* (1994, chapter 2.7) and Khalil (2002, chapters 4-7).

2.4.1 Singular value and structured singular value of a matrix

Here, we describe the following theorem 2.5 about how to compute the largest (unstructured) singular value $\bar{\sigma}(DMD^{-1})$ in (2.8) using LMI formulation.

Theorem 2.5 *(Packard & Doyle, 1993, theorem 3.9) Given $M \in \mathbb{C}^{n\times n}$ and $D \in \mathbb{C}^{n\times n}$ with $D^* = D \succ 0$ Then, $\bar{\sigma}(DMD^{-1}) \leq \beta$ if and only if $M^*D^2M - \beta^2 D^2 \preceq 0$.*

Proof:

$$\bar{\sigma}(DMD^{-1}) \leq \beta \iff \lambda_{max}(D^{-1}M^*DDMD^{-1}) \leq \beta^2 \tag{2.28a}$$

$$\iff D^{-1}M^*DDMD^{-1} - \beta^2 I \preceq 0 \tag{2.28b}$$

$$\iff M^*D^2M - \beta^2 D^2 \preceq 0. \tag{2.28c}$$

□

A direct corollary of theorem 2.5 is that the upper bound of structured singular value can be also computed using LMI:

Corollary 2.6 *Given matrix $M \in \mathbb{C}^{n\times n}$, uncertainty set $\underline{\Delta}$, and scaling matrix set $\underline{D}$ such that the $D \in \underline{D}$, $D^* = D \succ 0$ commute with $\Delta \in \underline{\Delta}$; i.e., $D\Delta = \Delta D$. Then, $\mu_{\underline{\Delta}}(M) \leq \beta$ if $M^*D^2M - \beta^2 D^2 \preceq 0$.*

Corollary 2.6 computes the upper bound of structured singular value using a linear matrix

inequality with variable D^2. Note that the present formulation of linear matrix inequalities and structured singular value can be also generalized to non-square matrices.

2.4.2 System property of a state-space model

In this subsection, we will describe how to certify the system property of a state-space model in (2.11).

Here, we examine the stability using LMI known as Lyapunov's inequality, which is formulated as (Boyd *et al.*, 1994, chapters 2.7.1 and 5.1).

Theorem 2.7 (Lyapunov's inequality) *Given $A \in \mathbb{R}^{n\times n}$. The system $\frac{d}{dt}\psi = A\psi$ is asymptotically stable if and only if there exists P such that*

$$P \succ 0 \tag{2.29a}$$

$$A^T P + PA \prec 0 \tag{2.29b}$$

.

Here, we note that by choosing a certain right-hand side of $A^\mathsf{T}P + PA \prec 0$ (e.g., setting $A^\mathsf{T}P + PA = -I$), the P matrix can be also computed using `lyap` command in MATLAB.

Then, we present the positive-real lemma that allows the certification of passivity using LMI (Boyd *et al.*, 1994, chapters 2.7.2 and 6.3.3). The notion of passivity has been employed in transitional channel flow, and the Reynolds number that can guarantee the passivity coincides with the energy Reynolds number that flow can guarantee stability based on the classical energy method (Zhao & Duncan, 2013).

Theorem 2.8 (Positive-real lemma) *Given $A \in \mathbb{R}^{n\times n}$, $B \in \mathbb{R}^{n\times p}$ and $C \in \mathbb{R}^{p\times n}$, where A is stable and the system (A, B, C) is minimal. The system $\frac{d}{dt}\psi = A\psi + Bf$, $\phi = C\psi$ is passive, i.e.,:*

$$\int_0^T \phi^T f \, dt \geq 0 \tag{2.30}$$

if and only if there exists P *such that*

$$P \succ 0 \tag{2.31a}$$

$$\begin{bmatrix} A^T P + PA & PB - C^T \\ B^T P - C & 0 \end{bmatrix} \preceq 0. \tag{2.31b}$$

Passivity in theorem 2.8 can be also directly computed from the transfer function requiring $H(s) + H(s)^* \succeq$ for all $\mathbb{R}e\,[s] > 0$.

Then, we present the bounded-real lemma, which is related to the $\mathcal{H}_\infty$ norm (Boyd *et al.*, 1994, chapters 2.7.3 and 6.3.2) that has previously been examined in § 2.1, as well as in channel flows (Jovanović, 2004; Schmid, 2007; Illingworth, 2020).

Theorem 2.9 (Bounded-real lemma) *Given* $A \in \mathbb{R}^{n\times n}$, $B \in \mathbb{R}^{n\times p}$ *and* $C \in \mathbb{R}^{p\times n}$, *where* A *is stable and the system* (A, B, C) *is minimal. The system* $\frac{d}{dt}\psi = A\psi + Bf$, $\phi = C\psi$ *has bounded* $\mathcal{L}_2$ *input-output gain* γ, *i.e.,:*

$$\int_0^T \phi^T \phi \, dt \leq \gamma^2 \int_0^T f^T f \, dt \tag{2.32}$$

if and only if there exists P *such that*

$$P \succ 0 \tag{2.33a}$$

$$\begin{bmatrix} A^T P + PA + C^T C & PB \\ B^T P & -\gamma^2 I \end{bmatrix} \preceq 0. \tag{2.33b}$$

The quantity γ is $\mathcal{L}_2$ input-output gain, and it can be also computed by $\mathcal{H}_\infty$ norm that is defined based on the largest singular value $\|H\|_\infty := \sup_{\omega\in\mathbb{R}} \bar{\sigma}[H(\mathrm{i}\omega)]$ (Khalil, 2002, theorem 5.4).

Then, we present the Kalman-Yakubovich-Popov (KYP) lemma following Rantzer (1996, theorem 1), which can be viewed as a unified statement of Lyapunov's inequality, positive-real lemma, and bounded-real lemma. This KYP lemma can translate a more general frequency

domain property to the formulation using LMI.

Theorem 2.10 (Kalman-Yakubovich-Popov lemma) *Given $A \in \mathbb{R}^{n\times n}$, $B \in \mathbb{R}^{n\times p}$, $Q \in \mathbb{R}^{(n+p)\times(n+p)}$, with $\det(i\omega I - A) \neq 0$ for $\omega \in \mathbb{R}$ and (A, B) controllable, the following two statements are equivalent:*

(a)

$$\begin{bmatrix}(i\omega I - A)^{-1}B \\ I\end{bmatrix}^* Q \begin{bmatrix}(i\omega I - A)^{-1}B \\ I\end{bmatrix} \preceq 0, \quad \forall \omega \in \mathbb{R} \cup \{\infty\}. \tag{2.34}$$

(b) There exists a matrix $P \in \mathbb{R}^{n\times n}$ such that $P = P^T$ and

$$Q + \begin{bmatrix}A^TP + PA & PB \\ B^TP & 0\end{bmatrix} \preceq 0. \tag{2.35}$$

2.5 Characterizing nonlinearity using input-output property

In the previous section, we have already seen that the LMI formulation can be employed to certify a wide range of system properties of a state-space model. It is then convenient to partition a nonlinear system as the feedback interconnection between the linear dynamical system and the nonlinear element (Khalil, 2002, figure 7.1), where a natural characterization of the nonlinear element is the input-output property that connects to the linear dynamical system. The property of the nonlinear system (feedback interconnection) can be obtained by e.g., passivity theorem (Khalil, 2002, theorem 6.1) or small-gain theorem (Khalil, 2002, theorem 5.6).

Here, figure 2.4 shows a high-level diagram of characterizing the nonlinearity $\boldsymbol{f} = \mathcal{N}[\boldsymbol{u}]$ that is outlined by (—) using input-output properties. The property that the nonlinearity has componentwise bounded input-output gain in a local region (– –) is employed in the structured input-output analysis in chapters 5-7. We illustrate this by the nonlinear function (2.24), where it satisfies

$$f^{\mathsf{T}} e_i e_i^{\mathsf{T}} f \leq \delta^2 \phi^{\mathsf{T}} M_f^{\mathsf{T}} e_i e_i^{\mathsf{T}} M_f \phi, \quad \text{when} \quad |w| \leq \delta, \tag{2.36}$$

where e_i is the unit vector with i^{th} element as one and other elements as zero. The model of this nonlinearity using structured uncertainty in (2.27) satisfies similar inequalities when the uncertainty w_i is bounded:

$$f_\xi^\mathsf{T} e_i e_i^\mathsf{T} f_\xi \leq \delta^2 \phi^\mathsf{T} M_f^\mathsf{T} e_i e_i^\mathsf{T} M_f \phi, \quad \text{when} \quad |w_\xi| \leq \delta. \tag{2.37}$$

We employ the frequency domain computation of structured singular value in chapters 5-7 instead of the LMI (also supported in the command `mussv`) because the previous one has a faster algorithm that allows us to approach the computation of the channel flow configuration directly based on Navier-Stokes equations. This componentwise bounded input-output gain in a local region (– –) is expected to be general for nonlinearity as they are ***non***-linear. This class of property ties in the bounded-real lemma and its general version of KYP lemma.

The ellipse outline by (– · –) represents the property of nonlinearity in the type of energy-conserving, which is widely employed in energy stability (Joseph, 2013; Straughan, 2013). For the illustrative nonlinearity (2.24), it satisfies $\phi^\mathsf{T} f = 0$. This class of property ties in the positive-real lemma. It is known that the energy stability analysis is typically conservative; see e.g., (Schmid & Henningson, 2012, chapter 5.6), which results from the fact that it certifies the stability for *any* $\boldsymbol{f}$ that satisfies the inner product property $\langle \boldsymbol{u}, \boldsymbol{f} \rangle = 0$, which is a more general class of functions than nonlinearity $\boldsymbol{f}$ itself outlined by (—).

The vector $\boldsymbol{n}$ within the ellipse outlined by (– · · –) is the orthogonal complement of nonlinearity $\boldsymbol{f}$ such that $\langle \boldsymbol{n}, \boldsymbol{f} \rangle = 0$. This can be also illustrated by the nonlinearity in (2.24), where we can find $n^\mathsf{T} = \begin{bmatrix} 1 & -1 & 0 \end{bmatrix}$ such that $n^\mathsf{T} f = 0$. This is motivated by the energy-Casimir method for studying the nonlinear stability widely employed for ideal fluids (Holm *et al.*, 1985; Salmon, 1988).

The LMI based algorithm discussed in chapter 8 will unify all three colored ellipses in figure 2.4. Certainly, the nonlinearity can be characterized by a wider range of properties, but these three classes of input-output properties in figure 2.4 fit into the formulation of LMI based on their quadratic form.

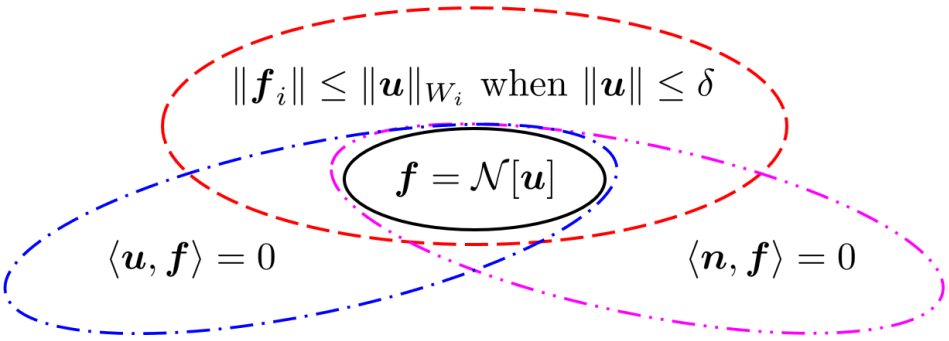

Figure 2.4: Characterizing the nonlinearity using the input-output property. Here, $\|\cdot\|$ is a norm, $\|\cdot\|_{W_i}$ is a weighted norm, and $\langle \cdot, \cdot \rangle$ represents an inner product. Their precise definition depends on the formulation of the nonlinearity $\boldsymbol{f} = \mathcal{N}[\boldsymbol{u}]$ outlined by (—). The ellipse (– –) represents the property of componentwise bounded input-output gain at a local region; the ellipse (– · –) represents the property in the form of energy-conserving such that $\langle \boldsymbol{u}, \boldsymbol{f} \rangle = 0$. The vector $\boldsymbol{n}$ is the orthogonal complement of the nonlinear term $\boldsymbol{f}$ such that it satisfies the property within the ellipse (– · · –): $\langle \boldsymbol{n}, \boldsymbol{f} \rangle = 0$.

Sum-of-squares (SOS) programming will be employed as a benchmark in chapter 8. It is a widely employed tool to analyze system stability and performance for the dynamical system described by polynomials. We refer to the examples in the reference (Papachristodoulou *et al.*, 2013; Papachristodoulou & Prajna, 2005*b*).

Chapter 3

Input–output based analysis of convective velocity in turbulent channel flows

> "If the velocity of the air stream which carries the eddies is very much greater than the turbulent velocity, one may assume that the sequence of changes in u at the fixed point are simply due to the passages of an unchanging pattern of turbulent motion over the point, i.e. one may assume that $u = \phi(t) = \phi(\frac{x}{U})$ where x is measured upstream at time $t = 0$ from the fixed point where u is measured."
>
> Geoffrey I. Taylor[1], 1938

This chapter employs traditional input-output analysis to analyze the breakdown of Taylor's frozen turbulence hypothesis in turbulent channel flow by evaluating the dependence of convective velocity on wall-normal height and wall-parallel length scales. We also employ this tool to isolate underlying mechanism for the deviation of convective velocity from the local mean velocity, in particular, at the near-wall region.

[1] (Taylor, 1938, p. 478)

3.1 Introduction

Taylor's frozen turbulence hypothesis (Taylor, 1938) and its variants have proven invaluable in the study of high Reynolds number wall-bounded turbulent flows (Marusic *et al.*, 2010; Smits *et al.*, 2011; LeHew *et al.*, 2011). However, its underlying assumption that the motion of turbulent fluctuations can be modeled as passive advection by the local mean velocity is known to break down in certain flow regimes (Lin, 1953; Dennis & Nickels, 2008; Squire *et al.*, 2017). In order to compensate for these known errors, the local mean velocity is often replaced by a convective velocity that better represents the spatio-temporal development of the fluctuations (Zaman & Hussain, 1981; Hutchins *et al.*, 2011). This convective velocity can be computed from simulation data (Kim & Hussain, 1993; del Álamo & Jiménez, 2009; Chung & McKeon, 2010; Lozano-Durán & Jiménez, 2014; Geng *et al.*, 2015; Renard & Deck, 2015) or obtained from spatio-temporally resolved experimental measurements (Krogstad *et al.*, 1998; LeHew *et al.*, 2010; LeHew *et al.*, 2011; de Kat & Ganapathisubramani, 2015). However, questions remain regarding how to obtain an accurate estimate of this quantity, particularly in situations where the relevant data are unavailable; e.g., in experiments using hotwire measurements or planar PIV. In addition, there is not yet a full understanding of the mechanisms contributing to the convective velocity in each region of the flow. Such knowledge is required both to characterize the transport properties of fluctuating quantities and to identify when the direct application of Taylor's hypothesis with the mean velocity is insufficient.

An early work by Lin (1953) suggests that Taylor's hypothesis works well when the mean flow is approximately spatially uniform and when turbulence intensities are low, but breaks down in regions of high shear. Lumley (1965) further refines this spatial uniformity requirement, suggesting that weak interactions between eddies of different sizes are also needed to ensure the validity of Taylor's hypothesis. Geng *et al.* (2015) provide support for the break down of Taylor's hypothesis in highly sheared regions of the flow by explicitly computing the contribution of advection by the mean flow (Taylor's hypothesis) to convective velocity in the viscous sublayer

using Direct Numerical Simulation (DNS) data from channel flows at $Re_\tau = 205$ and 932. In particular, they compute the average amplitudes of different terms in the momentum equation through DNS and illustrate that advection by the mean flow provides less than 50% of the streamwise momentum flux in the viscous sublayer. Taylor's hypothesis has also proven to inadequately describe the convection of large-scale components of the flow. Dennis & Nickels (2008) compare the spatial evolution of a turbulent flow inferred from the temporal information using Taylor's hypothesis with those obtained using Particle Image Velocimetry (PIV) at a wall parallel plane sufficiently removed from the wall so that the assumptions of Lin (1953) are satisfied. The authors find that even though the PIV fields are qualitatively similar, several large-scale features are not reproduced in the fields generated using Taylor's hypothesis.

The validity of Taylor's hypothesis across a range of flow scales is explored by Fisher & Davies (1964) who use two-point space-time correlation for statistically stationary turbulence to compute the convective velocity of streamwise velocity fluctuations as a function of streamwise spatial and temporal separation; i.e., a streamwise (or temporal) scale-dependent convective velocity. Fisher & Davies (1964) and subsequently Favre *et al.* (1967); Zaman & Hussain (1981) show that the convective velocity computed in this manner does not coincide with the local mean velocity and can be strongly dependent on the streamwise spatial or temporal separation. A similar phenomenon has also been observed in measurements of wall pressure (Willmarth & Wooldridge, 1962).

This scale dependence, particularly the increasing deviation of the convective velocity from the mean flow as spatial separation is increased, was identified as a possible explanation for the known discrepancy between the convective and mean velocities near the wall. In particular, the larger convective velocity versus the local mean velocity in the near-wall region has been attributed to faster moving structures centered further away from the wall whose influence extends to the wall due to their large size (Dinkelacker *et al.*, 1977; Kreplin & Eckelmann, 1979; Farabee & Casarella, 1991; Kim & Hussain, 1993; Hutchins *et al.*, 2011). del Álamo & Jiménez (2009) find that fast and wide streamwise elongated structures, coherent up to the core region,

provide a consistent contribution to the energy-weighted average convective velocity close to the wall. They relate these structures to the large modes (Bullock *et al.*, 1978; del Álamo *et al.*, 2004) reminiscent of Townsend's 'inactive' eddies (Townsend, 1961; Bradshaw, 1967) and the very large-scale motions (Guala *et al.*, 2006; Balakumar & Adrian, 2007; Hutchins & Marusic, 2007; Monty *et al.*, 2007), which have been shown to modulate small-scale structures (Mathis *et al.*, 2009*a*,*b*; Ganapathisubramani *et al.*, 2012; Yang & Howland, 2018). Although these works provide evidence that scale interactions contribute to the breakdown of Taylor's hypothesis at the wall, a full understanding of the underlying mechanisms across the full range of flow regimes has yet to be realized.

Understanding the transport of vortical structures and how it is affected through interactions across spatial scales is of wide interest because vortical structures and vorticity are widely used in both conceptual and predictive models of wall-bounded turbulent flows. For example, Perry *et al.* (1986) proposed Λ-shaped vortices as a candidate form for the attached eddy model (Marusic & Monty, 2019), which successfully reproduced statistical flow features such as the mean velocity and Reynolds stress profiles. Robinson (1991) similarly proposed a model based on vortical structures, including quasi-streamwise vortices and arch-like vortices, to represent turbulence production through sweep and ejection in low Reynolds number flows. Hairpin vortices packets are also the basis of the conceptual description of transport mechanisms of vorticity, momentum, and turbulent kinetic energy proposed by Adrian (2007). Streamwise vortices, in particular, have arisen as an important example of the coherent structures that have been shown to play a key role in the dynamics of wall-bounded turbulence; see e.g., Sharma & McKeon (2013). Streamwise vortices were also demonstrated to be linear optimal perturbations (Butler & Farrell, 1993) and to be associated with the largest energy amplification (Bamieh & Dahleh, 2001; Jovanović & Bamieh, 2005) in channel flow. These structures have also been associated with the high skin-friction regions that are of engineering interest in wall-bounded turbulent flows (Kim, 2011). Although there is a large body of work pointing to the importance of vorticity transport, there has yet to be a detailed analysis of scale dependent convective velocities for vorticity fluctuations.

In this chapter, we explore the mechanisms underlying the convective velocity of fluctuating quantities in wall-bounded turbulence using a spatio-temporal transfer function that enables us to isolate the contributions and interactions across the full range of flow scales. This approach allows us to compute quantities for a range of Reynolds numbers given an associated turbulent mean velocity profile. Our analytical framework is based on stochastically-forced Linearized Navier-Stokes (LNS) equations, which have a long history in the study of wall-bounded shear flows; e.g., in characterizing energy amplification associated with stochastic disturbances (Farrell & Ioannou, 1993*a*; Bamieh & Dahleh, 2001) and isolating the most sensitive input-output paths (Jovanović & Bamieh, 2005). The LNS equations have also proven useful in characterizing coherent structures (Smits *et al.*, 2011; McKeon, 2017; Jiménez, 2018). For example, low-rank approximations of the resolvent operator (McKeon & Sharma, 2010) have been used to explain the scalings of the very large-scale motions and to reconstruct the packet hairpin vortices (Sharma & McKeon, 2013). Luhar *et al.* (2014) also use the resolvent framework to predict the high-amplitude wall pressure previously observed in experiments and simulations. Moarref *et al.* (2013) combine this framework with term balancing arguments to reproduce the inner, outer, and geometrically self-similar scalings of the streamwise energy density in turbulent channel flows. Input-output analysis of the NS equations linearized about a base profile with an eddy viscosity term (Reynolds & Hussain, 1972) leads to accurate predictions of the spanwise spacing of near-wall streaks (del Álamo & Jiménez, 2006; Cossu *et al.*, 2009; Pujals *et al.*, 2009; Hwang & Cossu, 2010*a*,*b*) and large-scale structures (Illingworth *et al.*, 2018; Madhusudanan *et al.*, 2019; Morra *et al.*, 2019). Related work employing the impulse response (Vadarevu *et al.*, 2019) of the LNS transfer function has led to self-similar vortex structures.

The transfer function of the LNS has previously been used to compute quantities associated with the convective velocity of a fluctuating quantity in wall-bounded turbulent flows. For example, the resolvent framework was used to show that the phase speed of streamwise velocity fluctuations with peak contribution to the energy density deviates from the mean velocity in the near-wall region (Moarref *et al.*, 2013). Luhar *et al.* (2014) also used the resolvent framework to

investigate the scale dependence of wall pressure propagation speed, which showed agreement with the empirically determined convective velocity (Panton & Linebarger, 1974). Zare *et al.* (2017) also computed the convective velocity of streamwise velocity fluctuations for one specific flow scale based on the LNS equation with temporally correlated (colored) stochastic forcing. Their results show qualitatively similar behavior to convective velocities obtained by del Álamo & Jiménez (2009). These works demonstrate the utility of transfer function based approaches in computing the convective velocity. However, none of these works employed input-output analysis to investigate the underlying mechanisms that lead to the deviation of convective velocity from the local mean velocity.

This work takes steps in that direction by using an input-output framework to systematically investigate the scale-dependent convective velocity of velocity fluctuations in turbulent channels. We begin by demonstrating that the proposed approach provides good agreement with the mean convective velocity predictions for fluctuations of the three velocity components and three vorticity components previously published in the literature (Kim & Hussain, 1993; Geng *et al.*, 2015). We then direct our attention to the streamwise velocity fluctuations and exploit the analytical framework to compute the convective velocity for each streamwise–spanwise wavenumber pair at different wall-normal locations and to examine interactions between different scales. The results of our scale-dependent analysis are consistent with those obtained using DNS data (del Álamo & Jiménez, 2009). In particular, the convective velocities predicted using the input-output based approach employed here show more variation with scale closer to the wall, with the largest variation occurring in the viscous sublayer. Our analysis suggests that this viscous sublayer behavior arises due to structures that are self-similar in the spanwise and wall-normal plane and scale with wall-normal height, which supports Townsend's attached eddy hypothesis regarding the dominant dynamical structures in wall-bounded flows.

Finally, in the spirit of Lin's (1953) term–by–term analysis of the momentum equation, we examine how each linear term in the momentum equation contributes to the deviation of the convective velocity from the mean. A linear analysis is expected to yield insight in this regard

because both the mean shear term and the viscous term, which play critical roles in the dynamics of the near-wall region, are linear. Moreover, it was recently shown that resolvent analysis retains the fast pressure component arising from the linear interaction between the mean shear and turbulent wall-normal velocity (Luhar *et al.*, 2014), and therefore our computations also include these phenomena. Our analysis employs an expression for scale-dependent convective velocities derived by del Álamo & Jiménez (2009), who did not further analyze the various terms. This work also builds upon that of Geng *et al.* (2015) who quantify each term's contribution to the convective velocity at different wall-normal locations. Our results indicate that the viscous term provides the largest contribution to the deviation of the convective velocity from the mean in the near-wall region. Based on these observations, we propose a viscous correction to Taylor's hypothesis, and demonstrate that the revised model accurately reproduces the behavior of the near-wall convective velocity for large–scale structures. We analogously perform such a term-by-term analysis of convective velocity of vorticity fluctuations, and results indicate that the viscous term has a slightly larger contribution to convective velocity of streamwise vorticity than the mean shear in the viscous sublayer. Our results confirm that it is through this term that the large channel spanning structures influence the near-wall region.

The remainder of this chapter is organized as follows. Section 3.2 describes the problem setup. We detail our transfer function based approach and numerical scheme for calculating the convective velocities in sections 3.3 and 3.4, respectively. In section 3.5, we apply the input-output based approach using mean velocity profiles from turbulent channel flows obtained from Lee & Moser (2015) at three different Reynolds numbers ($Re_\tau = 550,\ 1000$, and 5200). We then discuss the physical origin of the near-wall convective velocities. Section 3.6 explores the wall-normal coherence of the structures contributing to the convective velocities at a particular wall-normal location. Section 3.7 analyzes the contribution of each of the linear terms in the momentum equation to the total convective velocity for each streamwise–spanwise wavenumber pair (flow scale). Based on this term-by-term analysis, a viscous correction to Taylor's hypothesis is proposed and discussed. We then perform a similar analysis for convective velocity of vorticity

fluctuations in § 3.8. Section 3.9 summarizes this chapter.

3.2 Problem setup

We consider incompressible flow between two infinite parallel plates driven by a streamwise pressure gradient as shown in figure 3.1(a), where x, y, z are the streamwise, wall-normal, and spanwise directions, respectively. We decompose the velocity field, $\boldsymbol{u} = \begin{bmatrix} u & v & w \end{bmatrix}^\mathsf{T}$, with $^\mathsf{T}$ indicating the transpose, and the pressure field, p, into mean and fluctuating quantities; i.e., $\boldsymbol{u} = \bar{u}(y)\boldsymbol{i} + \boldsymbol{u}'$ with $\boldsymbol{i}$ denoting the streamwise unit vector and $p = \bar{p} + p'$, where the overbars indicate time-averaged quantities, $\bar{\phi} = \lim_{T\to\infty} \frac{1}{T}\int_0^T \phi(t)\,dt$, and primes indicate fluctuating quantities. The dynamics of the fluctuations $\boldsymbol{u}'$ and p' are governed by

$$\partial_t \boldsymbol{u}' + \bar{u}\partial_x \boldsymbol{u}' + \boldsymbol{\nabla} p' + v' \frac{d\bar{u}}{dy}\boldsymbol{i} - \frac{1}{Re_\tau}\nabla^2 \boldsymbol{u}' = -\boldsymbol{u}' \cdot \boldsymbol{\nabla}\boldsymbol{u}' + \overline{\boldsymbol{u}' \cdot \boldsymbol{\nabla}\boldsymbol{u}}', \tag{3.1a}$$

$$\boldsymbol{\nabla} \cdot \boldsymbol{u}' = 0. \tag{3.1b}$$

The spatial variables are normalized by the half channel height δ; e.g., $y = y_*/\delta \in [-1, 1]$, where the subscript $*$ indicates dimensional quantities. The velocity is normalized by the friction velocity $U_\tau = \sqrt{\tau_\mathsf{w}/\rho}$, where τ_w is the time-averaged mean shear stress at the wall, and ρ is the density of the fluid, which leads to $u := u^+ = u_*/U_\tau$.[2] Time and pressure are normalized by δ/U_τ, and ρU_τ^2, respectively. We define the inner unit length scale as $\delta_v = \nu/U_\tau$ and use the superscript $+$ to denote the distances measured in inner units; i.e., $y^+ = y_*/\delta_v$. The friction Reynolds number is defined as $Re_\tau = \delta U_\tau/\nu = \delta^+$.

Invariance to shifts in (x, z, t) of equations (3.1) allows us to employ the (x, z, t) spatio-temporal Fourier transform,

$$\widehat{\psi}(y; k_x, k_z, c) = \mathcal{F}(\psi) \equiv \int_{-\infty}^{\infty}\int_{-\infty}^{\infty}\int_{-\infty}^{\infty} \psi(x, y, z, t)\mathrm{e}^{-\mathrm{i}(k_x(x-ct)+k_z z)}\,\mathrm{d}t\,\mathrm{d}x\,\mathrm{d}z, \tag{3.2}$$

[2] Note, in (3.1), we omit the $+$ superscripts for the velocity fluctuations for notational convenience.

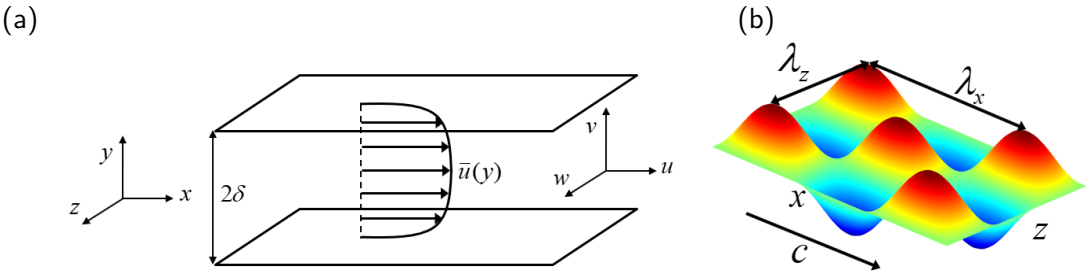

Figure 3.1: (a) Turbulent flow between two infinite parallel plates with mean profile $\bar{u}(y)$. (b) The fluctuations $\boldsymbol{u}'$ are decomposed into traveling waves with wavelengths λ_x, λ_z in the x, z directions and downstream phase speed $c = -\lambda_x\omega/2\pi$ using equation (3.2).

where $k_x = 2\pi/\lambda_x$ and $k_z = 2\pi/\lambda_z$ are the respective dimensionless x and z wavenumbers normalized by the channel half-height δ. The transform (3.2) decomposes the flow into traveling waves with wavelengths λ_x, λ_z in the x, z directions and downstream phase speed $c = -\omega/k_x = -\lambda_x\omega/2\pi$, where ω is the frequency; see figure 3.1(b). Applying the Fourier transform to (3.1) and denoting the nonlinear term as $\boldsymbol{f}'(x,y,z,t) \equiv -\boldsymbol{u}'\cdot\boldsymbol{\nabla}\boldsymbol{u}' + \overline{\boldsymbol{u}'\cdot\boldsymbol{\nabla}\boldsymbol{u}'}$ yields

$$\underbrace{\mathrm{i}k_x(\bar{u}-c)\widehat{\boldsymbol{u}}'}_{\mathrm{I}} \underbrace{+\widehat{\boldsymbol{\nabla}}\widehat{p}'}_{\mathrm{IIa}} \underbrace{+\widehat{v}'\frac{d\bar{u}}{dy}\boldsymbol{i}}_{\mathrm{IIb}} \underbrace{-\frac{1}{Re_\tau}\widehat{\nabla}^2\widehat{\boldsymbol{u}}'}_{\mathrm{IIc}} = \underbrace{\widehat{\boldsymbol{f}}'}_{\mathrm{III}}, \tag{3.3a}$$

$$\widehat{\boldsymbol{\nabla}}\cdot\widehat{\boldsymbol{u}}' = 0, \tag{3.3b}$$

where $\widehat{\boldsymbol{\nabla}} = \begin{bmatrix}\mathrm{i}k_x & \partial_y & \mathrm{i}k_z\end{bmatrix}^{\mathsf{T}}$ and $\widehat{\nabla}^2 = \partial_{yy} - (k_x^2 + k_z^2)$. The corresponding no-slip boundary conditions are given by

$$\widehat{\boldsymbol{u}}'(y=\pm1; k_x, k_z, c) = \begin{bmatrix}0 & 0 & 0\end{bmatrix}^{\mathsf{T}},\ \forall k_x, k_z, c \in \mathbb{R}. \tag{3.4}$$

The terms in (3.3a) can be grouped into: (I) advection of the fluctuations by the mean velocity in the frame of reference of the traveling wave fluctuations, terms (IIa)-(IIc), which capture the respective effects of pressure, shear, and viscosity, and (III) fluctuation-fluctuation nonlinear interactions.

Taylor's frozen turbulence hypothesis states that for sufficiently low turbulence intensities ($|\boldsymbol{u}'_{\mathrm{rms}}|_\infty/\bar{u} \to 0$), the spatio-temporal development of turbulent fluctuations can be described as downstream advection by the mean velocity $\bar{u}(y)$ (Taylor, 1938). This statement is equivalent

to setting all terms except (I) in (3.3a) to zero, which reduces the equation (3.3a) to the passive advection model:

$$\mathrm{i}k_x(\bar{u}-c)\widehat{\boldsymbol{u}}' = 0. \tag{3.5}$$

As previously discussed, the direct application of Taylor's hypothesis tends to be inaccurate in regions near the wall, where the terms in (IIa)-(IIc) and (III) in (3.3a) provide non-negligible contributions; see e.g., Lin (1953); Geng *et al.* (2015). It is well-known that the model in (3.5) can be improved by replacing the mean velocity, $\bar{u}$, with an empirically determined mean convective velocity ψ_c (Zaman & Hussain, 1981; Hutchins *et al.*, 2011) for the fluctuating quantity of interest. In the next section, we describe an input-output based approach to computing such a ψ_c.

3.3 Method for calculating scale-dependent convective velocities

In this section, we describe the employed input-output approach to computing spatio-temporal convective velocities of fluctuating quantities given a mean velocity profile $\bar{u}(y)$. First we rewrite (3.3) in the form

$$\mathcal{L}\begin{bmatrix}\widehat{\boldsymbol{u}}'\\ \widehat{p}'\end{bmatrix} = \mathcal{B}\widehat{\boldsymbol{f}}', \tag{3.6}$$

where

$$\mathcal{L} := \begin{bmatrix}(\mathrm{i}k_x(\bar{u}-c) - \frac{1}{Re_\tau}\widehat{\nabla}^2)\mathbf{I}_{3\times 3} + \frac{d\bar{u}}{dy}\mathbf{S} & \widehat{\boldsymbol{\nabla}}\\ \widehat{\boldsymbol{\nabla}}^{\mathsf{T}} & 0\end{bmatrix}, \qquad \mathcal{B} := \begin{bmatrix}\mathbf{I}_{3\times 3}\\ \mathbf{0}_{1\times 3}\end{bmatrix}, \tag{3.7}$$

and $\widehat{\boldsymbol{f}}'$ is parameterized as input forcing. In equation (3.7), $\mathbf{I}_{n\times n}$ and $\mathbf{0}_{m\times n}$ are respective identity and zero matrices with their sizes indicated by their subscripts, and $\mathbf{S} := \begin{bmatrix}0 & 1 & 0\\ 0 & 0 & 0\\ 0 & 0 & 0\end{bmatrix}$. A non-bold symbol represents a scalar; e.g., the 0 appearing in (3.7) is a scalar quantity. We then define an output variable

$$\widehat{\psi}' = \mathcal{C}_{\widehat{\psi}'}\begin{bmatrix}\widehat{\boldsymbol{u}}'\\ \widehat{p}'\end{bmatrix}, \tag{3.8}$$

where $\mathcal{C}_{\widehat{\psi}'} = \mathcal{C}_{\widehat{\psi}'}(y; k_x, k_z)$ is a linear operator that maps the state variables to the output of interest. Here, we use the primitive variables $\widehat{\boldsymbol{u}}'$ and $\widehat{p}'$ as states rather than the wall-normal velocity and vorticity coordinates of the commonly studied Orr-Sommerfeld and Squire equations because this form of the equations provides direct information about the pressure (Luhar *et al.*, 2014), which we will later exploit in the term-by-term analysis in section 3.7.

We define the input-output map $\mathcal{G}_{\widehat{\psi}'}$ between the input $\widehat{\boldsymbol{f}}'$ and the output $\widehat{\psi}'$, in the manner of McKeon & Sharma (2010); Luhar *et al.* (2014); McKeon (2017) as

$$\widehat{\psi}' = \mathcal{C}_{\widehat{\psi}'}\mathcal{L}^{-1}\mathcal{B}\widehat{\boldsymbol{f}}' = \mathcal{G}_{\widehat{\psi}'}(y; k_x, k_z, c)\widehat{\boldsymbol{f}}'. \tag{3.9}$$

The convective velocity of a fluctuating variable ψ' can be computed using the following two-point space-time correlation for statistically stationary turbulence:

$$R_{\widehat{\psi}'}(\xi, \tau; \boldsymbol{x}) = \langle \psi'(\boldsymbol{x}, t)\psi'(\boldsymbol{x} + \xi\boldsymbol{i}, t + \tau)\rangle, \tag{3.10}$$

where ξ and τ are the respective streamwise and temporal separation between two points. Convective velocities for fluctuations ψ' at some $\boldsymbol{x}$ are computed from (3.10) by fixing either ξ or τ and varying the other separation variable to maximize $R_{\widehat{\psi}'}(\xi, \tau; \boldsymbol{x})$ (Wills, 1964; Fisher & Davies, 1964; Kim & Hussain, 1993; Zaman & Hussain, 1981; Krogstad *et al.*, 1998). We adapt this idea to our approach by computing the Power Spectral Density (PSD) (Wills, 1964; del Álamo & Jiménez, 2009) for the input-output map (3.9) as

$$\Phi_{\widehat{\psi}'}(y; k_x, k_z, c) = \langle \widehat{\psi}'\widehat{\psi}'^{*}\rangle = \mathcal{G}_{\widehat{\psi}'}\langle \widehat{\boldsymbol{f}}'\widehat{\boldsymbol{f}}'^{*}\rangle\mathcal{G}^{*}_{\widehat{\psi}'} = \mathcal{G}_{\widehat{\psi}'}\mathcal{G}^{*}_{\widehat{\psi}'} \tag{3.11}$$

with $\boldsymbol{f}'(x, y, z, t)$ parametrized as spatio-temporal delta-correlated Gaussian noise with unit variance; i.e., noise that is white in space and time (Jovanović & Bamieh, 2005). The superscript $*$ in (3.11) denotes the complex conjugate, and the angle brackets $\langle\ \rangle$ indicate an ensemble averaging operation. The magnitude of this Gaussian noise does not influence the results of convective velocity computed using equation (3.12).

The convective velocity ψ_c is then obtained as

$$\psi_c(y; k_x, k_z) \equiv \arg\,\max_c \Phi_{\widehat{\psi'}}(y; k_x, k_z, c), \tag{3.12}$$

which represents convective velocities of the coherent structures with (x, z) spatial extents of $\lambda_x = 2\pi/k_x$ and $\lambda_z = 2\pi/k_z$ as a function of wall-normal location. This definition of convective velocity based on (3.12) neglects the distribution of the PSD for a given (λ_x, λ_z) pair, which is expected to contain energy at a range of temporal frequencies. The distribution of the spectrum could be partially accounted for by instead defining the convective velocity in terms of the center of gravity of the PSD. That quantity is commonly used to compute convective velocity in simulation (DNS and LES) studies as it requires time-averaging instead of Fourier transforming in the time domain; see e.g., del Álamo & Jiménez (2009); Chung & McKeon (2010); Renard & Deck (2015). Our approach can be adapted to accommodate such a definition (and others) through a suitable modification of equation (3.7). In the current work, we recomputed a subset of the results using the center of gravity method to ensure that the main conclusions of our study are not altered by our choice of definition.

Assuming that $\boldsymbol{f}'(x, y, z, t)$ is spatio-temporal delta-correlated Gaussian noise implies that the velocity itself is Gaussian. This is clearly not true as velocity probability density functions are known to have heavy tails and odd-order moments that do not vanish (Frisch & Kolmogorov, 1995). Colored-in-time forcing has been shown to produce more accurate statistics (Zare *et al.*, 2017). However, the Gaussian white-noise parametrization is appealing because it is a simple, analytically tractable forcing that has been widely used to provide important insights into the dynamics; e.g., Farrell & Ioannou (1993*a*); Bamieh & Dahleh (2001); Jovanović & Bamieh (2005). Therefore, this type of forcing provides a good starting point for understanding the role of linear mechanisms in determining the convective velocity and simplifies analysis because it does not introduce a preferential forcing in any of the spatial or temporal directions.

We focus on streamwise, wall-normal, and spanwise velocity fluctuations which are computed based on the respective output operators

$$\mathcal{C}_{\widehat{u'}} = \begin{bmatrix} 1 & 0 & 0 & 0 \end{bmatrix}, \quad \mathcal{C}_{\widehat{v'}} = \begin{bmatrix} 0 & 1 & 0 & 0 \end{bmatrix}, \quad \text{and} \quad \mathcal{C}_{\widehat{w'}} = \begin{bmatrix} 0 & 0 & 1 & 0 \end{bmatrix} \tag{3.13}$$

in (3.9). However, we note that the approach can be generalized to the calculation of the convective velocity for any fluctuating quantity, ψ', whose Fourier transform can be written in the form (3.8) with an appropriate choice of $\mathcal{C}_{\widehat{\psi'}}$. For example, the output operators corresponding to the vorticity fluctuations $\widehat{\omega}'_x$, $\widehat{\omega}'_y$, $\widehat{\omega}'_z$, and the pressure $\widehat{p}'$ are given by:

$$\begin{aligned} \mathcal{C}_{\widehat{\omega}'_x} &= \begin{bmatrix} 0 & -\mathrm{i}k_z & \partial_y & 0 \end{bmatrix}, \quad \mathcal{C}_{\widehat{\omega}'_y} = \begin{bmatrix} \mathrm{i}k_z & 0 & -\mathrm{i}k_x & 0 \end{bmatrix}, \\ \mathcal{C}_{\widehat{\omega}'_z} &= \begin{bmatrix} -\partial_y & \mathrm{i}k_x & 0 & 0 \end{bmatrix}, \quad \mathcal{C}_{\widehat{p}'} = \begin{bmatrix} 0 & 0 & 0 & 1 \end{bmatrix}, \end{aligned} \tag{3.14}$$

respectively. An analysis of the convective velocity of vorticity fluctuations is carried out later in § 3.8.

In the next section, we describe the numerical implementation of the input-output based approach for channel flow at three different Reynolds numbers. The resulting convective velocities are analyzed in subsequent sections.

3.4 Numerical approach

The operators in (3.11) are discretized using the Chebyshev differentiation matrices generated by the MATLAB routines of Weideman & Reddy (2000). We denote the discretization of $\mathcal{G}_{\widehat{\psi'}}$ as $\widetilde{\mathcal{G}}_{\widehat{\psi'}}$. The resulting discretized expression for the PSD at wall-normal location $y = y_i$ is given by

$$\widetilde{\Phi}_{\widehat{\psi'}}(y_i; k_x, k_z, c) = (\widetilde{\Phi}_{\widehat{\psi'}}(\mathbf{y}; k_x, k_z, c))_i = \left(\widetilde{\mathcal{G}}_{\widehat{\psi'}}(\mathbf{y}; k_x, k_z, c)\widetilde{\mathcal{G}}^*_{\widehat{\psi'}}(\mathbf{y}; k_x, k_z, c)\right)_{ii}, \tag{3.15}$$

where $\mathbf{y} = \{y_1, y_2, ...\}$ are the discrete grid points in the wall-normal direction, and $(\boldsymbol{A})_{ij}$ indicates the (i, j) element of the matrix $\boldsymbol{A}$. The convective velocity at a fixed $(y; k_x, k_z)$ can then be approximated through the discretized analog of (3.12). In computing this quantity, we

employ the Clenshaw–Curtis quadrature (Trefethen, 2000) to obtain the L_2 inner product for the Chebyshev spaced wall-normal grid. We implement the no-slip boundary condition $\widehat{\boldsymbol{u}}'(y = \pm 1) = \mathbf{0}$ explicitly following the approach of Luhar *et al.* (2014). This implementation allows us to use primitive variables $\widehat{\boldsymbol{u}}'$ and $\widehat{p}'$, which as previously discussed offers us direct information regarding the fast pressure. We performed the same analysis using the Orr-Sommerfeld and Squire form described in Jovanović & Bamieh (2005) and verified that results do not change.

The turbulent mean velocities in (3.1a) are obtained from the DNS of Lee & Moser (2015) at $Re_\tau = 550,\ 1000$, and 5200, which all use simulation domains with $L_{x*}/\delta = 8\pi$ and $L_{z*}/\delta = 3\pi$. For the $Re_\tau = 550$ and $Re_\tau = 1000$ cases, our calculations use 122 collocation points in the wall-normal direction. We employ 192 collocation points for the $Re_\tau = 5200$ calculations. We compute the optimal value of equation (3.12) by computing the PSD for 201 uniformly spaced points over the phase speed range $c^+ \in [0, 30]$ for each wavenumber pair (k_x, k_z). We then select the single c^+ that maximizes the PSD. This phase speed range and 90×90 logarithmically spaced points in the spectral range $k_x \in [10^{-2}, 10^3]$ and $k_z \in [10^{-2}, 10^3]$ are employed for all three Reynolds numbers. We verified that doubling either the number of collocation points in the wall-normal direction or the number of Fourier modes in the horizontal directions does not alter the results, indicating grid convergence.

3.5 Convective velocity in turbulent channels

In this section, we use the method described in sections 3.3 and 3.4 to compute the convective velocity of the velocity fluctuations for turbulent channel flow at $Re_\tau = 550$, $Re_\tau = 1000$, and $Re_\tau = 5200$. We first validate the approach by computing the mean convective velocities and comparing our results to those computed from DNS data (del Álamo & Jiménez, 2009; Geng *et al.*, 2015). We then take advantage of the analytical framework to further analyze the contribution of different length scales to the local convective velocity.

3.5.1 Validation of the input-output based approach

The weighted average convective velocity $[\psi_c]_h$ of a fluctuating quantity ψ' can be computed as:

$$[\psi_c]_h(y) = \frac{\int_\Omega \psi_c(y;k_x,k_z)h(y;k_x,k_z)\,\mathrm{d}k_x\mathrm{d}k_z}{\int_\Omega h(y;k_x,k_z)\,\mathrm{d}k_x\mathrm{d}k_z} \tag{3.16}$$

with an averaging domain Ω over (k_x, k_z) and a weighting function $h(y;k_x,k_z) = \langle|\mathcal{F}_{xz}(\psi')|^2\rangle k_x^2$, where $\mathcal{F}_{xz}$ is the x-z Fourier transform:

$$\mathcal{F}_{xz}(\psi')(y;k_x,k_z,t) \equiv \int_{-\infty}^{\infty}\int_{-\infty}^{\infty} \psi'(x,y,z,t)\mathrm{e}^{-\mathrm{i}(k_x x+k_z z)}\,\mathrm{d}x\,\mathrm{d}z. \tag{3.17}$$

We compute this average quantity for each of the three fluctuating velocity components by first computing the convective velocity of each component using (3.11) and (3.12) with the corresponding output operators given in (3.13). These quantities are then filled into (3.16) with an averaging domain $\Omega : (\lambda_x^+, \lambda_z^+) > (500, 80)$. The weighting function $h(y;k_x,k_z)$ in equation (3.16) is selected to provide the least-squares fit to the passive advection model: $\partial_t\psi' + [\psi_c]_h\partial_x\psi' = 0,\ \psi' = u', v', w'$ as discussed by del Álamo & Jiménez (2009). This choice allows a direct comparison with Geng *et al.* (2015), who explicitly employed this fit in their computations.

The averaging domain $\Omega : (\lambda_x^+, \lambda_z^+) > (500, 80)$ was chosen to include the sublayer streaks proposed as the source of the elevated near-wall convective velocity (Kim & Hussain, 1993) but to avoid the nonlinear effects that dominate at smaller scales, where our linear analysis is not expected to be valid. The limitations of our input-output based approach at these smaller scales can be understood by examining the energy spectrum that is compared to that of DNS data in figure 3.2. Here it is clear that the spectrum for DNS falls off much faster with decreasing wavelength than the spectrum obtained using the input-output based approach in this work. The relatively heavier weighting at the small scales (wavelength) structures imposed through

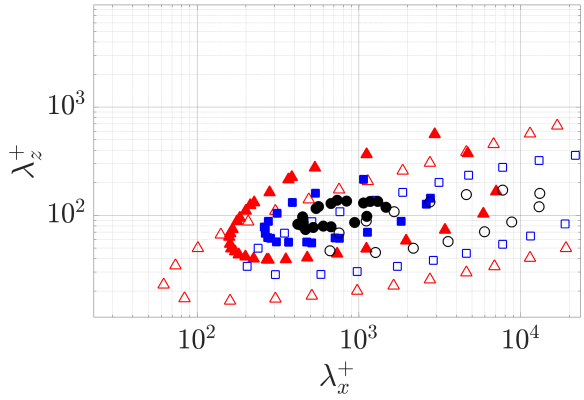

Figure 3.2: Premultiplied two-dimensional spectral density of streamwise velocity fluctuations $k_x k_z \int \Phi_{\widehat{u'}}(y; k_x, k_z, c) dc$ at $y^+ \approx 5$ for Reynolds number $Re_\tau = 1000$. Contours are shown for 0.2 (△); 0.5 (□); 0.8 (○) times the maximum value computed using the present approach. Results are plotted with the premultiplied spectral density of streamwise velocity fluctuations computed from DNS data. Contours are plotted at 0.2 (▲); 0.5 (■); 0.8 (●) times the maximum value from DNS data at $Re_\tau = 934$ (del Álamo *et al.*, 2004) (https://torroja.dmt.upm.es/channels/data/spectra/).

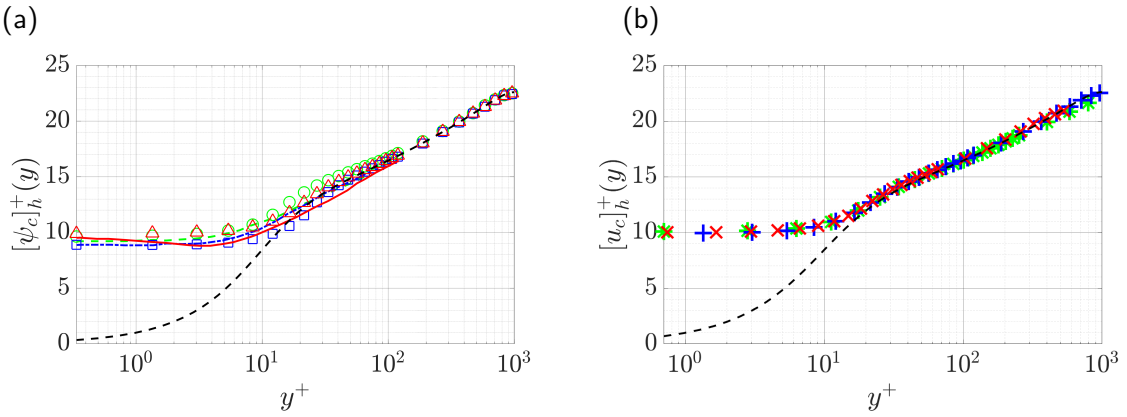

Figure 3.3: (a) The average convective velocity of velocity fluctuations, $[\psi_c]_h^+(y)$: $\psi' = u'$ (△); $\psi' = v'$ (□); $\psi' = w'$ (○) computed using the present approach and (3.16) with their corresponding weighting functions $h = \langle |\mathcal{F}_{xz}(\psi')|^2 \rangle k_x^2$ and an averaging domain of $(\lambda_x^+, \lambda_z^+) > (500, 80)$ at $Re_\tau = 1000$. Results are plotted with convective velocities computed from DNS data (Geng *et al.*, 2015) at $Re_\tau = 932$: $\psi' = u'$ (—); $\psi' = v'$ (- · -); $\psi' = w'$ (- -). (b) The model-based average convective velocity for streamwise fluctuations $\psi' = u'$ computed from (5.1) with the weighting function $h = \langle |\mathcal{F}_{xz}(u')|^2 \rangle k_x^2$ over averaging domain $(\lambda_x^+, \lambda_z^+) > (500, 80)$ at $Re_\tau = 550$ (×); $Re_\tau = 1000$ (+); $Re_\tau = 5200$ (✳). The black dashed lines in both (a) and (b) are the turbulent mean velocity profile at $Re_\tau \approx 1000$ from Lee & Moser (2015).

the present approach results in a lower overall convective velocity in these regions. Our choice of averaging domain eliminates the effect of this heavier weighting and implicitly assumes that smaller wavelengths are energetically negligible. Therefore, these small wavelength components do not contribute to the average convective velocity computed using our input-output approach.

The performance of the input-output based model at small scales may be improved by integrating known correlations from DNS or experimental data, e.g., shaping the forcing based on spatial or temporal correlations obtained via simulation data (Moarref *et al.*, 2014; Zare *et al.*, 2017). Improvements could also potentially be realized by using an eddy viscosity based enhancement of the LNS equations (Reynolds & Hussain, 1972), which Zare *et al.* (2017) have shown can provide similar improvements to the input-output response as the introduction of colored-in-time forcing. Understanding the relative benefits of each of these approaches over the current model is a topic of ongoing work.

Figure 3.3(a) compares the resulting mean convective velocities to those obtained from the DNS data based computations of Geng *et al.* (2015). The plot demonstrates that the model-based average convective velocities of the streamwise, wall-normal, and spanwise velocity fluctuations show good agreement with those computed from DNS data (Geng *et al.*, 2015).

Figure 3.3(b) replots the results for the streamwise velocity fluctuations in inner units for $Re_\tau = 550$, $Re_\tau = 1000$, and $Re_\tau = 5200$. The results collapse with the average convective velocities computed from the input-output based approach at different Reynolds numbers all tending to a constant value $\approx 10u_\tau$ near the wall. This Reynolds number invariance of convective velocities is consistent with the results reported in figure 3 of Geng *et al.* (2015).

The Reynolds number dependence can be analyzed by rewriting equations (3.3a) and (3.3b) using the following change of variables $k_x = k_x^+ Re_\tau$, $\widehat{\boldsymbol{\nabla}} = \widehat{\boldsymbol{\nabla}}^+ Re_\tau$, $\frac{d\bar{u}}{dy} = Re_\tau \frac{d\bar{u}}{dy^+}$ and $\widehat{\nabla}^2 =$

$\widehat{\nabla}^{2+} Re_\tau^2$, which gives:

$$\mathrm{i}k_x^+(\bar{u}-c)\widehat{\boldsymbol{u}}' - \widehat{\nabla}^{2+}\widehat{\boldsymbol{u}}' + \widehat{v}'\frac{d\bar{u}}{dy^+}\boldsymbol{i} + \widehat{\boldsymbol{\nabla}}^{+}\widehat{p}' = \frac{\widehat{\boldsymbol{f}}'}{Re_\tau}, \tag{3.18a}$$

$$\widehat{\boldsymbol{\nabla}}^{+} \cdot \widehat{\boldsymbol{u}}' = 0. \tag{3.18b}$$

As neither the mean velocity profile $\bar{u}$ nor the mean shear $d\bar{u}/dy^+$ at a specific y^+ varies over the Reynolds number in the near-wall region (see e.g., Chapter 7.1.4 of Pope (2000)), the left-hand side of equation (3.18a) does not significantly vary over Reynolds number. The right-hand side of equation (3.18a) is related to Re_τ, but the Reynolds number only influences the magnitude of stochastic forcing $\widehat{\boldsymbol{f}}'$. According to equation (3.11) and (3.12), the phase speed, c, at which $\Phi_{\widehat{u}'}$ peaks does not change, and thus, the convective velocity of the streamwise fluctuations, u_c remains unaffected. This leads to the Reynolds number independence observed in the right panel of figure 3.3.

This inner units scaling was also previously observed by Moarref *et al.* (2013) for streamwise energy density and further generalized by Sharma *et al.* (2017) in the framework of resolvent analysis. They end up with the same Re_τ^{-1} scaling for the spatio-temporal transfer function as shown in equation (A4) of Moarref *et al.* (2013), and they also pointed out that Re_τ independence of turbulent mean profile $\bar{u}(y)$ for $y^+ \lesssim 100$ is necessary for this inner units scaling.

Having validated the ability of the input-output based computations to reproduce the mean trends, we next investigate the scale dependence of the convective velocity.

3.5.2 Scale-by-scale analysis of convective velocity

The model-based approach employed herein allows one to calculate the contribution of each individual (λ_x, λ_z) wavelength pair to the local convective velocity at each wall-normal location; i.e., $u_c(y; k_x, k_z)$. We now take advantage of this feature to investigate the scale-dependence of the convective velocity and examine which scales contribute to its deviation from the local mean velocity in various regions of the flow. Figure 3.4 shows the convective velocity of the streamwise velocity fluctuations normalized by the local mean velocity: $u_c(y; k_x, k_z)/\bar{u}(y)$ for

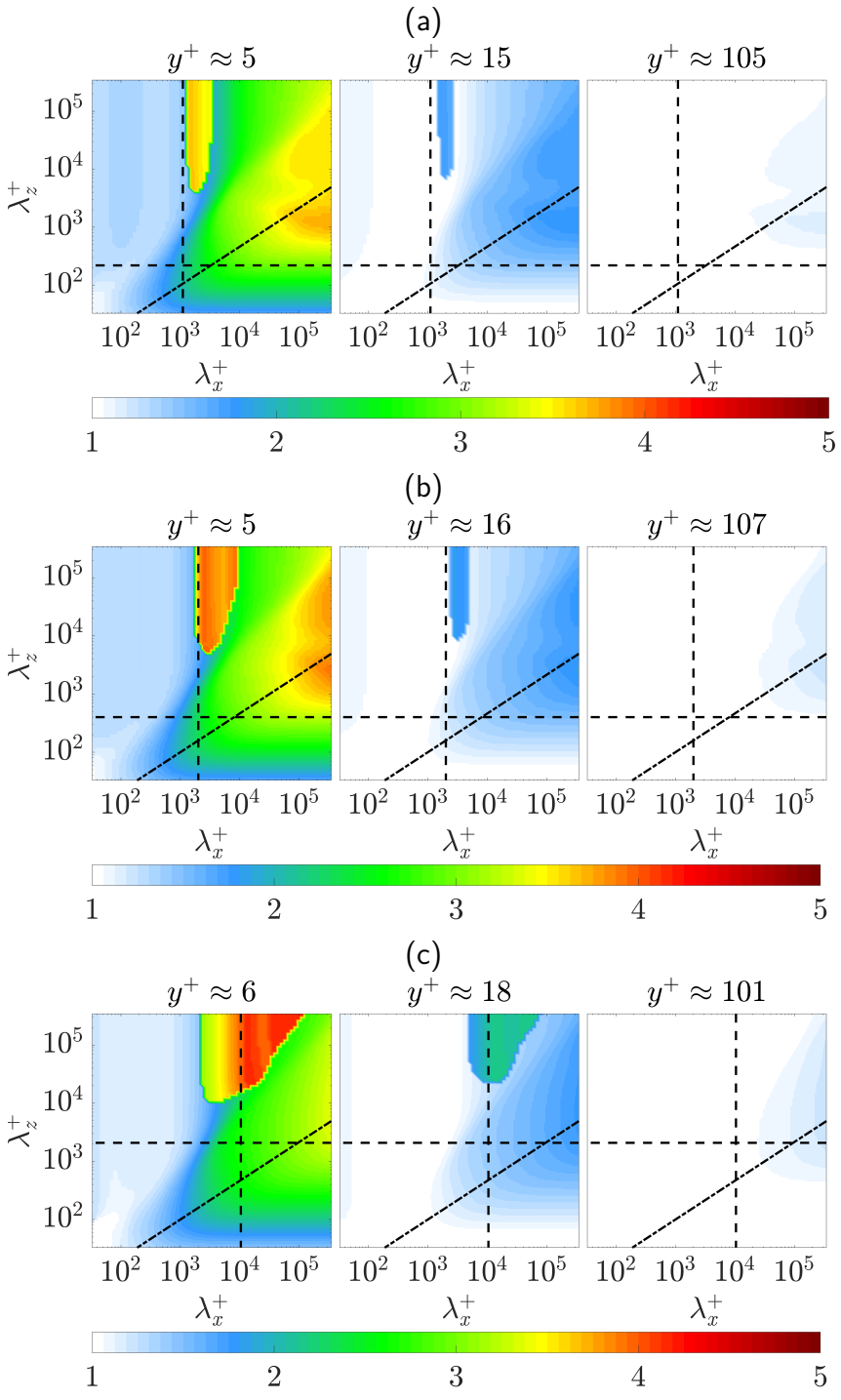

Figure 3.4: Scale-dependent convective velocity normalized by the local mean velocity $u_c(y;\lambda_x,\lambda_z)/\bar{u}(y)$ at (a) $Re_\tau = 550$, (b) $Re_\tau = 1000$, and (c) $Re_\tau = 5200$. The black dashed lines are given by $(\lambda_x,\lambda_z) = (2, 0.4)$, which are identified by del Álamo & Jiménez (2009) as the lower-bound of the large-scale convective velocity. The black dash-dot lines are $\lambda_z^+ = \lambda_x^{+\frac{2}{3}}$, which fit through the knee of these contours.

(a) $Re_\tau = 550$, (b) $Re_\tau = 1000$, and (c) $Re_\tau = 5200$, as a function of the streamwise-spanwise wavelengths $(\lambda_x^+, \lambda_z^+)$ at wall-normal locations associated with the viscous sublayer ($y^+ \approx 5$), the buffer layer ($y^+ \approx 15$), and the log-law region ($y^+ \approx 100$). As expected, the results in the viscous sublayer show the most significant deviations from the mean velocity, whereas there is little difference in the log-law region, which is consistent with the data in figure 3.3.

In figure 3.4, the convective velocities of structures in the intermediate scale range $\lambda_x \approx 2$ show a discontinuity as the streamwise wavelength λ_x varies. This phenomenon was also observed for the scale-dependent convective velocity of wall pressure in pipe flow predicted using resolvent analysis with broadband forcing; see figure 12(a) in Luhar *et al.* (2014). In the term-by-term analysis in section 3.7, we will further confirm that the convective velocity of structures associated with these scales is highly influenced by the pressure.

Figure 3.5 shows the PSD, $\Phi_{\widehat{u'}}(y; k_x, k_z, c)$ computed from equation (3.11), of the streamwise velocity fluctuations for $Re_\tau = 1000$ as a function of wall-normal location y^+ and phase speed c^+ at six different streamwise–spanwise wavelength pairs. Figures 3.5(a) and (b) show that the energy of the large wavelength structures at example points $\triangleleft$ $(\lambda_x^+, \lambda_z^+) = (133052, 857)$ and $\triangleright$ $(\lambda_x^+, \lambda_z^+) = (133052, 14756)$, are concentrated near $(y^+, c^+) \approx (200, 18.4)$, and that structures traveling at $c^+ \approx 18.4$ provide the largest contribution to the spectral density in the near-wall region. Figure 3.5(c) indicates that structures traveling at a higher velocity than the local mean also contribute most to the PSD in the near-wall region for the intermediate-scale structures. In contrast, the PSD distributions over (c^+, y^+) for structures with small streamwise wavelengths are more concentrated near the mean velocity profile $\bar{u}$ as shown in figures 3.5(d), and (e) for example points $\square$ $(\lambda_x^+, \lambda_z^+) = (11, 14756)$, and $\diamond$ $(\lambda_x^+, \lambda_z^+) = (11, 11)$.

Figure 3.5 indicates that the PSD distribution over phase speed is nearly symmetric about its peak in figures 3.5(a), (b), (d), and (e), which indicates close correspondence between the center of gravity and peak of the PSD definitions of convective velocity. For the representative intermediate flow scale plotted in figure 3.5(c), the PSD distribution over the phase speed shows skewness, which is expected to lead to differences in the convective velocity obtained by

considering the distribution. In order to evaluate the differences, we recomputed the results in figure 3.4(b) using a center of gravity definition $\check{\psi}_c(y;k_x,k_z) \equiv \frac{\int c\Phi_{\widehat{\psi'}}(y;k_x,k_z,c)dc}{\int \Phi_{\widehat{\psi'}}(y;k_x,k_z,c)dc}$ and found that there are indeed differences for these scales. Specifically, the discontinuity in the convective velocity as streamwise wavelength λ_x varies over larger λ_z is smoothed. Differences also occur at the flow scales that are very small in the spanwise direction but very long in the streamwise direction; e.g., the structures indicated by $\circ$ $(\lambda_x^+,\lambda_z^+) = (133052, 11)$ in figure 3.5(f). These differences are not surprising because figure 3.5(f) demonstrates that the PSD is quite flat and therefore advection does not dominate at these flow scales. Here, neither definition of convective velocity is physically meaningful, as the maximum is not associated with a clear peak and the center of gravity definition merely selects the center point of the computational domain. The comparison verified that the overall trends that are highlighted in this manuscript, such as the influence of the large-scale structures in the near-wall and buffer regions as well as the slope of the knee through the contours indicated by dash-dot lines in the panels of figure 3.4 were unchanged when we used the center of gravity in our computations. We therefore proceed with the definition in terms of the peak of the PSD in equation (3.12) in the remainder of the manuscript.

Both figures 3.4 and 3.5 indicate that large channel spanning structures have an influence on the convective velocity in both the viscous sublayer and the buffer layer. This phenomenon was investigated by del Álamo & Jiménez (2009), who identified large scales as structures of size $(\lambda_x,\lambda_z) > (2, 0.4)$. This large-scale cut-off is identified by horizontal and vertical dashed lines in each panel of figure 3.4.

Figure 3.6(a) plots the mean convective velocities obtained for the averaging domain $(\lambda_x,\lambda_z) > (2, 0.4)$ for $Re_\tau = 550$ and $Re_\tau = 1000$. A comparison to DNS data indicates that the model produces qualitatively and quantitatively similar behavior to results computed from DNS data (figure 5(a) in del Álamo & Jiménez (2009)). Note the results in figure 3.6(a) are scaled by the bulk velocity; i.e., $U_b = \frac{1}{2}\int_{-1}^{1} \bar{u}(y)dy$ for direct comparison with del Álamo & Jiménez (2009).

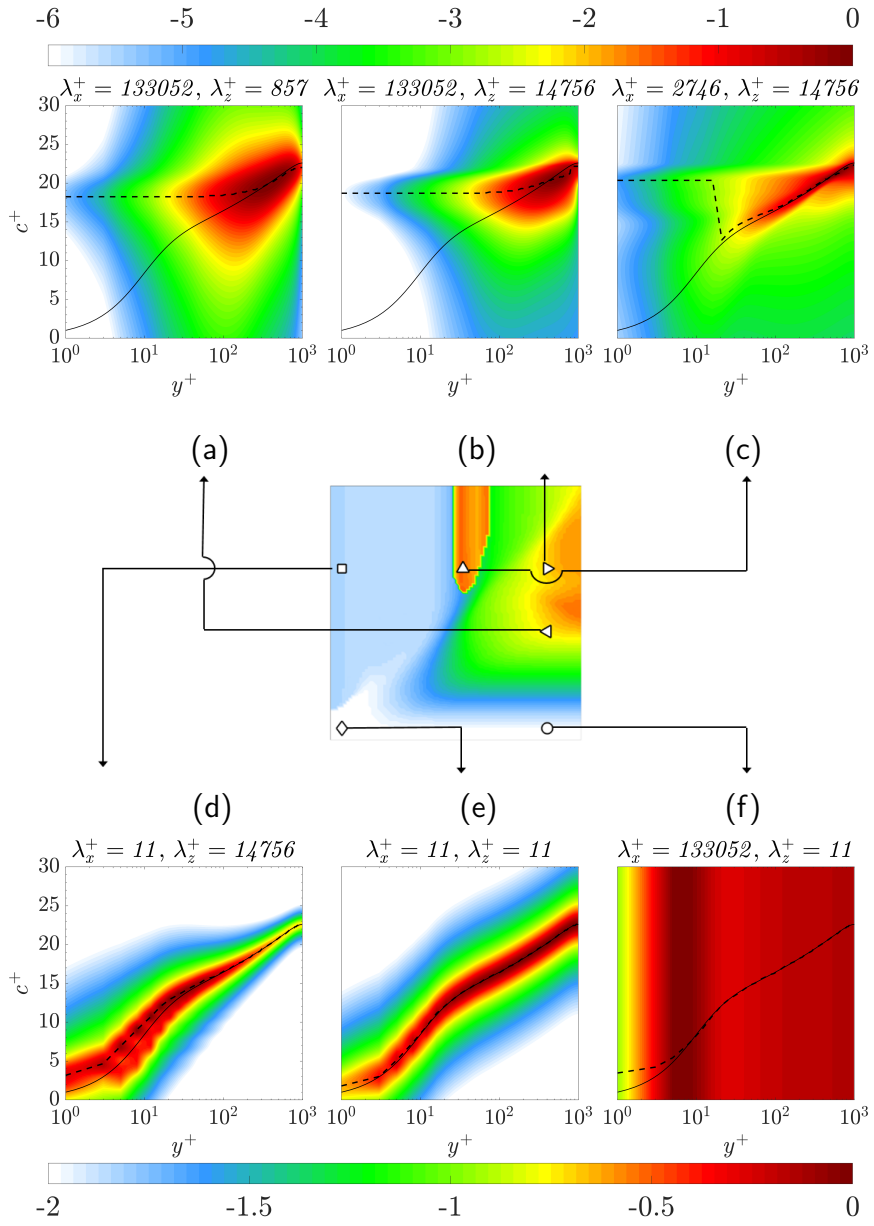

Figure 3.5: Normalized power spectral density of streamwise velocity fluctuations $\frac{\Phi_{\widehat{u'}}(y;k_x,k_z,c)}{\max_{c,y}(\Phi_{\widehat{u'}}(y;k_x,k_z,c))}$ over wall-normal location y^+ and phase speed c^+. The symbols represent locations associated with large-scale structures at (a) $\triangleleft$ $(\lambda_x^+, \lambda_z^+) = (133052, 857)$ and (b) $\triangleright$ $(\lambda_x^+, \lambda_z^+) = (133052, 14756)$; (c) intermediate-scale structures $\triangle$ $(\lambda_x^+, \lambda_z^+) = (2746, 14756)$, and structures with small streamwise or spanwise wavelengths, respectively: (d) $\square$ $(\lambda_x^+, \lambda_z^+) = (11, 14756)$, (e) $\diamond$ $(\lambda_x^+, \lambda_z^+) = (11, 11)$, and (f) $\circ$ $(\lambda_x^+, \lambda_z^+) = (133052, 11)$. The color is in base 10 logarithmic scale. The black solid lines represent the mean streamwise velocity profile and the black dashed lines are convective velocites computed using the method in section 3.3. The middle panel, which is reproduced from figure 3.4(b) at $y^+ \approx 5$ for $Re_\tau = 1000$, indicates the locations corresponding to each symbol.

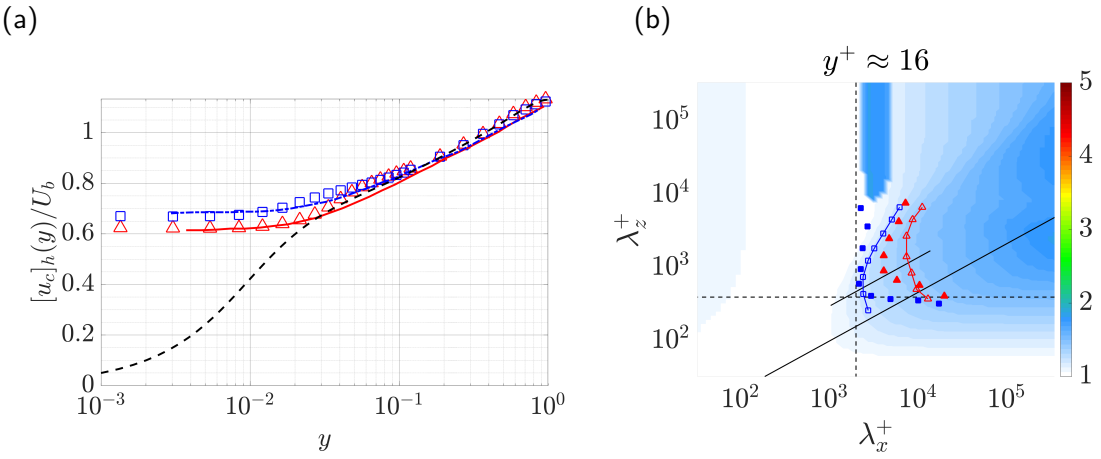

Figure 3.6: (a) The average convective velocity of streamwise fluctuations $[u_c]_h/U_b$ over $(\lambda_x, \lambda_z) > (2, 0.4)$. Model based results at $Re_\tau = 550$ (△) and $Re_\tau = 1000$ (□) are compared to convective velocities computed from DNS data (del Álamo & Jiménez, 2009) at $Re_\tau = 547$ (—) and $Re_\tau = 934$ (– · –). For direct comparison with del Álamo & Jiménez (2009), the results in (a) are scaled by the bulk velocity; i.e., $U_b = \frac{1}{2}\int_{-1}^{1} \bar{u}(y)dy$. The black dashed line is the mean velocity profile at $Re_\tau \approx 1000$ from Lee & Moser (2015). (b) Model based scale-dependent convective velocity at $y^+ \approx 16$ for $Re_\tau = 1000$: contour lines $u_c(y; k_x, k_z)/\bar{u}(y) = 1.40$ (—△—); $u_c(y; k_x, k_z)/\bar{u}(y) = 1.21$ (—□—); are compared to convective velocities computed from DNS data at $y^+ = 15$ and $Re_\tau = 934$ (del Álamo & Jiménez, 2009) $u_c(y; k_x, k_z)/\bar{u}(y) = 1.40$ (▲); $u_c(y; k_x, k_z)/\bar{u}(y) = 1.21$ (■). The black dashed lines are given by $(\lambda_x, \lambda_z) = (2, 0.4)$. The black solid lines are $\lambda_z^+ \sim \lambda_x^{+\frac{2}{3}}$, which fit through the knee of model based convective velocity and DNS data contours (del Álamo & Jiménez, 2009), respectively.

In figure 3.6(b), we further analyze the influence of the large scales by comparing the scale-dependent convective velocity at $y^+ \approx 16$ with $Re_\tau = 1000$ from our approach to figure 3(a) in del Álamo & Jiménez (2009). The darker blue region of the largest λ_x^+ and moderate to largest λ_z^+ in figure 3.6(b) indicates the influence of large and very large-scale motion on the convective velocity in this region, which supports previous studies (Kim & Hussain, 1993; Krogstad *et al.*, 1998) indicating that fast moving structures centered further away from the wall (where the local mean velocity is larger) have an influence very near the wall due to their large size (Dinkelacker *et al.*, 1977; Kreplin & Eckelmann, 1979; Farabee & Casarella, 1991; Kim & Hussain, 1993; Hutchins *et al.*, 2011).

A linear fit through the knee of the contour plot in figure 3.6(b) shows self-similar structures with a ratio $\lambda_z^+ \sim \lambda_x^{+\frac{2}{3}}$ in both our results and those reported in del Álamo & Jiménez (2009). This type of x–z similarity in energy spectra density has been previously observed in the context of geometric self-similarity (del Álamo *et al.*, 2004; Chandran *et al.*, 2017). For example, del

Álamo and co-authors (del Álamo & Jiménez, 2003; del Álamo *et al.*, 2004) found that the isocontours of the pre-multiplied energy spectrum of u' form a corner centered along $\lambda_z \sim \lambda_x^n$ with $\frac{1}{3} < n < 1$. In that work, the value of n changed over the wall-normal location with lower bound on n near the buffer layer ($y^+ \approx 15$), increasing to $n = \frac{1}{2}$ in the log-law region and reaching $n = 1$ in the outer region of the flow. Recent experimental measurements of two-dimensional spectra in zero-pressure gradient boundary layers indicate a $\lambda_z \sim \sqrt{\lambda_x}$ ($Re_\tau = 2430$) and $\lambda_z \sim \lambda_x$ ($Re_\tau = 26090$) relationship in the start of the log-law region (Chandran *et al.*, 2016, 2017).

The scaling law of convective velocity explored here is closely related to the temporal self-similarity previously observed in the literature. More specifically, Lozano-Durán & Jiménez (2014) showed that tall attached structures are both geometrically and temporally self-similar with lifetimes proportional to their distance from the wall. They also attribute the lifetime and deformation of these structures to the vertical gradient of their convective velocity. Long lifetimes, which require low dispersion, have been associated with coherent structures (Adrian, 2007); e.g., hairpin vortices that are observed to propagate downstream with small velocity dispersion (Adrian *et al.*, 2000). Non-dispersive coherent structures are implied by the isocontour lines of the scale dependent convective velocities in figures 3.4 and 3.6(b), which forms a $\lambda_z^+ \sim \lambda_x^{+\frac{2}{3}}$ knee. Based on this observation, we conjecture that the x–z similarity observed here is closely related to the scaling laws of energy spectra.

To explain the $\lambda_z^+ \sim (\lambda_x^+)^{2/3}$ scaling, we employ a simple model involving the bending of streamlines in the cross-plane due to the presence of a streamwise vortex. This simple model was originally proposed by Jiménez *et al.* (2004) to explain the contribution of high-momentum streaks to the energy spectrum. Consider convection of $\widehat{u}'$ due to a point vortex with circulation γ in the cross-plane $\partial_t u' + \frac{2\pi\gamma}{r^2}\frac{\partial u'}{\partial \theta} = 0$ where (r, θ) is the polar representation of the (y, z) plane, centered on the vortex. For a homogeneous shear initial condition, $u'(t = 0, r, \theta) \sim Sy = Sr\sin\theta$, with shear rate S, we have $u'(t, r, \theta) \sim Sr\sin(\theta - \gamma t/2\pi r^2)$. At a given time,

t, setting $\theta = \pi$ yields the 'size' of the vortex-distorted region as:

$$R_z = \sqrt{\gamma t / 2\pi^2}. \tag{3.19}$$

Moreover, the length of streak is determined by the velocity difference between its top and bottom with shear rate S, which can be roughly estimated as:

$$\lambda_x = S R_z t, \tag{3.20}$$

if we assume that the streak height is roughly equal to its width. We estimate the meandering magnitude of streaks by approximating the spanwise drift of the vortices under the induction of their reflected images across the wall, which leads to

$$\lambda_z = 2\sqrt{2} w' t, \tag{3.21}$$

where w' denotes a spanwise velocity fluctuation of the order of $w'^{+} \approx 1$ (Kim *et al.*, 1987). Combining equations (3.19), (3.20), and (3.21) gives the scaling:

$$\lambda_z^+ \sim (\lambda_x^+)^{\frac{2}{3}}. \tag{3.22}$$

Although this is an idealized analysis, it leads to the trends observed both here and in DNS based convective velocity analysis. The assumptions underlying this scaling are also consistent with the existence of structures at a wide variety of scales extending into the channel; i.e., structures reminiscent of Townsend's attached eddies (Townsend, 1976; Perry *et al.*, 1986; Marusic & Monty, 2019). We next calculate the wall-normal coherence of these structures to further examine this connection.

3.6 Wall-normal coherence of viscous sublayer structures

The convective velocity at each (λ_x, λ_z) wavelength pair, $u_c(y; k_x, k_z)$, is obtained via the maximization in (3.12), so we refer to the spectral component of u' defined by $(\lambda_x, \lambda_z, u_c)$ as the 'characteristic structure'. We hypothesize that the characteristic structure at a given

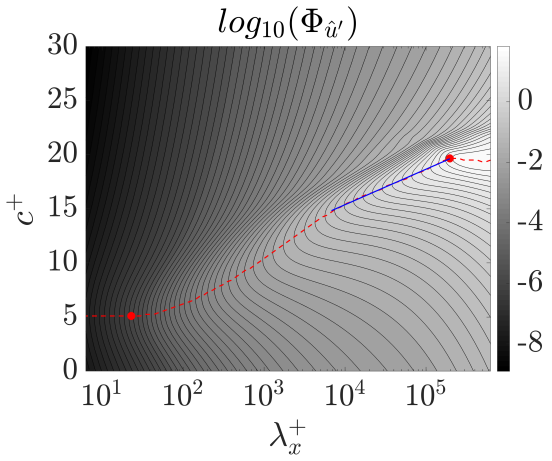

Figure 3.7: Isocontours of $\Phi_{\widehat{u'}}$ in the viscous sublayer ($y^+ \approx 5$) along $\lambda_z^+ = (\lambda_x^+)^{\frac{2}{3}}$ at $Re_\tau = 1000$, calculated using (3.11). The red dashed line indicates the c^+ at which $\Phi_{\widehat{u'}}$ peaks for each λ_x^+, and the blue solid line indicates the region of logarithmic increase. It therefore defines the convective velocity u_c as in (3.12). The markers (●) indicate the locations where we evaluate the two-point wall-normal coherence in figure 3.8.

wall-normal location, y_0, is responsible for the dominant convection at that location, and that it also contributes to the energetics elsewhere in the channel due to its wall-normal extent. In this section, we investigate this wall-normal extent using the spectral coherence between signals at two different wall-normal locations. We focus on the characteristic structures that provide the dominant convection in the viscous sublayer and on wavelength pairs along the knee of the isocontours of u_c in figure 3.4; i.e., along $\lambda_z^+ = (\lambda_x^+)^{\frac{2}{3}}$.

The u' frequency–wavenumber spectrum, $\Phi_{\widehat{u'}} = \langle |\widehat{u}'|^2 \rangle$ of streamwise fluctuations in the viscous sublayer ($y^+ \approx 5$) for $Re_\tau = 1000$, is shown in figure 3.7 in terms of phase speed and wavelengths along $\lambda_z^+ = (\lambda_x^+)^{\frac{2}{3}}$. The autocorrelation maxima defining the convective velocity are plotted as a dashed line. The ridge corresponding to these maximum values asymptote to constants at both the large and small wavelength limits, but show a region of linear growth followed by a region of logarithmic increase (blue solid line) between two red circle markers. The logarithmic behavior is similar to the variation of the mean velocity profile $\bar{u}(y)$ with y and is consistent with the assumption that the dominant viscous sublayer convection at streamwise wavelength λ_x arises due to a structure advecting at the local mean velocity at $y \sim \lambda_x^n$ for some $n > 0$.

The spectral coherence between two wall-normal locations y' and y, defined for a fluctuating variable ψ is defined as:

$$0 \leq \chi_{\psi';y'y}(k_x, k_z, c) \equiv \frac{|\Phi_{\widehat{\psi'},\text{cross}}(y', y; k_x, k_z, c)|^2}{\Phi_{\widehat{\psi'}}(y'; k_x, k_z, c)\Phi_{\widehat{\psi'}}(y; k_x, k_z, c)} \leq 1, \tag{3.23}$$

where $\Phi_{\widehat{\psi'},\text{cross}}$ is the cross-spectral density of ψ' between locations y' and y; i.e.,

$$\Phi_{\widehat{\psi'},\text{cross}}(y', y; k_x, k_z, c) = \langle \widehat{\psi}'^*(y'; k_x, k_z, c)\widehat{\psi}'(y; k_x, k_z, c)\rangle. \tag{3.24}$$

The cross-spectral densities are the off-diagonal components of the matrix obtained from the finite-dimensional representation (3.15) of $\Phi_{\widehat{\psi}}$. Figure 3.8 shows the two-point spectral coherence for streamwise velocity fluctuations $\chi_{u';y'y}$ for two characteristic structures along $\lambda_z^+ = (\lambda_x^+)^{\frac{2}{3}}$ in the near-wall region: (a) a short wavelength component, $(\lambda_x^+, \lambda_z^+) \approx (22, 8)$, and (b) a long wavelength component, $(\lambda_x^+, \lambda_z^+) \approx (2 \times 10^5, 3 \times 10^3)$. The phase speeds associated with these characteristic structures are indicated in figure 3.7 by circle markers. The shorter wavelength component is associated with the smaller convective velocity and the longer wavelength component with the larger convective velocity.

In figure 3.8, we see a wall-normal coherence that extends *from* the wall; i.e., it does not involve any wall-detached patches, consistent with Townsend's attached-eddy hypothesis (Townsend, 1976; Perry *et al.*, 1986; Marusic & Monty, 2019). As predicted by del Álamo & Jiménez (2009), the long wavelength component is more coherent further into the channel towards the core than the short wavelength component with its coherence falling to 0 in the core. This growth of coherence away from the wall with increasing wavelength suggests that the structures contributing to the convective velocity in the viscous sublayer extend from the wall deep into the log-law region, but only weakly into the wake region, reminiscent of the long meandering structures in the log-law region whose footprint extends to the near-wall region (Jiménez *et al.*, 2004; Hutchins & Marusic, 2007; Monty *et al.*, 2007; Guala *et al.*, 2006; Balakumar & Adrian, 2007).

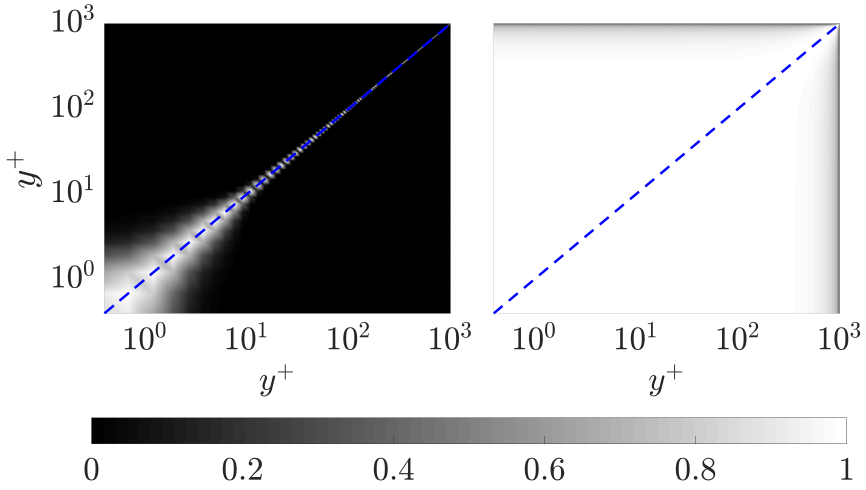

Figure 3.8: Two-point spectral coherence of streamwise velocity fluctuations $\chi_{u';y'y}$ for data at $Re_\tau = 1000$, as defined in (3.23) at $(\lambda_x^+, \lambda_z^+) \approx (22, 8)$ (left) and $(\lambda_x^+, \lambda_z^+) \approx (2\times10^5, 3\times10^3)$ (right) indicated by circle markers in figure 3.7. Both points are along $\lambda_z^+ = (\lambda_x^+)^{\frac{2}{3}}$, and their phase speeds in friction units are approximately $c^+ \approx 5$ for the small-scale structure and $c^+ \approx 20$ for the large one. Perfectly coherent signals have a spectral coherence of 1, and incoherent signals have a spectral coherence of 0.

Calculations (not presented here for brevity) indicate that components with identical convective velocity as determined by figure 3.4 also have nearly identical wall-normal coherence. This behavior, also suggested by del Álamo & Jiménez (2009), agrees with the hypothesis that a random arrangement of similar basic structures with dimensions given by $\lambda_z^+ = (\lambda_x^+)^{\frac{2}{3}}$, leads to the long-tailed behavior of the contours in figure 3.4.

Figure 3.9 shows the spectral coherence with respect to the viscous sublayer location ($y^+_{\text{sublayer}} \equiv 5$) $\chi_{u';y_{\text{sublayer}}y}(k_x, k_z, c)$ along $\lambda_z^+ = (\lambda_x^+)^{\frac{2}{3}}$. The monotonic behavior of the spectral coherence in figure 3.9 implies that structures larger in (x, z) are also larger in y. The wall-normal coherence for $\lambda_x^+ \gtrsim 200$ indicated by the dashed lines overlain on the (red) solid contours representing spectral coherences of 0.1 and 0.5 shows an aspect ratio $y^+ \sim (\lambda_x^+)^{\frac{2}{3}}$. The minimum wall-normal coherence length associated with these larger wavelengths is ~ 15 wall units, which is the approximate location of the buffer layer and also the location of the well-known peak in the root-mean-square (RMS) streamwise velocity fluctuations; see for example, Lee & Moser (2015). This self-similarity represented by a power-law relationship at larger wavelengths is also suggestive of the attached-eddy structures proposed by Townsend (1976); Perry *et al.* (1986);

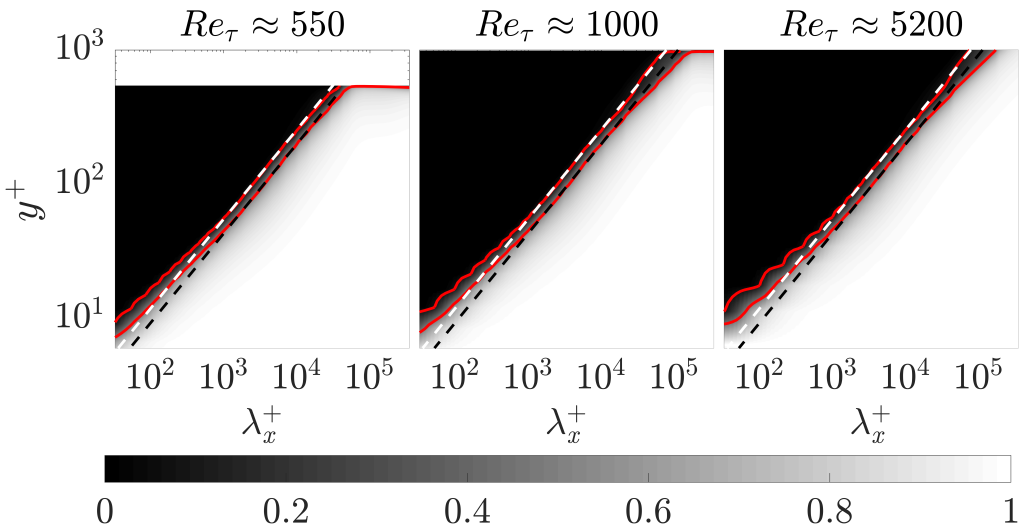

Figure 3.9: Two-point spectral coherence of streamwise velocity fluctuations $\chi_{u';y'y}$ at $Re_\tau \approx 550$, $Re_\tau \approx 1000$, and $Re_\tau \approx 5200$, as defined in (3.23), between $y'^+ \approx y^+_{\text{sublayer}} = 5$ and wall-normal locations above it for wavelengths defined by $\lambda_z^+ = (\lambda_x^+)^{\frac{2}{3}}$ and phase speeds indicated by the dashed maxima line in figure 3.7. The solid red lines serve to indicate the boundaries of regions of high/low coherence and are isocontours of spectral coherence with values 0.1 and 0.5. The white dashed lines are $y^+ = 0.55(\lambda_x^+)^{\frac{2}{3}}$ and the black dashed lines are $y^+ = 0.43(\lambda_x^+)^{\frac{2}{3}}$ and they serve as fits to the red lines. Perfectly coherent signals have a spectral coherence of 1, and incoherent signals have a spectral coherence of 0.

Marusic & Monty (2019).

From the power-law behavior $y^+ \sim (\lambda_x^+)^{\frac{2}{3}}$ for $\lambda_x^+ \gtrsim 200$ shown in figure 3.9, we can also extract the structure inclination angle contributing to this self-similar behavior. The 0.1 and 0.5 spectral coherence contour is fitted by $y^+ = \alpha(\lambda_x^+)^{\frac{2}{3}}$ with $\alpha = 0.55$ (white dash lines) and $\alpha = 0.43$ (black dash lines), respectively. We select the spectral coherence contours as 0.1 and 0.5 to fit the scaling laws because we observe significant variation of coherence between this range in figure 3.9, while outside of this range, the coherence show saturation. Such a saturation phenomenon is also observed in the coherence computed from the experimental data; see e.g., figure 4 of Baars *et al.* (2016) and figure 5(b) of Baars *et al.* (2017). Furthermore, the contours of two-dimensional spectral coherence of 0.1, 0.3, and 0.5 are shown to collapse when scaled with the wall-normal height of the structures; indicating the presence of self-similar structures, see figure 4 of Madhusudanan *et al.* (2019).

Thus, $y^+ \sim \lambda_z^+$ with a constant of proportionality α between 0.55 and 0.43, respectively,

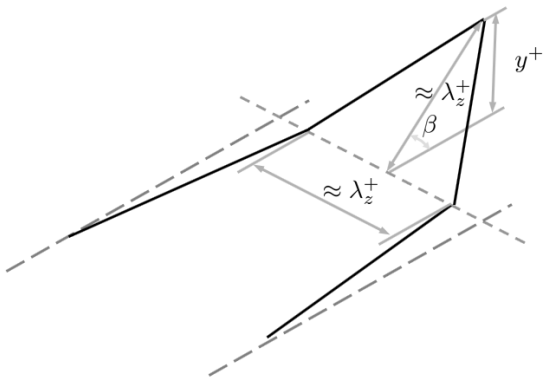

Figure 3.10: The structures of height/width aspect ratio 1 with an inclination angle β in analogy with Perry & Chong (1982).

imply that the projection of the structures onto the cross-stream plane has a smaller height than width. If we assume the structures contributing to the spectral coherence have a height/width aspect ratio of 1 as depicted in the cartoon in figure 3.10, then the dimensions of the cross-plane projection of the structure represented by spectral coherence between 0.1 and 0.5 implies a tilt angle $\beta = \arcsin(\alpha)$ between approximately $25°$ and $33°$.

Townsend (1976) suggests an inclination angle of $\sim 30°$ for attached double roller eddies (a pair of counter-rotating, inclined, approximately streamwise vortex structures) to explain the experimental observations of Grant (1958). Experimental observations in turbulent boundary layers, on the other hand, have yielded inclination angles between $15°$ and $20°$ (Brown & Thomas, 1977; Marusic & Heuer, 2007; Carper & Porté-Agel, 2004). The latter inclination angles were calculated using two-point temporal correlations and Taylor's hypothesis. In turbulent channel flows, hairpin vortices have been the focus of considerable interest. Although a single well-defined inclination angle cannot be associated with hairpin vortices, the inclinations of hairpin-like structures vary from $12°$ (elongated legs) to $45°$ (hairpin heads) (Adrian, 2007). The present work does not restrict the structures contributing to the convective velocities to any one of the structures discussed above, but does provide an inclination angle, assuming structures are roughly of aspect ratio 1, which is within the range of previous observations.

In figure 3.9, the structure inclination angle predicted by this model also shows Reynolds

number invariance, which is consistent with experimental observations (Marusic & Heuer, 2007). For different Reynolds numbers, $y^+ = \alpha(\lambda_x^+)^{\frac{2}{3}}$ with $\alpha = 0.55$ and $\alpha = 0.43$, corresponding to tilt angles 25° and 33°, always give good approximations for 0.1 and 0.5 spectral coherence, respectively. Structure inclination angles inferred from the cross correlation of x in the experimental studies of Marusic & Heuer (2007) are found to be invariant over 3 orders of magnitude change in Reynolds number.

Our results reveal that the contributions from the relatively larger scale structures lead to the elevated velocities in the viscous sublayer seen in figure 3.3 and that these structures have dimensions given by $y^+ \sim \lambda_z^+ \sim (\lambda_x^+)^{\frac{2}{3}}$ with a minimum size ≈ 15 friction units, which is the approximate location of the buffer layer. The inclination angles of these structures do not vary with Reynolds number, which is consistent with experimental observations. These observations are consistent with the attached-eddy hypothesis in that they predict wall-attached structures that are self-similar in the cross-plane and contribute to the dominant convection. However, the attached-eddy hypothesis predicts that these structures are also self-similar in the streamwise direction, which our approach does not show.

3.7 Term-by-term analysis of scale-dependent convective velocities

We next use the input-output framework to analyze the contribution of different linear mechanisms to the scale-dependent convective velocity of the streamwise velocity fluctuations.

We follow the method shown in equation (2.11) of del Álamo & Jiménez (2009) to obtain the normalized deviation of the convective velocity from the mean velocity contributed from various terms. In particular, we multiply the x-momentum in equation (3.3a) by $\widehat{u}'^*$ and take the imaginary part of the result to obtain:

$$\frac{u_c - \bar{u}(y)}{\bar{u}(y)} = \frac{\overbrace{k_x \mathrm{Re}\left\{\langle \widehat{p}' \widehat{u}'^* \rangle\right\}}^{\text{IIa}} + \mathrm{i}ag\left\{\overbrace{\frac{d\bar{u}}{dy}\langle \widehat{v}' \widehat{u}'^* \rangle}^{\text{IIb}} \overbrace{- \frac{1}{Re_\tau}\langle \widehat{u}'^* \partial_{yy}^2 \widehat{u}' \rangle}^{\text{IIc}} \overbrace{- \langle \widehat{f_u}' \widehat{u}'^* \rangle}^{\text{III}}\right\}}{k_x \bar{u}(y) \langle \widehat{u}' \widehat{u}'^* \rangle}. \tag{3.25}$$

Here Re$\{\cdot\}$ and Im$\{\cdot\}$ represent the respective real part and imaginary part of the argument. The terms in equation (3.25) represent the relative contributions of the pressure term (IIa), the mean shear term (IIb), and the viscous term (IIc), each normalized by $k_x\bar{u}(y)\langle\widehat{u}'\widehat{u}'^*\rangle$.

We compute each term in (3.25) by modifying the output operator in (3.9) and then computing the cross-spectra through an appropriate modification of (3.11). For example, we can use the output operator corresponding to the fluctuating pressure in (3.14) to obtain $\mathcal{G}_{\widehat{p}'}$ and then compute the cross-spectra as

$$\langle\widehat{p}'\widehat{u}'^*\rangle = \mathcal{G}_{\widehat{p}'}\langle\widehat{\boldsymbol{f}}'\widehat{\boldsymbol{f}}'^*\rangle\mathcal{G}^*_{\widehat{u}'} = \mathcal{G}_{\widehat{p}'}\mathcal{G}^*_{\widehat{u}'}. \tag{3.26}$$

The other terms in (3.25) can be computed in a similar manner.

Figure 3.11(a), (b), and (c) show the respective contributions from the pressure term (IIa), the mean shear term (IIb), and the viscous term (IIc) to the scale-dependent convective velocity of the streamwise velocity fluctuations ($Re_\tau \approx 1000$) at the same three wall-normal locations as in figure 3.4. As shown in figure 3.11(a), the pressure plays an important role for the intermediate scale structures ($\lambda_x \approx 2$ and $\lambda_z > \lambda_x$), which supports our conjecture that the discontinuity in these scales shown in figure 3.4 is related to the pressure. Luhar *et al.*'s (2014) figure 12(a) also showed a discontinuity of the scale-dependent convective velocity of wall pressure computed using resolvent analysis and the maximum of the PSD to define the convective velocity. As discussed in Section 3.5, using the center of gravity of the PSD to define the convective velocity eliminates the discontinuity. A similar smoothing effect resulting from the use of the center of gravity definition versus the maximum value of the PSD was also observed in figures 12(a) and (b) of Luhar *et al.* (2014), where the authors compared these two convective velocity definitions for pressure fluctuations. The overall convective velocity of these intermediate-scale structures also includes contributions from both the mean shear (figure 3.11(b)) and the viscous terms (figure 3.11(c)), which indicates that multiple physical mechanisms are at play.

For the large-scale structures with $(\lambda_x, \lambda_z) > (2, 0.4)$, the deviation of convective velocity from the mean is primarily due to the viscous and the mean shear terms. In the viscous sublayer

($y^+ \approx 5$), the viscous term provides a relatively larger contribution to the deviation of the convective velocity from the mean than the mean shear term, whereas these two terms provide approximately equal contribution to the convective velocity in the buffer layer ($y^+ \approx 15$).

For structures with small streamwise and spanwise wavelengths; i.e., $\lambda_x^+ \lesssim 10$ and $\lambda_z^+ \lesssim 10$, all of the terms in (3.25) are negligible (as indicated by the white region of the colormap). This suggests that they convect at the local mean velocity or that their convective velocity is not captured through the linear terms retained in our approach. However, as previously noted, the nonlinear fluctuation-fluctuation interactions likely dominate at these scales, so linear analysis is unlikely to fully explain the mechanisms at play. Understanding the effects of nonlinearity is beyond the scope of the current work, so we leave this as a topic of future work.

To gain more insight into the effect of each term, we next compute the convective velocities by neglecting the contribution of different terms in the linear dynamics that form the spatio-temporal transfer function in (3.9). In each case, we first describe how neglecting the term(s) of interest alters these operators and then evaluate the effect on the convective velocity. Setting the mean shear term to zero reduces the linear operator in (3.7) to

$$\mathcal{L} := \begin{bmatrix} (\mathrm{i}k_x(\bar{u} - c) - \frac{1}{Re_\tau}\widehat{\nabla}^2)\mathbf{I}_{3\times 3} & \widehat{\boldsymbol{\nabla}} \\ \widehat{\boldsymbol{\nabla}}^\mathsf{T} & 0 \end{bmatrix}. \tag{3.27}$$

In this case, the operators $\mathcal{B}$ and $\mathcal{C}$ in (3.13) remain the same. We note that although the mean shear term is zero, $\bar{u}(y)$ is still a function of wall-normal location; therefore there is still shear imposed by the mean flow. Figure 3.12(a) shows that the convective velocities of the large scales continue to deviate from the mean velocity even when we eliminate the linear term associated with the mean shear. However, the knee occurring at $\lambda_z^+ = \frac{5}{2}\sqrt{\lambda_x^+}$ shown in figure 3.12(a) is different from that at $\lambda_z^+ = \lambda_x^{+\frac{2}{3}}$ in figure 3.4 based on the full linear approach. This is consistent with figure 3.11(b), which indicates that the mean shear term plays a role in the self-similarity predicted in this approach.

We next isolate the role of the pressure. For this analysis we group the effect of the pressure gradient and the mass conservation terms because they both contribute to the nonlocality of the

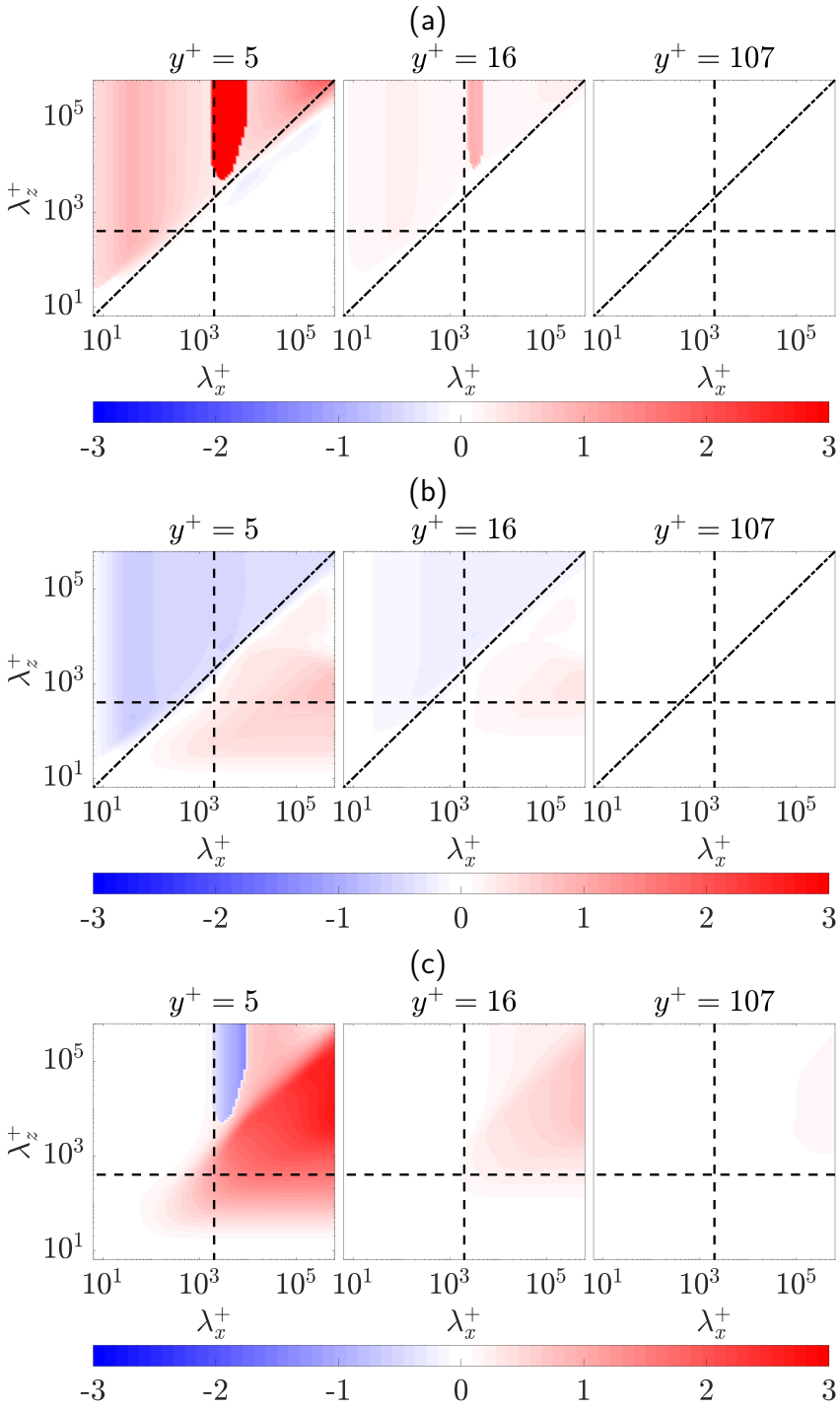

Figure 3.11: Different linear terms' contributions to scale-dependent convective velocities $(u_c(y;k_x,k_z)-\bar{u}(y))/\bar{u}(y)$ quantified using equation (3.25): (a) the pressure term (IIa), (b) the mean shear term (IIb), and (c) the viscous term (IIc). All terms are normalized by $k_x\bar{u}(y)\langle\widehat{u}'\widehat{u}'^*\rangle$. The Reynolds number is $Re_\tau = 1000$. The black dashed lines are given by $(\lambda_x,\lambda_z) = (2, 0.4)$, and the black dash-dot lines in (a) and (b) are $\lambda_z^+ = \lambda_x^+$. Note: the white region of the color map represents a value close to zero.

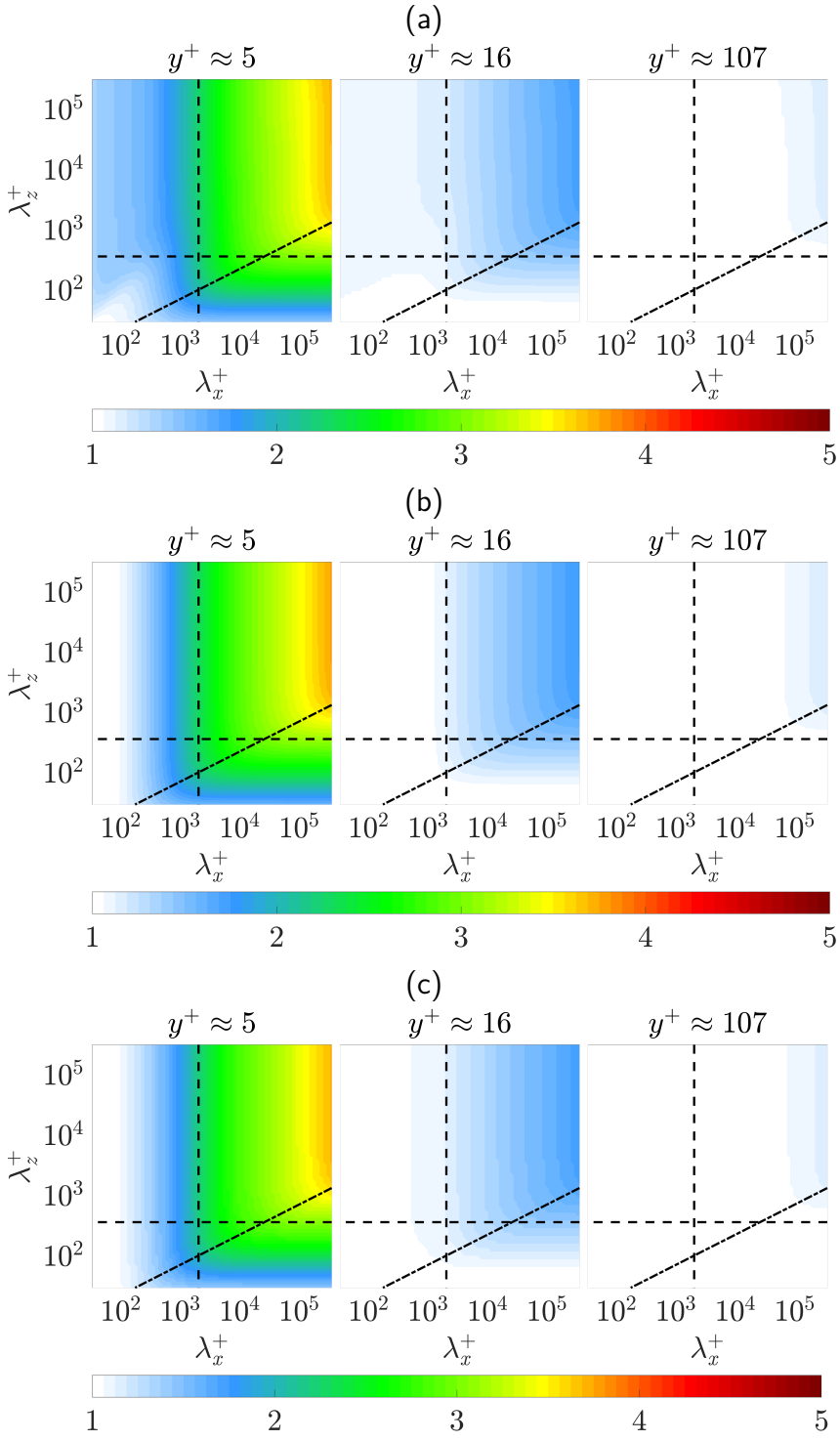

Figure 3.12: $u_c(y, \lambda_x, \lambda_z)/\bar{u}(y)$ at $Re_\tau = 1000$ (a) neglecting the mean shear term as (3.27), (b) neglecting the coupling from the pressure and mass conservation as (3.28), and (c) neglecting the mean shear term, the pressure term and mass conservation together as (3.29). The black dashed lines are given by $(\lambda_x, \lambda_z) = (2, 0.4)$. The black dash-dot lines are $\lambda_z^+ = \frac{5}{2}\sqrt{\lambda_x^+}$, which fit through the knee of these contours.

turbulent flow. This relationship can be understood by viewing the pressure in the momentum equation as the Lagrange multiplier that enforces the divergence-free velocity field; see e.g., section 5.6.2 in Schmid & Henningson (2012). Neglecting both the pressure term and the divergence-free constraint reduces the operators in the input-output map $\mathcal{G}_{\widehat{u}'} = \mathcal{C}_{\widehat{u}'}\mathcal{L}^{-1}\mathcal{B}$ to:

$$\mathcal{C}_{\widehat{u}'} := \begin{bmatrix} 1 & \mathbf{0}_{1\times 2} \end{bmatrix}, \mathcal{L} := \left[(ik_x(\bar{u} - c) - \tfrac{1}{Re_\tau}\widehat{\nabla}^2)\mathbf{I}_{3\times 3} + \tfrac{d\bar{u}}{dy}\mathbf{S} \right], \mathcal{B} := \mathbf{I}_{3\times 3}. \tag{3.28}$$

The resulting convective velocities in figure 3.12(b) are similar to those in figure 3.12(a) with the mean shear term set to zero. Neither of these terms appear to be responsible for the influence of the large-scale structures that leads to the observed behavior of the convective velocity in the near-wall region. They also do not reproduce the $\lambda_z^+ = \lambda_x^{+\frac{2}{3}}$ scaling, but they do emit self-similar structures with a different scaling exponent, $\lambda_z^+ = \frac{5}{2}\lambda_x^{+\frac{1}{2}}$.

In order to evaluate their combined effect, we next neglect the contributions of both the mean shear and pressure terms, leaving only the advective and viscous terms. The resulting input-output based approach for the streamwise velocity fluctuations is given by $\widehat{u}' = \mathcal{C}_{\widehat{u}'}\mathcal{L}^{-1}\mathcal{B}\widehat{f}_x$ with

$$\mathcal{C}_{\widehat{u}'} := \left[1\right], \quad \mathcal{L} := \left[ik_x(\bar{u} - c) - \tfrac{1}{Re_\tau}\widehat{\nabla}^2)\right], \quad \mathcal{B} := \left[1\right]. \tag{3.29}$$

Figure 3.12(c) shows the resulting convective velocity contours, which are similar to the results in panels (a) and (b). In particular, they reproduce the influence of the large-scale structures in the near-wall and buffer regions seen in the full LNS based approach. Figure 3.13 plots the power spectral density of the streamwise velocity fluctuations at different phase speeds c^+ and wall-normal locations y^+ computed using the model in equation (3.29). Although there are some differences from the results obtained using the full LNS system shown in figure 3.5, the phase speed that maximizes the energy spectrum; i.e., the convective velocity, still asymptotes to a constant value near the wall for large wavelength structures.

The main difference between these results and the full LNS based approach is that they show the same $\lambda_z^+ = \frac{5}{2}\lambda_x^{+\frac{1}{2}}$ scaling as the previous model in (3.29) with the influence of the pressure

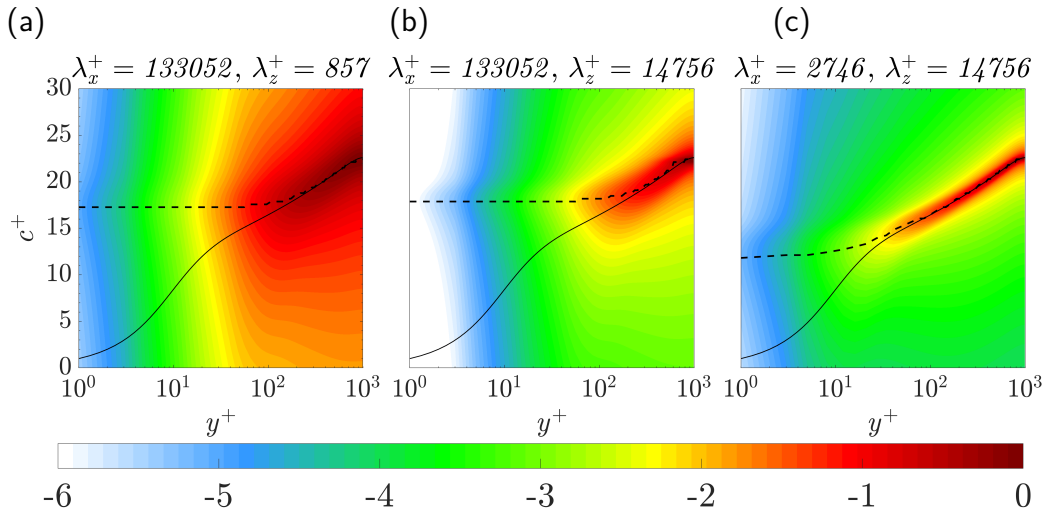

Figure 3.13: Power spectral density of streamwise velocity fluctuations over wall-normal location y^+ and phase speed c $\frac{\Phi_{\widehat{u'}}(y;k_x,k_z,c)}{\max_{c,y}(\Phi_{\widehat{u'}}(y;k_x,k_z,c))}$ at $Re_\tau = 1000$ from model (3.29) for representative large-scale structures $\triangleleft$ $(\lambda_x^+, \lambda_z^+) = (133052, 857)$, $\triangleright$ $(\lambda_x^+, \lambda_z^+) \approx (133052, 14756)$, and intermediate-scale structures $\triangle$ $(\lambda_x^+, \lambda_z^+) \approx (2746, 14756)$. The color is in base 10 logarithmic scale. The black solid lines represent the mean streamwise velocity profile, and the black dashed lines are convective velocities, which are defined in (3.12) as the phase speed that maximizes the PSD of the streamwise fluctuations $\Phi_{\widehat{u'}}(y; k_x, k_z, c)$.

and mean shear removed. The inability to reproduce the correct aspect ratio for the self-similar structures suggest that their morphology is due to interactions between viscous mechanisms and other inviscid mechanism arising due to the interaction of the fluctuations with the mean shear $\mathrm{d}\bar{u}/\mathrm{d}y$ and the pressure, such as the lift-up effect (Brandt, 2014) and the Orr mechanism (Farrell, 1987; Jiménez, 2013). However, the prediction of the main trends and scale interactions suggest that this type of model may provide a good balance between accuracy and simplicity. We next explore its potential as a viscous correction to Taylor's hypothesis.

We obtain this correction by rewriting equation (3.29) as

$$\mathrm{i}k_x(\bar{u}(y) - c)\widehat{u}' - \frac{\widehat{\nabla}^2}{Re_\tau}\widehat{u}' = \widehat{f}_x. \tag{3.30}$$

Figure 3.14 compares the average convective velocity of streamwise velocity fluctuations computed using the viscous correction (3.30) with its corresponding weighting functions $h =$

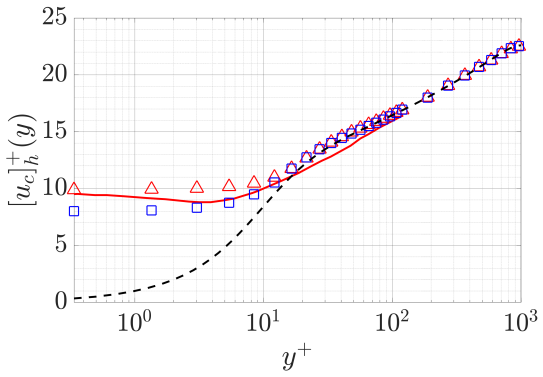

Figure 3.14: The average convective velocity of streamwise velocity fluctuations, $[u_c]_h^+(y)$: (□); computed using the viscous correction (7.6) with their corresponding weighting functions $h = \langle|\mathcal{F}_{xz}(u')|^2\rangle k_x^2$ and an averaging domain of $(\lambda_x^+, \lambda_z^+) > (500, 80)$ at $Re_\tau = 1000$. Results are plotted with convective velocities of streamwise velocity fluctuations computed from both the LNS based approach described herein for $Re_\tau = 1000$: (△) and DNS data (Geng *et al.*, 2015) at $Re_\tau = 932$: (—). The black dashed line is the turbulent mean velocity profile at $Re_\tau \approx 1000$ from Lee & Moser (2015).

$\langle|\mathcal{F}_{xz}(u')|^2\rangle k_x^2$ and an averaging domain of $(\lambda_x^+, \lambda_z^+) > (500, 80)$ at $Re_\tau = 1000$ to the results from the full LNS based approach and convective velocities obtained from DNS data at $Re_\tau = 932$ from Geng *et al.* (2015). This figure shows that the average convective velocity predicted from the viscous correction shows excellent agreement with results obtained from DNS data for $y^+ \in [5, 15]$, but begins to deviate for $y^+ \lesssim 3$. We therefore conclude that this viscous correction provides a potential dynamical modification on Taylor's hypothesis to improve the convective velocity estimates for use with experimental data.

This viscous correction introduced in equation (3.30) could be augmented using an eddy viscosity, in the spirit of the eddy viscosity enhanced LNS equations introduced in Reynolds & Hussain (1972). Such a dynamical correction was previously shown to provide similar improvements in model fidelity for certain structures as the inclusion of colored-in-time forcing (Zare *et al.*, 2017). This type of model enhancement may be particularly relevant in this context because the pertinent terms would all be retained in the associated modification of the viscous correction proposed in equation (3.30). Assessing the potential benefits of such an approach is a topic of future work.

The convective velocities computed with this viscous correction to Taylor's hypothesis for a range of Reynolds numbers are compared in figure 3.15. The results indicate that the regions in

$(\lambda_x^+,\ \lambda_z^+)$ where the convective velocities deviate from the local mean velocity are very similar across these Reynolds numbers, which is consistent with the observations in figure 3.4 indicating that the viscous correction preserves the previously observed Reynolds number invariance.

3.8 Convective velocity of vorticity fluctuations

Aside from the previous results for convective velocity of each component of velocity fluctuations, whether we can further extend them to the three vorticity component is also worth study because the similarity in the behavior of the near-wall convective velocities of velocity and vorticity components previously reported in the literature; see e.g., figures 3 and 5 of Geng *et al.* (2015). In this section, we further extend the formulation to investigate the convective velocity of vorticity fluctuations.

We first validate our approach by comparing the average convective velocities of vorticity fluctuations following (3.16) obtained from the model with those computed from DNS data (Geng *et al.*, 2015).

We specify the same averaging domain $\Omega : (\lambda_x^+, \lambda_z^+) > (500, 80)$ for our model-based results in order to include the effect of sublayer streaks proposed as the source of the elevated near-wall convective velocity (Kim & Hussain, 1993), while eliminating the very small scales where nonlinear interactions dominate (and our model is not expected to be valid). The average convective velocities of vorticity fluctuations are compared with those computed from DNS (Geng *et al.*, 2015) in Figure 3.16 (b). We note that convective velocities of the streamwise and spanwise vorticity components, which correspond to important flow dynamics such as the self-sustaining process, (see e.g., Waleffe (1997)), match results computed from DNS data well, while we over predict the wall-normal component.

Previous studies of convective velocities of both velocity and vorticity fluctuations show that large scale structures have higher convective velocities than the local mean velocity in the near-wall region (Kim & Hussain, 1993; Krogstad *et al.*, 1998; del Álamo & Jiménez, 2009). We now employ the model to investigate this scale dependence by examining the convective velocity at

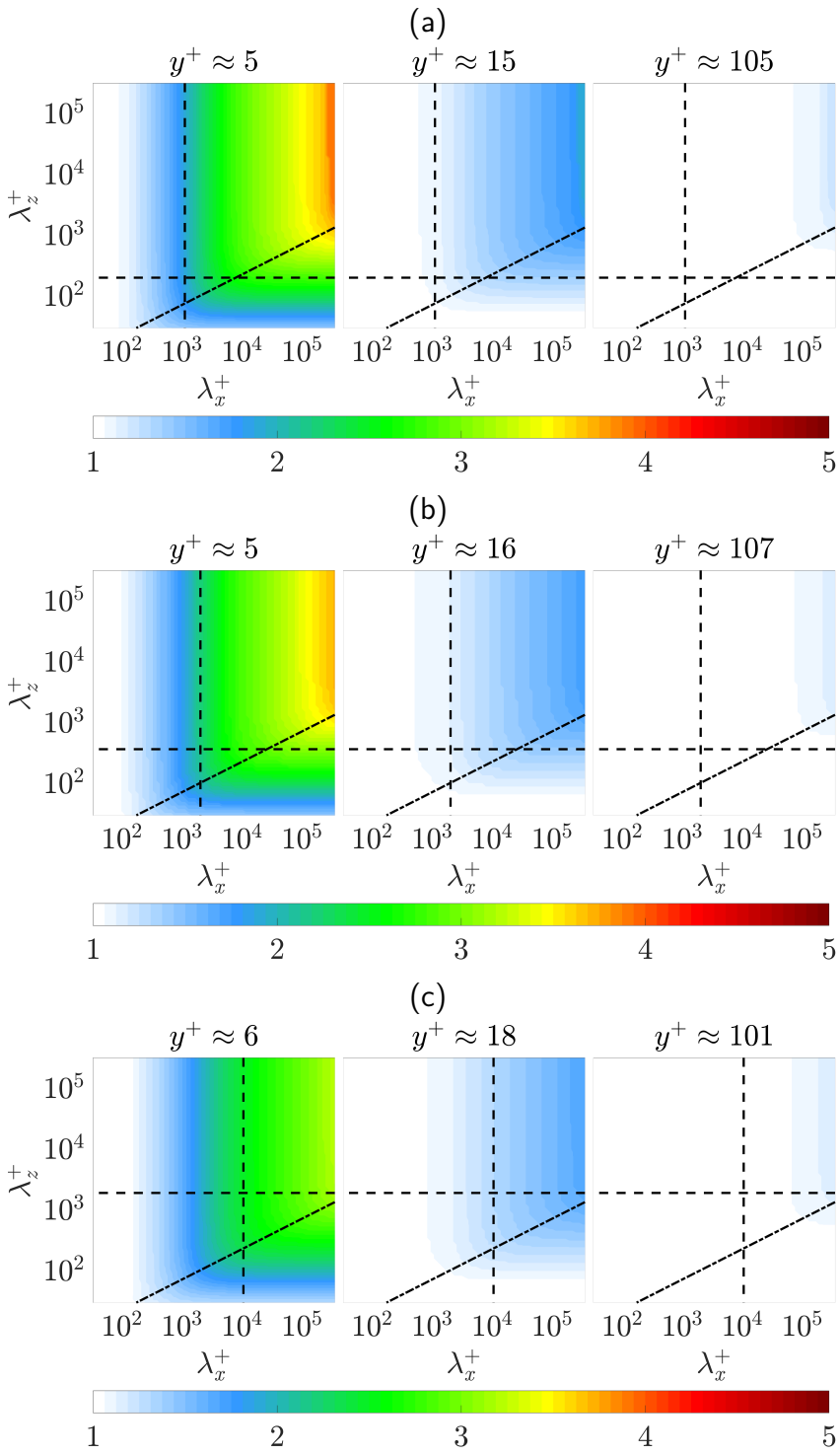

Figure 3.15: $u_c(y, \lambda_x, \lambda_z)/\bar{u}(y)$ predicted using the viscous correction to Taylor's hypothesis in equation (3.30) at (a) $Re_\tau = 550$, (b) $Re_\tau = 1000$, and (c) $Re_\tau = 5200$. The black dashed lines are given by $(\lambda_x, \lambda_z) = (2, 0.4)$. The black dash-dot lines are $\lambda_z^+ = \frac{5}{2}\sqrt{\lambda_x^+}$, which fits through the knee of these contours.

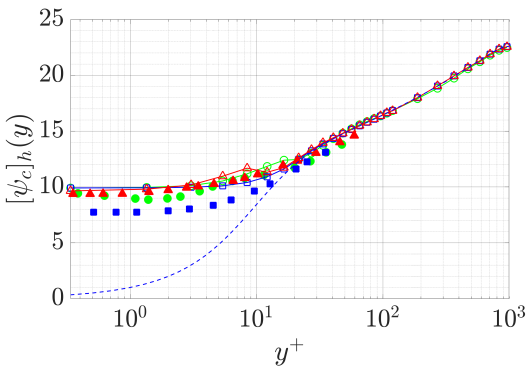

Figure 3.16: The average convective velocity in inner units of vorticity fluctuations, $[\psi_c]_h$: $\psi = \omega_x$ (—△—), $\psi = \omega_y$ (—□—), and $\psi = \omega_z$ (—○—) with weighting function $h = \overline{|\mathcal{F}_{xz}(\psi')|^2} k_x^2$ and averaging domain $(\lambda_x^+, \lambda_z^+) > (500, 80)$ obtained from the model at $Re_\tau \approx 1000$. Results are plotted with convective velocities computed from DNS data (Geng *et al.*, 2015) at $Re_\tau = 932$: $\psi = \omega_x$ (▲), $\psi = \omega_y$ (■), and $\psi = \omega_z$ (●). The blue dashed line indicate the mean velocity profile at $Re_\tau \approx 1000$ from Lee & Moser (2015).

different wall-normal locations as a function of streamwise and spanwise wavelengths. Figure 3.17 (a) shows the convective velocities of streamwise vorticity fluctuations normalized by the local mean velocity: $\omega_{xc}(y; k_x, k_z)/\bar{u}(y)$ as a function of the streamwise-spanwise wavelengths $(\lambda_x^+, \lambda_z^+)$ in the viscous sublayer $(y^+ \approx 5)$, the buffer layer $(y^+ \approx 16)$, and the log-law region $(y^+ \approx 96)$. The corresponding scale dependent convective velocities for the wall-normal and spanwise vorticity fluctuations are shown in figures 3.17 (b) and (c), respectively. In each case, the vorticity fluctuations are essentially convected at the mean velocity in the log-law region (right panels), while the greatest differences are seen in the near-wall region (the left panels), as expected.

del Álamo & Jiménez (2009) defined large scale structures as those with a length scale $(\lambda_x, \lambda_z) > (2, 0.4)$. To distinguish large and small scale structures, we have indicated this wavelength pair using black dashed lines on all plots in Figure 3.17. The higher convective velocity of these structures $(\lambda_x, \lambda_z) > (2, 0.4)$ is seen in both the viscous sublayer $(y^+ \approx 5)$ and the buffer layer $(y^+ \approx 16)$ (left and center panels) with convective velocities of these structures exceeding 3.5 times the mean flow in the viscous sublayer. The penetration of these structures into the near-wall region (Kim & Hussain, 1993; del Álamo & Jiménez, 2009) has been posited as the mechanism leading to the convective velocities of fluctuating quantities exceeding the

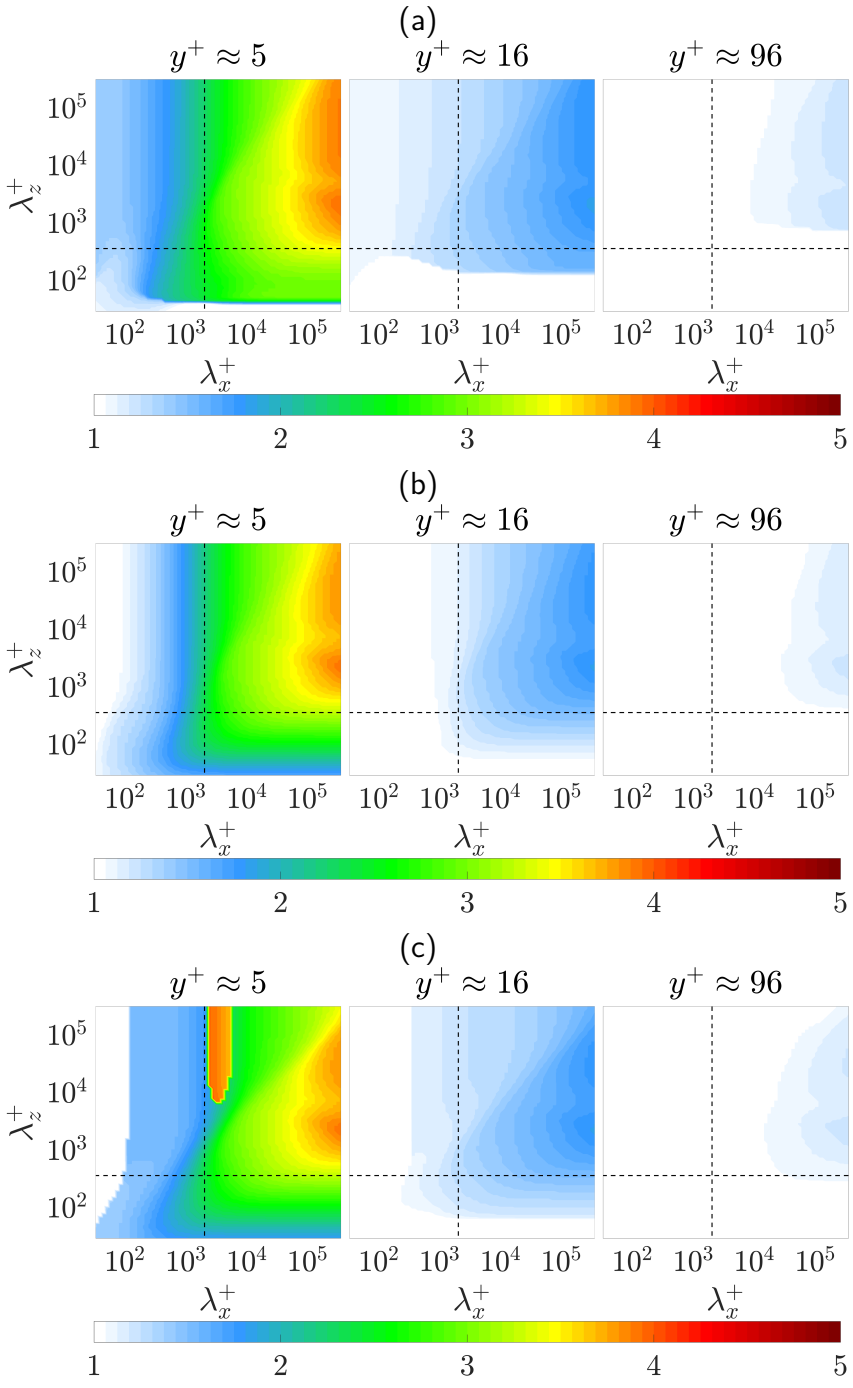

Figure 3.17: Scale dependent convective velocity of vorticity fluctuations at $Re_\tau = 1000$ normalized by the local mean velocity $\psi_c(y;\lambda_x,\lambda_z)/\bar{u}(y)$ in the viscous sublayer $y^+ \approx 5$, the buffer layer $y^+ \approx 16$, and the log-law region $y^+ \approx 96$. Panel (a) streamwise vorticity fluctuations $\psi = \omega_x$, (b) wall-normal vorticity fluctuations $\psi = \omega_y$, and (c) spanwise vorticity fluctuations $\psi = \omega_z$. The black dashed lines indicate the $(\lambda_x, \lambda_z) = (2, 0.4)$ cutoff for the large scales identified by del Álamo & Jiménez (2009).

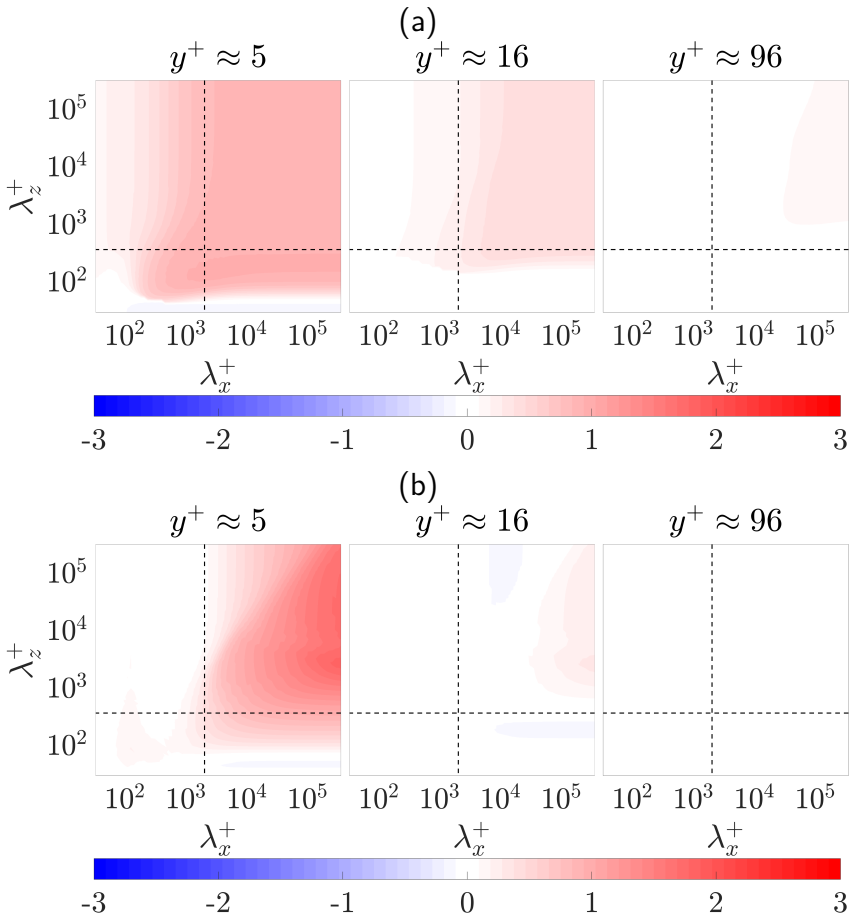

Figure 3.18: The deviation of convective velocity of streamwise vorticity fluctuations $\psi = \omega_x$ associated with (a) the mean shear term (IIa) and (b) the viscous term (IIb) in equation (3.32). All values are normalized by $k_x \bar{u}(y) \langle \widehat{\omega}_x' \widehat{\omega}_x'^* \rangle$, and the Reynolds number is $Re_\tau = 1000$. The black dashed lines indicate $(\lambda_x, \lambda_z) = (2, 0.4)$.

mean velocity near the wall.

The scale dependent convective velocity results in Figure 3.17 indicate the influence of fast moving structures centered further away from the wall, but with a footprint very near the wall due to their large size (Hutchins *et al.*, 2011). These large wavelength structures predicted through the input-output mapping employed here resemble the large, channel-filling modes of Bullock *et al.* (1978). This connection was also proposed by del Álamo & Jiménez (2009) based on their finding that u_c at the largest wavelengths is coherent throughout the channel.

We next use the input-output framework to further analyze the contribution of different linear mechanisms to the convective velocity of the vorticity fluctuations. The linearized equation of streamwise vorticity fluctuations is given by:

$$\mathrm{i}k_x(\bar{u}-c)\widehat{\omega}_x' + \overbrace{\frac{d\bar{u}}{dy}\mathrm{i}k_x w'}^{\text{IIa}} \overbrace{-\frac{1}{Re_\tau}\widehat{\nabla^2}\widehat{\omega}_x'}^{\text{IIb}} = [\widehat{\boldsymbol{\nabla}}\times\widehat{\boldsymbol{f}}]_x. \tag{3.31}$$

Here, the term (IIa) is induced by the mean shear, which represents the net effects of the tilting and stretching of the vorticity fluctuations by the mean flow and those of the mean vorticity $\boldsymbol{\nabla}\times\bar{u}$ by the velocity fluctuations. Term (IIb) represents the viscous diffusion in the wall-normal direction.

We perform a similar analysis to del Álamo & Jiménez (2009) for the streamwise vorticity ω_x in equation (3.31). In particular, we first multiply it by $\widehat{\omega_x}'^*$ and then take the imaginary part of the result to obtain the following expression for $\frac{c-\bar{u}(y)}{\bar{u}(y)}$:

$$\frac{\mathrm{Im}\left\{\overbrace{\frac{d\bar{u}}{dy}\mathrm{i}k_x\langle\widehat{w}'\widehat{\omega}_x'^*\rangle}^{\text{IIa}} \overbrace{-\frac{\langle\partial_{yy}\widehat{\omega}_x'\widehat{\omega}_x'^*\rangle}{Re_\tau}}^{\text{IIb}} - \langle[\widehat{\boldsymbol{\nabla}}\times\widehat{\boldsymbol{f}}]_x\widehat{\omega}_x'^*\rangle\right\}}{k_x\bar{u}(y)\langle\widehat{\omega}_x'\widehat{\omega}_x'^*\rangle}. \tag{3.32}$$

Equation (3.32) allows us to quantify each linear term's contribution to the deviation of convective velocity from the mean velocity.

In our framework, modifying the output operator allows us to directly compute the response

of each of the terms in equation (3.32). For example, we can redefine the output operator $\mathcal{C}_{\partial^2_{yy}\widehat{\omega}'_x} = \partial^2_{yy}\mathcal{C}_{\widehat{\omega}'_x}$ to obtain: $\partial^2_{yy}\widehat{\omega}'_x$ via equation (3.9). The cross-spectra $\langle \widehat{w}'\widehat{\omega_x}'^* \rangle$ and $\langle \partial^2_{yy}\widehat{\omega_x}'\widehat{\omega_x}'^* \rangle$ are then determined using a similar approach as in (3.11); for example:

$$\langle \widehat{w}'\widehat{\omega}'^*_x \rangle = \mathcal{G}_{\widehat{w}'}\langle \widehat{\boldsymbol{f}}'\widehat{\boldsymbol{f}}'^* \rangle \mathcal{G}^*_{\widehat{\omega}'_x} = \mathcal{G}_{\widehat{w}'}\mathcal{G}^*_{\widehat{\omega}'_x}. \tag{3.33}$$

Figures 3.18 (a) and (b) show the respective contribution from the mean shear term (IIa) and the viscous term (IIb) to the convective velocity of the streamwise vorticity fluctuations. The results indicate that the mean shear contributes slightly more to the deviation of the convective velocity from the mean than the viscous term in the buffer layer ($y^+ \approx 16$). However, in the viscous sublayer ($y^+ \approx 5$), the viscous term provides a relatively larger contribution to the deviation of the convective velocity from the mean than the mean shear, which is similar to the observations regarding the streamwise velocity fluctuations in figure 3.11. The term (IIa) may be estimated as $\sim O(C/y)$, while the term (IIb) as $\sim O(C/y^2)$. This estimation suggests that the viscous diffusion effect is decreasing faster than the mean shear as the distance from the wall increases, but the viscous diffusion is more important as we approach the wall. This is consistent with the observation in Figure 3.18.

3.9 Summary

In this work, we analyze convective velocities of fluctuating quantities based on the stochastically-forced linearized Navier–Stokes equations with a given turbulent mean velocity profile. This approach allows for a detailed investigation of the scale-dependent convective velocities at all wall-normal locations, which enables a comprehensive examination of the mechanisms at play in the generation of convective velocities.

The convective velocities of velocity fluctuations obtained using the input-output based model reproduce trends previously observed in the literature, such as the deviation of the average convective velocity from the mean velocity and its tendency toward a constant value in the near-wall region. The model-based results indicate that the convective velocity of the streamwise

velocity fluctuations closer to the wall show a stronger dependence on wavelength. The model predicted convective velocities show Reynolds number invariance when normalized in inner units, which is connected to the inner unit scaling of the resolvent operator (Moarref *et al.*, 2013) and consistent with observations from DNS data (Geng *et al.*, 2015) and experimental measurements (Marusic & Heuer, 2007).

Our analysis also indicates that a wide range of structures contribute to the convective velocity especially in the viscous sublayer, where the convective velocity has been shown to be strongly scale-dependent.

The primary structures contributing to the near-wall convective velocity based on the model are larger than the height of the buffer layer and are inclined at an angle between 25° and 33°. These predictions confirm the findings of Kim & Hussain (1993), who suggested that buffer layer structures are responsible for elevated convective velocities near the wall. However, our analysis suggests that a range of larger structures also contribute to this near-wall convective velocity. We demonstrate that these structures are self-similar in the cross-plane, similar to Townsend's attached-eddies, yet scale as the $\frac{2}{3}$ power of a cross-plane dimension in the streamwise direction. Our model suggests that there is a connection between the convective velocity and structures whose signatures in measurements of power spectra scale as $\lambda_z^+ \sim \lambda_x^{+\frac{2}{3}}$.

We isolate and quantify the contributions from the pressure, mean shear, and viscous terms to the deviation of convective velocity from the local mean velocity. Based on this term- by-term analysis, a viscous correction to Taylor's hypothesis is proposed. The proposed correction leads to a simplified model that accurately reproduces the behavior of near-wall convective velocity of the streamwise velocity fluctuations of large-scale structures.

This framework is then extended to analyze convective velocities of vorticity fluctuations. The average and scale dependent convective velocities obtained using the proposed model reproduce the trends previously observed in the literature also for vorticity fluctuations. A term by term analysis indicates that the viscous term has a slightly larger contribution to the convective velocity of streamwise vorticity than the mean shear but that it is this term that captures the

influence of large scale structures on the near-wall region.

The results presented here could be extended in a number of ways. For example, the representation of the forcing could be more closely tied to the nonlinearity observed in experimental or numerical simulation results by e.g., using simulation data to generate correlations for colored forcing (Moarref *et al.*, 2014; Zare *et al.*, 2017). Introducing an eddy viscosity based LNS representation (Reynolds & Hussain, 1972) is another direction of ongoing work. The present approach has been specifically developed for wall-bounded flows with two homogenous spatial directions, and its efficacy has been demonstrated in the particular case of turbulent channel flow. The applicability of such a model, and other stochastically-forced models based on the linearized Navier–Stokes equations to a broader class of turbulent flows, including turbulent boundary layers, is the subject of ongoing work.

Chapter 4

Spatial input–output analysis of large-scale structures in actuated turbulent boundary layers

> "If you want to find the secrets of the universe, think in terms of energy, frequency and vibration."
>
> Nikola Tesla[1], 1942

The previous chapter 3 has examined the dependence of convective velocity on wall-normal height and wall-parallel length scales. An important flow feature highlighted in that analysis is the importance of large-scale structures in contributing the near-wall convective velocity in turbulent channel flows. In this chapter, we will analyze large-scale structures due to an external spatially localized actuation that imposes a dominant frequency. However, this actuation also breaks the shift-invariance in the streamwise direction, which directly suggests characterization of streamwise variation by a downstream marching rather than streamwise wavenumber employed in the input-output analysis as in chapter 3. This chapter introduces the spatial input-output to perform downstream marching in a computationally tractable framework that embeds a height-dependent convective velocity to model large-scale structures introduced by actuation in the turbulent boundary layer.

[1] Bergstresser

4.1 Introduction

Large-scale structures in turbulent boundary layers (TBL) are known to contribute significantly to the turbulent kinetic energy and Reynolds stress production (Balakumar & Adrian, 2007; Guala *et al.*, 2006) that influence the near-wall small-scale structures (Mathis *et al.*, 2009*a*,*b*; Marusic *et al.*, 2010) and local skin friction (Hwang & Sung, 2017). This influence of the large-scale structures in TBL dynamics has been shown to increase with Reynolds number (Smits *et al.*, 2011). Large-scale structures can also be manipulated to change the properties of the boundary layer; e.g. to reduce drag in a high Reynolds number TBL (Abbassi *et al.*, 2017); see e.g., review (Corke & Thomas, 2018). Therefore, understanding their dynamics and interactions with the overall TBL can provide insight into the underlying physics.

The dynamics of large-scale structures can be studied by analyzing the flow response to an external large-scale perturbation; e.g., single harmonic perturbations provide an attractive approach to tracking the linear response of the turbulent boundary layer at the same frequency through phase-locked analysis. This approach dates back to Hussain & Reynolds (1970, 1972), where a thin vibrating ribbon near the wall is used to introduce perturbations into turbulent channel flow. They analyzed the experimental results by introducing a triple decomposition of the instantaneous velocity into a temporal mean, phase-locked harmonic perturbations (organized waves), and the remaining turbulence. Periodic perturbations can be also experimentally introduced into a turbulent boundary layer through a dynamic (temporally oscillating) roughness, which provides a reference phase to isolate synthetic large-scale structures and small-scale flow structures (Jacobi & McKeon, 2011*b*,*a*, 2013; McKeon *et al.*, 2018). The introduced periodic perturbation was shown to alter the phase relation between large and small scales and modulation coefficient in a quasi-deterministic manner (Duvvuri & McKeon, 2015). Moreover, temporal periodic perturbations can be also introduced by a wall jet (Bhatt & Gnanamanickam, 2020; Artham *et al.*, 2021) and a wall-mounted piezoelectric actuator (Tang *et al.*, 2019; Tang & Jiang, 2020; Tang *et al.*, 2021). Instead of introducing the perturbation very close to the wall,

Ranade *et al.* (2019) performed the experimental study where the perturbation is introduced at the outer region as a forced shear layer. Their results support the existence of a critical layer inside the wake region of the turbulent boundary layer that is responsible for the amplified level of turbulence in that region. Focusing on the perturbation within the region of boundary layer thickness, Lozier *et al.* (2019, 2020, 2021) further introduced large-scale perturbations through a dielectric barrier discharge (DBD) plasma actuator and performed phase-locked decomposition to obtain synthetic large-scale structures and to investigate their interactions with the residual turbulence.

Modeling large-scale structures due to external periodic perturbation can also date back to Reynolds & Hussain (1972), where various closure models are employed to modify the Orr-Sommerfeld equation describing the evolution of organized waves in turbulent channel flows. Jacobi & McKeon (2011*a*) further compared the phase-locked velocity measured in TBL perturbed by dynamic roughness with the prediction from the resolvent analysis (McKeon & Sharma, 2010), which was shown to provide a reasonably accurate prediction.

In the above experiments, the dominant temporal frequency of the perturbation determines the frequency for the velocity decomposition and modeling of the phenomena. However, how to choose a suitable streamwise wavenumber is not fully understood. There have been a number of methods used to determine the streamwise wavenumber of interest. For example, Jacobi & McKeon (2011*a*) determined the streamwise wavenumber based on a least-squares fit over the several downstream measurements for modeling of synthetic large-scale structures using resolvent analysis. However, the spatially localized perturbations introduced into the flow also breaks the shift-invariance in the streamwise direction that suggests characterizing the streamwise variation by a complex wavenumber to include the downstream growing or decaying (Jacobi & McKeon, 2011*a*; Huynh & McKeon, 2020*a*). It was also shown that a single frequency perturbation is associated with broadband streamwise wavenumbers (Huynh & McKeon, 2020*a*). If we employ an estimation using Taylor's frozen turbulence hypothesis (Taylor, 1938), the single frequency that is introduced through the perturbation will result in different streamwise wavenumber at

different wall-normal heights depending on their local mean velocity (Jacobi & McKeon, 2011*a*; Huynh & McKeon, 2020*a*).

An alternative approach to obtaining this information without the limitation to a single streamwise wavenumber is to perform analysis based on downstream marching in the streamwise direction rather than the typical temporal evolution equations. Spatial equations do not require empirical determination of a streamwise wavenumber as they inherently represent the behavior across the streamwise spectra and also suitable to describe flow response due to spatially localized actuation. However, directly converting temporal marching equations into spatial marching will lead to ill-posed problems that require regularizations to obtain a well-posed PDE (Kreiss, 1970; Trefethen & Halpern, 1986). One-way spatial integration of hyperbolic equations, recently developed by Towne & Colonius (2015), provide a well-posed one-way approximation of linear hyperbolic systems. Different from the parabolized stability equations (PSE) (Bertolotti *et al.*, 1992; Huerre & Monkewitz, 1990) that may not fully filter out upstream modes (Li & Malik, 1996) leading to numerical instability as integrating downstream (Towne *et al.*, 2019), one-way spatial integration (Towne & Colonius, 2015) provides an exact one-way equation, and it has potential to offer a systematic and convergent alternative to regularizations as employed in PSE. This one-way spatial integration was also recently extended to viscous flow and high amplitude perturbation (Harris & Hack, 2020).

In this work, we propose spatial input–output analysis based on recently developed one-way spatial integration (Towne & Colonius, 2015) for the modeling of large-scale structures in the actuated turbulent boundary layer. This downstream marching embeds a wall-normal dependent convective velocity for actuated large-scale structures associated with a dominant temporal frequency. The effect of the plasma actuator is modeled as a streamwise body force associated with a dominant temporal frequency. The magnitude of this body force is modeled as a Dirac delta function in the streamwise direction, a Gaussian function in the wall-normal direction, and uniform in the spanwise direction. The results are compared with large-scale structures in

experimental measurements, where the perturbation is introduced through a dielectric barrier discharge plasma spanwise-uniform actuator. The statistics and topology of introduced large-scale structures is obtained through measurements from hot-wire anemometry and a phase-locked analysis. Large-scale structures obtained from this spatial input–output analysis show good qualitative agreement with experimental measurements. We then employ this framework to examine the flow response of the actuated large-scale structures propagating downstream. The structures are shown to be more inclined towards the wall at downstream resulting from different convective velocities dependent on the distance from the wall. The wall-normal velocity is instead nearly uniform across the wall-normal distance. The actuation frequency influence the characteristic streamwise length scale and the higher frequency response decays faster as propagating downstream. The actuator height instead determines a convective velocity for flow structures associated with the local mean velocity at that height. We also apply the quadrant analysis (Wallace *et al.*, 1972; Wallace, 2016) to results of actuated large-scale structures, and its quadrant trajectory order shares similarity to observation in turbulent pipe flows (Nagano & Tagawa, 1995), which implies that our actuation creates structures consistent with those in canonical wall-bounded turbulent flows. These quadrant orders of actuated large-scale structures are found to be independent of actuator height further supporting the robustness of this property of the large-scale structures regardless of how the they are introduced. By varying the actuation frequency, we can control the dominance of different quadrants. For higher frequencies, Q1 (inward interaction) and Q3 (outward interaction) are more dominant than Q2 (ejection interaction) and Q4 (sweep interaction), which is consistent with canonical wall-bounded turbulence that Q2 and Q4 are associated with a larger time scale (Wallace *et al.*, 1972). This work shows the promise of a spatial framework in modeling and analyzing large-scale structures induced by a spatially localized perturbation with a dominant temporal frequency.

The remainder of this chapter is organized as follows. Section 4.2 describes the spatial input–output analysis framework. In Section 4.3, we present experimental setup to obtain the

actuated large-scale structures and compare these with results obtained from this spatial input–output analysis. Section 4.4 further employs this spatial input-output analysis to analyze the downstream evolution of actuated large-scale structures and analyzes the influence of actuation frequency and wall-normal height on the actuated large-scale structures. Section 4.5 summarizes this chapter.

4.2 Spatial input–output analysis of an actuated turbulent boundary layer

In order to model the flow response of actuated turbulent boundary layer as shown in figure 4.1, we consider incompressible flow above an infinite parallel plate driven by a streamwise pressure gradient, where x, y, z are the streamwise, wall-normal, and spanwise directions, respectively. Here, we invoke the quasi-parallel assumption that the streamwise variation of mean velocity is negligible, which was quantified as a reasonable assumption by spatio-temporal measurement (Huynh & McKeon, 2020*a*). We decompose the velocity field, $\boldsymbol{u}_{\text{tot}} = \begin{bmatrix} u_{\text{tot}} & v_{\text{tot}} & w_{\text{tot}} \end{bmatrix}^{\mathsf{T}}$ and the pressure field, p_{tot} into mean and fluctuating quantities $\boldsymbol{u}_{\text{tot}} = \bar{u}(y)\boldsymbol{e}_x + \boldsymbol{u}$ and $p_{\text{tot}} = \bar{p} + p$, where $^{\mathsf{T}}$ indicating the transpose, $\boldsymbol{e}_x$ denoting the streamwise unit vector and, the overbars representing time-averaged quantities, $\bar{\phi} = \lim_{T\to\infty} \frac{1}{T} \int_0^T \phi(t)\, dt$.

Then, we employ streamwise body force $f_x \boldsymbol{e}_x$ to model the effect of the plasma actuation, while we neglect the body force induced by the plasma actuator in the wall-normal or spanwise directions. The dynamics of the fluctuations $\boldsymbol{u}$ and p linearized around the turbulent mean velocity forced by this streamwise forcing $f_x \boldsymbol{e}_x$ is governed by:

$$\partial_t \boldsymbol{u} + \bar{u}\partial_x \boldsymbol{u} + v\frac{d\bar{u}}{dy}\boldsymbol{e}_x + \frac{\boldsymbol{\nabla} p}{\rho} - \nu\nabla^2 \boldsymbol{u} = f_x \boldsymbol{e}_x, \tag{4.1a}$$

$$\boldsymbol{\nabla} \cdot \boldsymbol{u} = 0. \tag{4.1b}$$

In equation (4.1), ρ is the density of the fluid, ν is kinematic viscosity. The friction velocity is defined as $u_\tau = \sqrt{\tau_{\text{w}}/\rho}$, where τ_{w} is the time-averaged mean shear stress at the wall. We denote the velocity normalized by the friction velocity with a superscript $^+$; i.e., $u^+ = u/u_\tau$.

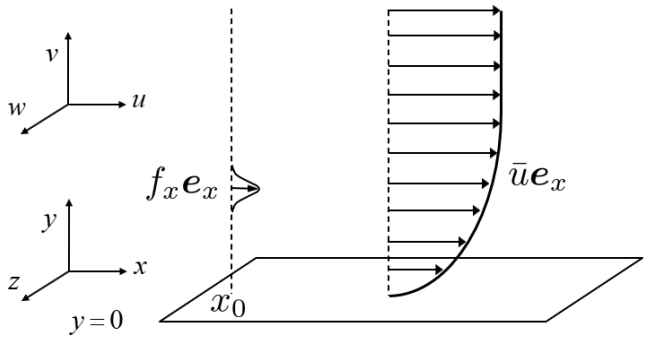

Figure 4.1: Illustration of an actuated turbulent boundary layer.

We also use superscript $^+$ to denote the length normalized by the inner unit length scale as $\delta_v := \nu/u_\tau$ and the time normalized by δ_v/u_τ; i.e., $y^+ = y/\delta_v$ and $t^+ = tu_\tau/\delta_v$. The flow can be characterized by the friction Reynolds number defined as $Re_\tau := \delta_{99}u_\tau/\nu$, where δ_{99} is the boundary layer thickness.

We then derive the spatial state-transition matrix to obtain the solution to spatial input-output by assuming solutions of the form:

$$\psi(x,y,z,t) = \check{\psi}(x,y;\omega,\eta,k_z)\mathrm{e}^{\mathrm{i}(k_z z-\omega t)}\mathrm{e}^{\eta t}, \tag{4.2}$$

where $k_z = 2\pi/\lambda_z$ is spanwise wavenumber and $\mathrm{i} = \sqrt{-1}$ is the imaginary unit. η and ω respectively denote temporal growth rate and frequency, where η is introduced here for partitioning the upstream and downstream modes following Towne & Colonius (2015) based on Briggs (1964)'s criteria. These assumptions allow us to rewrite equation (4.1) as:

$$\frac{\partial}{\partial x}\check{\boldsymbol{q}}_S = \check{\boldsymbol{A}}_S\check{\boldsymbol{q}}_S + \check{\boldsymbol{B}}_{S,x}\check{f}_x, \tag{4.3}$$

where $\check{\boldsymbol{q}}_S := \begin{bmatrix}\check{u} & \check{v} & \check{v}_x & \check{w} & \check{w}_x & \check{p}/\rho\end{bmatrix}^\mathsf{T}$. The operators $\check{\boldsymbol{A}}_S$ and $\check{\boldsymbol{B}}_{S,x}$ are defined as:

$$\check{\boldsymbol{A}}_S(y;\omega,\eta,k_z) := \begin{bmatrix} 0 & -\partial_y & 0 & -\mathrm{i}k_z & 0 & 0 \\ 0 & 0 & 1 & 0 & 0 & 0 \\ 0 & -M/\nu & \bar{u}/\nu & 0 & 0 & \partial_y/\nu \\ 0 & 0 & 0 & 0 & 1 & 0 \\ 0 & 0 & 0 & -M/\nu & \bar{u}/\nu & \mathrm{i}k_z/\nu \\ M & -\frac{d\bar{u}}{dy}+\bar{u}\partial_y & -\nu\partial_y & \mathrm{i}k_z\bar{u} & -\mathrm{i}k_z\nu & 0 \end{bmatrix}, \quad \check{\boldsymbol{B}}_{S,x} := \begin{bmatrix}0\\0\\0\\0\\0\\1\end{bmatrix} \tag{4.4}$$

with

$$M := \nu(\partial_y^2 - k_z^2) - \eta + \mathrm{i}\omega. \tag{4.5}$$

The operator similar to $\check{\boldsymbol{A}}_{\boldsymbol{S}}$ in equation (4.4) is previously defined in Schmid & Henningson (2012, equation (7.110)- (7.111)). We impose boundary conditions:

$$\check{u}(y=0) = \check{u}(y=\infty) = 0, \tag{4.6a}$$

$$\check{v}(y=0) = \check{v}(y=\infty) = 0, \quad \text{and} \tag{4.6b}$$

$$\check{w}(y=0) = \check{w}(y=\infty) = 0, \tag{4.6c}$$

which correspond to no-slip at the wall and no fluctuation at the free-stream location.

In order to obtain the solution to equation (4.3), we need to identify the upstream and downstream modes contained in $\check{\boldsymbol{A}}_S(y;\omega,\eta=0,k_z)$ because the upstream decaying modes are growing in the downstream direction resulting in a numerical instability for downstream flow response. Here, we implement the one-way spatial equation (Towne & Colonius, 2015) to explicitly identify upstream modes based on Briggs (1964)'s criteria; see e.g., (Briggs, 1964; Huerre & Monkewitz, 1990; Towne & Colonius, 2015; Huerre *et al.*, 2000, Section 3.3). Following Towne & Colonius (2015), we identify the eigenvalue of $\mathrm{i}k_x(\omega,\eta=0,k_z)$ of $\check{\boldsymbol{A}}_S(y;\omega,\eta=0,k_z)$ by tracking the eigenvalues $\mathrm{i}k_x(\omega,\eta,k_z)$ of $\check{\boldsymbol{A}}_S(y;\omega,\eta,k_z)$ as a function of η. This mode $k_x(\omega,\eta=0,k_z)$ is propagating downstream if

$$\lim_{\eta\to+\infty} \mathbb{I}\mathrm{m}[k_x(\omega,\eta,k_z)] = +\infty, \tag{4.7}$$

and propagating upstream if

$$\lim_{\eta\to+\infty} \mathbb{I}\mathrm{m}[k_x(\omega,\eta,k_z)] = -\infty, \tag{4.8}$$

where $\mathbb{I}\mathrm{m}[\cdot]$ represents the imaginary part of the argument. Then, we can perform an eigenvalue

decomposition

$$\check{\boldsymbol{A}}_S(y;\omega,\eta=0,k_z) = \boldsymbol{V}\boldsymbol{\Lambda}\boldsymbol{V}^{-1}, \tag{4.9}$$

where $\boldsymbol{\Lambda}$ is a diagonal matrix containing eigenvalues and $\boldsymbol{V}$ is a matrix containing eigenvectors of $\check{\boldsymbol{A}}_S(y;\omega,\eta=0,k_z)$. Then, we define a matrix $\boldsymbol{D}$ that is dependent on x

$$\boldsymbol{D}_{ii}(x) = \begin{cases} e^{\boldsymbol{\Lambda}_{ii}x}, & \text{if } \boldsymbol{\Lambda}_{ii} \text{ is downstream,} \\ 0, & \text{if } \boldsymbol{\Lambda}_{ii} \text{ is upstream.} \end{cases} \tag{4.10}$$

Here, the subscript ii represents the i^{th} diagonal element of matrix $\boldsymbol{D}$ or $\boldsymbol{\Lambda}$. The element $\boldsymbol{D}_{ii}$ is the exponential of $\boldsymbol{\Lambda}_{ii}$ multiplied by a streamwise distance x corresponding to downstream modes or is set as zero corresponding to upstream modes.

The spatial state-transition matrix mapping the state $\boldsymbol{q}_S(x_0,y;\omega,k_z)$ at $x = x_0$ to the state $\boldsymbol{q}_S(x_m,y;\omega,k_z)$ at another downstream location $x = x_m$ under the same spatio-temporal wavenumber-frequency pair (ω,k_z); i.e., $\boldsymbol{q}_S(x_m,y;\omega,k_z) = \check{\boldsymbol{\Psi}}(x_m,x_0,y;\omega,k_z)\boldsymbol{q}_S(x_0,y;\omega,k_z)$ is given by:

$$\check{\boldsymbol{\Psi}}(x_m,x_0,y;\omega,k_z) := \boldsymbol{V}\boldsymbol{D}(x_m-x_0)\boldsymbol{V}^{-1}. \tag{4.11}$$

This spatial state-transition matrix $\check{\boldsymbol{\Psi}}$ will be employed later to compute the response due to external forcing f_x.

4.2.1 Numerical method

We compute the spatial state-transition matrix in (4.11) by first discretizing the operators in equation (4.4) using the Chebyshev differential matrices generated by the MATLAB routines of Weideman & Reddy (2000). The mean profile $\bar{u}$ employed in this work is the asymptotic consistent turbulent boundary layer profile obtained from Monkewitz *et al.* (2007) as detailed in Appendix A, which is also used; e.g., in Cossu *et al.* (2009). The numerical implementation of the spatial framework is validated against the results of the spatial eigenvalue problem in Schmid & Henningson (2012, figure 7.18). We implement algebraic stretching following Schmid

& Henningson (2012, equations (A.53)-(A.54)), and this stretched grid is validated against eigenvalue results for the Blasius boundary layer in Schmid & Henningson (2012, Table A.4). We use $N_y = 82$ grid points in the range $y^+ \in [0, 1690]$ with half of the grid points in the range of $y^+ \in [0, 345]$. The number of total grid points is increased to $N_y = 122$, and it is validated that results do not alter. We identify upstream and downstream modes in equations (4.7)-(4.8) through the `eigenshuffle` (D'Errico, 2020) function, which tracks the variation of each eigenvalue numerically based on its continuity with varying parameter η. This numerical method is selected because analytical tracking is typically challenging; see e.g., Alves *et al.* (2019). For results in this work, we use 60 logarithmically spaced values in the range $\eta^+ \in [10^{-3}, 10]$ to approximate $\eta \to \infty$ in equations (4.7)-(4.8). We verified that this is sufficient by checking that the results do not change if we increase this to 90 logarithmically spaced values in the range $\eta^+ \in [10^{-4}, 10^2]$.

4.3 Comparison with experimental results

In this section, we compare the large-scale structures from the model with experimental measurements. We describe the experimental setup in subsection 4.3.1 that excites large-scale structures by plasma actuator and isolates these structures using a phase-locked analysis. Then we describe the model calibration in subsection 4.3.2 based on this experimental setup and show comparison results.

4.3.1 Experimental setup and phase-locked decomposition

Experiments were performed in one of the low-turbulence, subsonic, in-draft wind tunnels located at the Hessert Laboratory for Aerospace Research at the University of Notre Dame. The wind tunnel has an inlet contraction ratio of 6:1 and a series of 12 turbulence-management screens at the front of the inlet give rise to tunnel free stream turbulence levels of less than 0.1% (0.06% for frequencies above 10 Hz). Experiments are performed in a test section of 0.610 m square cross-section and 1.82 m in length. The experimental set-up is shown schematically in

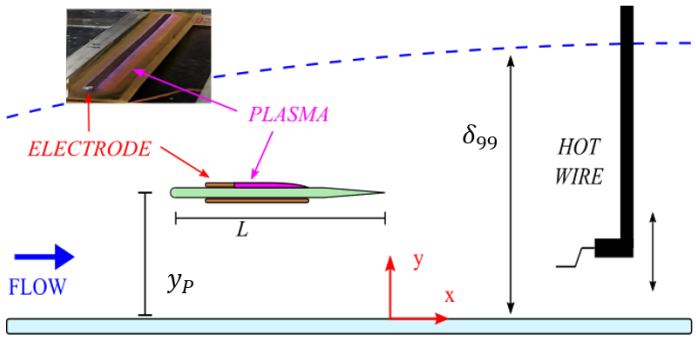

Figure 4.2: Schematic of the experimental set-up of active large-scale structures actuator based on dielectric barrier discharge plasma.

Figure 4.2. For this study, a two-meter long boundary layer development plate with a distributed roughness element attached to the leading edge was installed in the central height of the tunnel test section. A constant temperature anemometer (CTA) with a single boundary layer hot-wire probe (Dantec 55P15) with diameter $5\ \mu m$ and length $l = 1.25$ mm was used to collect time-series of the streamwise velocity component. A computer-controlled traversing stage was inserted through the top wall of the tunnel along the midpoint of the tunnel span to allow the hot-wire probe to traverse the test section and make measurements at different wall-normal (y) locations. A plasma actuator device, as described below, was attached to the top side of the boundary layer development plate at a fixed streamwise location of 140 cm from the leading edge of the boundary layer development plate. The streamwise position of the hot-wire probe traverse system is adjustable so the probe was positioned at four streamwise (x) locations as measured downstream of the plasma actuators trailing edge to measure the evolution of the TBL response. The streamwise locations selected for this study were 51 mm, 102 mm, 170 mm, and 272 mm, which correspond to $1.5\delta_{99}$, $3\delta_{99}$, $5\delta_{99}$, and $8\delta_{99}$, respectively, based on the experimentally measured boundary layer thickness, δ_{99}, near the actuator trailing edge. A set of representative turbulent boundary layer characteristics were measured at the downstream location of $x = 5\delta_{99}$ using the hot-wire probe. These parameters are summarized in Table 4.1 for reference. The skin friction velocity of u_τ was found using the Clauser method. In all of the experiments described in this study, the wind tunnel free stream velocity was 7 m/s and was measured to be within $\pm 1\%$ of the expected free stream velocity before each test.

As shown in Figure 4.2, a plasma-based active large-scale structure actuator (ALSSA) device was used in this study to modify the dynamics of the outer layer of the boundary layer with periodic plasma-induced force. The plasma actuator was supported above the boundary layer development plate by vertical, symmetrical NACA0010 airfoils on both sides which were 4 mm thick, had a 50 mm wide chord, and was made at height intervals, y_p, at 10 mm $(0.3\delta_{99})$. In this manner, the synthetic large-scale structures could be introduced into the TBL at different heights. The plasma actuator was $W = 25$ cm (≈8 δ_{99}) wide in the spanwise direction and $L = 32$ mm (≈1 δ_{99}) long in the streamwise direction. The actuator plate was made of a 2 mm thick sheet of Ultem dielectric polymer. An upper surface electrode of 0.05 mm thick copper foil tape was located 15 mm from the plate leading edge and was 4 mm in length and 22 cm in width. On the lower surface, a second copper foil electrode was located 15 mm from the leading edge in line with the top electrode and was 12 mm in length and 22 cm in width. The corners of the electrodes were rounded, and they were mounted in alignment to eliminate extraneous regions of plasma generation and regions of highly concentrated plasma. The leading edge of the actuator plate was rounded, and the last 10 mm of the trailing edge were linearly tapered to reduce the separation region behind the trailing edge of the plate. The alternating current dielectric barrier discharge (AC-DBD) plasma formed on the actuator was produced using a high voltage AC source which consisted of a function generator, power amplifiers, and a transformer (Thomas *et al.*, 2009). The electrodes placed on the top and bottom of the actuator were connected to the high voltage AC source which provided a 40 kV peak-to-peak sinusoidal waveform excitation to the electrodes at a frequency of 4 kHz. The peak-to-peak voltage was maintained within -5% of the expected excitation voltage during experiments. As shown in figure 4.2, plasma formed on the top surface of the plate above the exposed portion of the bottom surface electrode. At the 4 kHz carrier frequency, the plasma actuator operates in a quasi-steady mode, essentially creating a spanwise-uniform steady jet in the streamwise direction. To introduce periodic forcing with frequency f_p, the sinusoidal waveform was modulated by a square wave with a fifty percent duty cycle.

δ_{99}	U_∞	u_τ	C_f	H	Re_θ	Re_τ
34.8 mm	6.99 m/s	0.298 m/s	0.0036	1.33	1857	690

Table 4.1: Turbulent boundary layer parameters at the downstream location $x = 5\delta_{99}$.

The measured velocity time series were then processed by a narrow bandstop filter around 4 kHz to eliminate electronic noise associated with the high voltage AC source supplying the actuator. Since the actuator introduced periodic forcing into the flow, it is convenient to phase-locked the results to the actuation frequency. To do so, a triple phase-locked Reynolds decomposition of the velocity was considered, as shown in equation (4.12a) where u is the instantaneous velocity, $\bar{u}$ is the time mean component of velocity, $\tilde{u}$ is a phase-locked modal velocity component, u' is a residual fluctuating turbulent component, ϕ is the phase, defined by the relationship in equation (4.12b), and n is the number of realizations as described below

$$u(y,t) = \bar{u}(y) + \tilde{u}(y,\phi) + u'(y,\phi,n), \tag{4.12a}$$

$$\phi = \left(\frac{t_n}{T_p} - n\right) 2\pi. \tag{4.12b}$$

Here, t_n is a time in the n^{th} realization, which is related to the phase angle, ϕ, by the period of the forcing repetition cycle, $T_p = 1/f_p$. The output of the function generator was used to ensure the data was phase-locked with the repetition cycle of the plasma. These n realizations are then ensemble-averaged to find the modal component of velocity, $\tilde{u}(y,\phi)$, as a function of the phase angle.

4.3.2 Model calibration and comparison results

In this subsection, we will describe the forcing model and calibrate the parameters in the spatial input-output analysis based on the experimental setup in subsection 4.3.1 and show comparison results to demonstrate the efficacy of the spatial input-output analysis described in section 4.2 in reproducing the phase-locked velocity in experiments.

Based on the actuator geometry described in 4.3.1, we model the effect of actuation on the flow by assuming the streamwise body force $\check{f}_x$ is in the form of a Gaussian function over the

wall-normal direction, a Dirac delta function over the streamwise direction, and uniform in the spanwise direction:

$$\breve{f}_x(x, y; \omega, k_z) = F_0 \mathrm{e}^{-\frac{(y-y_f)^2}{2\sigma_p^2}} \delta(x - x_0) \mathrm{e}^{\mathrm{i}\phi_0}, \tag{4.13}$$

where F_0 represents the magnitude of this body force and ϕ_0 represents the initial phase of this body force induced by the plasma actuator. We calibrate the initial phase of the body force model as $\phi_0 = 1.15\pi$ and the magnitude as $F_0^+ = 38.2$ based on experimental measurements of phase-locked velocity at $x_m = 1.5\delta_{99}$. The values of the parameters ϕ_0 and F_0^+ do not influence the shape of phase-locked velocity due to linearity. In analog to the vibrating ribbon problem (Ashpis & Reshotko, 1990) in studying transitional boundary layer or signaling problem (Huerre *et al.*, 2000; Huerre & Monkewitz, 1985, Section 3), the streamwise variation of this body force in (4.13) is modeled as a Dirac delta $\delta(x - x_0)$ function over the streamwise direction that is localized in the streamwise position x_0, which is set as $x_0 = 0$. The Gaussian function in the wall-normal direction is motivated by (Jovanovic & Bamieh, 2001; Vadarevu *et al.*, 2019), where this function is also employed to model localized forcing. y_f and σ_p in the Gaussian function are respectively the center of the peak and standard deviation determining the wall-normal shape of plasma-induced body force. We set $\sigma_p^+ = 60$ and the body force center to be $y_f = 0.13\delta_{99} + y_p$, i.e., $0.13\delta_{99}$ higher than the actuator plate height. This height correction and the standard deviation σ_p^+ in forcing function are employed to match the peak of phase-locked velocity in experiments at $x_m/\delta_{99} = 1.5$ induced by the ALSSA device. The calibrated values F_0^+, ϕ_0, y_f, and σ_p^+ are kept the same in this work. The spanwise wavenumber in equation (4.4) is chosen as $k_z = 0$ as the plasma actuation in the experiment is spanwise uniform and the fact that the experimental measurements of flow response do not show significant spanwise variation. Here, we set the frequency to $\omega^+ = 2\pi f_p^+$ to match that of the plasma actuation. We specify the Reynolds number $Re_\tau = 690$ to match experimental measurements in both the determination of the mean velocity profile and the computations.

The corresponding solution of equation (4.3) at downstream measurement position x_m with

respect to the streamwise localized forcing $\check{f}_x$ can be computed using the spatial state-transition matrix in (4.11):

$$\check{\boldsymbol{q}}_S(x_m, y; \omega, k_z) = \check{\boldsymbol{\Psi}}(x_m, x_0, y; \omega, k_z)\check{\boldsymbol{B}}_{S,x} F_0 \mathrm{e}^{-\frac{(y-y_f)^2}{2\sigma_p^2}} \mathrm{e}^{\mathrm{i}\phi_0}. \tag{4.14}$$

In order to compare with hot-wire measurements described in 4.3.1, we obtain streamwise velocity as:

$$\check{u} = \check{\boldsymbol{C}}_{S,u}\check{\boldsymbol{q}}_S, \tag{4.15a}$$

$$\check{\boldsymbol{C}}_{S,u} := \begin{bmatrix} 1 & 0 & 0 & 0 & 0 & 0 \end{bmatrix}. \tag{4.15b}$$

Based on the computation of phase-locked velocity from experiments in equation (4.12), we can similarly obtain the phase-locked velocity at a certain downstream measurement location x_m by multiplying $\mathrm{e}^{-\mathrm{i}\phi}$ to shift the phase:

$$\tilde{u}(x_m, y; \omega, k_z, \phi) = \mathbb{R}\mathrm{e}[\check{u}(x_m, y; \omega, k_z)\mathrm{e}^{-\mathrm{i}\phi}], \tag{4.16}$$

where $\mathbb{R}\mathrm{e}[\cdot]$ represents the real part of the argument. Note that the minus sign of $\mathrm{e}^{-\mathrm{i}\phi}$ in equation (4.16) is based on the fact that an increased phase corresponding to later time moments is consistent with the phase-locked analysis of experimental results presented in section 4.3.1 and ansatz in equation (4.2).

We compare the phase-locked velocity obtained from the proposed spatial input–output analysis against results from experimental measurements associated with an actuation frequency $f_p = 80$ Hz ($0.3983U_\infty/\delta_{99}$ and $f_p^+ = 0.0135$) and the actuator plate height $y_p/\delta_{99} = 0.3$. This actuator plate height $y_p/\delta_{99} = 0.3$ corresponds to the top boundary of the log-law layer (Pope, 2000). Figure 4.3 compares the phase-locked velocity at four different downstream measurement locations $x_m/\delta_{99} = 1.5$, $x_m/\delta_{99} = 3$, $x_m/\delta_{99} = 5$, and $x_m/\delta_{99} = 8$ from experimental measurements (top panels) and the model (bottom panels). In all panels, the long black dashed line (– –, black) corresponds to the height of actuator plate y_p and the short black solid line (—, black) is the height of the body force center y_f modeling the effect of plasma

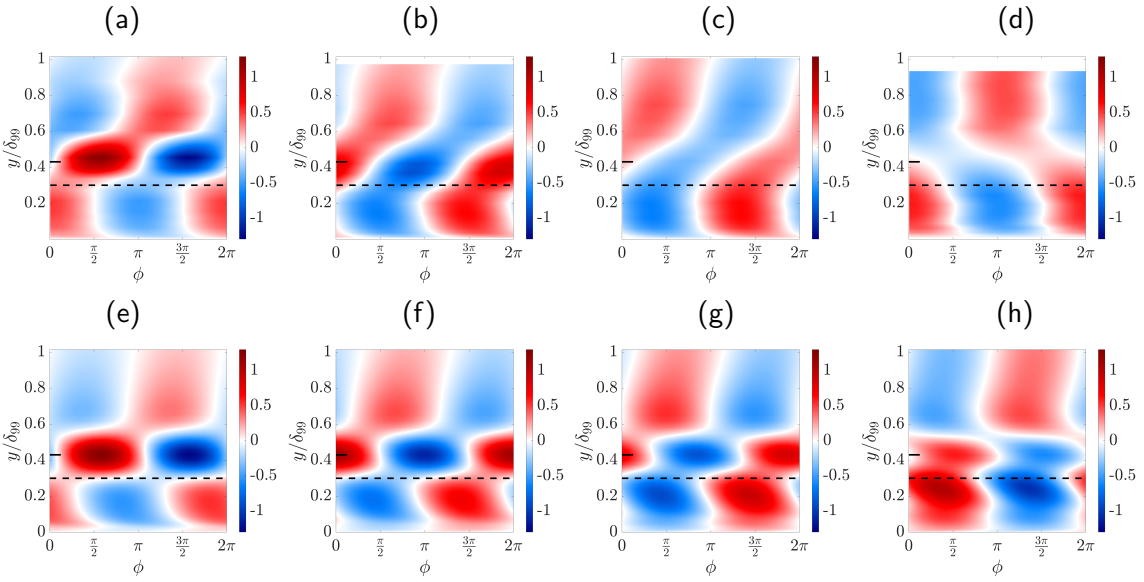

Figure 4.3: A comparison of phase-locked modal velocity $\tilde{u}^+$ measured from experiments in (4.12) against the results from model $\tilde{u}^+$ in (4.16) obtained for $y_p/\delta_{99} = 0.3$ and $f_p = 80$ Hz. Panels (a)-(d) are results from experimental measurements $\tilde{u}^+$ with the downstream measurement location (a) $x_m/\delta_{99} = 1.5$, (b) $x_m/\delta_{99} = 3$, (c) $x_m/\delta_{99} = 5$, and (d) $x_m/\delta_{99} = 8$. Panels (e)-(h) are results from spatial input-output analysis $\tilde{u}^+$ with the downstream measurement location (e) $x_m/\delta_{99} = 1.5$, (f) $x_m/\delta_{99} = 3$, (g) $x_m/\delta_{99} = 5$, and (h) $x_m/\delta_{99} = 8$. In all panels, (- -) represents plate height $y_p/\delta_{99} = 0.3$ employed in experiments; and (—) represents the body force center $y_f = y_p + 0.13\delta_{99}$ employed in the body force model in equation (4.13).

actuation. Here, we can see that the model provides reasonable agreement with experimental measurement. At the downstream location $x_m/\delta_{99} = 1.5$, the phase-locked velocity was isolated into three distinct regions across the boundary layer thickness. We refer to the region below the plate $y \in [0, 0.3\delta_{99}]$ as the bottom region, the region $y \in (0.3\delta_{99}, 0.56\delta_{99})$ with y_f in the middle as the central region that is strongly influenced by the actuation, and the region $y \in [0.56\delta_{99}, \delta_{99})$ as the top region. Here, we notice that there is a clear phase shift between these regions in both the experimental and model results. This is reminiscent of the results from previous studies where they had two similar regions above the actuator (mounted at the wall) (Jacobi & McKeon, 2011*a*; Duvvuri & McKeon, 2016, 2017; Bhatt & Gnanamanickam, 2020; Huynh & McKeon, 2020*a*). These regions correspond to our results in the second and third regions that are close to the plate (where the actuator is mounted and exerts a strong influence) and near the free stream, respectively. The bottom regions observed here are not visible in these previous studies (Jacobi & McKeon, 2011*a*; Duvvuri & McKeon, 2016, 2017; Bhatt &

Gnanamanickam, 2020; Huynh & McKeon, 2020*a*) due to their wall-mounted perturbations.

Both the experimental results and the model show that the phase-locked velocity $\tilde{u}$ at the central regions are decaying as they propagate downstream. This downstream spatio-temporal characteristic of the phase lock velocity as it decays was recently highlighted using particle image velocimetry (PIV) measurements that directly track the streamwise evolution of the velocity field (Huynh & McKeon, 2020*a*). The experimental results show that the velocity at the bottom region at (b) $x_m/\delta_{99} = 3$ is larger than that at (a) $x_m/\delta_{99} = 1.5$, a trend that is also reflected in the model prediction in panels (e) and (f). The larger phase-locked velocity amplitude below the center of perturbation suggests a spatial transient growth mechanism for the near-wall region. However, such spatial growth is not visible for the top region. At downstream $x_m/\delta_{99} = 8$ in figure 4.3(d), the phase-locked velocity is also shifting the direction; e.g., the phase-locked velocities in figure 4.3(a)-(c) have a larger phase ϕ at a larger y that is opposite to observation in figure 4.3(d). The results from the model in figure 4.3(e)-(h) also capture this phenomenon qualitatively. This phenomenon is likely due to different convective velocities at different wall-normal heights, which will be examined in the following section.

4.4 Downstream propagation of large-scale structures

Aside from the streamwise velocity, the wall-normal velocity is also typically measured by PIV; e.g., (Jacobi & McKeon, 2011*a*; Huynh & McKeon, 2020*a*). Using the combined information of streamwise and wall-normal velocity can also provide insight into the influence of large-scale structures on Reynolds shear stress. As a result, we also modify the output operator to obtain the wall-normal velocity:

$$\check{v} = \check{\boldsymbol{C}}_{S,v} \check{\boldsymbol{q}}_S, \tag{4.17a}$$

$$\check{\boldsymbol{C}}_{S,v} := \begin{bmatrix} 0 & 1 & 0 & 0 & 0 & 0 \end{bmatrix}. \tag{4.17b}$$

Because the flow is mainly characterized by (u, v) velocity in the (x, y) plane and nearly uniform in the spanwise direction due to a spanwise uniform actuation, the vorticity of interest is spanwise vorticity that can be also obtained by modifying output operator:

$$\breve{\omega}_z = \boldsymbol{\breve{C}}_{S,\omega_z} \boldsymbol{\breve{q}}_S, \tag{4.18a}$$

$$\boldsymbol{\breve{C}}_{S,\omega_z} := \begin{bmatrix} -\partial_y & \partial_x & 0 & 0 & 0 & 0 \end{bmatrix}. \tag{4.18b}$$

The downstream evolution of large-scale structures is also of interest in canonical wall-bounded turbulent flows (Adrian, 2007). Aside from performing a phase-locked analysis by modifying the phase, this spatial input-output analysis can also provide the downstream evolution of phase-locked velocity by directly changing different downstream measurement locations x_m. We define:

$$u_s(x_m, y; \omega, k_z) = \mathbb{R}\mathrm{e}[\breve{u}(x_m, y; \omega, k_z)], \tag{4.19a}$$

$$v_s(x_m, y; \omega, k_z) = \mathbb{R}\mathrm{e}[\breve{v}(x_m, y; \omega, k_z)], \tag{4.19b}$$

$$\omega_{z,s}(x_m, y; \omega, k_z) = \mathbb{R}\mathrm{e}[\breve{\omega}_z(x_m, y; \omega, k_z)]. \tag{4.19c}$$

Figure 4.4(a) presents the u_s^+ as a function of streamwise measurement location x_m and wall-normal height y. We note that the results in figure 4.3 are fixing a downstream location, and a larger phase corresponds to a later time as (4.12b). At a fixed time, a larger phase corresponds to the upstream direction, and this corresponds to the trend observed in comparing figures 4.4 and 4.3. The spatial evolution shown in figure 4.4 is not perfectly periodic in the spatial domain, which is due to different convective velocities at different heights embedded within the turbulent mean velocity profile. This is the benefit of the spatial input-output analysis that does not require selecting a specific streamwise wavenumber but directly performing downstream marching. Here, we can see that near the inflow region, u_s^+ in panel (a) shows alternating positive and negative values over the wall-normal direction, with phase jumps evident at the two wall-normal locations

separating the top, central, and bottom regions. Moving downstream, one can see that the flow at the central region is traveling faster than that at the bottom region. The dotted line $(\cdots)$ in figure 4.4 (a) measures the downstream distance after three periods, which shows the effect of wall-normal dependent convective velocity. A direct result of this is the shape of phase-locked velocity observed in figure 4.3. In particular, figure 4.4(a) at $x_m/\delta_{99} \approx 8$ shows a phase shift between the central and top regions, which is consistent with the observation in comparing figure 4.3(e)-(h). Changes in the convective velocities of large-scale structures as a function of wall-normal heights were also previously employed to explain the stretching and intensifying of the legs of hairpin vortices as they propagate downstream (Adrian, 2007).

The wall-normal velocity component of phase-locked velocity v_s^+ is shown in figure 4.4(b). Here, positive and negative values are seen at the region above or below the center of the forcing y_f near the inflow region $x_m = 0$, but farther downstream, the wall-normal velocity is more uniform across the wall-normal height. Such a nearly uniform wall-normal velocity was also observed in (Jacobi & McKeon, 2011*a*; Huynh & McKeon, 2020*a*). Figure 4.4(c) presents the spanwise vorticity $\omega_{z,s}^+$ as contour with velocity vectors (u_s, v_s) superimposed. Here, we can see that this body force model generates counter-rotating spanwise vorticity near the inflow region. As the actuated large-scale structures are propagating downstream, the bottom spanwise vorticity is more inclined towards the wall.

Next, we combine our proposed input-output framework with quadrant analysis (Wallace *et al.*, 1972; Wallace, 2016) to study the impact of the large-scale structures resulting from actuation on the Reynolds shear stress. The quadrants are defined in terms of u_s and v_s phase-locked velocities. We adopt the traditional definitions in which the first quadrant Q1 corresponds to outward interactions $(u_s > 0, v_s > 0)$, the second quadrant Q2 is ejection $(u_s < 0, v_s > 0)$, the third quadrant Q3 corresponds to inward interactions $(u_s < 0, v_s < 0)$ and the fourth quadrant Q4 is sweep $(u_s > 0, v_s < 0)$ (Wallace, 2016). Figure 4.4(d) plots these quadrants as a contour with velocity vectors (u_s, v_s) superimposed. Figure 4.4(d) shows that at the central region close to the actuator $x_m = 0$, the Q4 and Q2 quadrant events are

the strongest, and they are spreading towards the top and bottom regions moving downstream. Moving from the upstream to downstream direction, we can see the quadrant events in the order Q4→Q3→Q2→Q1 at the top region, but at the bottom region, the quadrant events are in the order of Q1→Q2→Q3→Q4. This is consistent with the counter-rotating vorticity patterns appearing in the top and bottom regions as shown in figure 4.4(c). The quadrant trajectory analysis was previously employed to characterize 36 distinct evolution patterns for (u, v) in turbulent pipe flow and the trajectories Q2→Q1→Q4, Q2→Q3→Q4, Q4→Q1→Q2, and Q4→Q3→Q2 were shown to play the most important role in the dynamics and transport of near-wall turbulence (Nagano & Tagawa, 1995). These four important quadrant trajectories are also observed here by actuated large-scale structures as outlined in four different boxes in figure 4.4(d). At far downstream locations, we notice that the quadrant events are alternating Q1/Q2 events or Q3/Q4 events (we refer to these patterns as Q1/Q2-Q3/Q4 later) as the wall-normal height changes, which corresponds to the nearly uniform wall-normal velocity as a function of wall-normal height seen in figure 4.4(b). The results in figure 4.4 demonstrate that the spatial input-output analysis can provide detailed downstream evolution of actuated large-scale structures.

4.4.1 Effect of actuation frequency and actuator height

Previous work has focused on the introduction of the temporal periodic perturbation over a wide range of frequencies that are injected at the wall (Hussain & Reynolds, 1970, 1972; Reynolds & Hussain, 1972; Jacobi & McKeon, 2011*a*; Duvvuri & McKeon, 2016, 2017; Bhatt & Gnanamanickam, 2020; Artham *et al.*, 2021; Huynh & McKeon, 2020*a*; Tang *et al.*, 2019; Tang & Jiang, 2020; Tang *et al.*, 2021). Recent experiments have focused on the perturbation introduced in the outer layer (Ranade *et al.*, 2019; Lozier *et al.*, 2019, 2020, 2021). However, the effect of varying the actuator height and frequency for flow actuation in the outer layer is less understood. This subsection further employs spatial input-output analysis to study the effect of

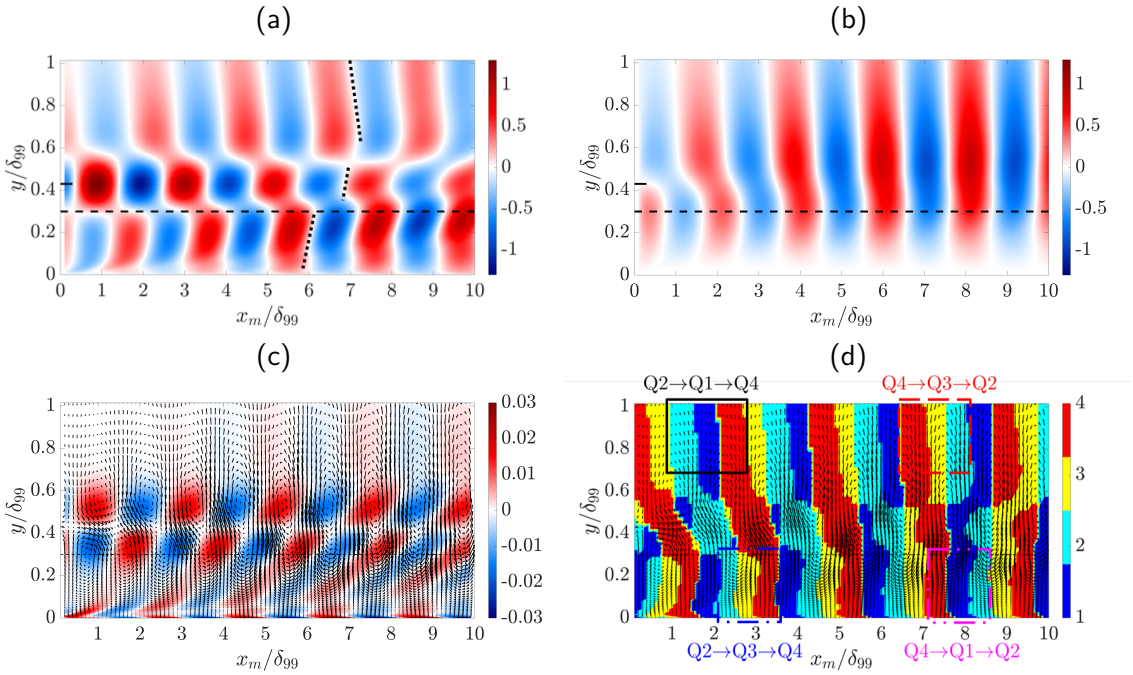

Figure 4.4: Downstream evolution of (a) u_s^+, (b) v_s^+, and (c) spanwise vorticity $\omega_{z,s}^+$ with $f_p = 80$ Hz, $y_p/\delta_{99} = 0.3$. The dotted line $(\cdots)$ in panel (a) measures the downstream distance after three periods. The contour in panel (d) is presenting quadrant numbers. The velocity vector field $(u_s^+\ v_s^+)$ is superimposed on contours in panels (c) and (d). In panel (d), the box outlined by (—, black) represents Q2→Q1→Q4, the box outlined by (– –, red) represents Q4→Q3→Q2, the box outlined by (– · –, blue) represents Q2→Q3→Q4, and the box outline by (– · · –, magenta) represents Q4→Q1→Q2. In all panels, long horizontal line (– –) represents plate height $y_p/\delta_{99} = 0.3$ employed in experiments; and short horizontal line (—) represents the body force center $y_f = y_p + 0.13\delta_{99}$ employed in the body force model in equation (4.13).

varying actuation frequency f_p and actuator plate height y_p for the set-up described in the previous subsection. Here, we study four cases in total. We first investigate the effect of actuation frequency by setting $f_p = 20$ Hz and $f_p = 200$ Hz, and we keep the $y_p/\delta_{99} = 0.3$ the same as previous results in figure 4.4. Then, we analyze the effect of varying actuator height by setting $y_p/\delta_{99} = 0.1$ and $y_p/\delta_{99} = 0.5$, and we keep the actuation frequency $f_p = 80$ Hz the same as figure 4.4.

We first investigate the influence of actuation frequency f_p, and we keep the actuation plate height as $y_p/\delta_{99} = 0.3$. In figure 4.5, we present (a) u_s^+, (b) v_s^+, (c) $\omega_{z,s}^+$, and (d) quadrant number at $f_p = 20$ Hz $(0.0996U_\infty/\delta_{99}$ and $f_p^+ = 0.0034)$. The results at $f_p = 20$ Hz in figure 4.5 show that the streamwise wavelength of the actuated large-scale structures is longer than previous results at $f = 80$ Hz in figure 4.4. Figure 4.6 plots the same quantities (a) u_s^+, (b) v_s^+,

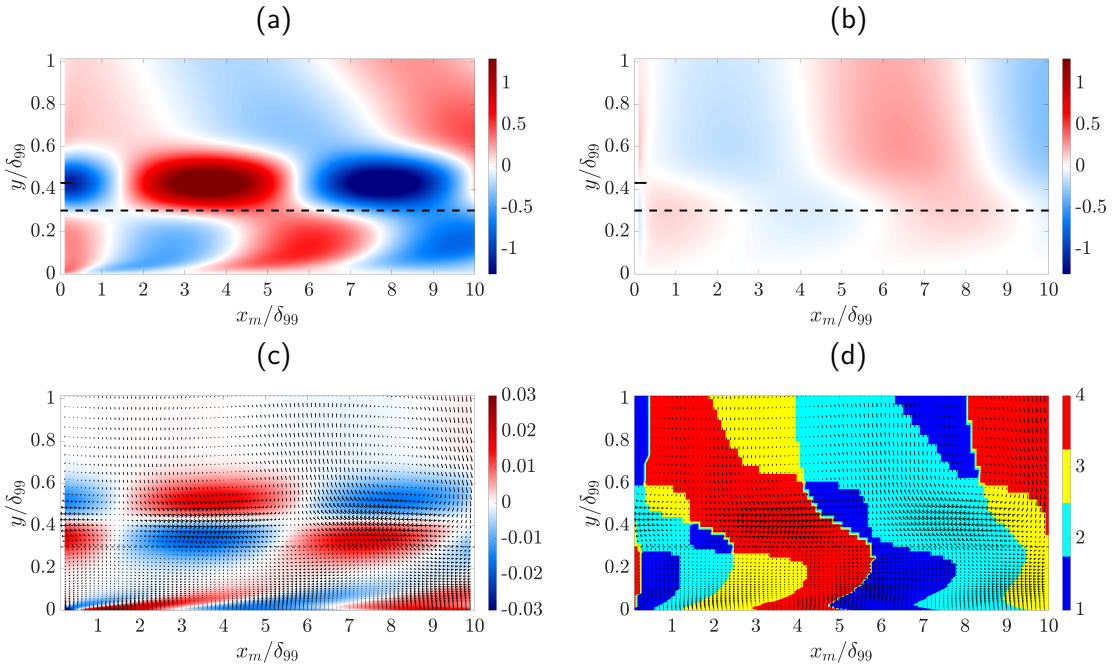

Figure 4.5: Downstream evolution of (a) u_s^+, (b) v_s^+, and (c) spanwise vorticity $\omega_{z,s}^+$ with $f_p = 20$ Hz, $y_p/\delta_{99} = 0.3$. The contour in panel (d) is presenting quadrant numbers. The velocity vector field $(u_s^+ \; v_s^+)$ is superimposed on contours in panels (c) and (d). In all panels, (– –) represents plate height $y_p/\delta_{99} = 0.3$ employed in experiments; and (—) represents the body force center $y_f = y_p + 0.13\delta_{99}$ employed in the body force model in equation (4.13).

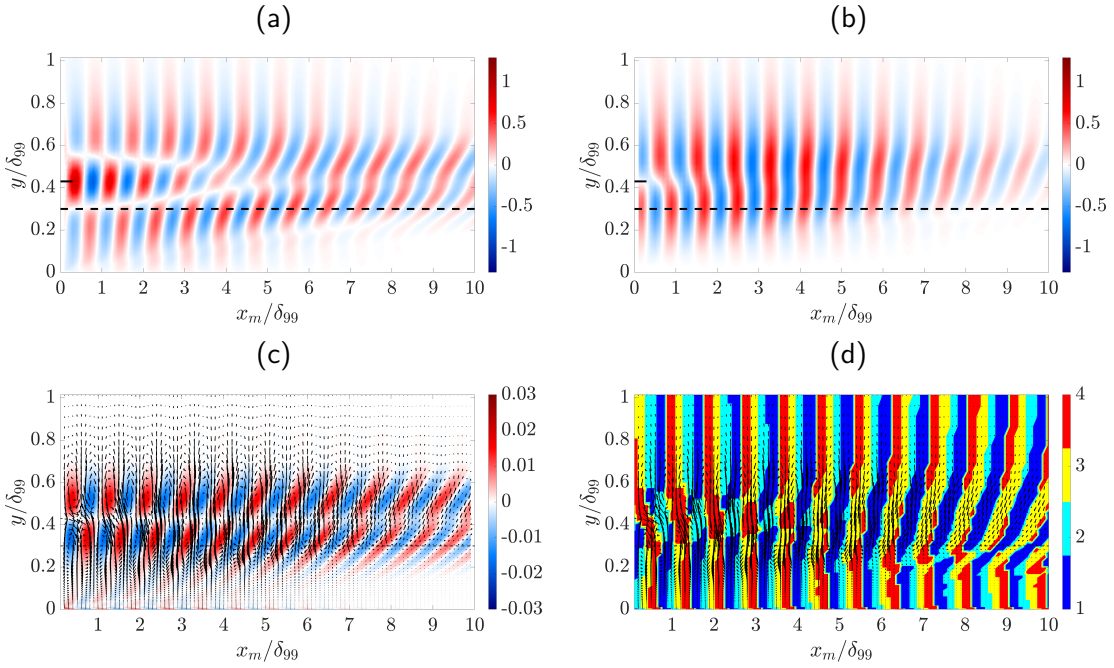

Figure 4.6: Downstream evolution of (a) u_s^+, (b) v_s^+, and (c) spanwise vorticity $\omega_{z,s}^+$ with $f_p = 200$ Hz, $y_p/\delta_{99} = 0.3$. The contour in panel (d) is presenting quadrant numbers. The velocity vector field $(u_s^+ \; v_s^+)$ is superimposed on contours in panels (c) and (d). In all panels, (– –) represents plate height $y_p/\delta_{99} = 0.3$ employed in experiments; and (—) represents the body force center $y_f = y_p + 0.13\delta_{99}$ employed in the body force model in equation (4.13).

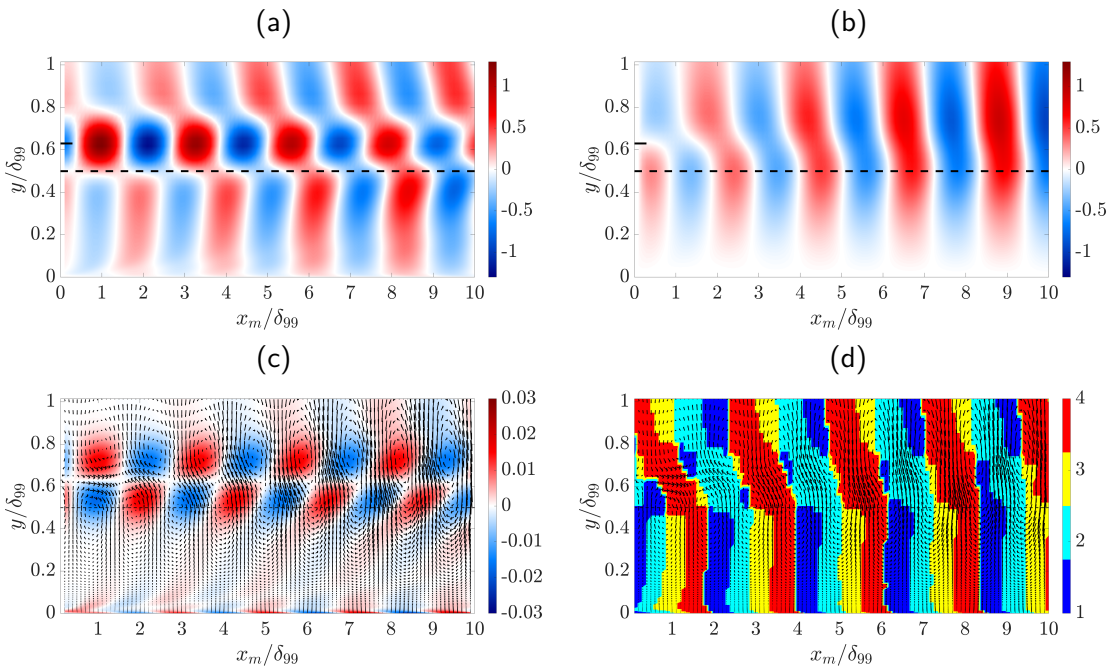

Figure 4.7: Downstream evolution of (a) u_s^+, (b) v_s^+, and (c) spanwise vorticity $\omega_{z,s}^+$ with $f_p = 80$ Hz, $y_p/\delta_{99} = 0.5$. The contour in panel (d) is presenting quadrant numbers. The velocity vector field $(u_s^+ \ v_s^+)$ is superimposed on contours in panels (c) and (d). In all panels, (– –) represents plate height $y_p/\delta_{99} = 0.5$ employed in experiments; and (—) represents the body force center $y_f = y_p + 0.13\delta_{99}$ employed in the body force model in equation (4.13).

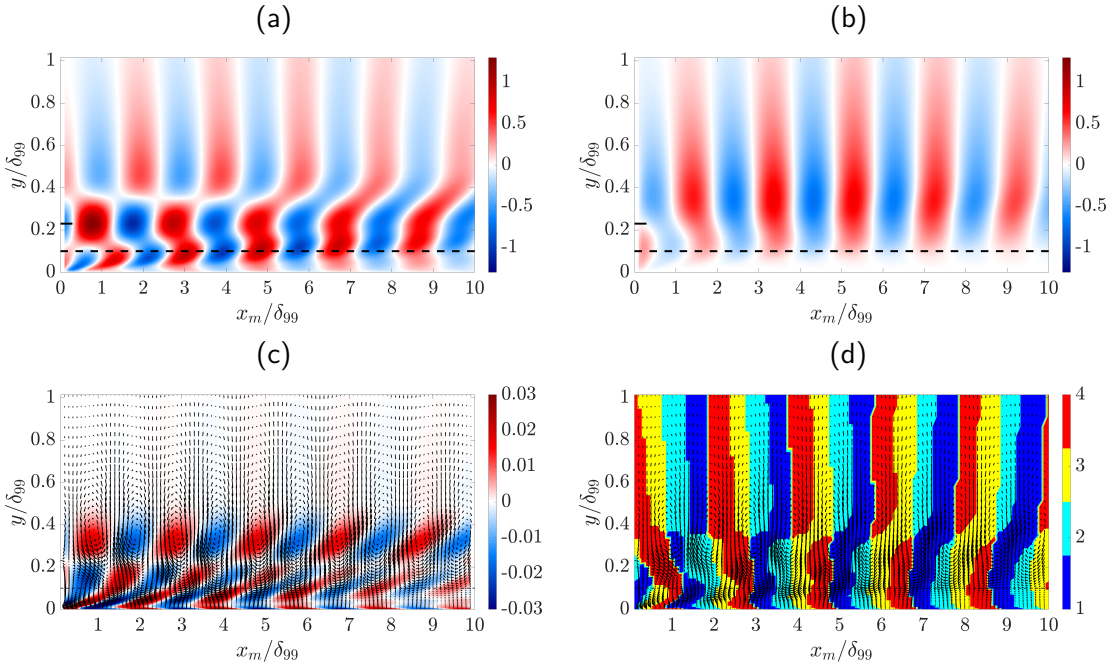

Figure 4.8: Downstream evolution of (a) u_s^+, (b) v_s^+, and (c) spanwise vorticity $\omega_{z,s}^+$ with $f_p = 80$ Hz, $y_p/\delta_{99} = 0.1$. The contour in panel (d) is presenting quadrant numbers. The velocity vector field $(u_s^+ \ v_s^+)$ is superimposed on contours in panels (c) and (d). In all panels, (– –) represents plate height $y_p/\delta_{99} = 0.1$ employed in experiments; and (—) represents the body force center $y_f = y_p + 0.13\delta_{99}$ employed in the body force model in equation (4.13).

(c) $\omega_{z,s}^{+}$, and (d) quadrant number at $f_p = 200$ Hz ($0.996U_\infty/\delta_{99}$ and $f_p^{+} = 0.034$). Here, the large-scale structures show a much smaller streamwise wavelength and they are decaying much faster downstream; see e.g., the streamwise velocity of the central region shown in 4.6(a). Similar variations with temporal frequencies were also observed by Huynh & McKeon (2020*a*), who found a linear correlation between temporal frequency and streamwise wavenumber. Furthermore, the streamwise velocity at low-frequency $f_p = 20$ Hz in figure 4.5(a) is stronger than that seen in the structures generated by high-frequency $f_p = 200$ Hz actuation in figure 4.6(a). Instead, the amplitude of wall-normal velocity for the lower frequency $f_p = 20$ Hz actuation in figure 4.5(b) is relatively smaller than that due to the higher frequency $f_p = 200$ Hz actuation in figure 4.6(b). As the actuated large-scale structures propagating downstream at different frequencies, they are more inclined towards the wall due to their height-dependent convective velocity; see e.g., figures 4.5(c), 4.4(c), and 4.6(c) showing spanwise vorticity.

We also perform quadrant analysis at actuation frequency $f_p = 20$ Hz in figure 4.5(d) and actuation frequency $f_p = 200$ Hz in figure 4.6(d). Figure 4.5(d) at low actuation frequency $f_p = 20$ Hz shows that the ejection (Q2) and sweep (Q4) are occupying more region over the (x_m, y) plane compared with higher frequencies results; e.g., $f_p = 80$ Hz in figure 4.4(d) and $f_p = 200$ Hz in figure 4.6(d). This suggests that the Q2 and Q4 events contributing to the Reynolds shear stress are strongly influenced by the actuation at $f_p = 20$ Hz. These dominant Q2 and Q4 events are also observed at $f_p = 80$ Hz in figure 4.4(d) but restricted to downstream regions close to the actuator location $x_m/\delta_{99} \lesssim 5$. This difference is consistent with the observation that $f_p = 20$ Hz introduces large-scale structures with a larger streamwise wavelength compared with $f_p = 80$ Hz. Close to the actuator $x_m/\delta_{99} \lesssim 2$, the quadrant number at high actuation frequency $f_p = 200$ Hz in figure 4.6(d) looks similar to the previous analysis in figure 4.4(d) that separated into different vertical bands with alternating Q1/Q2 quadrant and Q3/Q4 quadrant (Q1/Q2-Q3/Q4) events. However, further downstream, the events in figure 4.6(d) corresponding to quadrant Q1 and Q3 are dominant and stronger than events for quadrant Q2 and Q4. This can be related to the observation that Q2 and Q4 are associated

with a larger time scale (smaller frequency) than Q1 and Q3 events in fully developed turbulent channel flow without forcing (Wallace *et al.*, 1972; Wallace, 2016). Figure 4.6(d) shows that the high-frequency actuation directly results in Q1 and Q3 events to be more prominent for actuated large-scale structures than other lower frequencies farther downstream.

We next study the effect of different plate heights at a fixed actuation frequency of $f_p = 80$ Hz. Figure 4.7 presents (a) u_s^+, (b) v_s^+, (c) $\omega_{z,s}^+$, and (d) quadrant number with $y_p/\delta_{99} = 0.5$. Comparing these plots with the results at $y_p/\delta_{99} = 0.3$ shown in figure 4.4, we also observe that the characteristic streamwise wavelength is longer. This phenomenon results from a larger convective velocity associated with the central region due to a larger local mean velocity at a higher plate height. Figure 4.8 shows the same quantities (a) u_s^+, (b) v_s^+, (c) $\omega_{z,s}^+$, and (d) quadrant number obtained for actuation at $y_p/\delta_{99} = 0.1$ again for $f_p = 80$ Hz. Here, the effect of different convective velocities between the central region and bottom region is more visible. This is because the mean velocity gradient will be larger in the near-wall region. In figure 4.8, the (b) wall-normal velocity v_s, (c) spanwise vorticity $\omega_{z,s}$ and (d) quadrant contours also resemble the previous results at $y_p/\delta_{99} = 0.3$ in figure 4.4 and $y_p/\delta_{99} = 0.5$ in figure 4.7. In particular, the wall-normal velocity v_s is still nearly uniform across the wall-normal height for downstream positions $x_m/\delta_{99} \in [0, 10]$. The quadrant analysis results for these two different plate heights in figures 4.7(d) and 4.8(d) are also separated into different vertical bands with alternating Q1/Q2 quadrant and Q3/Q4 quadrant (Q1/Q2-Q3/Q4) activity. The quadrant order is still the same as for plate height $y_p/\delta_{99} = 0.3$ with Q4→Q3→Q2→Q1 at the top region, and Q1→Q2→Q3→Q4 at the bottom region. This suggests that quadrant trajectory orders observed in canonical wall-bounded turbulent flows are robust to these types of perturbations, and the large-scale structures actuated by the external forcing produce similar motions to those observed in canonical flows without forcing.

4.5 Summary

This work proposes spatial input–output analysis for analyzing the behavior of large-scale structures in actuated turbulent boundary layers. This framework employs downstream marching based on recently developed one-way spatial integration (Towne & Colonius, 2015) in order to overcome ambiguity imposed by the need to specify streamwise wavenumber in inputoutput (resolvent) analysis. In particular, this downstream marching embeds a wall-normal dependent convective velocity for actuated large-scale structures associated with a dominant temporal frequency. The effect of the plasma actuator is modeled as a streamwise body force localized in streamwise and wall-normal direction resembling impulse forcing (Jovanovic & Bamieh, 2001; Ashpis & Reshotko, 1990). The results are compared with large-scale structures in experimental measurements, where the perturbation is introduced through a dielectric barrier discharge plasma actuator, and the shape of large-scale structures is obtained through hot-wire anemometry measurements and a phase-locked analysis.

Large-scale structures obtained from this spatial input–output analysis show good qualitative agreement with experimental measurements. Three distinct regions of streamwise phase-locked velocity with an apparent phase shift occur above and below the actuation device. As the actuated large-scale structures propagate downstream, they are more inclined towards the wall because structures at the top region propagate faster than that at the lower region; i.e., wall-normal dependent convective velocities. The wall-normal velocity is instead nearly uniform across the wall-normal distance consistent with previous experimental observations (Jacobi & McKeon, 2011*a*; Huynh & McKeon, 2020*b*). This spatial input-output analysis provides details on the spatial evolution of the actuated large-scale structures. The actuation frequency influences the characteristic streamwise length scale and responses to higher perturbation frequencies decay faster as they propagate downstream. The three-phase regions persisted for a longer distance (above $x_m/\delta_{99} = 10$) when reducing the frequency that leads to increase in the streamwise length scale. The actuator height instead determines a convective velocity for flow structures

close to the local mean velocity at that height. The variation of actuator height and frequency can be used to study the large-scale structures associated with different wall-normal locations and temporal frequencies.

Our analysis is then employed to quantify the impact on momentum transfer of such coherent motion by evaluating the ejection-sweep cycle via quadrant analysis (Wallace *et al.*, 1972; Wallace, 2016). The obtained quadrant orders Q4→Q3→Q2→Q1 at the top region and Q1→Q2→Q3→Q4 at the bottom region share similarities with observations in turbulent pipe flows without forcing (Nagano & Tagawa, 1995), which implies that our actuation creates structures consistent with those in canonical wall-bounded turbulent flows. These quadrant orders of actuated large-scale structures are found to be independent of actuator height further supporting the robustness of this property of the large-scale structures regardless of how they are introduced. By varying the actuation frequency, we can control the dominance of different quadrants. For higher frequencies, Q1 (inward interaction) and Q3 (outward interaction) are more dominant than Q2 (ejection interaction) and Q4 (sweep interaction), which is consistent with canonical wall-bounded turbulence where Q2 and Q4 events are associated with a larger time scale (Wallace *et al.*, 1972).

The results demonstrate that the proposed spatial input-output analysis can provide insights into the large-scale flow structures induced by temporally periodic and spatially localized perturbations in wall-bounded turbulent flows. This work also shows promise to analyze dynamics of large-scale structures by introducing external perturbations in a controlled manner. Moreover, this spatial input-output analysis can be naturally extended to study flow structures with spanwise variation by setting $k_z \neq 0$ and spanwise velocity by modifying the output operator.

Chapter 5

Structured input–output analysis of transitional wall-bounded flows

> "...the critical velocity was very sensitive to disturbance in the water before entering the tubes..."
>
> Osborne Reynolds[1], 1883

5.1 Introduction

Interest in transitional wall-bounded shear flow dates back to early studies by Reynolds (1883), who noted that the flow in a pipe was sensitive to disturbances. Though much progress has been made, a full understanding of the phenomena has yet to be realized. One of the main challenges lies in the fact that linear stability analysis fails to accurately predict the Reynolds numbers at which flows are observed to transition to turbulence. For example, plane Couette flow is linearly stable for any Reynolds number (Romanov, 1973) yet is observed to transition to turbulence at Reynolds numbers as low as 360 ± 10 (Tillmark & Alfredsson, 1992). This failure has led researchers to study the mechanisms underlying transition by instead analyzing energy growth. In particular, there has been an emphasis on characterizing the types of finite-amplitude perturbations that are most likely to lead to transition as well as, the flow structures that dominate in this regime, see e.g. Schmid & Henningson (1992); Lundbladh *et al.* (1994);

[1] Reynolds (1883, p. 943)

Reddy *et al.* (1998); Philip *et al.* (2007); Duguet *et al.* (2010*a*, 2013); Farano *et al.* (2015).

Reddy *et al.* (1998) examined the relative effect of different transition-inducing flow perturbations in both plane Couette flow and Poiseuille flow through extensive direct numerical simulations (DNS). These authors observed that both streamwise vortices and oblique waves require less energy density than random noise to trigger transition (Reddy *et al.*, 1998, figures 19 and 23) in both flows. They further showed that in Poiseuille flow even perturbations in the form of TollmienSchlichting (TS) waves, which are linearly unstable at $Re > 5772$ (Orszag, 1971), require larger energy density to trigger transition than either streamwise vortices or oblique waves (Reddy *et al.*, 1998, figure 19). Similar behavior has been observed in studies of the transient energy growth and input–output response of the linearized Navier-Stokes (LNS) equations (Reddy & Henningson, 1993; Jovanović & Bamieh, 2005). In fact, input–output analysis of channel flow suggests that streamwise constant structures have larger energy growth than the linearly unstable TS waves, even at supercritical Reynolds numbers (i.e. above the Reynolds number at which the laminar flow is no longer linearly stable) (Jovanović & Bamieh, 2004; Jovanović, 2004). Studies of the LNS have indicated that streamwise vortical structures represent both the initial condition (optimal perturbation) that leads to the largest energy growth (Gustavsson, 1991; Butler & Farrell, 1992; Reddy & Henningson, 1993; Schmid & Henningson, 2012), as well as the type of structures that sustains the highest energy growth, see e.g. (Farrell & Ioannou, 1993*a*; Bamieh & Dahleh, 2001; Jovanović & Bamieh, 2005). The importance of streamwise vortices was also confirmed by Bottin *et al.* (1998), who connected experimental results with this form of exact coherent structures in plane Couette flow.

On the other hand, the simulations of Schmid & Henningson (1992) and Reddy *et al.* (1998), as well as the experiments of Elofsson & Alfredsson (1998) indicate that perturbations of oblique waves require slightly less energy than streamwise vortices to initiate transition. Nonlinear optimal perturbations (NLOP) to plane Couette flow, i.e. the initial perturbations that require the least energy to transition the flow from laminar to turbulent, also take the form of oblique waves that are localized in the streamwise direction, see e.g., (Duguet *et al.*, 2010*a*, 2013;

Monokrousos *et al.*, 2011; Rabin *et al.*, 2012; Cherubini & De Palma, 2013, 2015). For plane Poiseuille flow, hairpin vortices associated with the very short timescale of the Orr mechanism represent the NLOP (Farano *et al.*, 2015, 2016). These results suggest that traditional linear analysis does not capture the full range of highly amplified structures in transitional flows.

Recent experiments and DNS of plane Couette flow with very large channel size ($\sim O(100)$ times the channel half-height) have also uncovered oblique turbulent bands (turbulent stripes) in the transitional flow regime of wall-bounded shear flows, see e.g. (Prigent *et al.*, 2002, 2003; Duguet *et al.*, 2010*b*; De Souza *et al.*, 2020; Tuckerman *et al.*, 2020). These turbulent-laminar patterns were also observed in DNS of transitional plane Poiseuille flow with sufficiently large channel size (Tsukahara *et al.*, 2005; Xiong *et al.*, 2015; Tao *et al.*, 2018; Kanazawa, 2018; Shimizu & Manneville, 2019; Xiao & Song, 2020; Song & Xiao, 2020). The presence of such structures was later confirmed by experiments (Tsukahara *et al.*, 2014; Paranjape, 2019; Paranjape *et al.*, 2020, figure 1). There is strong evidence that the mechanisms leading to the growth and maintenance of these oblique turbulent bands are nonlinear in both plane Couette (Barkley & Tuckerman, 2007; Tuckerman & Barkley, 2011; Duguet & Schlatter, 2013) and plane Poiseuille flow (Tuckerman *et al.*, 2014). That view has been further supported by analysis of exact equilibrium and traveling wave solutions of the nonlinear Navier-Stokes (NS) equations; see e.g., for plane Couette flow (Deguchi & Hall, 2015; Reetz *et al.*, 2019) and Poiseuille flow (Paranjape *et al.*, 2020).

The literature described above points to the benefit of nonlinear methods in characterizing the full range of flow structures in transitional channel flow. However, these methods have far larger computational costs than linear analysis methods; see e.g., (Kerswell *et al.*, 2014; Kerswell, 2018). This trade-off between obtaining a more comprehensive characterization of the phenomena and analysis that is computationally tractable is long-standing. However, there is significant evidence to suggest that insight can be gained through parametrizing or bounding the effect of the nonlinearity rather than undertaking the full computational burden of resolving it. For example, Kreiss *et al.* (1994) and Chapman (2002) employed a bound on the nonlinearity

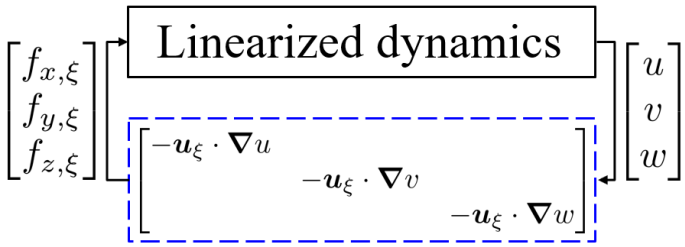

Figure 5.1: Block diagram representing structured input–output feedback interconnection between the linearized dynamics and (– –) structured forcing (modeling the nonlinearity). In particular, each component of the forcing is modeled as an input–output mapping from the respective component of velocity gradient $\boldsymbol{\nabla} u$, $\boldsymbol{\nabla} v$, $\boldsymbol{\nabla} w$ to the respective component forcings $f_{x,\xi}$, $f_{y,\xi}$, $f_{z,\xi}$ of the linearized dynamics with the gain $-\boldsymbol{u}_\xi$ defined in terms of the structured singular value of a linearized closed-loop system response.

to derive a finite-amplitude permissible perturbation that a flow could sustain while remaining laminar. More recently, finite-amplitude stability analysis of transitional shear flows employed local componentwise (sector) bounds on the nonlinearity and exploited the passivity of the nonlinear operator to develop linear matrix inequality (LMI) based approaches to compute bounds on permissible perturbations for a range of shear flow models; see e.g., Kalur *et al.* (2021*b*, 2020, 2021*a*); Liu & Gayme (2020*b*). The inclusion of information about the nonlinear behavior produced results that matched simulation data better than those derived through previous linear approaches. Data-driven methods to parametrize or color (in space or time) input (forcing) applied to the dynamics linearized around the turbulent mean velocity have also enabled nonlinear effects to be captured within the input–output framework; leading to better prediction of flow statistics (Chevalier *et al.*, 2006; Zare *et al.*, 2017; Morra *et al.*, 2021; Nogueira *et al.*, 2021). The effect of the nonlinearity in the NS equations has also been incorporated directly into input–output and resolvent analysis through shaping or parametrizing the forcing, e.g. by including larger amplitude forcing in the near-wall region (Jovanović & Bamieh, 2001; Hœpffner *et al.*, 2005).

In this work, we build on this notion of including the effect of the nonlinearity within a computationally tractable linear framework using the concept of a *structured* uncertainty, see e.g., (Packard & Doyle, 1993; Zhou *et al.*, 1996). In particular, we partition the NS equations into a feedback interconnection between the linearized dynamics and a model of the nonlinear

forcing, as shown in figure 5.1. We then structure the feedback to enforce a block-diagonal structure (bottom block outlined by the blue dashed line – –). In particular, the feedback defines the componentwise inputs to the linearized momentum equations, which are modeled in terms of an uncertain gain $-\boldsymbol{u}_\xi$ of an input–output mapping from each component $\boldsymbol{\nabla} u$, $\boldsymbol{\nabla} v$ and $\boldsymbol{\nabla} w$ to the respective forcings $f_{x,\xi}$, $f_{y,\xi}$ and $f_{z,\xi}$. We represent this gain using the *structured* singular value (Doyle, 1982; Safonov, 1982), μ, which we use to define the largest gain under the structured forcing (Packard & Doyle, 1993). Conceptually the approach allows us to develop a feedback interconnection between the LNS and a structured forcing that is explicitly constrained to preserve the componentwise structure of the nonlinearity in the NS equations.

Structured input–output analysis shares the advantages of all methods employing the spatio-temporal frequency response based analysis techniques upon which it is built, see e.g., (Farrell & Ioannou, 1993*a*; Bamieh & Dahleh, 2001; Jovanović & Bamieh, 2005; McKeon & Sharma, 2010; McKeon *et al.*, 2013; McKeon, 2017; Illingworth *et al.*, 2018; Vadarevu *et al.*, 2019; Madhusudanan *et al.*, 2019; Symon *et al.*, 2021; Liu & Gayme, 2019, 2020*a*). Of greatest interest in this work is its computational tractability versus nonlinear approaches and the lack of finite channel size effects that can plague both DNS and experimental studies. This approach is most closely related to the analysis of the largest singular value ($\mathcal{H}_\infty$ norm) of the spatio-temporal frequency response of the linearized dynamics (top-block of figure 5.1), which measures the structure that sustains the highest input–output growth, see e.g., Jovanović (2004, chapter 8.1.2); Schmid (2007); Hwang & Cossu (2010*a*,*b*); Illingworth (2020). However, in that work, the forcing is assumed to excite the dynamics at all frequencies (e.g., delta-correlated spatio-temporal white noise); in this sense, it can be thought of as the open-loop response of the top-block in figure 5.1.

We apply the proposed *structured* input–output analysis to transitional plane Couette and plane Poiseuille flow. The results indicate that the addition of a structured feedback interconnection enables identification and analysis of the wider range of transition-inducing flow structures

identified in the literature without the computational burden of nonlinear optimization or extensive simulations. More specifically, the results for transitional plane Couette flow reproduce results from DNS based analysis (Reddy *et al.*, 1998) and predictions of NLOP approaches (Rabin *et al.*, 2012), which both indicate that oblique waves require less energy to induce transition than the streamwise elongated structures emphasized in traditional input–output analysis. In plane Poiseuille flow, these transition-inducing flow structures are consistent with DNS (Reddy *et al.*, 1998) emphasizing oblique waves and NLOP analysis that highlights the importance of spatially localized structures with streamwise wavelengths larger than their spanwise extent (Farano *et al.*, 2015). The proposed approach also reproduces the characteristic wavelengths and angle of the oblique turbulent band observed in very large channel studies of transitional plane Couette flow (Prigent *et al.*, 2003). The wavelengths of oblique turbulent bands in transitional plane Poiseuille flow with very large channel size (Kanazawa, 2018) also fall within the range of flow structures showing large structured input–output response.

The agreement between predictions from structured input–output analysis and observation in experiments, DNS, and NLOP show that this framework captures important nonlinear effects. In particular, the results suggest that restricting the feedback in a componentwise manner preserves the structure of the nonlinear mechanisms that weaken the streaks developed through the lift-up effect, in which cross-stream forcing amplifies streamwise streaks (Ellingsen & Palm, 1975; Landahl, 1975; Brandt, 2014). Traditional input–output analysis instead predicts the dominance of streamwise elongated structures associated with the lift-up mechanism, see e.g. the discussion in Jovanović (2021). An examination of Reynolds number trends supports the notion that imposing a structured feedback interconnection based on certain input–output properties associated with the nonlinearity in the NS equations leads to a weakening of the amplification of streamwise elongated structures.

The remainder of this paper is organized as follows. Section 5.2 describes the flow configurations of interest and describes the details of the structured input–output analysis approach. Section 5.3 analyzes the results obtained from the application of structured input–output analysis

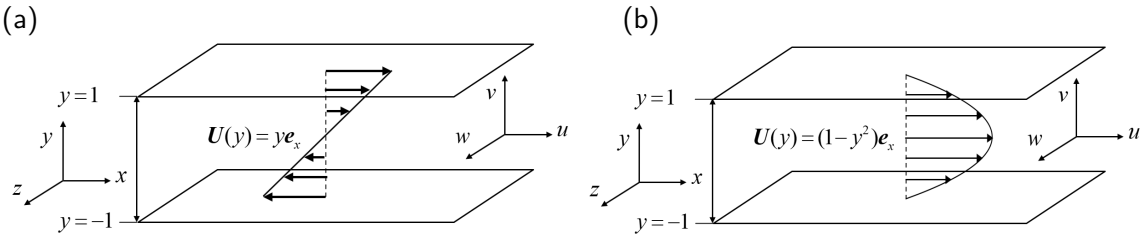

Figure 5.2: Illustrations of flows between two parallel flat plates: (a) plane Couette flow with laminar base flow $\boldsymbol{U}(y) = y\boldsymbol{e}_x$ and (b) plane Poiseuille flow with laminar base flow $\boldsymbol{U}(y) = (1-y^2)\boldsymbol{e}_x$.

to both plane Couette and plane Poiseuille flow. We then analyze Reynolds number dependence in § 5.4. This paper is concluded in § 5.5.

5.2 Formulating the structured input–output model

5.2.1 Governing Equations

We consider incompressible flow between two infinite parallel plates and employ x, y, and z to respectively denote the streamwise, wall-normal, and spanwise directions. The corresponding velocity components are denoted by u, v, and w. The coordinate frames and configurations being used for plane Couette and plane Poiseuille flows are shown in figure 5.2. We express the velocity field as a vector $\boldsymbol{u}_{\text{tot}} = \begin{bmatrix} u_{\text{tot}} & v_{\text{tot}} & w_{\text{tot}} \end{bmatrix}^{\mathsf{T}}$ with $^{\mathsf{T}}$ indicating the transpose. We then decompose the velocity field into the sum of a laminar base flow ($U(y) = y$ for plane Couette flow and $U(y) = 1 - y^2$ for plane Poiseuille flow) and fluctuations about the base flow $\boldsymbol{u}$; i.e., $\boldsymbol{u}_{\text{tot}} = U(y)\boldsymbol{e}_x + \boldsymbol{u}$ with $\boldsymbol{e}_x$ denoting the x-direction (streamwise) unit vector. The pressure field is similarly decomposed into $p_{\text{tot}} = P + p$. The dynamics of the fluctuations $\boldsymbol{u}$ and p are governed by the NS equations:

$$\partial_t \boldsymbol{u} + U\partial_x \boldsymbol{u} + v\,\frac{dU}{dy}\boldsymbol{e}_x + \boldsymbol{\nabla} p - \frac{1}{Re}\nabla^2 \boldsymbol{u} = -\boldsymbol{u}\cdot\boldsymbol{\nabla}\boldsymbol{u}, \tag{5.1a}$$

$$\boldsymbol{\nabla}\cdot\boldsymbol{u} = 0. \tag{5.1b}$$

Here, the spatial variables are normalized by the channel half-height h: e.g., $y = y_*/h \in [-1, 1]$, where the subscript $*$ indicates dimensional quantities. The velocity is normalized by a nominal

characteristic velocity U_n, where $\pm U_n$ is the velocity at the channel walls for plane Couette flow, and U_n is the channel centerline velocity for plane Poiseuille flow. Time and pressure are normalized by h/U_n and ρU_n^2, respectively. The Reynolds number is defined as $Re = U_n h/\nu$, where ν is the kinematic viscosity. In equation (5.1), $\boldsymbol{\nabla} := \begin{bmatrix}\partial_x & \partial_y & \partial_z\end{bmatrix}^\mathsf{T}$ represents the gradient operator, and $\nabla^2 := \partial_x^2 + \partial_y^2 + \partial_z^2$ represents the Laplacian operator. We impose no-slip boundary conditions at the wall; i.e., $\boldsymbol{u}(y = \pm 1) = \boldsymbol{0}$ for both flows. Finally, we write the nonlinear term in equation (5.1a) as

$$\boldsymbol{f} := -\boldsymbol{u}\cdot\boldsymbol{\nabla}\boldsymbol{u} = \begin{bmatrix}-\boldsymbol{u}\cdot\boldsymbol{\nabla}u & -\boldsymbol{u}\cdot\boldsymbol{\nabla}v & -\boldsymbol{u}\cdot\boldsymbol{\nabla}w\end{bmatrix}^\mathsf{T} =: \begin{bmatrix}f_x & f_y & f_z\end{bmatrix}^\mathsf{T}, \tag{5.2}$$

where $=:$ indicates that the right-hand side is defined by the left-hand side. We refer to f_x, f_y, and f_z as the respective streamwise, wall-normal, and spanwise components of the nonlinearity and collectively as the nonlinear components of (5.1). This expression of the nonlinearity as forcing terms makes (5.1) into a set of forced linear evolution equations. This approach builds on the growing body of work that has shown promise in capturing critical features of this forced system response using linear analysis techniques, see e.g. the reviews of Schmid (2007); McKeon (2017); Jovanović (2021) and the references therein.

We next construct the model of the nonlinearity that will allow us to build the feedback interconnection of figure 5.1. The velocity field $-\boldsymbol{u}$ in (5.2) associated with the forcing components can be viewed as the gain operator of an input–output system in which the velocity gradients $\boldsymbol{\nabla}u$, $\boldsymbol{\nabla}v$, $\boldsymbol{\nabla}w$ act as the respective inputs and the forcing components f_x, f_y and f_z act as the respective output. It is this gain that we seek to model through $-\boldsymbol{u}_\xi$ in figure 5.1. This input–output model of the nonlinear components is given by

$$\boldsymbol{f}_\xi := -\boldsymbol{u}_\xi\cdot\boldsymbol{\nabla}\boldsymbol{u} = \begin{bmatrix}-\boldsymbol{u}_\xi\cdot\boldsymbol{\nabla}u & -\boldsymbol{u}_\xi\cdot\boldsymbol{\nabla}v & -\boldsymbol{u}_\xi\cdot\boldsymbol{\nabla}w\end{bmatrix}^\mathsf{T} =: \begin{bmatrix}f_{x,\xi} & f_{y,\xi} & f_{z,\xi}\end{bmatrix}^\mathsf{T}, \tag{5.3}$$

where $-\boldsymbol{u}_\xi = [-u_\xi, -v_\xi, -w_\xi]^\mathsf{T}$ maps the corresponding velocity gradient into each component of the modeled forcing driving linearized dynamics. The next subsection describes how we construct this input–output map so that it enables us to analyze the perturbations that are

most likely to induce transition using the structured singular value formalism (Packard & Doyle, 1993; Zhou *et al.*, 1996).

5.2.2 Structured input–output response

We now define the spatio-temporal frequency response $\mathcal{H}_\nabla(y;k_x,k_z,\omega)$ that will form the basis of the structured input–output response. We first perform the standard transformation to express the dynamics (5.1) in terms of the wall-normal velocity v and wall-normal vorticity $\omega_y := \partial_z u - \partial_x w$ (Schmid & Henningson, 2012), which enforces (5.1b) and eliminates the pressure dependence. This formulation similarly imposes the divergence-free condition on the forcing model, since any component of the input forcing that can be written as the gradient of a scalar function $\widehat{\boldsymbol{f}}_\phi = \widehat{\boldsymbol{\nabla}}\widehat{\phi}$ will be absorbed into the pressure gradient and eliminated. We then exploit the shift-invariance in the (x,z) spatial directions of the two flow configurations of interest and assume invariance to shifts in t, which allows us to perform the following triple Fourier transform for a variable ψ:

$$\widehat{\psi}(y;k_x,k_z,\omega) := \int_{-\infty}^{\infty}\int_{-\infty}^{\infty}\int_{-\infty}^{\infty} \psi(x,y,z,t) e^{-\mathrm{i}(k_x x + k_z z + \omega t)}\, dx\, dz\, dt, \tag{5.4}$$

where $\mathrm{i} = \sqrt{-1}$ is the imaginary unit and ω is the temporal frequency. $k_x = 2\pi/\lambda_x$ and $k_z = 2\pi/\lambda_z$ are the respective dimensionless x and z wavenumbers.

The resulting system of equations describing the transformed linearized equations subject to the modeled forcing $\boldsymbol{f}_\xi$ is

$$\mathrm{i}\omega \begin{bmatrix}\widehat{v}\\ \widehat{\omega}_y\end{bmatrix} = \widehat{\mathcal{A}}\begin{bmatrix}\widehat{v}\\ \widehat{\omega}_y\end{bmatrix} + \widehat{\mathcal{B}}\begin{bmatrix}\widehat{f}_{x,\xi}\\ \widehat{f}_{y,\xi}\\ \widehat{f}_{z,\xi}\end{bmatrix}, \quad \begin{bmatrix}\widehat{u}\\ \widehat{v}\\ \widehat{w}\end{bmatrix} = \widehat{\mathcal{C}}\begin{bmatrix}\widehat{v}\\ \widehat{\omega}_y\end{bmatrix}. \tag{5.5a,b}$$

The operators in equation (5.5) are defined following Jovanović & Bamieh (2005):

$$\widehat{\mathcal{A}}(k_x,k_z) := \begin{bmatrix}\widehat{\nabla}^2 & 0\\ 0 & \mathcal{I}\end{bmatrix}^{-1}\begin{bmatrix}-\mathrm{i}k_x U\widehat{\nabla}^2 + \mathrm{i}k_x U'' + \widehat{\nabla}^4/Re & 0\\ -\mathrm{i}k_z U' & -\mathrm{i}k_x U + \widehat{\nabla}^2/Re\end{bmatrix}, \tag{5.6a}$$

$$\widehat{\mathcal{B}}(k_x,k_z) := \begin{bmatrix}\widehat{\nabla}^2 & 0\\ 0 & \mathcal{I}\end{bmatrix}^{-1}\begin{bmatrix}-\mathrm{i}k_x\partial_y & -(k_x^2+k_z^2) & -\mathrm{i}k_z\partial_y\\ \mathrm{i}k_z & 0 & -\mathrm{i}k_x\end{bmatrix}, \tag{5.6b}$$

$$\widehat{\mathcal{C}}(k_x,k_z) := \frac{1}{k_x^2+k_z^2}\begin{bmatrix} \mathrm{i}k_x\partial_y & -\mathrm{i}k_z \\ k_x^2+k_z^2 & 0 \\ \mathrm{i}k_z\partial_y & \mathrm{i}k_x \end{bmatrix}, \tag{5.6c}$$

where $U' := dU(y)/dy$, $U'' := d^2U(y)/dy^2$, $\widehat{\nabla}^2 := \partial_{yy} - k_x^2 - k_z^2$, and $\widehat{\nabla}^4 := \partial_y^{(4)} - 2(k_x^2 + k_z^2)\partial_{yy} + (k_x^2+k_z^2)^2$. The boundary conditions, which can be derived from the no-slip conditions, are

$$\widehat{v}(y=\pm 1) = \frac{\partial \widehat{v}}{\partial y}(y=\pm 1) = \widehat{\omega}_y(y=\pm 1) = 0. \tag{5.7}$$

The spatio-temporal frequency response $\mathcal{H}$ of the system in (5.5) that maps the input forcing $\widehat{\boldsymbol{f}}_\xi(y;k_x,k_z,\omega)$ to the velocity vector $\widehat{\boldsymbol{u}}(y;k_x,k_z,\omega)$ at the same spatial-temporal wavenumber-frequency triplet; i.e., $\widehat{\boldsymbol{u}}(y;k_x,k_z,\omega) = \mathcal{H}(y;k_x,k_z,\omega)\widehat{\boldsymbol{f}}_\xi(y;k_x,k_z,\omega)$ is given by

$$\mathcal{H}(y;k_x,k_z,\omega) := \widehat{\mathcal{C}}\left(\mathrm{i}\omega\,\mathcal{I}_{2\times 2} - \widehat{\mathcal{A}}\right)^{-1}\widehat{\mathcal{B}}. \tag{5.8}$$

Here $\mathcal{I}_{2\times 2} := \mathrm{diag}(\mathcal{I},\mathcal{I})$, where $\mathcal{I}$ is the identity operator and $\mathrm{diag}(\cdot)$ indicates a block diagonal operation. Following the language in Jovanović (2021), we also refer to $\mathcal{H}(y;k_x,k_y,\omega)$ defined in (5.8) as the frequency response operator.

The linear form of (5.3) allows us to also perform the spatio-temporal Fourier transform (5.4) on this forcing model to obtain

$$\widehat{\boldsymbol{f}}_\xi = -\widehat{\boldsymbol{u}}_\xi \cdot \widehat{\boldsymbol{\nabla}}\widehat{\boldsymbol{u}} = \begin{bmatrix}\widehat{f}_{x,\xi}\\ \widehat{f}_{y,\xi}\\ \widehat{f}_{z,\xi}\end{bmatrix} = \begin{bmatrix} -\widehat{\boldsymbol{u}}_\xi^{\mathsf{T}} & & \\ & -\widehat{\boldsymbol{u}}_\xi^{\mathsf{T}} & \\ & & -\widehat{\boldsymbol{u}}_\xi^{\mathsf{T}} \end{bmatrix}\begin{bmatrix}\widehat{\boldsymbol{\nabla}}\widehat{u}\\ \widehat{\boldsymbol{\nabla}}\widehat{v}\\ \widehat{\boldsymbol{\nabla}}\widehat{w}\end{bmatrix}, \tag{5.9}$$

which can be decomposed as

$$\begin{bmatrix}\widehat{f}_{x,\xi}\\ \widehat{f}_{y,\xi}\\ \widehat{f}_{z,\xi}\end{bmatrix} = \mathrm{diag}\left(-\widehat{\boldsymbol{u}}_\xi^{\mathsf{T}}, -\widehat{\boldsymbol{u}}_\xi^{\mathsf{T}}, -\widehat{\boldsymbol{u}}_\xi^{\mathsf{T}}\right)\mathrm{diag}\left(\widehat{\boldsymbol{\nabla}},\widehat{\boldsymbol{\nabla}},\widehat{\boldsymbol{\nabla}}\right)\begin{bmatrix}\widehat{u}\\ \widehat{v}\\ \widehat{w}\end{bmatrix}. \tag{5.10}$$

This decomposition of the forcing function is illustrated in the two blocks inside the blue dashed line (– –) in figure 5.3(a), where the velocity field arising from the spatio-temporal frequency response $\mathcal{H}$ is the input and the forcing is the output.

In order to isolate the gain $-\boldsymbol{u}_\xi$ that we seek to model, it is analytically convenient to combine the linear gradient operator with the spatio-temporal frequency response. We denote

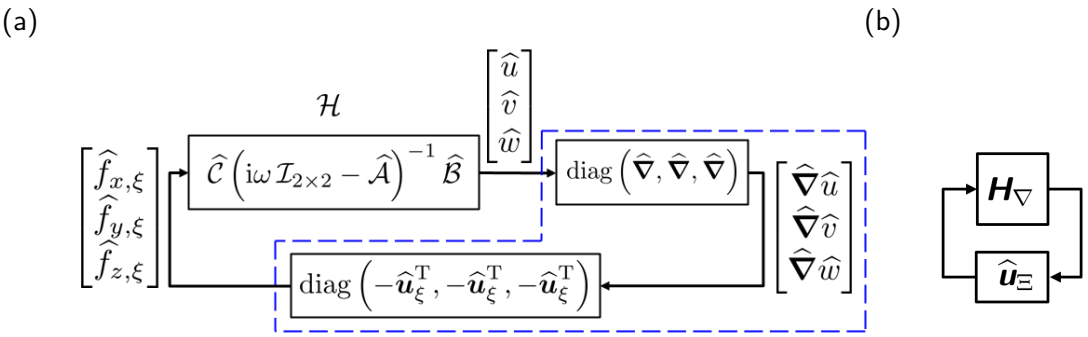

Figure 5.3: Illustration of structured input–output analysis: (a) a componentwise description, where blocks inside of (– –, blue) represent the modeled forcing in equation (5.10) corresponding to the bottom block of figure 5.1; (b) a high-level description after discretization.

the resulting modified frequency response operator as

$$\mathcal{H}_\nabla(y;k_x,k_z,\omega) := \mathrm{diag}\left(\widehat{\boldsymbol{\nabla}},\widehat{\boldsymbol{\nabla}},\widehat{\boldsymbol{\nabla}}\right)\mathcal{H}(y;k_x,k_z,\omega). \tag{5.11}$$

We note that this operator in (5.11) can be also obtained by modifying $\widehat{\mathcal{C}}$ in equation (5.8) such that the output corresponds to a vectorized velocity gradient. Then, we redraw the system as a feedback interconnection between this linear operator in (5.11) and the structured uncertainty

$$\widehat{\boldsymbol{u}}_\Xi := \mathrm{diag}\left(-\widehat{\boldsymbol{u}}_\xi^{\mathsf{T}},-\widehat{\boldsymbol{u}}_\xi^{\mathsf{T}},-\widehat{\boldsymbol{u}}_\xi^{\mathsf{T}}\right). \tag{5.12}$$

The structured uncertainty $\widehat{\boldsymbol{u}}_\Xi$ in (5.12) has a block-diagonal structure such that the resulting feedback interconnection leads to a forcing model that retains the componentwise structure of the nonlinearity. Figure 5.3(b) describes the resulting feedback interconnection between the modified spatio-temporal frequency response and the structured uncertainty, where $\boldsymbol{H}_\nabla$ and $\widehat{\boldsymbol{u}}_\Xi$ respectively represent the spatial discretizations (numerical approximations) of $\mathcal{H}_\nabla$ in (5.11) and $\widehat{\boldsymbol{u}}_\Xi$ in (5.12).

We are interested in characterizing the perturbations associated with the most amplified flow structures under structured forcing. This amplification under structured forcing can be quantified by the structured singular value of the modified frequency response operator $\mathcal{H}_\nabla$; see e.g., Packard & Doyle (1993, definition 3.1); Zhou *et al.* (1996, definition 11.1), which is defined as follows.

Definition 5.1 *Given wavenumber and frequency pair (k_x, k_z, ω), the structured singular value $\mu_{\widehat{\boldsymbol{U}}_\Xi}[\boldsymbol{H}_\nabla(k_x, k_z, \omega)]$ is defined as*

$$\mu_{\widehat{\boldsymbol{U}}_\Xi}[\boldsymbol{H}_\nabla(k_x, k_z, \omega)] := \frac{1}{min\{\bar{\sigma}[\widehat{\boldsymbol{u}}_\Xi] \,:\, \widehat{\boldsymbol{u}}_\Xi \in \widehat{\boldsymbol{U}}_\Xi,\, det[\boldsymbol{I} - \boldsymbol{H}_\nabla(k_x, k_z, \omega)\widehat{\boldsymbol{u}}_\Xi] = 0\}}, \tag{5.13}$$

unless no $\widehat{\boldsymbol{u}}_\Xi \in \widehat{\boldsymbol{U}}_\Xi$ makes $\boldsymbol{I} - \boldsymbol{H}_\nabla \widehat{\boldsymbol{u}}_\Xi$ singular, in which case $\mu_{\widehat{\boldsymbol{U}}_\Xi}[\boldsymbol{H}_\nabla] := 0$.

Here, $\bar{\sigma}[\cdot]$ is the largest singular value, $det[\cdot]$ is the determinant of the argument, and $\boldsymbol{I}$ is the identity matrix. The subscript of μ in (5.13) is a set $\widehat{\boldsymbol{U}}_\Xi$ containing all uncertainties having the same block-diagonal structure as $\widehat{\boldsymbol{u}}_\Xi$; i.e.,

$$\widehat{\boldsymbol{U}}_\Xi := \left\{ diag\left(-\widehat{\boldsymbol{u}}_\xi^T, -\widehat{\boldsymbol{u}}_\xi^T, -\widehat{\boldsymbol{u}}_\xi^T\right) : -\widehat{\boldsymbol{u}}_\xi^T \in \mathbb{C}^{N_y \times 3N_y} \right\}, \tag{5.14}$$

where N_y denotes the number of grid points in y.

For ease of computation and analysis, the form of the structured uncertainty in equation (5.14) allows the full degrees of freedom for the complex matrix $-\widehat{\boldsymbol{u}}_\xi^{\mathsf{T}} \in \mathbb{C}^{N_y \times 3N_y}$. A natural refinement to better represent the physics would be to enforce a diagonal structure for each of the sub-blocks of this matrix. This approach is not pursued here because it requires extensions of both the analysis and computational tools to properly evaluate the response. These extensions are beyond the scope of the current work.

The largest structured singular value across all temporal frequencies characterizes the largest response associated with a stable structured feedback interconnection (i.e. the full block diagram in figure 5.3(b)). Here, stability is defined in terms of the small gain theorem (Zhou *et al.*, 1996, theorem 11.8).

Proposition 5.2 (Small Gain Theorem) *Given $0 < \beta < \infty$ and wavenumber pair (k_x, k_z). The loop shown in figure 5.3(b) is stable for all $\widehat{\boldsymbol{u}}_\Xi \in \widehat{\boldsymbol{U}}_\Xi$ with $\|\widehat{\boldsymbol{u}}_\Xi\|_\infty := \sup_{\omega \in \mathbb{R}} \bar{\sigma}[\widehat{\boldsymbol{u}}_\Xi] < \frac{1}{\beta}$ if and only if:*

$$\|\mathcal{H}_\nabla\|_\mu(k_x, k_z) := \sup_{\omega \in \mathbb{R}} \mu_{\widehat{\boldsymbol{U}}_\Xi}[\boldsymbol{H}_\nabla(k_x, k_z, \omega)] \leq \beta. \tag{5.15}$$

Here, sup represents supremum (least upper bound) operation, and we abuse the notation by writing $\|\cdot\|_\mu$ (Packard & Doyle, 1993), although μ is not a proper norm (i.e. it does not necessarily satisfy the triangle inequality). This value $\|\mathcal{H}_\nabla\|_\mu(k_x, k_z)$ in (5.15) directly quantifies most amplified flow structures (characterized by the associated (k_x, k_z) pair) under structured forcing. This $\|\mathcal{H}_\nabla\|_\mu(k_x, k_z)$ is closely related to input–output analysis based on the $\mathcal{H}_\infty$ norm (Jovanović, 2004; Schmid, 2007; Illingworth, 2020) and characterizations of transient growth (see e.g. (Schmid, 2007)), where flow structures with high amplification under external input forcing or high transient energy growth are associated with transition.

5.2.3 Numerical Method

The operators in equation (5.6) are discretized using the Chebyshev differentiation matrices generated by the MATLAB routines of Weideman & Reddy (2000). The boundary conditions in equation (5.7) are implemented following Trefethen (2000, chapters 7 and 14). We employ the Clenshaw–Curtis quadrature (Trefethen, 2000, chapter 12) in computing both singular and structured singular values to ensure that they are independent of the number of Chebyshev spaced wall-normal grid points. The numerical implementation of the operators is validated through comparisons of the plane Poiseuille flow results for computations of the $\mathcal{H}_\infty$ norm in Jovanović (2004, chapter 8.1.2) and Schmid (2007, figure 5), and plane Couette flow in Jovanović (2004, chapter 8.2). We use $N_y = 30$ collocation points (excluding the boundary points), which is the same number employed in Jovanović & Bamieh (2005); Jovanović (2004). We verified that doubling the number of collocation points in the wall-normal direction does not alter results, indicating grid convergence. We employ, respectively, 50 and 90 logarithmically spaced points in the spectral range $k_x \in [10^{-4}, 10^{0.48}]$ and $k_z \in [10^{-2}, 10^{1.2}]$ similar to those employed in Jovanović & Bamieh (2005).

We compute $\|\mathcal{H}_\nabla\|_\mu$ in equation (5.15) for each wavenumber pair (k_x, k_z) using the `mussv`

command in the Robust Control Toolbox (Balas *et al.*, 2005) of MATLAB R2020a. The arguments of `mussv` employed here include the state-space model of $\boldsymbol{H}_{\nabla}$ that samples the frequency domain adaptively[2]. The `BlockStructure` argument comprises three full $N_y \times 3N_y$ complex matrices, and we use the `'Uf'` algorithm option. The average computation time for each wavenumber pair (k_x, k_z) is around $11s$ on a computer with a 3.4 GHz Intel Core i7-3770 CPU and 16GB RAM. These computations can be easily parallelized over either the k_x or k_z domain e.g., using the `parfor` command in the Parallel Computing Toolbox in MATLAB.

5.3 Structured spatio-temporal frequency response

In this section, we use $\|\mathcal{H}_{\nabla}\|_{\mu}(k_x, k_z)$ in equation (5.15) to characterize the flow structures (i.e., the (k_x,k_z) wavenumber pairs) that are most amplified in transitional plane Couette flow and plane Poiseuille flow. In order to illustrate the relative effect of the feedback interconnection versus the imposed structure we compare the results to

$$\|\mathcal{H}\|_{\infty}(k_x, k_z) := \sup_{\omega \in \mathbb{R}} \bar{\sigma}\left[\boldsymbol{H}(k_x, k_z, \omega)\right], \tag{5.16}$$

where $\boldsymbol{H}$ is the discretization of spatio-temporal frequency response operator $\mathcal{H}$ in (5.8). This quantity, which was previously analyzed for transitional flows (Jovanović, 2004; Schmid, 2007; Illingworth, 2020), describes the maximum singular value of the frequency response operator $\mathcal{H}$. This quantity represents the maximal gain of $\mathcal{H}$ over all temporal frequencies, i.e., the worst-case amplification over harmonic inputs. Therefore the highest values of $\|\mathcal{H}\|_{\infty}$ correspond to structures that are most amplified but not those with the largest sustained energy density that is often reported in the literature, see e.g., Farrell & Ioannou (1993*a*); Bamieh & Dahleh (2001); Jovanović & Bamieh (2005).

In order to isolate the effect of the structure imposed on the nonlinearity from the effect of

[2]The command `mussv` can adaptively sample frequency domain $\omega \in \mathbb{R}^{+}$, and the frequency domain $\omega \in \mathbb{R}^{-}$ can be computed by modifying the state-space model

the closed-loop feedback interconnection, we also compute

$$\|\mathcal{H}_\nabla\|_\infty(k_x,k_z) := \sup_{\omega\in\mathbb{R}} \bar{\sigma}\left[\boldsymbol{H}_\nabla(k_x,k_z,\omega)\right]. \tag{5.17}$$

This quantity is the unstructured counterpart of $\|\mathcal{H}_\nabla\|_\mu$, which is obtained by replacing the uncertainty set $\widehat{\boldsymbol{U}}_\Xi$ with the set of full complex matrices $\mathbb{C}^{3N_y\times 9N_y}$ (Packard & Doyle, 1993; Zhou *et al.*, 1996). In other words, the definition does not specify a particular feedback pathway associated with each component of forcing, which leads to an unstructured feedback interconnection[3]. Comparisons between $\|\mathcal{H}_\nabla\|_\mu$ and $\|\mathcal{H}_\nabla\|_\infty$, therefore highlight the effect of the structured uncertainty. The values $\|\mathcal{H}\|_\infty$ in (5.16) and $\|\mathcal{H}_\nabla\|_\infty$ in (5.17) are computed using the `hinfnorm` command in the Robust Control Toolbox (Balas *et al.*, 2005) of MATLAB.

In the next subsection we analyze plane Couette flow at $Re = 358$. This is followed by a study of plane Poiseuille flow at $Re = 690$ in § 5.3.2. These Reynolds numbers are within the ranges of $Re \in [340, 393]$ and $Re \in [660, 720]$, where oblique turbulent bands are respectively observed in plane Couette flow (Prigent *et al.*, 2003) and plane Poiseuille flow (Kanazawa, 2018). These particular values were selected because there is data from previous studies (Prigent *et al.*, 2003; Kanazawa, 2018) available for comparison. This section ends with a discussion of the role of the componentwise structure of feedback interconnection in the proposed structured input–output analysis in § 5.3.3.

5.3.1 Plane Couette flow at $Re = 358$

In this subsection, we use the proposed approach to analyze the perturbations that are most likely to trigger transition in plane Couette flow at $Re = 358$ using the $\|\mathcal{H}_\nabla\|_\mu$ formulation described in the previous section. Figure 5.4(a) shows this quantity alongside results obtained using an input–output analysis based approach describing the most amplified flow structures in terms of $\|\mathcal{H}\|_\infty$ in panel (b) and $\|\mathcal{H}_\nabla\|_\infty$ in equation (5.17) in panel (c). In all panels, we indicate the structures with $k_x \approx 0$ and $k_z = 2$ representing streamwise vortices using (✳, blue) and indicate $k_x = 1$

[3]We note that by definition $\|\mathcal{H}_\nabla\|_\mu(k_x,k_z) \leq \|\mathcal{H}_\nabla\|_\infty(k_x,k_z)$ (Packard & Doyle, 1993, equation (3.4)).

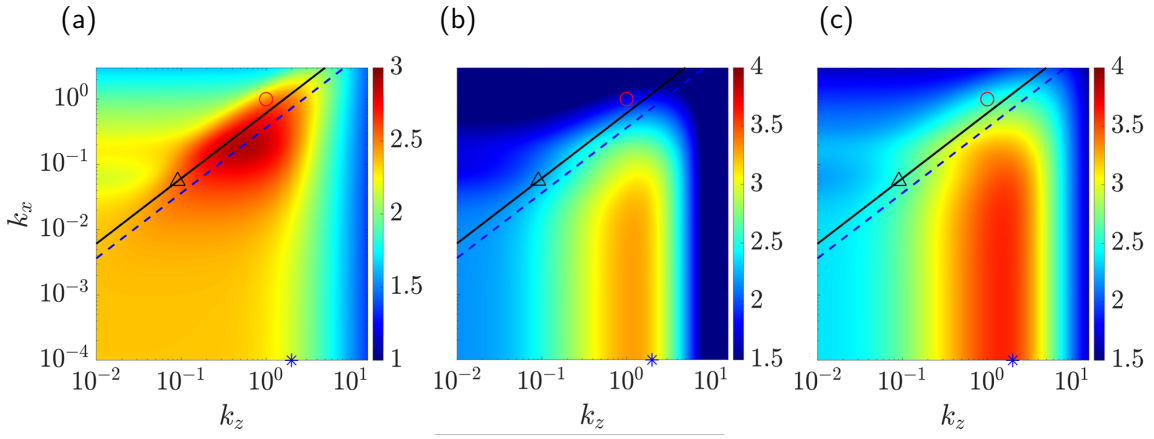

Figure 5.4: (a) $\log_{10}[\|\mathcal{H}_\nabla\|_\mu(k_x,k_z)]$, (b) $\log_{10}[\|\mathcal{H}\|_\infty(k_x,k_z)]$, and (c) $\log_{10}[\|\mathcal{H}_\nabla\|_\infty(k_x,k_z)]$ for plane Couette flow at $Re = 358$. Here the symbols (✳, blue) indicates streamwise vortices with $k_x \approx 0$, $k_z = 2$; (○, red) marks oblique waves with $k_x = k_z = 1$ as studied by (Reddy *et al.*, 1998). The symbol (△, black) marks $\lambda_x = 113$, $\lambda_z = 69$ which are the observed wavelengths of the oblique turbulent band at $Re = 358$ (Prigent *et al.*, 2003). The black solid line (—) is $\lambda_z = \lambda_x \tan(32^\circ)$ representing a 32° angle of the oblique turbulent band, and the blue dashed line (– –, blue) represents $\lambda_z = \lambda_x \tan(20^\circ)$.

and $k_z = 1$ representing the oblique waves that were observed as the structures requiring the least energy to trigger transition in the DNS of Reddy *et al.* (1998) using (○, red). In general, the wavenumber pair $k_x \approx 0$ and $k_z = 2$ marked by (✳, blue) represents streamwise elongated flow structures that include both streamwise vortices and streamwise streaks. However, we will refer to $(k_x \approx 0, k_z = 2)$ as streamwise vortices when comparing with the results in Reddy *et al.* (1998) because that work explicitly introduced streamwise vortices associated with this wavenumber pair. The figure shows clear differences in the dominant structures identified using the structured input–output approach. The largest magnitudes of $\|\mathcal{H}_\nabla\|_\mu$ in figure 5.4(a) are associated with oblique waves with $k_x \in [10^{-2}, 1]$ and $k_z \in [10^{-1}, 1]$, while the streamwise elongated structures that are dominant in panels (b) and (c) have a lesser but still large magnitude. This result is consistent with findings of Reddy *et al.* (1998, figure 23) showing that oblique waves require less perturbation energy to trigger turbulence in plane Couette flow than streamwise vortices. A comparison of $\|\mathcal{H}_\nabla\|_\infty$ in figure 5.4(c) and $\|\mathcal{H}\|_\infty$ in figure 5.4(b) indicates that it is not the feedback interconnection that significantly changes the dominant flow structures but rather the imposition of the componentwise structure of the nonlinearity. In addition, we observe that the magnitude of $\|\mathcal{H}_\nabla\|_\mu$ in figure 5.4(a) is lower than $\|\mathcal{H}_\nabla\|_\infty$ in figure 5.4(c) for each (k_x, k_z)

pair, which is consistent with the fact that the unstructured gain $\|\mathcal{H}_\nabla\|_\infty$ provides an upper bound on the structured one, $\|\mathcal{H}_\nabla\|_\mu$ (Packard & Doyle, 1993).

The difference between the results in figure 5.4 mirrors the differences between the optimal perturbation structures predicted by linear and nonlinear optimal perturbation (NLOP) analysis. In particular, the structures predicted using $\|\mathcal{H}_\nabla\|_\mu$ are streamwise localized oblique waves reminiscent of those obtained as NLOP of plane Couette flow (Monokrousos *et al.*, 2011; Duguet *et al.*, 2010*a*, 2013; Rabin *et al.*, 2012; Cherubini & De Palma, 2013, 2015), whereas the results obtained using $\|\mathcal{H}\|_\infty$ in figure 5.4(b) indicate the dominance of the types of streamwise elongated flow structures predicted as linear optimal perturbations (Butler & Farrell, 1992). Our results also reflect previous findings that the NLOP is wider in the spanwise direction than the linear optimal perturbation (Rabin *et al.*, 2012, figure 11). The results in figure 5.4 therefore indicate that the current structured input–output framework provides closer agreement with both DNS and NLOP based predictions of perturbations to which the flow is most sensitive than traditional input–output methods focusing on the spatio-temporal frequency response $\mathcal{H}$. The inclusion of a feedback loop for $\|\mathcal{H}_\nabla\|_\infty$ in figure 5.4(c) does lead to small improvements in the width of the structures predicted, but it does not lead to identification of the dominance of the oblique waves. This behavior suggests that the weakening of the amplification of the streamwise elongated structures is a direct result of the structure imposed in the feedback interconnection.

Oblique turbulent bands have also been observed to be prominent in the transitional-regime of plane Couette flow with very large channel size (Prigent *et al.*, 2003; Duguet *et al.*, 2010*b*). Figure 5.4 indicates the wavelength pair $\lambda_x = 113$ and $\lambda_z = 69$ ($\triangle$, black) associated with the oblique turbulent bands that are observed to have horizontal extents in the range $\lambda_x \in [107, 118]$ and $\lambda_z \in [62, 76]$ in very large channel studies of plane Couette flow at $Re = 358$, see (Prigent *et al.*, 2003, figures 3(b) and 5). The characteristic inclination angle measured from the streamwise direction in $x - z$ plane is $\theta := \tan^{-1}(\lambda_z/\lambda_x) = \tan^{-1}(69/113) \approx 32^\circ$. This value is indicated by the black solid line $(-)$: $\lambda_z = \lambda_x \tan(32^\circ)$ in figure 5.4 and falls

within the mid-range of the angles $\theta \in [28^\circ, 35^\circ]$ corresponding to the spread of the data in Prigent *et al.* (2003, figure 5). Other simulations employing a tilted domain to impose an angle constrained by periodic boundary conditions in the streamwise and spanwise directions indicate that the oblique turbulent bands can be maintained by an angle as low as 20°; see e.g., Duguet *et al.* (2010*b*, figure 6). In figure 5.4, we also plot the angle 20° represented by (– –, blue) $\lambda_z = \lambda_x \tan(20^\circ)$, which is shown to correspond to the center of the peak region. he results in the literature indicate that oblique structures associated with a range of wavelengths and inclination angles may provide large amplification, which may be the reason for the large peak region of $\|\mathcal{H}_\nabla\|_\mu$ in figure 5.4(a). These results suggest that structured input–output analysis captures both the wavelengths and the angle of the oblique turbulent band in transitional plane Couette flow. While there is some footprint of these types of structures in all three panels, the range of characteristic wavelengths and angles are most clearly associated with the peak region of $\|\mathcal{H}_\nabla\|_\mu$ in figure 5.4(a), and the line representing the angle of the structures is quite consistent with the shape of the peak region. The fact that these structures become more prominent through this analysis suggests that these turbulent bands arise in transitional flows due to their large amplification (sensitivity to disturbances).

5.3.2 Plane Poiseuille flow at $Re = 690$

In this subsection, we apply the proposed structured input–output analysis to investigate highly amplified flow structures in plane Poiseuille flow at $Re = 690$. Figure 5.5 compares (a) $\|\mathcal{H}_\nabla\|_\mu$, (b) $\|\mathcal{H}\|_\infty$, and (c) $\|\mathcal{H}_\nabla\|_\infty$ for this flow configuration. In each panel, we also indicate the streamwise vortices with $k_x \approx 0$ and $k_z = 2$ ($\ast$, blue), oblique waves with $k_x = k_z = 1$ ($\bigcirc$, black), and TS waves with $k_x = 1$ and $k_z \approx 0$ ($\square$, magenta) that were identified as transition-inducing perturbations in Reddy *et al.* (1998). Similar to the results for plane Couette flow in figure 5.4, the quantities $\|\mathcal{H}\|_\infty$ and $\|\mathcal{H}_\nabla\|_\infty$ show qualitatively similar behavior; the highest values for both correspond to streamwise streaks and vortices. In figures 5.5(b) and 5.5(c), the TS wave structure appears as a local peak with a magnitude that is about an order of magnitude

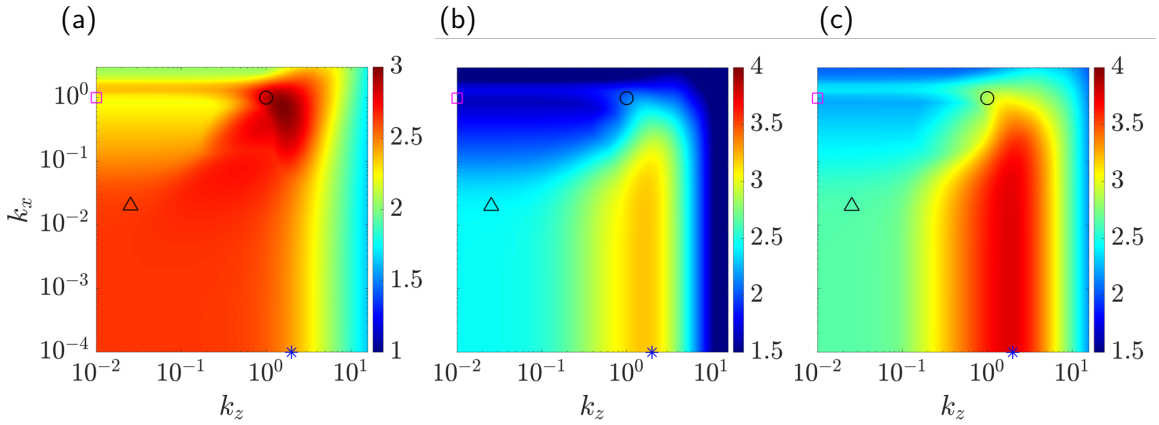

Figure 5.5: (a) $\log_{10}[\|\mathcal{H}_\nabla\|_\mu(k_x,k_z)]$, (b) $\log_{10}[\|\mathcal{H}\|_\infty(k_x,k_z)]$, and (c) $\log_{10}[\|\mathcal{H}_\nabla\|_\infty(k_x,k_z)]$ for plane Poiseuille flow at $Re = 690$. Here the symbols (✳, blue): $k_x \approx 0$, $k_z = 2$ marks streamwise vortices; (○, black): $k_x = k_z = 1$ marks oblique waves; (□, magenta): $k_x = 1$, $k_z \approx 0$ marks TS wave as studied by (Reddy *et al.*, 1998). The symbol (△, black): $\lambda_x = 314$, $\lambda_z = 248$ indicates the wavelengths of the oblique turbulent band at $Re = 690$ observed in Kanazawa (2018).

smaller than the values associated with the streamwise vortices in $\|\mathcal{H}_\nabla\|_\infty$ and $\|\mathcal{H}\|_\infty$. In these two panels, the values for the oblique waves are of a similar order of magnitude as the peak corresponding to the TS waves in $\|\mathcal{H}\|_\infty$ and slightly higher in $\|\mathcal{H}_\nabla\|_\infty$. These findings agree with previous analyses of $\|\mathcal{H}\|_\infty$ in Jovanović (2004); Schmid (2007). The similarity of the $\|\mathcal{H}_\nabla\|_\infty$ and $\|\mathcal{H}\|_\infty$ results indicate that an unstructured feedback interconnection does not lead to substantial changes in most prominent structures.

The overall shape of $\|\mathcal{H}_\nabla\|_\mu$ is somewhat different than that of either $\|\mathcal{H}\|_\infty$ or $\|\mathcal{H}_\nabla\|_\infty$. The streamwise elongated structures that are dominant in panels (b) and (c) have a lesser but still large magnitude, while the peak value corresponds to oblique waves. The TS wave corresponds to a local peak in $\|\mathcal{H}_\nabla\|_\mu$, but the magnitudes are smaller than the peak values associated with oblique waves. This result is consistent with findings of Reddy *et al.* (1998, figure 19) showing that oblique waves require slightly less perturbation energy to trigger turbulence in plane Poiseuille flow than streamwise vortices. Both the peak region and the large region of very high values in the bottom left quadrant of figure 5.5(a) are consistent with the short-timescale NLOP of plane Poiseuille flow, which was shown to be spatially localized with streamwise wavelength larger than spanwise wavelength (Farano *et al.*, 2015). These results indicate that the inclusion of structured uncertainty uncovers a broader range of transition-inducing structures

and correctly orders their relative amplification in the sense of their transition-inducing potential.

There is evidence that the oblique turbulent bands that are observed in very large channel studies also play a role in transition. Their ability to trigger transition has been exploited in a number of studies that employ flow fields with a sustained oblique turbulent bands at a relatively high Re as the initial conditions to trigger the banded turbulent-laminar patterns associated with transitioning flows at a Reynolds number of interest; see e.g., (Tsukahara *et al.*, 2005; Tuckerman *et al.*, 2014; Tao *et al.*, 2018; Xiao & Song, 2020). The characteristic wavelength pair ($\lambda_x = 314$, $\lambda_z = 248$) associated with this structure in plane Poiseuille flow at $Re = 690$ (estimated from Kanazawa (2018, figure 5.1(b))) is indicated in each panel of figure 5.5 using ($\triangle$). These characteristic wavelengths are located within the range of large values of $\|\mathcal{H}_\nabla\|_\mu$. They are not associated with peak regions of $\|\mathcal{H}\|_\infty$ or $\|\mathcal{H}_\nabla\|_\infty$ in figures 5.5(b) or (c), although a footprint of these flow structures is visible in both. Figure 5.5(a) indicates that the flow structure associated with the oblique turbulent band has a similar amplification under structured forcing as streamwise elongated structures, although both of their magnitudes are smaller than that associated with the oblique waves. Further analysis of these structures and their role in transition is a topic of ongoing work.

5.3.3 Componentwise structure of nonlinearity: weakening of the lift-up mechanism

The results in the previous subsections, particularly the differences between $\|\mathcal{H}_\nabla\|_\mu$ and $\|\mathcal{H}_\nabla\|_\infty$ in figures 5.4 and 5.5 highlight the role of the feedback interconnection structure in the identification of the perturbations to which the flow is most sensitive. In particular, the imposition of the componentwise structure leads to lesser prominence of streamwise elongated structures ($k_x \approx 0, k_z = 2$) in $\|\mathcal{H}_\nabla\|_\mu$ versus $\|\mathcal{H}\|_\infty$ or $\|\mathcal{H}_\nabla\|_\infty$ in both plane Couette and Poiseuille flows (see figures 5.4 and 5.5).

The mechanisms underlying the differences in $\|\mathcal{H}_\nabla\|_\mu$ and $\|\mathcal{H}_\nabla\|_\infty$ can be analyzed by isolating the effect of forcing in each component of the momentum equation, i.e. f_x, f_y, f_z in equation (5.2) on the amplification of each velocity component u, v, w. These nine quantities

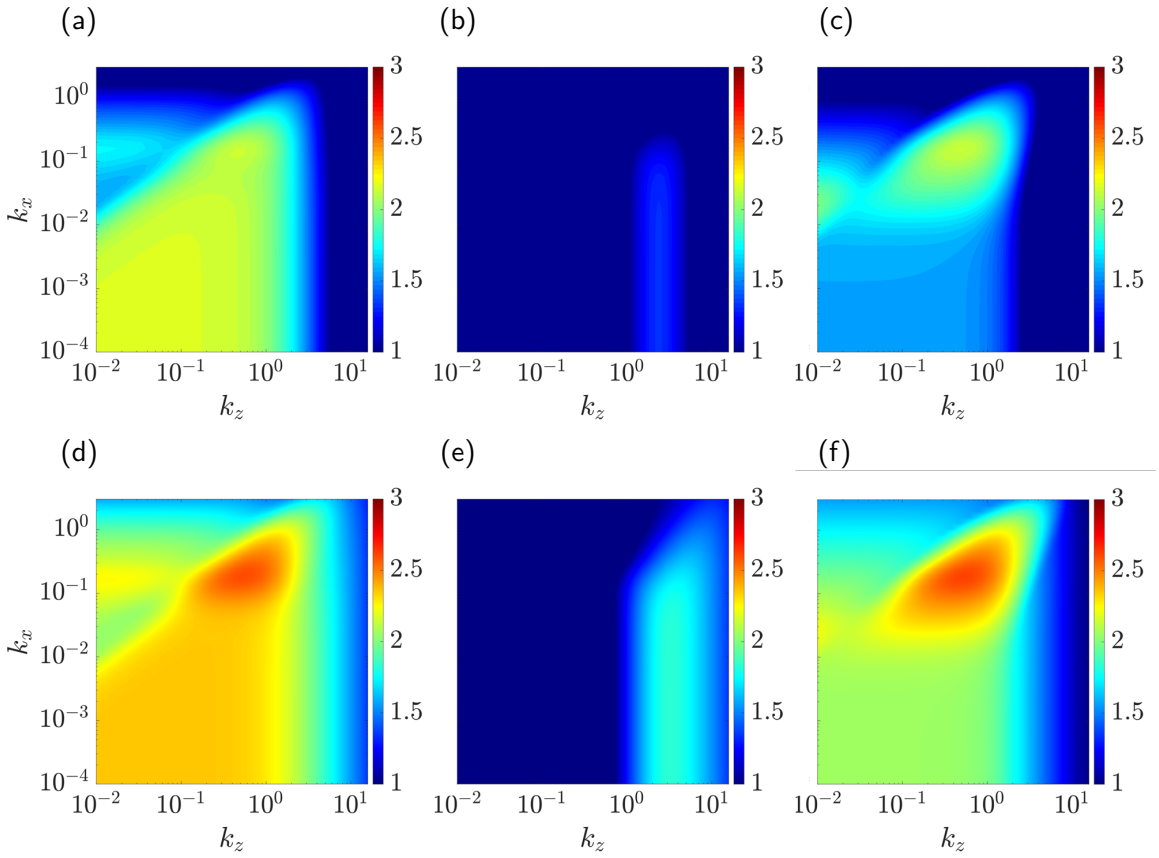

Figure 5.6: (a) $\log_{10}[\|\mathcal{H}_{ux}\|_\infty(k_x,k_z)]$, (b) $\log_{10}[\|\mathcal{H}_{vy}\|_\infty(k_x,k_z)]$, (c) $\log_{10}[\|\mathcal{H}_{wz}\|_\infty(k_x,k_z)]$, (d) $\log_{10}[\|\mathcal{H}_{\nabla ux}\|_\infty(k_x,k_z)]$, (e) $\log_{10}[\|\mathcal{H}_{\nabla vy}\|_\infty(k_x,k_z)]$, and (f) $\log_{10}[\|\mathcal{H}_{\nabla wz}\|_\infty(k_x,k_z)]$ for plane Couette flow at $Re = 358$.

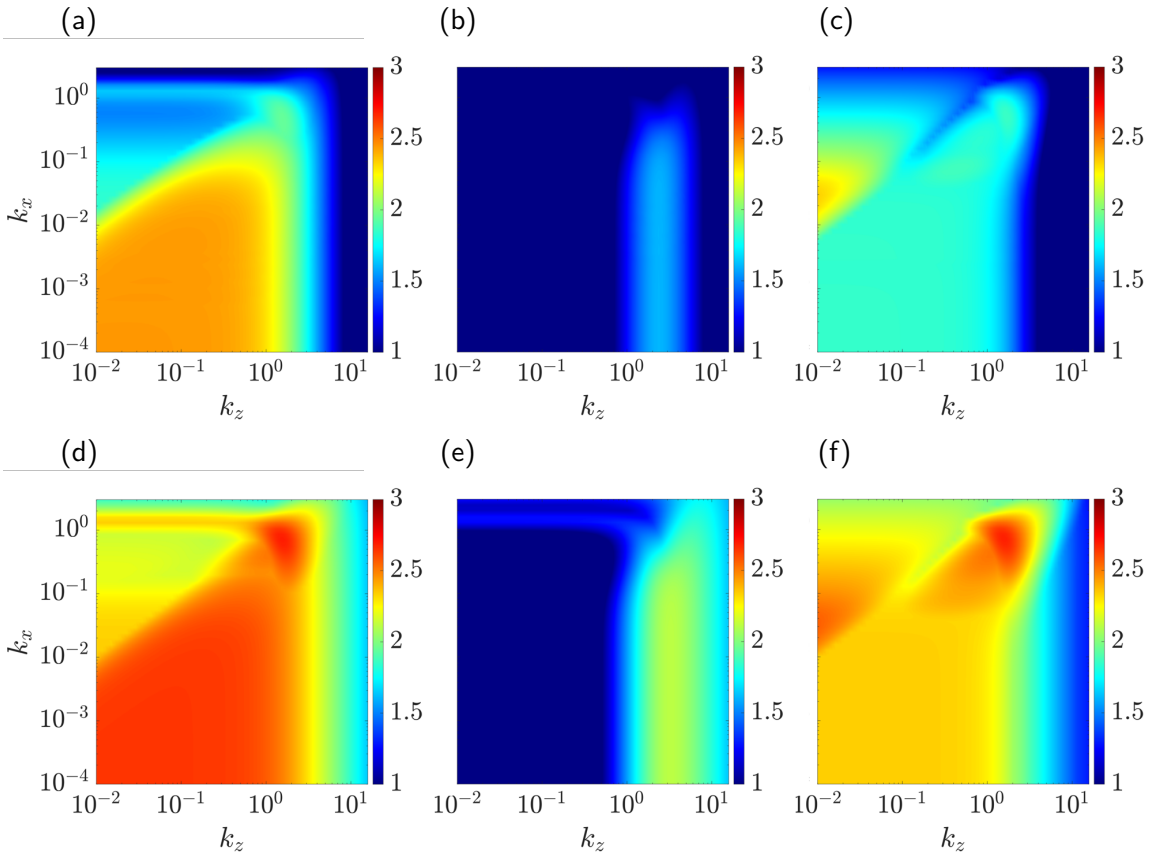

Figure 5.7: (a) $\log_{10}[\|\mathcal{H}_{ux}\|_\infty(k_x,k_z)]$, (b) $\log_{10}[\|\mathcal{H}_{vy}\|_\infty(k_x,k_z)]$, (c) $\log_{10}[\|\mathcal{H}_{wz}\|_\infty(k_x,k_z)]$, (d) $\log_{10}[\|\mathcal{H}_{\nabla ux}\|_\infty(k_x,k_z)]$, (e) $\log_{10}[\|\mathcal{H}_{\nabla vy}\|_\infty(k_x,k_z)]$, and (f) $\log_{10}[\|\mathcal{H}_{\nabla wz}\|_\infty(k_x,k_z)]$ for plane Poiseuille flow at $Re = 690$.

are associated with $\|\mathcal{H}_{ij}\|_\infty$, where the spatio-temporal frequency response operator $\mathcal{H}_{ij}$ from each forcing component ($j = x, y, z$) to each velocity component ($i = u, v, w$) is given by (Jovanović & Bamieh, 2005)

$$\mathcal{H}_{ij} = \widehat{\mathcal{C}}_i \left(\mathrm{i}\omega \mathcal{I}_{2\times 2} - \widehat{\mathcal{A}} \right)^{-1} \widehat{\mathcal{B}}_j \tag{5.18}$$

with

$$\widehat{\mathcal{B}}_x := \widehat{\mathcal{B}} \begin{bmatrix} \mathcal{I} & 0 & 0 \end{bmatrix}^{\mathsf{T}}, \quad \widehat{\mathcal{B}}_y := \widehat{\mathcal{B}} \begin{bmatrix} 0 & \mathcal{I} & 0 \end{bmatrix}^{\mathsf{T}}, \quad \widehat{\mathcal{B}}_z := \widehat{\mathcal{B}} \begin{bmatrix} 0 & 0 & \mathcal{I} \end{bmatrix}^{\mathsf{T}}, \tag{5.19a}$$

$$\widehat{\mathcal{C}}_u := \begin{bmatrix} \mathcal{I} & 0 & 0 \end{bmatrix} \widehat{\mathcal{C}}, \quad \widehat{\mathcal{C}}_v := \begin{bmatrix} 0 & \mathcal{I} & 0 \end{bmatrix} \widehat{\mathcal{C}}, \quad \widehat{\mathcal{C}}_w := \begin{bmatrix} 0 & 0 & \mathcal{I} \end{bmatrix} \widehat{\mathcal{C}}. \tag{5.19b}$$

These quantities were analyzed in (Jovanović, 2004) and (Schmid, 2007). Those results indicate that the most significant amplification is seen when forcing is applied in the cross-stream and the output is the streamwise velocity component; i.e., that associated with respective frequency response operators $\mathcal{H}_{uy}$, $\mathcal{H}_{uz}$ and input–output pathway $f_y \to u$, $f_z \to u$. Similar behavior occurs if we isolate $\mathcal{H}_\nabla$ by examining each input–output response pathways:

$$\mathcal{H}_{\nabla ij} := \widehat{\boldsymbol{\nabla}} \mathcal{H}_{ij}. \tag{5.20}$$

In this prior work, the input forcing (applied either directly to the LNS (top-block in figure 5.1) or through a feedback interconnection) was unstructured in the sense that there was no restriction in terms of the permissible input–output pathways. The behavior of the largest $\|\mathcal{H}_{ij}\|_\infty$ ($\|\mathcal{H}_{\nabla ij}\|_\infty$) response therefore dominates the overall $\|\mathcal{H}\|_\infty$ ($\|\mathcal{H}_\nabla\|_\infty$) response.

The structured input–output analysis framework introduced here instead imposes a correlation between each component of the modeled forcing $f_{x,\xi}$, $f_{y,\xi}$, and $f_{z,\xi}$ and the respective velocity components u, v, and w by constraining the feedback interconnection to retain the componentwise structure of our input–output model of the forcing. This model of the forcing in terms of componentwise input–output relationships from $\boldsymbol{\nabla} u$, $\boldsymbol{\nabla} v$, $\boldsymbol{\nabla} w$ to the respective components $f_{x,\xi} = -\boldsymbol{u}_\xi \cdot \boldsymbol{\nabla} u$, $f_{y,\xi} = -\boldsymbol{u}_\xi \cdot \boldsymbol{\nabla} v$, and $f_{z,\xi} = -\boldsymbol{u}_\xi \cdot \boldsymbol{\nabla} w$ with the gain defined in

terms of $-\boldsymbol{u}_\xi$ constrains the feedback relationships such that each component of the forcing is most strongly influenced by that component of the velocity field and velocity gradient. These constraints on the permissible feedback pathways within our model of the nonlinear interactions limit the influence of the input–output pathways $f_y \to u$ and $f_z \to u$. The structured input–output response $\|\mathcal{H}_\nabla\|_\mu$ is instead associated with input–output pathways $f_x \to u$, $f_y \to v$, and $f_z \to w$ as illustrated in figures 5.6 and 5.7, which respectively plot (a) $\|\mathcal{H}_{ux}\|_\infty$, (b) $\|\mathcal{H}_{vy}\|_\infty$, (c) $\|\mathcal{H}_{wz}\|_\infty$, (d) $\|\mathcal{H}_{\nabla ux}\|_\infty$, (e) $\|\mathcal{H}_{\nabla vy}\|_\infty$, (f) $\|\mathcal{H}_{\nabla wz}\|_\infty$ for the plane Couette and Poiseuille cases respectively discussed in § 5.3.1 and § 5.3.2. Here, we can see that the results of structured input–output analysis $\|\mathcal{H}_\nabla\|_\mu$ for both of these flows in figures 5.4(a) and 5.5(a) resemble the combined effect of this limited set of input–output pathways. Moreover, the quantity $\|\mathcal{H}_\nabla\|_\mu$ at each wavenumber pair (k_x, k_z) is lower bounded by $\|\mathcal{H}_{\nabla ux}\|_\infty$, $\|\mathcal{H}_{\nabla vy}\|_\infty$, and $\|\mathcal{H}_{\nabla wz}\|_\infty$ as described in theorem 5.3, whose proof is provided in Appendix B.1. The relationship in theorem 5.3 is evident when comparing results in figures 5.4(a) and 5.6(d)-(f) for plane Couette flow and comparing results in figures 5.5(a) and 5.7(d)-(f) for plane Poiseuille flow.

Theorem 5.3 *Given wavenumber pair* (k_x, k_z).

$$\|\mathcal{H}_\nabla\|_\mu \geq \mathit{max}[\|\mathcal{H}_{\nabla ux}\|_\infty, \|\mathcal{H}_{\nabla vy}\|_\infty, \|\mathcal{H}_{\nabla wz}\|_\infty]. \tag{5.21}$$

The input–output pathways that dominate the overall unstructured response $\|\mathcal{H}\|_\infty$ ($\|\mathcal{H}_{uy}\|_\infty$ and $\|\mathcal{H}_{uz}\|_\infty$) emphasize amplification of streamwise streaks by cross-stream forcing; i.e., the lift-up mechanism, see e.g., the discussion in Jovanović (2021) for further details. The lift-up mechanism therefore appears to be weakened through the imposition of the componentwise structure of the nonlinearity, which is consistent with results suggesting that nonlinear mechanisms disadvantage the growth of streaks, see e.g, Duguet *et al.* (2013); Brandt (2014). These results suggest that the preservation of the componentwise structure of nonlinearity within the proposed approach enables the method to capture important nonlinear effects, leading to better

agreement with DNS and experimental studies and nonlinear analysis of the perturbations that require less energy to initiate transition, e.g. NLOP.

5.4 Reynolds number dependence

In this section, we aggregate results across a range of (k_x, k_z) scales to study the Reynolds number dependence and the associated scaling law of $\|\mathcal{H}_\nabla\|_\mu$ for both plane Couette flow and plane Poiseuille flows. In particular, we compute

$$\|\mathcal{H}_\nabla\|_\mu^M := \max_{k_z,\,k_x} \|\mathcal{H}_\nabla\|_\mu(k_x, k_z), \tag{5.22}$$

where $\max_{k_z,\,k_x}$ corresponds to the maximum value over the wavenumber pairs (k_x, k_z) in the computational range of $k_x \in [10^{-4}, 10^{0.48}]$ and $k_z \in [10^{-2}, 10^{1.2}]$.

In order to compare our results to the scaling relationships of $\|\mathcal{H}\|_\infty$ previously described in the literature and to isolate the effect of the structure in the feedback loop, we analogously define

$$\|\mathcal{H}\|_\infty^M := \max_{k_z,\,k_x} \|\mathcal{H}\|_\infty(k_x, k_z), \tag{5.23a}$$

$$\|\mathcal{H}_\nabla\|_\infty^M := \max_{k_z,\,k_x} \|\mathcal{H}_\nabla\|_\infty(k_x, k_z). \tag{5.23b}$$

The scaling of quantities related to $\|\mathcal{H}\|_\infty$ and $\|\mathcal{H}\|_\infty^M$ with different input–output pathways, i.e. different $\widehat{\mathcal{B}}$ and $\widehat{\mathcal{C}}$ matrices in equation (5.19), has been widely studied. For example, Trefethen *et al.* (1993, table 1) showed that $\sup_{\omega\in\mathbb{R}} \|(\mathrm{i}\omega\mathcal{I} - \widehat{\mathcal{A}})^{-1}\| \sim Re^2$ for plane Couette flow and plane Poiseuille flow are respectively associated with wavenumber pairs $(k_x, k_z) = (0, 1.18)$ and $(k_x, k_z) = (0, 1.62)$. Here, the operator norm $\|\cdot\|$ is defined such that $\sup_{\omega\in\mathbb{R}} \|\cdot\|$ is equivalent to the definition of $\|\cdot\|_\infty$ employed in (5.16). Kreiss *et al.* (1994) showed that the related quantity maximized over a range of (k_x, k_z), i.e.,

$$\max_{\mathbb{R}e[s]\geq 0} \|(s\mathcal{I} - \widehat{\mathcal{A}})^{-1}\| \sim Re^2$$

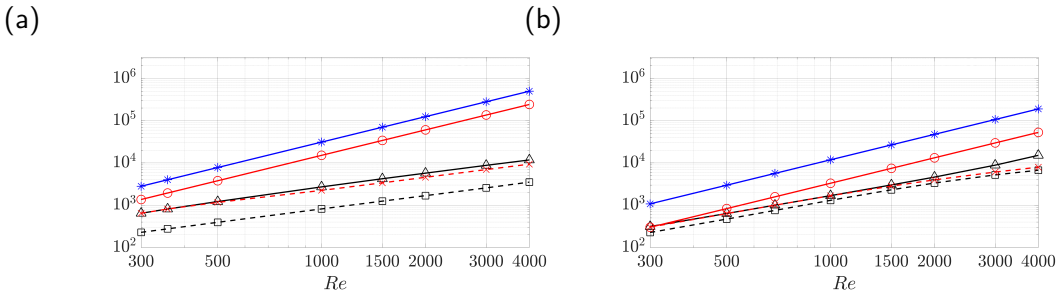

Figure 5.8: The Reynolds number dependence of $\|\mathcal{H}_\nabla\|_\mu^M$ (△—, black); $\|\mathcal{H}\|_\infty^M$ (○—, red); $\|\mathcal{H}_\nabla\|_\infty^M$ (✳—, blue); $\|\mathcal{H}_\nabla\|_\mu(1,1)$ (□– –, black). Here, panel (a) is plane Couette flow with (×– –, red) marks $\|\mathcal{H}_\nabla\|_\mu(0.19, 0.58)$ and panel (b) is plane Poiseuille flow with (×– –, red) marks $\|\mathcal{H}_\nabla\|_\mu(0.69, 1.56)$.

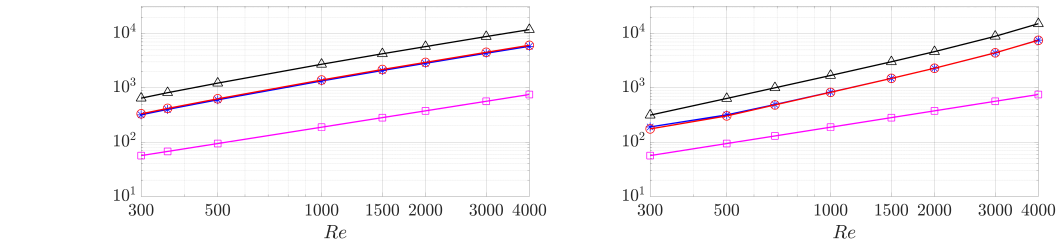

Figure 5.9: The Reynolds number dependence of $\|\mathcal{H}_\nabla\|_\mu^M$ (△—, black); $\|\mathcal{H}_{\nabla ux}\|_\infty^M$ (✳—, blue); $\|\mathcal{H}_{\nabla vy}\|_\infty^M$ (□—, magenta); $\|\mathcal{H}_{\nabla wz}\|_\infty^M$ (○—, red). Here, panel (a) is plane Couette flow and panel (b) is plane Poiseuille flow.

for plane Couette flow, where $\mathbb{R}e[s]$ denotes the real part of Laplace variable s. Jovanović (2004, theorem 11) analytically derived the same $\sim Re^2$ scaling for the special case of $\|\mathcal{H}\|_\infty$ restricted to $k_x = 0$ for both plane Couette and Poiseuille flows.

Figure 5.8 plots the quantities in equations (5.22)-(5.23) as a function of Reynolds number ($Re \in [300, 4000]$) for (a) plane Couette flow and (b) plane Poiseuille flow. The upper bound of $Re = 4000$ was selected to remain below the known linear stability limit for plane Poiseuille flow of $Re \simeq 5772$ (Orszag, 1971). As expected all of these quantities increase with the Reynolds number and the values of $\|\mathcal{H}_\nabla\|_\infty^M$ are larger than those of $\|\mathcal{H}_\nabla\|_\mu^M$. We obtain a Reynolds number scaling of each quantity by fitting the lines in figure 5.8 to $c_0 Re^\eta$, where c_0 is a constant scalar and η is the corresponding scaling exponent. The results show that $\|\mathcal{H}\|_\infty^M$ and $\|\mathcal{H}_\nabla\|_\infty^M$ scale as $\sim Re^2$ in the range $Re \in [300, 4000]$ for both plane Couette and plane Poiseuille flows. This scaling is consistent with the results in Trefethen *et al.* (1993) for the frequency response operator with identity operators for $\widehat{\mathcal{C}}$ and $\widehat{\mathcal{B}}$ as well as the related quantity in Kreiss *et al.*

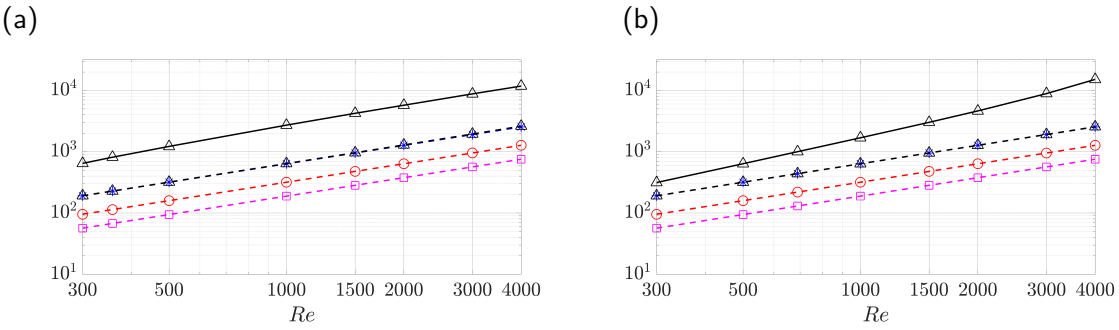

Figure 5.10: The Reynolds number dependence of $\|\mathcal{H}_\nabla\|_\mu^M$ (△—, black); $\|\mathcal{H}_\nabla\|_\mu^{sc}$ (△– –, black); $\|\mathcal{H}_{\nabla ux}\|_\infty^{sc}$ (✳– –, blue); $\|\mathcal{H}_{\nabla vy}\|_\infty^{sc}$ (□– –, magenta); $\|\mathcal{H}_{\nabla wz}\|_\infty^{sc}$ (○– –, red). Here, panel (a) is plane Couette flow and panel (b) is plane Poiseuille flow.

(1994). The fact that the scaling of this quantity for the modified frequency response operator $\mathcal{H}_\nabla$ is the same as that of $\mathcal{H}$ suggests that adding an unstructured uncertainty in the feedback loop to represent the nonlinear interactions does not change the Reynolds number scaling.

The quantity $\|\mathcal{H}_\nabla\|_\mu^M$ in figure 5.8 instead shows scalings of $\sim Re^{1.1}$ over $Re \in [300, 4000]$ for plane Couette flow and $\sim Re^{1.5}$ for plane Poiseuille flow in the range $Re \in [500, 4000]$. The difference between the scaling of $\|\mathcal{H}_\nabla\|_\mu^M$ and the $\sim Re^2$ scaling associated with either $\|\mathcal{H}\|_\infty^M$ or $\|\mathcal{H}_\nabla\|_\infty^M$ again arises through the imposition of the componentwise structure of nonlinearity. As discussed in § 5.3.3, the reduced scaling is related to the smaller amplification in the input–output pathways $f_x \to u$, $f_y \to v$, and $f_z \to w$ and associated $f_x \to \boldsymbol{\nabla} u$, $f_y \to \boldsymbol{\nabla} v$, and $f_z \to \boldsymbol{\nabla} w$. The scaling for these input–output pathways can be evaluated directly through

$$\|\mathcal{H}_{\nabla ij}\|_\infty^M := \max_{k_z, k_x} \|\mathcal{H}_{\nabla ij}\|_\infty(k_x, k_z). \tag{5.24}$$

These quantities are plotted in figure 5.9 alongside $\|\mathcal{H}_\nabla\|_\mu^M$. Performing a similar fit we find that both $\|\mathcal{H}_{\nabla ux}\|_\infty^M$ and $\|\mathcal{H}_{\nabla wz}\|_\infty^M$ respectively scale as $\sim Re^{1.1}$ for plane Couette flow and $\sim Re^{1.5}$ for plane Poiseuille flow, which matches the scaling of $\|\mathcal{H}_\nabla\|_\mu$. On the other hand, $\|\mathcal{H}_{\nabla vy}\|_\infty^M$ is much smaller than these three quantities and scales as $\|\mathcal{H}_{\nabla vy}\|_\infty^M \sim Re$ for both plane Couette and Poiseuille flows.

In order to understand the role of the oblique waves in this scaling, we also plot the quantity $\|\mathcal{H}_\nabla\|_\mu(1, 1)$ corresponding to the wavenumber pair associated with the oblique waves discussed

in § 5.3.1 and § 5.3.2 in figure 5.8. In both flows, these values are lower than and not exactly parallel with $\|\mathcal{H}_\nabla\|_\mu^M$, indicating that they are not associated with the peak amplification of $\|\mathcal{H}_\nabla\|_\mu$ in figure 5.4(a) and 5.5(a). However, they do seem to provide the majority of the contribution to $\|\mathcal{H}_\nabla\|_\mu^M$. This observation is consistent with figures 5.4(a) and 5.5(a), where $(k_x, k_z) = (1, 1)$ is close to but different from the (k_x^M, k_z^M) wavenumber pair that reaches the maximum value of $\|\mathcal{H}_\nabla\|_\mu(k_x, k_z)$ defined as:

$$(k_x^M, k_z^M) := \arg\max_{k_x, k_z} \|\mathcal{H}_\nabla\|_\mu(k_x, k_z). \tag{5.25}$$

These wavenumber pairs are $(k_x^M, k_z^M) = (0.19, 0.58)$ for plane Couette flow at $Re = 358$ and $(k_x^M, k_z^M) = (0.69, 1.56)$ for plane Poiseuille flow at $Re = 690$. We also plot the Reynolds number dependence of $\|\mathcal{H}_\nabla\|_\mu(0.19, 0.58) \sim Re$ for plane Couette flow and $\|\mathcal{H}_\nabla\|_\mu(0.69, 1.56) \sim Re^{1.3}$ for plane Poiseuille flow as (×- - , red) markers in figure 5.8. Here, we observe that they overlap with $\|\mathcal{H}_\nabla\|_\mu^M$ at low Reynolds numbers, but deviate as the Reynolds number increases leading to a reduced Re scaling compared with $\|\mathcal{H}_\nabla\|_\mu^M$. These results show that these oblique flow structures continue to show very high (close to the maximum overall amplification value) throughout the Reynolds number range. However, the wavenumber pair (k_x^M, k_z^M) that reaches the maximum value over $\|\mathcal{H}_\nabla\|_\mu(k_x, k_z)$ depends on the Reynolds number.

The observed importance and analytical tractability of streamwise elongated structures have motivated previous analysis of the streamwise constant $(k_x = 0)$ component of the frequency response operator. In order to compare our analysis to these results we also evaluate this behavior by computing analogous quantities

$$\|\mathcal{H}_\nabla\|_\mu^{sc} := \max_{k_z,\, k_x = 10^{-4}} \|\mathcal{H}_\nabla\|_\mu(k_x, k_z), \tag{5.26a}$$

$$\|\mathcal{H}_{\nabla ij}\|_\infty^{sc} := \max_{k_z,\, k_x = 10^{-4}} \|\mathcal{H}_{\nabla ij}\|_\infty(k_x, k_z), \tag{5.26b}$$

which restricts the streamwise wavenumber to $k_x = 10^{-4}$ to approximate the streamwise constant modes. In figure 5.10, we replot $\|\mathcal{H}_\nabla\|_\mu^M$ alongside $\|\mathcal{H}_\nabla\|_\mu^{sc}$ (△- -, black) , and observe that $\|\mathcal{H}_\nabla\|_\mu^{sc} \sim Re$ for both plane Couette and Poiseuille flows. Figure 5.10 also shows

$\|\mathcal{H}_{\nabla ux}\|_\infty^{sc}$, $\|\mathcal{H}_{\nabla vy}\|_\infty^{sc}$, and $\|\mathcal{H}_{\nabla wz}\|_\infty^{sc}$. Here, we find that $\|\mathcal{H}_{\nabla}\|_\mu^{sc}$ overlaps with $\|\mathcal{H}_{\nabla ux}\|_\infty^{sc}$ and thus shows the same scaling $\sim Re$. These three input–output pathways $\|\mathcal{H}_{\nabla ij}\|_\infty^{sc}$ $(ij = ux,\ vy,\ wz)$ scale as $\sim Re$ for both plane Couette and Poiseuille flows. This behavior is consistent with the results in Jovanović (2004, theorem 11), which showed that $\|\mathcal{H}_{ij}\|_\infty \sim Re$ $(ij = ux,\ vy,\ wz)$ when it is restricted to $k_x = 0$ for both plane Couette and plane Poiseuille flows. The following theorem provides an analogous analytical Re scaling for $\|\mathcal{H}_{\nabla ij}\|_\infty$ at $k_x = 0$, i.e., the streamwise constant component.

Theorem 5.4 *Given streamwise constant ($k_x = 0$) plane Couette flow or plane Poiseuille flow. Each component of $\|\mathcal{H}_{\nabla ij}\|_\infty$ ($i = u, v, w$ and $j = x, y, z$) scales as:*

$$\begin{bmatrix} \|\mathcal{H}_{\nabla ux}\|_\infty & \|\mathcal{H}_{\nabla uy}\|_\infty & \|\mathcal{H}_{\nabla uz}\|_\infty \\ \|\mathcal{H}_{\nabla vx}\|_\infty & \|\mathcal{H}_{\nabla vy}\|_\infty & \|\mathcal{H}_{\nabla vz}\|_\infty \\ \|\mathcal{H}_{\nabla wx}\|_\infty & \|\mathcal{H}_{\nabla wy}\|_\infty & \|\mathcal{H}_{\nabla wz}\|_\infty \end{bmatrix}$$

$$= \begin{bmatrix} Re\, h_{\nabla ux}(k_z) & Re^2\, h_{\nabla uy}(k_z) & Re^2\, h_{\nabla uz}(k_z) \\ 0 & Re\, h_{\nabla vy}(k_z) & Re\, h_{\nabla vz}(k_z) \\ 0 & Re\, h_{\nabla wy}(k_z) & Re\, h_{\nabla wz}(k_z) \end{bmatrix}, \tag{5.27}$$

where functions $h_{\nabla ij}(k_z)$ are independent of the Re.

The proof of theorem 5.4 in Appendix B.2 follows the procedure in (Jovanović, 2004; Jovanović & Bamieh, 2005; Jovanović, 2021), which involves the change of variable $\Omega := \omega Re$. Comparing scaling of this $\|\mathcal{H}_{\nabla ij}\|_\infty$ in theorem 5.4 with that of $\|\mathcal{H}_{ij}\|_\infty$ at $k_x = 0$ in Jovanović (2004, theorem 11) shows that the modification of the operator to provide the output $\widehat{\boldsymbol{\nabla}}\widehat{u}$, $\widehat{\boldsymbol{\nabla}}\widehat{v}$, and $\widehat{\boldsymbol{\nabla}}\widehat{w}$ does not modify the Reynolds number scaling, which is expected since this operation amounts to a Reynolds number independent transformation of the system output.

Combining results in theorems 5.3-5.4, we have the following corollary 5.5 providing an analytical lower bound of $\|\mathcal{H}_{\nabla}\|_\mu$ at $k_x = 0$.

Corollary 5.5 *Given streamwise constant ($k_x = 0$) plane Couette flow or plane Poiseuille flow.*

$$\|\mathcal{H}_{\nabla}\|_\mu(0, k_z) \geq max[Re\, h_{\nabla ux}(k_z), Re\, h_{\nabla vy}(k_z), Re\, h_{\nabla wz}(k_z)], \tag{5.28}$$

where functions $h_{\nabla ij}(k_z)$ *with* $ij = ux, vy, wz$ *are independent of the* Re.

The previous numerical observations of $\|\mathcal{H}_\nabla\|_\mu^{sc} \sim Re$ in figure 5.10 for both plane Couette and plane Poiseuille flows are consistent with corollary 5.5.

The reduced scaling exponent η of the largest structured gain $\|\mathcal{H}_\nabla\|_\mu^M \sim Re^\eta$ observed here compared with $\eta = 2$ for unstructured gain (Trefethen *et al.*, 1993; Kreiss *et al.*, 1994; Jovanović, 2004) further highlights the importance of the componentwise structure of nonlinearity imposed in this framework, which appears to weaken the large amplification associated with the lift-up mechanism.

5.5 Conclusions and future work

This work proposes a *structured* input–output analysis that augments the traditional spatio-temporal frequency response with structured uncertainty. The structure preserves the componentwise input–output structure of the nonlinearity in the NS equations. We then analyze the spatio-temporal response of the resulting feedback interconnection between the LNS quations and the structured forcing in terms of the structured singular value of the associated spatio-temporal frequency response operator.

We apply the structured input–output analysis to transitional plane Couette and plane Poiseuille flows. Comparisons of the results to those of traditional analysis and an unstructured feedback interconnection indicate that the addition of a structured feedback interconnection enables the prediction of a wider range of known dominant flow structures to be identified without the computational burden of nonlinear optimization or extensive simulations. More specifically, the results for transitional plane Couette flow reproduce the findings from direct numerical simulation (DNS) (Reddy *et al.*, 1998) and nonlinear optimal perturbation (NLOP) (Rabin *et al.*, 2012) in showing that oblique waves require less energy to induce transition than the streamwise elongated structures emphasized in traditional input–output analysis. In plane Poiseuille flow the results again predict the oblique wave structure as in DNS (Reddy *et al.*,

1998). They also highlight the importance of spatially localized structures with a streamwise wavelength larger than spanwise similar to NLOP (Farano *et al.*, 2015). The framework also reproduces the oblique turbulent bands (Prigent *et al.*, 2003; Kanazawa, 2018) that have been associated with transitioning flows with very large channel sizes ($\sim O(100)$ times the channel half-height) in both experiments and DNS.

The agreement between the predictions from structured input–output analysis and observation in experiments, DNS, and NLOP indicate that the structured feedback interconnection reproduces important nonlinear effects. Our analysis suggests that restricting the feedback pathways preserves the structure of the nonlinear mechanisms that weaken the streaks developed through the lift-up effect, in which cross-stream forcing amplifies streamwise streaks (Ellingsen & Palm, 1975; Landahl, 1975; Brandt, 2014). Traditional input–output analysis instead predicts the dominance of streamwise elongated structures associated with the lift-up mechanism, see e.g. the discussion in Jovanović (2021). The Reynolds number dependence observed in our studies further supports the notion that imposing a structured feedback interconnection based on certain input–output properties associated with the nonlinearity in the NS equations leads to a weakening of the amplification of streamwise elongated structures.

The results here suggest the promise of this computationally tractable approach and opens up many directions for future work. Further refinement of the structured uncertainty may provide additional physical insight. This extension and the development of the associated computational tools are the subjects of ongoing work. The results here are associated with the maximum amplification over all frequencies but it may be also interesting to isolate each temporal frequency and examine the frequency that maximizes the amplification under this structured feedback interconnection. Another natural direction is an extension to pipe flow, where the subcritical transition is also widely studied; see e.g., (Hof *et al.*, 2003; Peixinho & Mullin, 2007; Eckhardt *et al.*, 2007*b*; Mellibovsky & Meseguer, 2009; Mullin, 2011; Pringle & Kerswell, 2010; Pringle *et al.*, 2012; Barkley, 2016). Adaptions of this approach to the fully developed turbulent regime, where the resolvent framework and input–output analysis have provided important insights is

another direction of ongoing study.

Chapter 6

Identifying spatial scales of flow structures in stratified plane Couette flow

> "It is well known that when the wind near the ground drops at night owing to the cooling of the ground, the wind at a higher level frequently remains unchanged so that the effect of a decrease in density with height is to enable a large velocity gradient to be maintained. This implies that the turbulence is suppressed or at any rate much reduced by the density gradient."
>
> Geoffrey I. Taylor[1], 1931

In chapter 5, we focus on the modeling of the advection nonlinearity by structured uncertainty. This advection nonlinearity is not only appearing in the momentum equations, but also appearing in the more general advection(-diffusion) equation that can be employed to describe the transport phenomena of density, temperature, salinity, and concentration in fluid motions. In this chapter, we demonstrated how the structured input-output analysis in chapter 5 can be extended to study such flow phenomenon, and we focused on stratified plane Couette flow that also observed oblique turbulent bands at certain flow regime similar to plane Couette flow studied in chapter 5.

[1] (Taylor, 1931, p. 499)

6.1 Introduction

Density stratification in wall-bounded shear flows plays an important role in industrial and environmental applications. Stable stratification, in particular, is widely observed in industrial processes; e.g., in cooling equipment (Zonta & Soldati, 2018). Stable density stratification is also prominent in turbulent boundary layers governing atmospheric and oceanic flows (Vallis, 2017; Pedlosky, 2013). Stable stratification in the atmospheric boundary layer arising from strong ground cooling effects is of particular importance at night (Nieuwstadt, 1984; Mahrt, 1999, 2014) and near the polar region (Grachev *et al.*, 2005). At the ocean floor, stable density stratification is also found to influence the boundary layer thickness (Weatherly & Martin, 1978; Lien & Sanford, 2004).

The use of stratified plane Couette flow (PCF) as a canonical model for stratified wall-bounded shear flow dates back to Davey & Reid (1977). One benefit of this model is that its constant background velocity gradient allows the definition of a natural bulk Richardson number (Ri_b) when the density gradient is also constant. This flow provides an excellent venue for studying the effects of stratification in a flow that also has interesting properties. For example, unstratified plane Couette flow provides an appealing model of subcritical Reynolds number transition because it has no linear instability for any Reynolds number (Re) (Romanov, 1973), but transition to turbulence is still observed at Reynolds numbers as low as $Re = 360 \pm 10$ (Tillmark & Alfredsson, 1992).

Stable stratification provides a restoring buoyancy force suppressing vertical motion (Turner, 1979; Davidson, 2013) assuming gravity in the vertical direction. Thus, transition to turbulence in stratified PCF typically occurs at a higher Reynolds number than unstratified PCF; see e.g., (Deusebio *et al.*, 2015; Eaves & Caulfield, 2015; Olvera & Kerswell, 2017; Deguchi, 2017). In the transitional regime, both stratified PCF and unstratified PCF show spatial intermittency; i.e., the coexistence of laminar and turbulent regions. For example, at relatively low-Re low-Ri_b

intermittent regime, the spatial intermittency in stratified PCF is characterized by oblique turbulent bands (Deusebio *et al.*, 2015; Taylor *et al.*, 2016) similar to the unstratified PCF (Prigent *et al.*, 2003; Duguet *et al.*, 2010*b*) with a very large channel size ($\sim O(100)$ times of channel half-height). In the high-Re high-Ri_b intermittent regime, stratified PCF is instead characterized by quasi-horizontal flow structures that separate into vertical turbulent and laminar layers due to the strong buoyancy effect (Deusebio *et al.*, 2015). This spatial intermittency directly imposes challenges to compute an averaged measurement of flow behavior (e.g, mixing efficiency and dissipation rate), and thus understanding the underlying mechanism is important for the parameterization of mixing efficiency and turbulence modeling in stratified flows (Caulfield, 2020, 2021).

Whether a unique critical Richardson number exists number that separates flow into laminar and turbulent regimes remain questionable (Galperin *et al.*, 2007; Andreas, 2002). A threshold value of 0.25 was supported by some field measurements (Kundu & Beardsley, 1991) and experiments (Rohr *et al.*, 1988), although other field measurements reported Richardson number up to 0.99 without a clear critical Richardson number (Lyons *et al.*, 1964). Recent studies show that stably stratified flow was observed to self-organize to maintain the Richardson number near 0.25 in field observations (Smyth & Moum, 2013; Smyth *et al.*, 2019) and simulations (Salehipour *et al.*, 2018). This threshold value 0.25 also appears in the Miles-Howard theorem (Miles, 1961; Howard, 1961), which provides a sufficient condition for linear stability when the Richardson number larger than 0.25 (and a necessary condition for linear instability when the Richardson number less than 0.25) of inviscid, nondiffusive, and stratified parallel shear flow. Insight can be gained into the role of the threshold value around 0.25 in other flows through the study of underlying flow structures in canonical stably stratified PCF.

The Prandtl number (Pr) was shown to play an important role in characterizing underlying flow structures. For example, at a low Prandtl number limit, the averaged density profile coincides with the same $PrRi_b$ (Langham *et al.*, 2020). This observation that $PrRi_b$ jointly determines flow behavior at a low Prandtl number limit was widely observed in stratified shear

flows; see e.g., (Lignieres, 1999; Garaud *et al.*, 2015, 2017; Garaud, 2021). At a high Prandtl number regime, exact coherent structures in stratified PCF (Langham *et al.*, 2020) show that a nearly uniform density region forms near the channel center, and the influence of bulk Richardson number was mitigated. Moreover, a multi-parameter criterion of layer formation (a step-like layer of nearly uniform density separated by thin interface) was developed in stratified PCF suggesting that layering is favored for a large Prandtl number (Taylor & Zhou, 2017). The sharpness of the density interfaces also appears to increase as the Prandtl number increases (Zhou *et al.*, 2017*b*), and increasing the Prandtl number has a larger influence on the mean temperature than mean velocity (Zhou *et al.*, 2017*a*).

The oblique turbulent bands observed in the intermittent regime of stratified plane Couette flow (Deusebio *et al.*, 2015; Taylor *et al.*, 2016) require a very large channel size to fully accommodate them, which poses challenges for both simulations and experiments. The three different flow parameters of interest, Re, Pr, and Ri_b also lead to computational challenges in exploring the full range of flow regimes. To overcome these challenges, we adapt input-output (resolvent) analysis based on spatio-temporal frequency response, which has been widely employed in unstratified wall-bounded shear flows (Farrell & Ioannou, 1993*a*; Bamieh & Dahleh, 2001; Jovanović & Bamieh, 2005; McKeon & Sharma, 2010; McKeon, 2017). This analysis framework has advantages of computational tractability and is not subject to finite channel effects. Related analysis has shown promise in studying stratified flows including inviscid stratified shear flow with constant shear (Farrell & Ioannou, 1993*b*), stratified plane Couette flow (Jose *et al.*, 2015, 2018) and stratified turbulent channel flow (Ahmed *et al.*, 2021).

In this work, we extend the structured input-output analysis originally developed for unstratified plane Couette flow (chapter 5) to stratified PCF. This framework includes the effect of the nonlinearity in momentum and density equations (under Boussinesq approximation) within a computationally tractable linear framework through a feedback interconnection between the linearized dynamics and a structured forcing that is explicitly constrained to preserve the componentwise structure of the nonlinearity in the momentum and density equations. We then

compute the structured singular value (Doyle, 1982; Safonov, 1982) of the spatio-temporal frequency response associated with this feedback interconnection at each streamwise and spanwise length scale. This value can be interpreted as the flow structures that show the largest input-output gain (amplification) given the structured feedback interconnection.

We then apply the structured input–output analysis to characterize highly amplified flow structures in the intermittent regime of stratified plane Couette flow and investigate the behavior of the flow across a range of Re, Pr, and Ri_b. We first examine how Re and Ri_b affect flow structures with $Pr = 0.7$. This approach predicts the characteristic wavelengths and angle of the oblique turbulent bands observed in very large channel size DNS of the low-Re low-Ri_b intermittent regime of stratified plane Couette flow (Deusebio *et al.*, 2015; Taylor *et al.*, 2016). At the high-Re high-Ri_b intermittent regime, this approach also identifies quasi-horizontal flow structures resembling turbulent-laminar layers (Deusebio *et al.*, 2015) that are associated with amplification close to oblique turbulent bands. We then show that increasing bulk Richardson number is suppressing the amplification of streamwise varying flow structures, which is close to that of streamwise independent flow structures above threshold value $Ri_b > 0.25$. This phenomenon is robust against a wide range of Re and valid at $Pr \approx 1$.

We then examine flow behavior at different Ri_b and Pr. At $Pr \ll 1$, a larger bulk Richardson number is required to suppress streamwise varying flow structures to the same level as streamwise independent ones compared with $Pr \approx 1$. The largest amplification also coincides with the same $PrRi_b$ consistent with the observation of overlapped averaged density profile with the same $PrRi_b$ at the $Pr \ll 1$ regime (Langham *et al.*, 2020). At $Pr \gg 1$, we identify another quasi-horizontal flow structure independent of Ri_b. By decomposing input-output pathways into each velocity and density component, we show that these quasi-horizontal flow structures at $Pr \gg 1$ are associated with density. The importance of this density-associated flow structure at $Pr \gg 1$ is further highlighted by the analytical scaling of amplification over Re and Pr under passive scalar and streamwise constant assumptions. The above observations using structured input-output analysis distinguish two types of quasi-horizontal flow structures, one associated

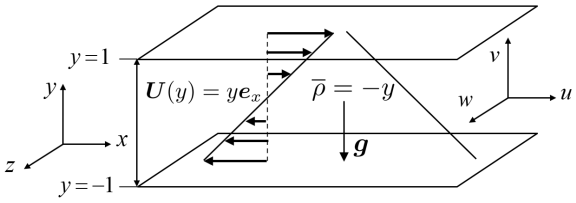

Figure 6.1: Stably stratified plane Couette flow with laminar base flow $\boldsymbol{U}(y) = y\boldsymbol{e}_x$ and background density $\overline{\rho} = -y$. The gravity $\boldsymbol{g} = -g\boldsymbol{e}_y$ is orthogonal to channel walls.

with the high-Re high-Ri_b regime and the other one associated with density that emerges in the high Pr regime.

The remainder of this chapter is organized as follows. Section 6.2 describes the flow configurations of stratified plane Couette flow and then develops the structured input–output analysis for this flow. Section 6.3 analyzes the results obtained from structured input–output analysis focusing on the wall-parallel length scale of flow structures in this flow. We then develop analytical scaling over Re and Pr under passive scalar and streamwise constant assumptions to study the high Pr effect at § 6.4. This chapter is summarized in § 6.5.

6.2 Structured input-output response of stratified flow

6.2.1 Governing Equations

We consider stably stratified plane Couette flow between two infinite parallel plates and employ x, y, and z to respectively denote the streamwise, wall-normal, and spanwise directions. The corresponding velocity components are denoted as u, v, and w. The coordinate frames and configurations for this stratified plane Couette flow are shown in figure 6.1. We express the velocity field as a vector $\boldsymbol{u}_{\text{tot}} = \begin{bmatrix} u_{\text{tot}} & v_{\text{tot}} & w_{\text{tot}} \end{bmatrix}^{\mathsf{T}}$ with $^{\mathsf{T}}$ indicating the transpose. We then decompose the velocity field into the sum of a laminar base flow $U(y) = y$ and fluctuations about the base flow $\boldsymbol{u}$; i.e., $\boldsymbol{u}_{\text{tot}} = U(y)\boldsymbol{e}_x + \boldsymbol{u}$ with $\boldsymbol{e}_x$ denoting the x-direction (streamwise) unit vector. The pressure field is similarly decomposed as $p_{\text{tot}} = P + p$. Here, we also decompose the density ρ_{tot} as the sum of a reference density ρ_r, background density $\overline{\rho} = -y$ and density fluctuation ρ; i.e., $\rho_{\text{tot}} = \rho_r + \overline{\rho} + \rho$. We use ρ_0 to denote half of density difference between the

top and bottom walls, and it is assumed to have a much lower value than a reference density $\rho_0 \ll \rho_r$ so the Boussinesq approximation can be used. The dynamics of the fluctuations $\boldsymbol{u}$, p, and ρ are governed by Navier-Stokes equations under Boussinesq approximation:

$$\partial_t \boldsymbol{u} + U\partial_x \boldsymbol{u} + v\,\frac{dU}{dy}\boldsymbol{e}_x + Ri_b\,\rho\,\boldsymbol{e}_y + \boldsymbol{\nabla} p - \frac{1}{Re}\nabla^2 \boldsymbol{u} = -\boldsymbol{u}\cdot\boldsymbol{\nabla}\boldsymbol{u}, \tag{6.1a}$$

$$\partial_t \rho + U\partial_x \rho + v\frac{d\overline{\rho}}{dy} - \frac{1}{RePr}\nabla^2 \rho = -\boldsymbol{u}\cdot\boldsymbol{\nabla}\rho, \tag{6.1b}$$

$$\boldsymbol{\nabla}\cdot\boldsymbol{u} = 0. \tag{6.1c}$$

Here, the spatial variables are normalized by the channel half-height h, the velocity is normalized by half of the velocity difference between the top and bottom walls U_w, where $\pm U_w$ is the velocity at channel walls. Time and pressure are normalized by h/U_w and $\rho_r U_w^2$, respectively. The background density $\overline{\rho}$ and the density fluctuations ρ are normalized by ρ_0. Under this normalization, the background density profile $\overline{\rho} = -y$ is maintained by static pressure $P = Ri_b y^2/2$. Here, non-dimensional numbers including the Reynolds number Re, the Prandtl number Pr, and the bulk Richardson number Ri_b are defined as:

$$Re := \frac{U_w h}{\nu}, \quad Pr := \frac{\nu}{\kappa}, \quad Ri_b := \frac{g\rho_0 h}{\rho_r U_w^2}, \tag{6.2a-c}$$

where ν is the kinematic viscosity, κ is the molecular diffusivity of the density scalar and g is the magnitude of gravity. The gravity is in the direction orthogonal to the wall $\boldsymbol{g} = -g\boldsymbol{e}_y$ with $\boldsymbol{e}_y$ denoting the y-direction (wall-normal) unit vector. In equation (6.1), $\boldsymbol{\nabla} := \begin{bmatrix}\partial_x & \partial_y & \partial_z\end{bmatrix}^\mathsf{T}$ represents the gradient operator, and $\nabla^2 := \partial_x^2 + \partial_y^2 + \partial_z^2$ represents the Laplacian operator. We impose no-slip boundary conditions at the wall $\boldsymbol{u}(y = \pm 1) = \boldsymbol{0}$ and Dirichlet boundary conditions for density fluctuation $\rho(y = \pm 1) = 0$ that can be maintained by e.g., constant temperatures at the wall with a linear equation of state (with the hotter plate at the top). Finally, we write the nonlinear terms in each momentum equation (6.1a) as:

$$\boldsymbol{f_u} := -\boldsymbol{u}\cdot\boldsymbol{\nabla}\boldsymbol{u} = \begin{bmatrix}-\boldsymbol{u}\cdot\boldsymbol{\nabla}u & -\boldsymbol{u}\cdot\boldsymbol{\nabla}v & -\boldsymbol{u}\cdot\boldsymbol{\nabla}w\end{bmatrix}^\mathsf{T} =: \begin{bmatrix}f_x & f_y & f_z\end{bmatrix}^\mathsf{T}. \tag{6.3}$$

We similarly write the nonlinear term in the density equation (6.1b) as:

$$f_\rho := -\boldsymbol{u}\cdot\boldsymbol{\nabla}\rho, \tag{6.4}$$

which turns (6.1) into a set of linear evolution equations subject to these forcing terms $\boldsymbol{f_u}$ and f_ρ.

We then construct the model of the nonlinearity, where the velocity field $-\boldsymbol{u}$ in (6.3) and (6.4) associated with the forcing components can be viewed as the gain operator of an input-output system in which the velocity and density gradients $\boldsymbol{\nabla}u$, $\boldsymbol{\nabla}v$, $\boldsymbol{\nabla}w$, $\boldsymbol{\nabla}\rho$ act as the respective inputs and the forcing components f_x, f_y, f_z, and f_ρ act as the respective output. This input-output model of the nonlinear components in momentum equation (6.3) is given by

$$\boldsymbol{f}_{\boldsymbol{u},\xi} := -\boldsymbol{u}_\xi\cdot\boldsymbol{\nabla}\boldsymbol{u} = \begin{bmatrix} -\boldsymbol{u}_\xi\cdot\boldsymbol{\nabla}u & -\boldsymbol{u}_\xi\cdot\boldsymbol{\nabla}v & -\boldsymbol{u}_\xi\cdot\boldsymbol{\nabla}w \end{bmatrix}^{\mathsf{T}} =: \begin{bmatrix} f_{x,\xi} & f_{y,\xi} & f_{z,\xi} \end{bmatrix}^{\mathsf{T}}. \tag{6.5}$$

Similarly, the input-output model of the nonlinearity in density equation (6.4) is given by:

$$f_{\rho,\xi} := -\boldsymbol{u}_\xi\cdot\boldsymbol{\nabla}\rho. \tag{6.6}$$

Here, $-\boldsymbol{u}_\xi$ in equations (6.5)-(6.6) maps the corresponding velocity and density gradient into each component of the modeled forcing driving linearized dynamics. The next subsection describes how we construct the input-output map enables us to analyze the perturbations that are prominent in the intermittent regime using the structured singular value formalism (Packard & Doyle, 1993; Zhou *et al.*, 1996).

6.2.2 Structured input-output response

We now define the spatio-temporal frequency response $\mathcal{H}^S_\nabla(y;k_x,k_z,\omega)$ of stratified PCF that will form the basis of the structured input-output response. We use the superscript ^{S} to distinguish this operator from its counterpart for unstratified wall-bounded flow (chapter 5). We employ the standard transformation to express the velocity field dynamics in (6.1) in terms

of the formulation of v and wall-normal vorticity $\omega_y := \partial_z u - \partial_x w$ (Schmid & Henningson, 2012). This transformation enforces the constraint in (6.1c) and eliminates the pressure. We then exploit shift-invariance in the (x, z) spatial directions and assume shift-invariance in time t, which allows us to perform the following triple Fourier transform: $\widehat{\psi}(y; k_x, k_z, \omega) := \int_{-\infty}^{\infty}\int_{-\infty}^{\infty}\int_{-\infty}^{\infty} \psi(x, y, z, t) e^{-\mathrm{i}(k_x x + k_z z + \omega t)}\, dx\, dz\, dt$, where $\mathrm{i} = \sqrt{-1}$ is the imaginary unit, ω is the temporal frequency, and $k_x = 2\pi/\lambda_x$ and $k_z = 2\pi/\lambda_z$ are the respective x and z wavenumbers.

The resulting equations describing the transformed linearized equations subject to the forcing $\begin{bmatrix} \boldsymbol{f}_{\boldsymbol{u},\xi} \\ f_{\rho,\xi} \end{bmatrix}$ are given by

$$\mathrm{i}\omega \begin{bmatrix} \widehat{v} \\ \widehat{\omega}_y \\ \widehat{\rho} \end{bmatrix} = \widehat{\mathcal{A}}^S \begin{bmatrix} \widehat{v} \\ \widehat{\omega}_y \\ \widehat{\rho} \end{bmatrix} + \widehat{\mathcal{B}}^S \begin{bmatrix} \widehat{f}_{x,\xi} \\ \widehat{f}_{y,\xi} \\ \widehat{f}_{z,\xi} \\ \widehat{f}_{\rho,\xi} \end{bmatrix}, \tag{6.7a}$$

$$\begin{bmatrix} \widehat{u} \\ \widehat{v} \\ \widehat{w} \\ \widehat{\rho} \end{bmatrix} = \widehat{\mathcal{C}}^S \begin{bmatrix} \widehat{v} \\ \widehat{\omega}_y \\ \widehat{\rho} \end{bmatrix}. \tag{6.7b}$$

The operators in equation (6.7) are defined as:

$$\widehat{\mathcal{A}}^S(k_x, k_z) := \widehat{\mathcal{M}}^{-1} \begin{bmatrix} -\mathrm{i}k_x U \widehat{\nabla}^2 + \mathrm{i}k_x U'' + \frac{\widehat{\nabla}^4}{Re} & 0 & Ri_b(k_x^2 + k_z^2) \\ -\mathrm{i}k_z U' & -\mathrm{i}k_x U + \frac{\widehat{\nabla}^2}{Re} & 0 \\ -\overline{\rho}' & 0 & -\mathrm{i}k_x U + \frac{\widehat{\nabla}^2}{RePr} \end{bmatrix}, \tag{6.8a}$$

$$\widehat{\mathcal{B}}^S(k_x, k_z) := \widehat{\mathcal{M}}^{-1} \begin{bmatrix} -\mathrm{i}k_x\partial_y & -(k_x^2 + k_z^2) & -\mathrm{i}k_z\partial_y & 0 \\ \mathrm{i}k_z & 0 & -\mathrm{i}k_x & 0 \\ 0 & 0 & 0 & \mathcal{I} \end{bmatrix}, \quad \widehat{\mathcal{M}} := \begin{bmatrix} \widehat{\nabla}^2 & 0 & 0 \\ 0 & \mathcal{I} & 0 \\ 0 & 0 & \mathcal{I} \end{bmatrix}, \tag{6.8b}$$

$$\widehat{\mathcal{C}}^S(k_x, k_z) := \frac{1}{k_x^2 + k_z^2} \begin{bmatrix} \mathrm{i}k_x\partial_y & -\mathrm{i}k_z & 0 \\ k_x^2 + k_z^2 & 0 & 0 \\ \mathrm{i}k_z\partial_y & \mathrm{i}k_x & 0 \\ 0 & 0 & k_x^2 + k_z^2 \end{bmatrix}, \tag{6.8c}$$

where $U' := dU(y)/dy$, $U'' := d^2U(y)/dy^2$, $\overline{\rho}' := d\overline{\rho}(y)/dy$, $\widehat{\nabla}^2 := \partial_{yy} - k_x^2 - k_z^2$, $\widehat{\nabla}^4 := \partial_y^{(4)} - 2(k_x^2 + k_z^2)\partial_{yy} + (k_x^2 + k_z^2)^2$, and $\mathcal{I}$ is the identity operator. The equation associated with $\widehat{\mathcal{A}}^S$ operator in (6.8a) can be obtained by modifying the Taylor-Goldstein equation (Taylor,

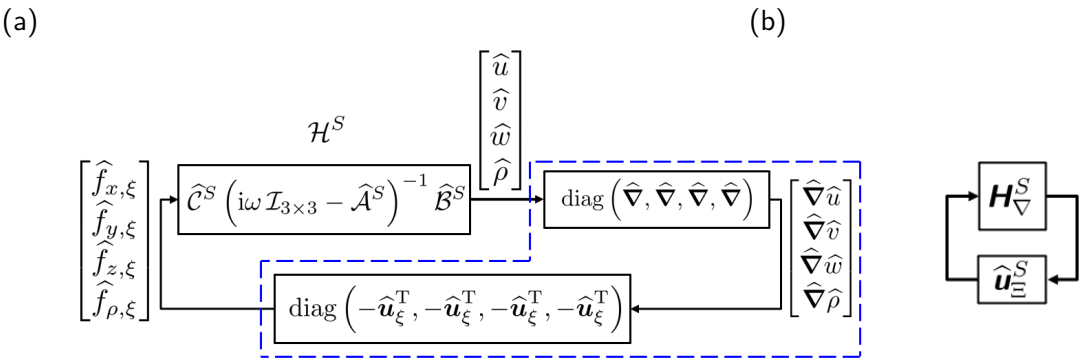

Figure 6.2: Illustration of structured input–output analysis of stratified plane Couette flow: (a) a componentwise description, where blocks inside of (– –, blue) represent the modeled forcing in equation (6.10); (b) a high-level description after discretization.

1931; Goldstein, 1931; Smyth & Carpenter, 2019) by adding viscosity, density diffusivity, and the coupling with wall-normal vorticity $\widehat{\omega}_y$. The boundary conditions associated with (6.7) are $\widehat{v}(y=\pm1)=\frac{\partial\widehat{v}}{\partial y}(y=\pm1)=\widehat{\omega}_y(y=\pm1)=\widehat{\rho}(y=\pm1)=0$.

The spatio-temporal frequency response $\mathcal{H}^S$ of the system in (6.7), which maps the input forcing $\begin{bmatrix}\widehat{\boldsymbol{f}}_{\boldsymbol{u},\xi}(y;k_x,k_z,\omega)\\ \widehat{f}_{\rho,\xi}(y;k_x,k_z,\omega)\end{bmatrix}$ to the velocity and density fields $\begin{bmatrix}\widehat{\boldsymbol{u}}(y;k_x,k_z,\omega)\\ \widehat{\rho}(y;k_x,k_z,\omega)\end{bmatrix}$ at the same spatial-temporal wavenumber-frequency triplet; i.e., $\begin{bmatrix}\widehat{\boldsymbol{u}}(y;k_x,k_z,\omega)\\ \widehat{\rho}(y;k_x,k_z,\omega)\end{bmatrix}=\mathcal{H}^S(y;k_x,k_z,\omega)\begin{bmatrix}\widehat{\boldsymbol{f}}_{\boldsymbol{u},\xi}(y;k_x,k_z,\omega)\\ \widehat{f}_{\rho,\xi}(y;k_x,k_z,\omega)\end{bmatrix}$ is given by

$$\mathcal{H}^S(y;k_x,k_z,\omega):=\widehat{\mathcal{C}}^S\left(\mathrm{i}\omega\,\mathcal{I}_{3\times3}-\widehat{\mathcal{A}}^S\right)^{-1}\widehat{\mathcal{B}}^S. \tag{6.9}$$

Here $\mathcal{I}_{3\times3}:=\mathrm{diag}(\mathcal{I},\mathcal{I},\mathcal{I})$, where $\mathrm{diag}(\cdot)$ indicates a block diagonal operation.

The linear form of (6.5)-(6.6) allows us to perform the same spatio-temporal Fourier transform on the model of the nonlinearity, which can be decomposed as

$$\begin{bmatrix}\widehat{f}_{x,\xi}\\ \widehat{f}_{y,\xi}\\ \widehat{f}_{z,\xi}\\ \widehat{f}_{\rho,\xi}\end{bmatrix}=\mathrm{diag}\left(-\widehat{\boldsymbol{u}}_\xi^{\mathsf{T}},-\widehat{\boldsymbol{u}}_\xi^{\mathsf{T}},-\widehat{\boldsymbol{u}}_\xi^{\mathsf{T}},-\widehat{\boldsymbol{u}}_\xi^{\mathsf{T}}\right)\mathrm{diag}\left(\widehat{\boldsymbol{\nabla}},\widehat{\boldsymbol{\nabla}},\widehat{\boldsymbol{\nabla}},\widehat{\boldsymbol{\nabla}}\right)\begin{bmatrix}\widehat{u}\\ \widehat{v}\\ \widehat{w}\\ \widehat{\rho}\end{bmatrix}. \tag{6.10}$$

A block diagram illustrating this is shown inside the blue dashed line (– –) in figure 6.2(a), where the velocity and density fields arising from the spatio-temporal frequency response $\mathcal{H}^S$ is the input and the forcing is the output.

In order to isolate the gain $-\boldsymbol{u}_\xi$ (which is associated with the response that we seek to

find), we combine the linear gradient operator with the spatio-temporal frequency response. The resulting modified frequency response operator is denoted as

$$\mathcal{H}^S_\nabla(y;k_x,k_z,\omega) := \text{diag}\left(\widehat{\boldsymbol{\nabla}},\widehat{\boldsymbol{\nabla}},\widehat{\boldsymbol{\nabla}},\widehat{\boldsymbol{\nabla}}\right)\mathcal{H}^S(y;k_x,k_z,\omega). \tag{6.11}$$

The resulting system model can be redrawn as a feedback interconnection between this linear operator and the structured uncertainty

$$\widehat{\boldsymbol{u}}^S_\Xi := \text{diag}\left(-\widehat{\boldsymbol{u}}^\mathsf{T}_\xi,-\widehat{\boldsymbol{u}}^\mathsf{T}_\xi,-\widehat{\boldsymbol{u}}^\mathsf{T}_\xi,-\widehat{\boldsymbol{u}}^\mathsf{T}_\xi\right). \tag{6.12}$$

The structured uncertainty $\widehat{\boldsymbol{u}}^S_\Xi$ in (6.12) results in a forcing model that retains the componentwise structure of the nonlinearity. Figure 6.2(b) describes the resulting feedback interconnection between the modified spatio-temporal frequency response and the structured uncertainty, where $\boldsymbol{H}^S_\nabla$ and $\widehat{\boldsymbol{u}}^S_\Xi$ respectively represent the spatial discretizations (numerical approximations) of $\mathcal{H}^S_\nabla$ in (6.11) and $\widehat{\boldsymbol{u}}^S_\Xi$ in (6.12).

We are interested in characterizing the horizontal length scale of the most amplified flow structures under structured forcing, while maintaining a stable feedback interconnection. This amplification under structured forcing can be quantified by the structured singular value of the modified frequency response operator $\mathcal{H}^S_\nabla$; see e.g., Packard & Doyle (1993, definition 3.1); Zhou *et al.* (1996, definition 11.1), which is defined as follows.

Definition 6.1 *Given wavenumber and frequency pair (k_x,k_z,ω), the structured singular value $\mu_{\widehat{\boldsymbol{U}}^S_\Xi}\left[\boldsymbol{H}^S_\nabla(k_x,k_z,\omega)\right]$ is defined:*

$$\mu_{\widehat{\boldsymbol{U}}^S_\Xi}\left[\boldsymbol{H}^S_\nabla(k_x,k_z,\omega)\right] := \frac{1}{\mathit{min}\{\bar{\sigma}[\widehat{\boldsymbol{u}}^S_\Xi] \,:\, \widehat{\boldsymbol{u}}^S_\Xi \in \widehat{\boldsymbol{U}}^S_\Xi,\ \mathit{det}[\boldsymbol{I}-\boldsymbol{H}^S_\nabla(k_x,k_z,\omega)\widehat{\boldsymbol{u}}^S_\Xi]=0\}}, \tag{6.13}$$

unless no $\widehat{\boldsymbol{u}}^S_\Xi \in \widehat{\boldsymbol{U}}^S_\Xi$ makes $\boldsymbol{I}-\boldsymbol{H}^S_\nabla\widehat{\boldsymbol{u}}^S_\Xi$ singular, in which case $\mu_{\widehat{\boldsymbol{U}}^S_\Xi}[\boldsymbol{H}^S_\nabla]:=0$.

Here, $\bar{\sigma}[\cdot]$ is the largest singular value, $\mathit{det}[\cdot]$ is the determinant of the argument, and $\boldsymbol{I}$ is the identity matrix. The subscript of μ in (6.13) is a set $\widehat{\boldsymbol{U}}^S_\Xi$ containing all uncertainties having

the same block-diagonal structure as $\widehat{\boldsymbol{u}}_{\Xi}^{S}$*; i.e.,*

$$\widehat{\boldsymbol{U}}_{\Xi}^{S} := \left\{ diag\left(-\widehat{\boldsymbol{u}}_{\xi}^{T}, -\widehat{\boldsymbol{u}}_{\xi}^{T}, -\widehat{\boldsymbol{u}}_{\xi}^{T}, -\widehat{\boldsymbol{u}}_{\xi}^{T}\right) : -\widehat{\boldsymbol{u}}_{\xi}^{T} \in \mathbb{C}^{N_y \times 3N_y} \right\}, \tag{6.14}$$

where N_y *denotes the number of grid points in* y*.*

We then aggregate results of structured singular value across temporal frequencies in the manner described in (chapter 5):

$$\|\mathcal{H}_{\nabla}^{S}\|_{\mu}(k_x, k_z) := \sup_{\omega \in \mathbb{R}} \mu_{\widehat{\boldsymbol{U}}_{\Xi}^{S}}\left[\boldsymbol{H}_{\nabla}^{S}(k_x, k_z, \omega)\right]. \tag{6.15}$$

Here, sup represents a supremum (least upper bound) operation, and we abuse the notation by writing $\|\cdot\|_{\mu}$ (Packard & Doyle, 1993), which is not necessarily a norm. This value $\|\mathcal{H}_{\nabla}^{S}\|_{\mu}(k_x, k_z)$ directly quantifies the streamwise and spanwise length scales of flow structures that are prominent in the intermittent regime. A larger value indicates that the corresponding flow structures (associated with k_x and k_z pair) have a larger amplification under structured feedback forcing in figure 6.2(b), which suggests their prevalence in the intermittent regime.

6.2.3 Numerical Method

We employ the Chebyshev differential matrix (Weideman & Reddy, 2000; Trefethen, 2000) to discretize the operators in equation (6.8). Our code is validated through comparison with unstratified plane Couette and Poiseuille flow results in Jovanović (2004); Jovanović & Bamieh (2005); Schmid (2007). The implementation of stratification is validated by reproducing the maximum growth rate of linear normal mode in a layered stratified plane Couette flow determined by Eaves & Caulfield (2017, figures 3 and 6(a)) as well as linear instability results for the unstable stratification configuration in Olvera & Kerswell (2017, figure 1 and Appendix B). We use $N_y = 60$ collocation points not including the boundary points over the wall-normal extent and 48 and 36 logarithmically spaced streamwise and spanwise wavenumbers in the respective spectral range $k_x \in [10^{-4}, 10^{0.48}]$ and $k_z \in [10^{-2}, 10^{1.2}]$, unless otherwise mentioned. We also compute results with 1.5 times the number of collocation points in the wall-normal direction

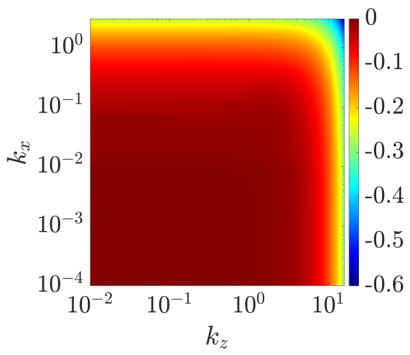

Figure 6.3: $R(\widehat{\mathcal{A}}^S)(k_x, k_z)$ for stratified plane Couette flow at $Re = 865$, $Ri_b = 0.02$, and $Pr = 0.7$.

and verify that results do not change indicating grid convergence. The quantity $\|\mathcal{H}_\nabla^S\|_\mu$ in equation (6.15) for each wavenumber pair (k_x, k_z) is computed using the `mussv` command in the Robust Control Toolbox (Balas *et al.*, 2005) of MATLAB. The arguments of `mussv` employed here include the state-space model of $\boldsymbol{H}_\nabla^S$ that sample the frequency domain adaptively. The `BlockStructure` argument comprises four full $N_y \times 3N_y$ complex matrices, and we use the '`Uf`' algorithm option.

6.3 Structured spatio-temporal frequency response of stratified flow

In this section, we use the structured input-output analysis based on the value $\|\mathcal{H}_\nabla^S\|_\mu$ in equation (6.15) to characterize the flow structures that are most amplified in stably stratified plane Couette flow. We focus on horizontal length scales of flow structures prevalent in the intermittent regimes. More specifically, we analyze stratified plane Couette flow at the low-Re low-Ri_b and the high-Re high-Ri_b regimes at § 6.3.1. Our results suggest that the $Ri_b > 0.25$ threshold suggested by the Miles-Howard theorem (Miles, 1961; Howard, 1961) is associated with suppressing amplification of streamwise varying flow structures in stratified PCF at $Pr \approx 1$ in § 6.3.2. However, this threshold is not associated with a similar change in the flow characteristics in the low or high Prandtl number limits ($Pr \ll 1$ or $Pr \gg 1$) in § 6.3.3.

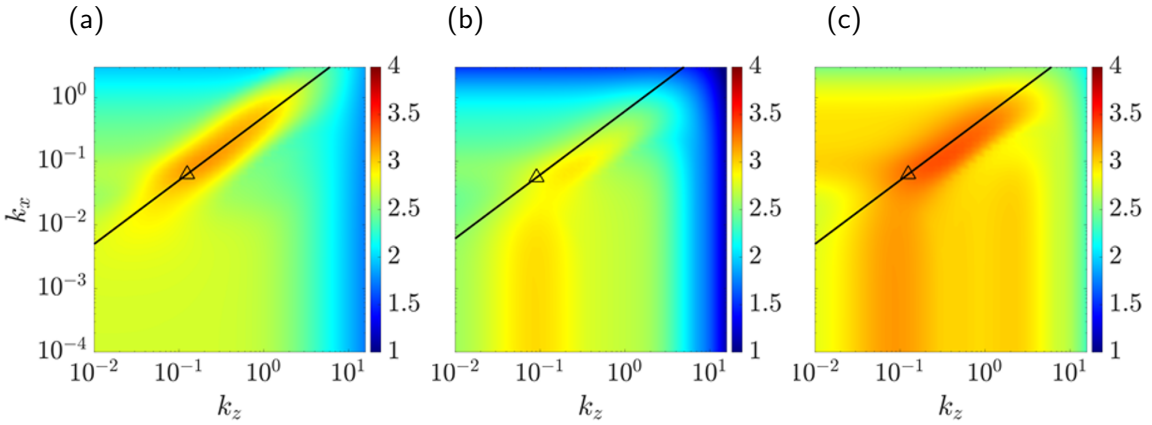

Figure 6.4: (a)$\log_{10}[\|\mathcal{H}^S_\nabla\|_\mu(k_x,k_z)]$, (b)$\log_{10}[\|\mathcal{H}^S\|_\infty(k_x,k_z)]$, and (c)$\log_{10}[\|\mathcal{H}^S_\nabla\|_\infty(k_x,k_z)]$ for stratified plane Couette flow at $Re = 865$, $Ri_b = 0.02$, and $Pr = 0.7$. Here symbols ($\triangle$) are characteristic wavelengths ($\lambda_x = 32\pi$, $\lambda_z = 16\pi$) of oblique turbulent band observed in DNS at the same flow regime (Deusebio *et al.*, 2015; Taylor *et al.*, 2016). The lines (—) are $\lambda_z = \lambda_x \tan(27^\circ)$ representing a 27° angle of the oblique turbulent bands.

6.3.1 Low-Re low-Ri_b versus high-Re high-Ri_b intermittency

In this subsection, we analyze flow structures that are prominent in the low-Re low-Ri_b and the high-Re high-Ri_b intermittent regimes, where flow structures show different characteristics in these regimes (Deusebio *et al.*, 2015). Here, we keep the Prandtl number $Pr = 0.7$ corresponding to heat in the air the same as studied by Deusebio *et al.* (2015). We start at the flow regime at $Re = 865$, $Pr = 0.7$, and $Ri_b = 0.02$, where oblique turbulent bands were observed (Deusebio *et al.*, 2015; Taylor *et al.*, 2016).

We compare our results with the growth rate of the dynamics in equation (6.7) computed as:

$$R[\widehat{\mathcal{A}}^S(k_x,k_z)] := \max\left\{\mathbb{R}e\left[\text{eig}\left(\widehat{\boldsymbol{A}}^S(k_x,k_z)\right)\right]\right\}, \tag{6.16}$$

where $\text{eig}(\cdot)$ is the eigenvalue of the argument, $\mathbb{R}e[\cdot]$ represents the real part, $\max\{\cdot\}$ is the maximum value of the argument, and $\widehat{\boldsymbol{A}}^S$ is the discretization of operator $\widehat{\mathcal{A}}^S$. In order to isolate the relative effect of the feedback interconnection from the imposed structure, we compare the results to

$$\|\mathcal{H}^S\|_\infty(k_x,k_z) := \sup_{\omega\in\mathbb{R}} \bar{\sigma}\left[\boldsymbol{H}^S(k_x,k_z,\omega)\right], \tag{6.17}$$

where $\boldsymbol{H}^S$ is the discretization of spatio-temporal frequency response operator $\mathcal{H}^S$ in (6.9), i.e. the spatio-temporal frequency operator governing linear dynamics with no feedback interconnection. The $\|\mathcal{H}\|_\infty$ for unstratified plane Couette and plane Poiseuille flows was previously analyzed in Jovanović (2004); Schmid (2007); Illingworth (2020). The quantity in (6.17) describes the maximum singular value of the frequency response operator $\mathcal{H}^S$ which represents the maximal gain of $\mathcal{H}^S$ over all temporal frequencies; i.e., the worst-case amplification over harmonic inputs. To isolate the effect of the structure imposed on the nonlinearity from the effect of imposing the closed-loop feedback interconnection, we also compute

$$\|\mathcal{H}^S_\nabla\|_\infty(k_x,k_z) := \sup_{\omega\in\mathbb{R}} \bar{\sigma}\left[\boldsymbol{H}^S_\nabla(k_x,k_z,\omega)\right]. \tag{6.18}$$

This quantity is the unstructured counterpart of $\|\mathcal{H}^S_\nabla\|_\mu$, which is obtained by replacing the uncertainty set $\widehat{\boldsymbol{U}}^S_\Xi$ with the set of full complex matrices $\mathbb{C}^{4N_y\times 12N_y}$.

Figure 6.3 shows the growth rate $R(\widehat{\mathcal{A}}^S)(k_x,k_z)$ in (6.16). Here, we observe that the modal growth rate $R(\widehat{\mathcal{A}}^S)(k_x,k_z)$ cannot distinguish a preferential structure size over a wide range of wavenumbers $k_x \lesssim 1$ and $k_z \lesssim 10$ and there is no identified instability consistent with Davey & Reid (1977).

On the other hand, figure 6.4 shows input-output based analyses in panels (a) $\|\mathcal{H}^S_\nabla\|_\mu$ alongside (b) $\|\mathcal{H}^S\|_\infty$, and (c) $\|\mathcal{H}^S_\nabla\|_\infty$, which reveals distinct wavenumber pairs as showing the largest amplification. In all cases, there is streamwise varying flow structures that shows a large response, although these structures are most prominent in panels (a) and (c) which respectively include the structured and unstructured feedback pathways associated with the nonlinear flow interaction model in (6.15) and (6.18). We indicate the characteristic wavelength pair $\lambda_x = 32\pi$, $\lambda_z = 16\pi$ corresponding to the oblique turbulent bands observed in DNS under the same flow regime (Deusebio *et al.*, 2015; Taylor *et al.*, 2016, figure 2(b)) in these panels using the symbol ($\triangle$, black). These structures are observed to have a characteristic inclination angle (measured from the streamwise direction in $x-z$ plane) of $\theta := \tan^{-1}(\lambda_z/\lambda_x) \approx 27^\circ$, which is indicated in all panels by the black solid line (—) that plots $\lambda_z = \lambda_x \tan(27^\circ)$. While there is some

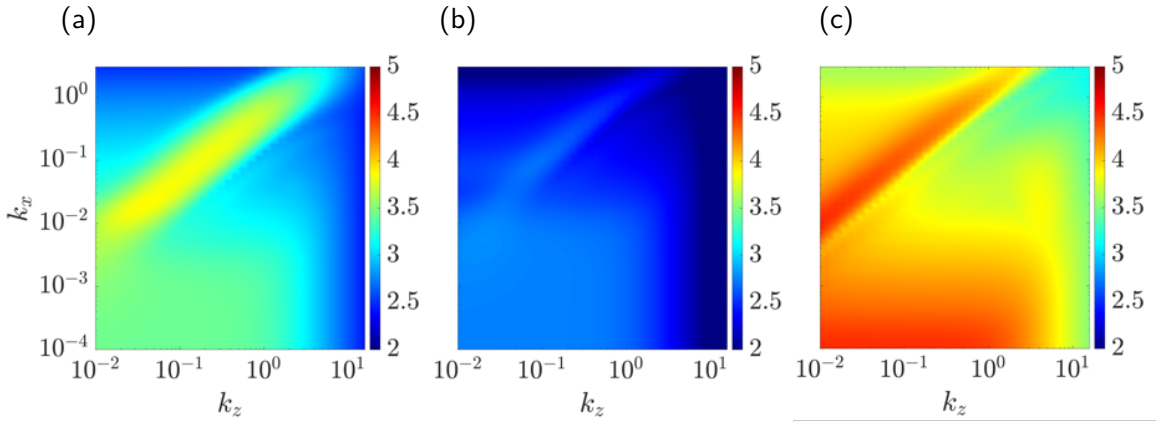

Figure 6.5: $\log_{10}[\|\mathcal{H}_{\nabla}^{S}\|_{\mu}(k_x, k_z)]$ at $Pr = 0.7$ and: (a) $Re = 4250$ and $Ri_b = 0.02$; (b) $Re = 865$ and $Ri_b = 0.2541$, and (c) $Re = 52630$ and $Ri_b = 0.15$.

footprint of these structures and this angle in all three panels, the characteristic wavelengths and angle of the oblique turbulent bands reported in DNS (Deusebio *et al.*, 2015; Taylor *et al.*, 2016) correspond to streamwise and spanwise wavenumbers associated with the peak value of $\|\mathcal{H}_{\nabla}^{S}\|_{\mu}$ in panel (a). In fact, the line representing the angle of oblique turbulent bands is quite consistent with the shape of the peak region. The traditional input-output analysis $\|\mathcal{H}^{S}\|_{\infty}$ in panel (b) leads to a noticeable improvement compared with growth rate analysis $R(\widehat{\mathcal{A}}^{S})$ in figure 6.3 and is also able to identify the preferred wavenumber pair in this intermittent regime. However, this analysis suggests larger amplification of the streamwise elongated modes. Moreover, the inclusion of an unstructured feedback loop for $\|\mathcal{H}_{\nabla}^{S}\|_{\infty}$ in figure panel (c) further leads to further improvements and correctly orders the relative of amplification between the oblique turbulent bands and streamwise elongated structures ($k_x \approx 0$). The imposition of the componentwise structure from the nonlinear terms in (6.3) further improves the prediction of the oblique turbulent bands.

This suggests that structured input–output analysis captures both the wavelengths and angle of the oblique turbulent bands in the intermittent regime of stratified plane Couette flow. This analysis suggests that these oblique turbulent bands arise in the intermittent regime of stratified plane Couette flow due to their large amplification (sensitivity to disturbances).

We move to the high-Re high-Ri_b regime with a fixed Prandtl number $Pr = 0.7$, which

was shown to have a qualitative difference of flow structures in the low-Re low-Ri_b regime (Deusebio *et al.*, 2015). We first isolate the effect of increasing either the Reynolds number or bulk Richardson number. Figure 6.5(a) presents $\|\mathcal{H}^S_\nabla\|_\mu$ at $Ri_b = 0.02$ and $Re = 4250$, which as expected has a much higher magnitude than $\|\mathcal{H}^S_\nabla\|_\mu$ in figure 6.4(a) at $Ri_b = 0.02$ and $Re = 865$. We can see that the wavenumber pair of the peak region is extending towards smaller values (larger wavelength) than those associated with the oblique turbulent bands that were in the peak region in figure 6.4(a). Figure 6.5(b) presents $\|\mathcal{H}^S_\nabla\|_\mu$ for a higher bulk Richardson number $Ri_b = 0.2541$ and the same Re and Pr values as figure 6.4(a). Here it is clear that the amplification associated with the streamwise varying flow structures such as oblique turbulent bands observed in figure 6.4(a) is significantly suppressed due to the stronger stratification, but the quasi-horizontal flow structures with $(k_x \approx 0, k_z \approx 0)$ in the bottom left corner ($k_x \approx 0$, $k_z \approx 0$) of figure 6.5(b) are less influenced by increasing bulk Richardson number.

We next focus on the high-Re high-Ri_b intermittent regime ($Re = 52630$ and $Ri_b = 0.15$), which are the values corresponding to results in Deusebio *et al.* (2015, figure 7). Figure 6.5(c) presents $\|\mathcal{H}^S_\nabla\|_\mu$ for these parameter values with an increased wall-normal grid including $N_y = 90$. Here, the amplification of the oblique turbulent band is of a similar order to that of flow structures with a wide range of wavenumbers $k_x \lesssim 10^{-2}$ and $k_z \lesssim 1$ down to $k_x \approx 0$ and $k_z \approx 0$. The latter flow structures resemble the quasi-horizontal flow structures that have a horizontal length scale much larger than the vertical length scale. The response in this regime, therefore, shows a large qualitative difference from that in the low-Re low-Ri_b ($Re = 865$ and $Ri_b = 0.02$) intermittent regime in figure 6.4(a). This qualitative difference also mirrors the different features in intermittent regimes described by Deusebio *et al.* (2015), where oblique turbulent bands are prevalent in the low-Re low-Ri_b regime, but the high-Re high-Ri_b regime is characterized by alternating turbulent-laminar layers in the vertical direction.

In figure 6.5(c), we also observe that the quasi-horizontal flow structures have a streamwise wavelength much larger than their spanwise wavelength ($\lambda_x \gg \lambda_z$), which is also consistent

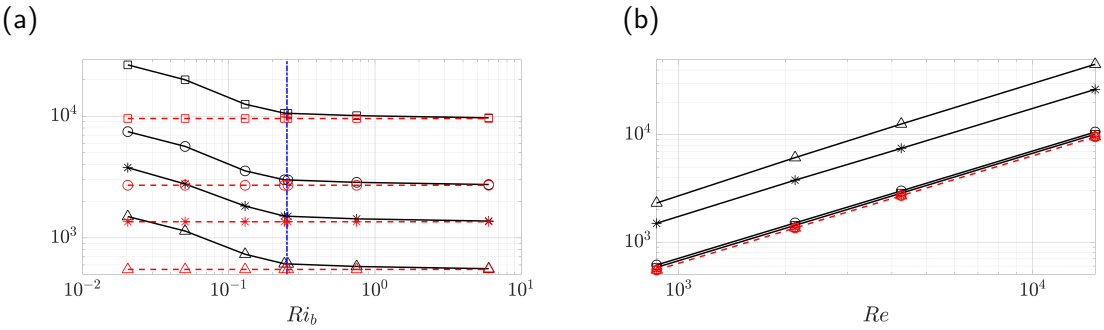

Figure 6.6: The dependence on Ri_b and Re of $\|\mathcal{H}_\nabla^S\|_\mu^M$ and $\|\mathcal{H}_\nabla^{sc}\|_\mu^M$ at $Pr = 0.7$. (a) The black solid lines (—) are $\|\mathcal{H}_\nabla^S\|_\mu^M$ at $Re = 865$ (△), $Re = 2130$ (✳), $Re = 4250$ (○), and $Re = 15000$ (□). The red dashed lines (– –) represent $\|\mathcal{H}_\nabla^S\|_\mu^{sc}$ at $Re = 865$ (△, red), $Re = 2130$ (✳, red), $Re = 4250$ (○, red), and $Re = 15000$ (□, red). The vertical line (– · –, blue) represents $Ri_b = 0.25$. (b) The black solid lines (—) are $\|\mathcal{H}_\nabla^S\|_\mu^M$ at $Ri_b = 0$ (△), $Ri_b = 0.02$ (✳), $Ri_b = 0.24$ (○), and $Ri_b = 0.75$ (□). The red dashed lines (– –) are $\|\mathcal{H}_\nabla^S\|_\mu^{sc}$ at $Ri_b = 0$ (△, red), $Ri_b = 0.02$ (✳, red), $Ri_b = 0.24$ (○, red), and $Ri_b = 0.75$ (□, red).

with the observation in Deusebio *et al.* (2015) that the turbulent and laminar layers at the high-Re high-Ri_b intermittent regime are homogeneous in the streamwise direction. This behavior can be understood through an order of magnitude estimation of the terms in the continuity equation. We assume $v \approx 0$ under strong stratification, which simplifies the continuity equation to $\frac{\partial u}{\partial x} + \frac{\partial w}{\partial z} = 0$. We further assume that the restoring buoyancy force due to stratification does not have a preference between streamwise or spanwise directions and, therefore, we also assume $\frac{\partial u}{\partial x}$ and $\frac{\partial w}{\partial z}$ are in the same order of magnitude. However, in the current stratified plane Couette flow configuration, streamwise velocity is associated with a characteristic velocity much larger than its spanwise counterpart due to the background velocity. As a result, streamwise variation is reduced much faster than spanwise ($k_x \ll k_z$) to keep $\frac{\partial u}{\partial x}$ and $\frac{\partial w}{\partial z}$ of the same order of magnitude.

6.3.2 $Ri_b > 0.25$: suppressing amplification of streamwise varying structures

The Miles-Howard theorem (Miles, 1961; Howard, 1961) suggests that $Ri_b > 0.25$ is sufficient for linear stability ($Ri_b < 0.25$ is necessary for linear instability) in an inviscid, nondiffusive, and stratified parallel shear flow. Stratified shear flow was also observed to have Richardson number near this threshold value in field measurement (Smyth *et al.*, 2019) and simulations (Salehipour *et al.*, 2018). In the previous section, we also observe that increasing Ri_b will suppress the

amplification associated with (k_x, k_z) wavenumber pairs at different levels. In this subsection, we further investigate whether this threshold $Ri_b > 0.25$ is associated with a change in flow structures and whether this behavior is independent of Reynolds number. As in the previous subsection, the Prandtl number is kept the same as $Pr = 0.7$.

Here, we aggregate results varying over a range of (k_x, k_z) wavenumber pairs in terms of the maximum value:

$$\|\mathcal{H}^S_\nabla\|^M_\mu := \max_{k_z,\, k_x} \|\mathcal{H}^S_\nabla\|_\mu(k_x, k_z), \tag{6.19}$$

where max represents the maximum value over the wavenumber domain $k_x \in [10^{-6}, 10^{0.48}]$ and $k_z \in [10^{-6}, 10^{0.48}]$. The increase in the wavenumber domain over that considered in the previous subsection is motivated by the observation in figure 6.5 that the wavenumber pair corresponding to the peak region decreases with increasing Reynolds and Richardson numbers. To isolate streamwise varying and streamwise independent flow structures, we similarly evaluate

$$\|\mathcal{H}^S_\nabla\|^{sc}_\mu := \max_{k_z,\, k_x = 10^{-6}} \|\mathcal{H}^S_\nabla\|_\mu(k_x, k_z). \tag{6.20}$$

This quantity restricts the streamwise wavenumber to $k_x = 10^{-6}$ to approximate the streamwise constant modes and compute the maximum value over $k_z \in [10^{-6}, 10^{0.48}]$. This restriction naturally includes the quasi-horizontal flow structures prevalent in the high-Re high-Ri_b regime ($k_x \approx 0$, $k_z \approx 0$) as an extreme case, but excludes streamwise varying flow structures such as oblique turbulent bands observed in the low-Re low-Ri_b regime as discussed in § 6.3.1.

Figure 6.6 presents $\|\mathcal{H}^S_\nabla\|^M_\mu$ (solid lines) and $\|\mathcal{H}^S_\nabla\|^{sc}_\mu$ (dashed lines) for Reynolds number $Re \in [865, 15000]$ and bulk Richardson number $Ri_b \in [0, 6]$. Here, we can observe that the amplification of streamwise varying flow structures is significantly suppressed when $Ri_b > 0.25$ for the full range of Reynolds numbers $Re \in [865, 15000]$ in figure 6.6(a). The quantities $\|\mathcal{H}^S_\nabla\|^M_\mu$ (solid lines) are very close to $\|\mathcal{H}^S_\nabla\|^{sc}_\mu$ (dashed lines) when $Ri_b > 0.25$. These trends suggest that the threshold value $Ri_b > 0.25$ by the Miles-Howard theorem (Miles, 1961; Howard, 1961) is associated with reducing the amplification of streamwise varying flow structures in

stratified PCF.

The plots in figure 6.6 show that the largest amplification of the streamwise constant modes represented by $\|\mathcal{H}_{\nabla}^{S}\|_{\mu}^{sc}$ (dashed lines) do not appear to be influenced by Ri_b as shown by the horizontal dashed lines in figure 6.6(a) and the overlapping dashed lines in figure 6.6(b). We further explore this Ri_b independence for streamwise constant flow structures by considering the limit of horizontal invariance $\partial_x(\cdot) = 0$ and $\partial_z(\cdot) = 0$ ($k_x = 0$ and $k_z = 0$), which directly results in $\partial_y v = 0$ due to the continuity equation. The boundary condition $v(y = \pm 1) = 0$ then directly results in $v = 0$. Using these assumptions, the advection terms vanish (i.e., $U\partial_x(\cdot) = 0$, and $\boldsymbol{u}\cdot\boldsymbol{\nabla}(\cdot) = 0$) in each momentum and density equation. The terms associated with the background shear and density gradient also vanish due to zero wall-normal velocity; i.e, $vU' = v\overline{\rho}' = 0$. These observations lead to a simplification of the momentum and density equation in (6.1) to:

$$\partial_t u = \frac{1}{Re}\partial_{yy} u, \quad \partial_y p = -Ri_b \rho, \tag{6.21a,b}$$

$$\partial_t w = \frac{1}{Re}\partial_{yy} w, \quad \partial_t \rho = \frac{1}{RePr}\partial_{yy}\rho. \tag{6.21c,d}$$

Here, we can see that horizontal momentum and density field are reduced to the diffusion equation, and the wall-normal momentum equation is reduced to a balance between buoyancy force and the vertical pressure gradient; i.e., the hydrostatic balance. This balance suggests that the variation of bulk Richardson number can be absorbed in the pressure by rescaling pressure and thus does not influence the quasi-horizontal flow structures. The observations in figures 6.4(a) and 6.5 suggest that flow structures with $k_x = 10^{-4}$ are associated with a constant quantity at a wide range of spanwise wavenumbers $k_z \leq 1$ and thus have the same amplification $\|\mathcal{H}_{\nabla}^{S}\|_{\mu}^{sc}$ as the quasi-horizontal flow structures $(k_x \approx 0, k_z \approx 0)$ that are independent on the bulk Richardson number.

This analysis suggests that quasi-horizontal flow structures are associated with amplification independent of the bulk Richardson number. Instead, a high bulk Richardson number (strong

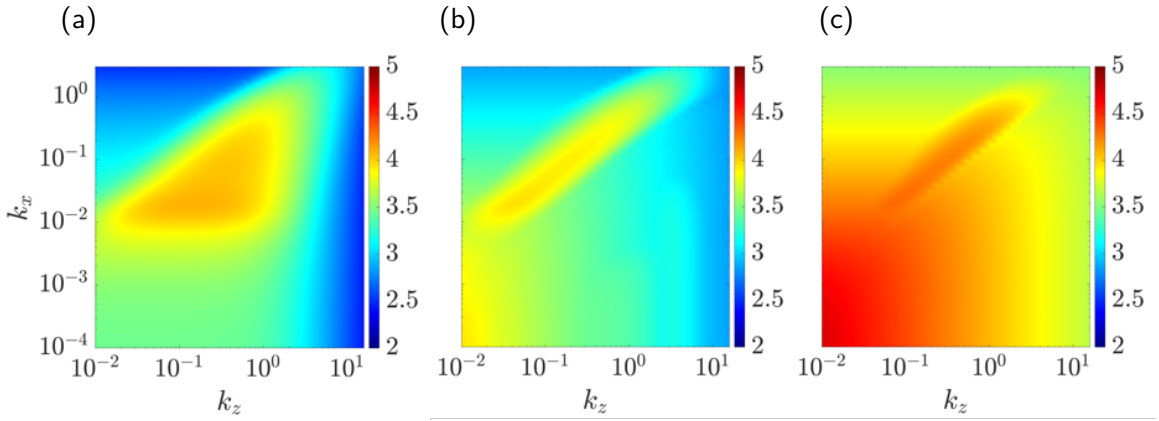

Figure 6.7: $\log_{10}[\|\mathcal{H}^S_\nabla\|_\mu(k_x, k_z)]$ at $Re = 4250$, $Ri_b = 0.02$ with three different Prandtl numbers at (a) $Pr = 10^{-4}$, (b) $Pr = 7$, and (c) $Pr = 70$.

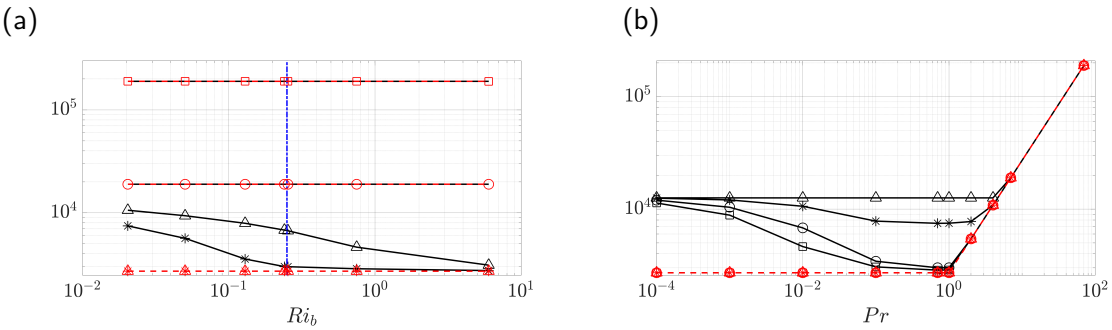

Figure 6.8: The dependence on Ri_b and Pr of $\|\mathcal{H}^S_\nabla\|^M_\mu$ and $\|\mathcal{H}^{sc}_\nabla\|^M_\mu$ at $Re = 4250$. (a) The black solid lines (—) are $\|\mathcal{H}^S_\nabla\|^M_\mu$ at $Pr = 0.01$ (△), $Pr = 0.7$ (✳), $Pr = 7$ (○), and $Pr = 70$ (□). The red dashed lines (– –) represent $\|\mathcal{H}^S_\nabla\|^{sc}_\mu$ at $Pr = 0.01$ (△, red), $Pr = 0.7$ (✳, red), $Pr = 7$ (○, red), and $Pr = 70$ (□, red). The blue vertical line (– · –, blue) represents $Ri_b = 0.25$. (b) The black solid lines (—) are $\|\mathcal{H}^S_\nabla\|^M_\mu$ at $Ri_b = 0$ (△), $Ri_b = 0.02$ (✳), $Ri_b = 0.24$ (○), and $Ri_b = 0.75$ (□). The red dashed lines (– –) are $\|\mathcal{H}^S_\nabla\|^{sc}_\mu$ at $Ri_b = 0$ (△, red), $Ri_b = 0.02$ (✳, red), $Ri_b = 0.24$ (○, red), and $Ri_b = 0.75$ (□, red).

stratification) will suppress the amplification of other flow structures that show horizontal variation such as the oblique turbulent bands observed in the low-Re low-Ri_b intermittent regime of stably stratified plane Couette flow. Furthermore, $\|\mathcal{H}^S_\nabla\|^{sc}_\mu \sim Re$ in figure 6.6(b) shows that quasi-horizontal flow structures are also associated with amplification that is increasing over Reynolds number. This suggests that quasi-horizontal flow structures prefer a high-Re high-Ri_b regime. We will further explore this scaling law $\|\mathcal{H}^S_\nabla\|^{sc}_\mu \sim Re$ by developing analytical scaling of $\|\mathcal{H}^S_\nabla\|_\mu$ under streamwise constant and passive scalar assumptions in § 6.4.

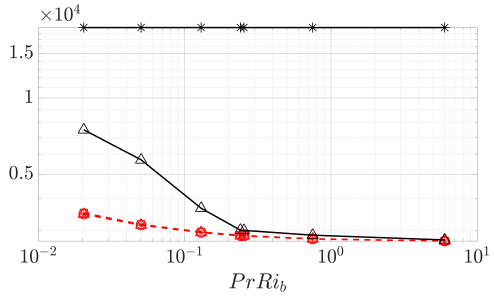

Figure 6.9: The dependence on $PrRi_b$ of $\|\mathcal{H}_\nabla^S\|_\mu^M$ at $Re = 4250$. The red dashed lines (– –) are $\|\mathcal{H}_\nabla^S\|_\mu^M$ at $Pr = 10^{-4}$ (△, red), $Pr = 10^{-3}$ (✳, red), $Pr = 10^{-2}$ (○, red), and $Pr = 10^{-1}$ (□, red). The black solid lines (—) are $\|\mathcal{H}_\nabla^S\|_\mu^M$ at $Pr = 1$ (△) and $Pr = 7$ (✳).

6.3.3 The low and high Pr effect

The Prandtl number is not well-defined within the inviscid and nondiffusive assumptions of the Miles-Howard theorem. However, the Prandtl number is also known to play an important role in characterizing flow structures in stratified PCF (Zhou *et al.*, 2017*b*,*a*; Taylor & Zhou, 2017; Langham *et al.*, 2020). In this subsection, we explore the effect of low or high Prandtl numbers on flow structures. Here, we keep the Reynolds number at $Re = 4250$ the same as studies by Zhou *et al.* (2017*b*,*a*).

Figure 6.7 presents $\|\mathcal{H}_\nabla^S\|_\mu(k_x, k_z)$ at (a) $Pr = 10^{-4}$, (b) $Pr = 7$ and (c) $Pr = 70$ for $Ri_b = 0.02$. The Prandtl number $Pr = 10^{-4}$ is chosen to illustrate the effect of a low Prandtl number $Pr \ll 1$, which is relevant for the flow in the stellar interior; see e.g., (Garaud, 2021). The Prandtl number $Pr = 7$ corresponds to the heat in the water. The Prandtl number $Pr = 70$ is chosen to study the high Prandtl number effect $Pr \gg 1$ and as an intermediate value between 7 and 700, where the latter is the Schmidt number of salt in water. In order to fully resolve the additional scales introduced at high Pr, we increase the number of wall-normal grid points to $N_y = 120$ at $Pr = 70$. We also similarly plot $\|\mathcal{H}_\nabla^S\|_\mu^M$ and $\|\mathcal{H}_\nabla^S\|_\mu^{sc}$ in figure 6.8 varying a range of the bulk Richardson numbers $Ri_b \in [0, 6]$ and the Prandtl number $Pr \in [10^{-4}, 70]$.

We first investigate the low Prandtl number effect by comparing it to the results at $Pr = 0.7$ in figure 6.5(a). The peak region of the low Prandtl number results in figure 6.7(a) resembles the shape of the peak region in unstratified plane Couette flow (figure 5.4(a) in chapter 5).

This similarity suggests that for the same bulk Richardson number, a low Prandtl number will result in a weakening of the stabilizing effect of stratification. The results of the low Prandtl number in figure 6.8 further confirm this behavior. In particular, figure 6.8(a) shows that the threshold value $Ri_b > 0.25$ does not indicate changes in the types of flow features undergoing the largest amplification at a low Prandtl number. Figure 6.8(b) further suggests that a lower Prandtl number will require a larger bulk Richardson number to fully suppress the amplification of streamwise varying flow structures to the same level as streamwise constant structures. This phenomenon is also consistent with the observation that the exact coherent structures at a low Prandtl number limit require a larger bulk Richardson number to feel the effect of stratification in plane Couette flow (Langham *et al.*, 2020).

The cross-channel density profiles of exact coherent structures in stratified PCF were shown to collapse with the same $PrRi_b$ at $Pr \in [10^{-4}, 10^{-2}]$ (Langham *et al.*, 2020, figure 3). This combined measure $PrRi_b$ has been proposed as scaling for stably stratified shear flows at the low Prandtl number limit $Pr \ll 1$ (Lignieres, 1999; Garaud *et al.*, 2015). In order to further explore this scaling, we plot $\|\mathcal{H}^S_\nabla\|^M_\mu$ as a function of $PrRi_b$ for Prandtl numbers in the range $Pr \in [10^{-4}, 7]$ in figure 6.9. Here, the results $\|\mathcal{H}^S_\nabla\|^M_\mu$ for $Pr \in [10^{-4}, 10^{-1}]$ show a collapse with $PrRi_b$. This behavior breaks down at $Pr \geq 1$ as shown in figure 6.9, which is also consistent with the results in figure 6.8 showing different behaviors at $Pr \ll 1$ and $Pr \gg 1$. A similar end to the region of $PrRi_b$ collapse is observed in studies using exact coherent structures, where the density profile at $Pr = 0.1$ deviates from the overlapped profile at $Pr \in [10^{-4}, 10^{-2}]$ for fixed $PrRi_b$ (Langham *et al.*, 2020, figure 3).

The results in figures 6.7(b) and 6.7(c) show that the amplification associated with the wavenumber pair $k_x = 10^{-4}$ and $k_z = 10^{-2}$ increases with Pr. More specifically, the value of $\|\mathcal{H}^S_\nabla\|_\mu$ associated with $k_x = 10^{-4}$ and $k_z = 10^{-2}$ becomes comparable to the values associated with the oblique turbulent bands at $Pr = 7$, and it has the largest magnitude over (k_x, k_z) contour at $Pr = 70$ in figure 6.7(c). Figure 6.8 further shows that at high Prandtl number the quantities $\|\mathcal{H}^S_\nabla\|^M_\mu$ and $\|\mathcal{H}^S_\nabla\|^{sc}_\mu$ are the same over a wide range of the bulk Richardson number

$Ri_b \in [0, 6]$; note the horizontal lines in figure 6.8(a) for different Ri_b results collapse as one line at $Pr \gg 1$ regime in figure 6.8(b). This observation is also consistent with Langham *et al.* (2020) who noted that in the high Prandtl number limit $Pr \gg 1$, the effect of increasing Ri_b is mitigated. This phenomenon can be attributed to the dominance of the quasi-horizontal flow structures ($k_x \approx 0$, $k_z \approx 0$) that show high magnitudes in figures 6.7(b) and 6.7(c).

The quasi-horizontal flow structures ($k_x \approx 0$, $k_z \approx 0$) observed at high Pr have different features from those previously observed at the high-Re, high-Ri_b regime as described in § 6.3.1. This indicates that a new type of quasi-horizontal flow structure appears at a high Prandtl number. The appearance of this flow structure at a high Prandtl number suggests that this flow structure is associated with density. This notion can be further explored by isolating the input-output pathway for each component of the momentum and density equation, i.e. inputs f_x, f_y, f_z, f_ρ in equations (6.3)-(6.4) to outputs u, v, w, and ρ. These sixteen input-output pathways can be studies through the definition of operators $\mathcal{H}^S_{ij}$, where j defines the forcing component ($j = x, y, z, \rho$) and $i = u, v, w, \rho$ describes each velocity or density component:

$$\mathcal{H}^S_{ij} = \widehat{\mathcal{C}}^S_i \left(\mathrm{i}\omega \mathcal{I}_{3\times 3} - \widehat{\mathcal{A}}^S \right)^{-1} \widehat{\mathcal{B}}^S_j \tag{6.22}$$

with

$$\widehat{\mathcal{B}}^S_x := \widehat{\mathcal{B}}^S \begin{bmatrix} \mathcal{I} & 0 & 0 & 0 \end{bmatrix}^\mathsf{T}, \quad \widehat{\mathcal{B}}^S_y := \widehat{\mathcal{B}}^S \begin{bmatrix} 0 & \mathcal{I} & 0 & 0 \end{bmatrix}^\mathsf{T}, \tag{6.23a,b}$$

$$\widehat{\mathcal{B}}^S_z := \widehat{\mathcal{B}}^S \begin{bmatrix} 0 & 0 & \mathcal{I} & 0 \end{bmatrix}^\mathsf{T}, \quad \widehat{\mathcal{B}}^S_\rho := \widehat{\mathcal{B}}^S \begin{bmatrix} 0 & 0 & 0 & \mathcal{I} \end{bmatrix}^\mathsf{T}, \tag{6.23c,d}$$

$$\widehat{\mathcal{C}}^S_u := \begin{bmatrix} \mathcal{I} & 0 & 0 & 0 \end{bmatrix} \widehat{\mathcal{C}}^S, \quad \widehat{\mathcal{C}}^S_v := \begin{bmatrix} 0 & \mathcal{I} & 0 & 0 \end{bmatrix} \widehat{\mathcal{C}}^S, \tag{6.23e,f}$$

$$\widehat{\mathcal{C}}^S_w := \begin{bmatrix} 0 & 0 & \mathcal{I} & 0 \end{bmatrix} \widehat{\mathcal{C}}^S, \quad \widehat{\mathcal{C}}^S_\rho := \begin{bmatrix} 0 & 0 & 0 & \mathcal{I} \end{bmatrix} \widehat{\mathcal{C}}^S. \tag{6.23g,h}$$

Figures 6.10 and 6.11 present these sixteen quantities $\|\mathcal{H}^S_{ij}\|_\infty$ for the respective parameters $Re = 865$, $Pr = 0.7$, and $Ri_b = 0.02$, and $Re = 4250$, $Pr = 70$ and $Ri_b = 0.02$. Here, we can see that the combined effect of the diagonal panels resembles the shape of $\|\mathcal{H}^S_\nabla\|_\mu$ at the

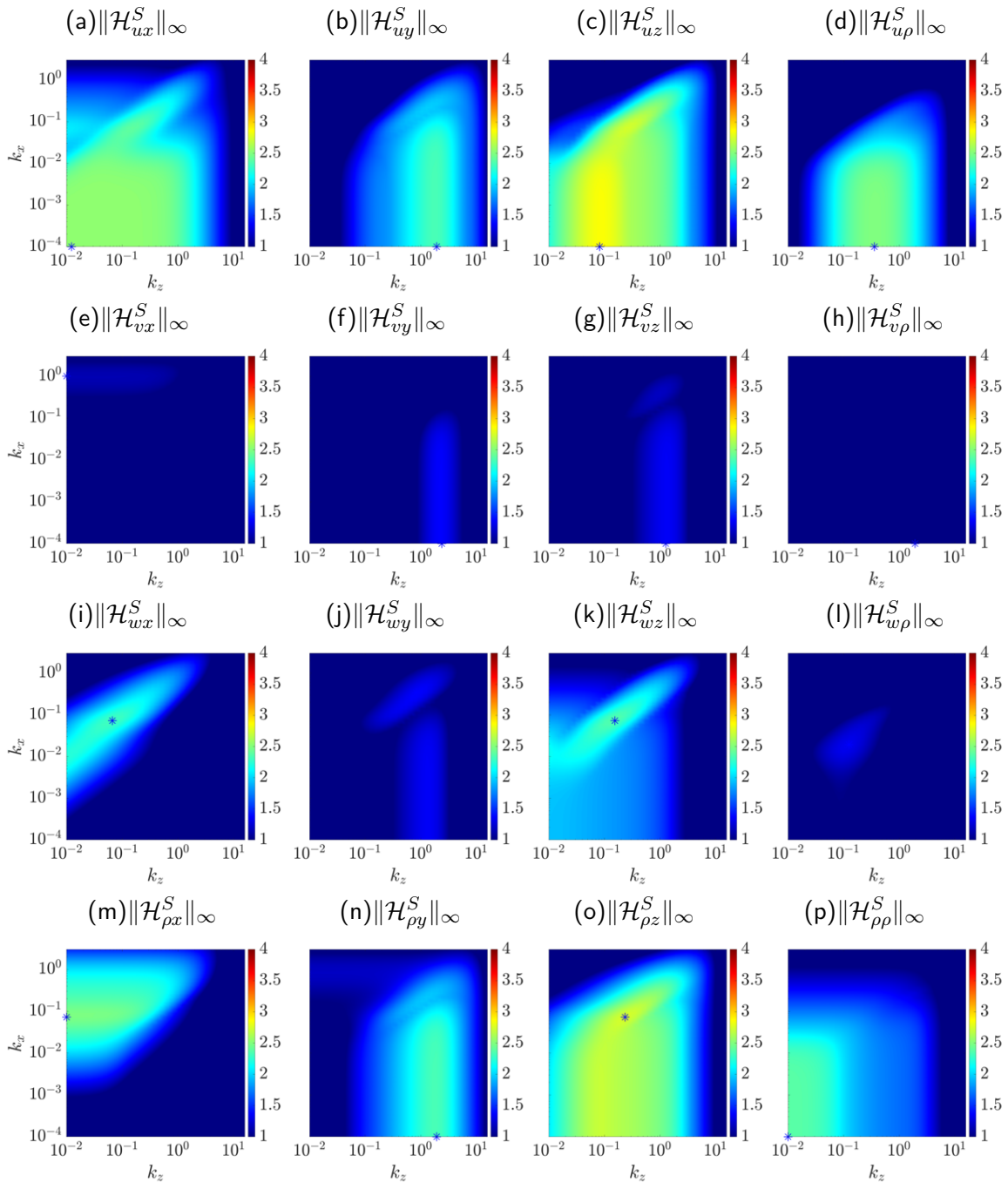

Figure 6.10: Componentwise analysis $\log_{10}[\|\mathcal{H}^S_{ij}\|_\infty](k_x, k_z)$ at $Re = 865$, $Ri_b = 0.02$, $Pr = 0.7$ ($i = u, v, w, \rho$ and $j = x, y, z, \rho$). Each column from left to right corresponds to input f_x, f_y, f_z, and f_ρ, and each row from top to bottom corresponds to output u, v, w, and ρ. The symbol (✳, blue) in each panel marks the wavenumber pair (k_x, k_z) that reaches the maximum value of $\|\mathcal{H}^S_{ij}\|_\infty(k_x, k_z)$.

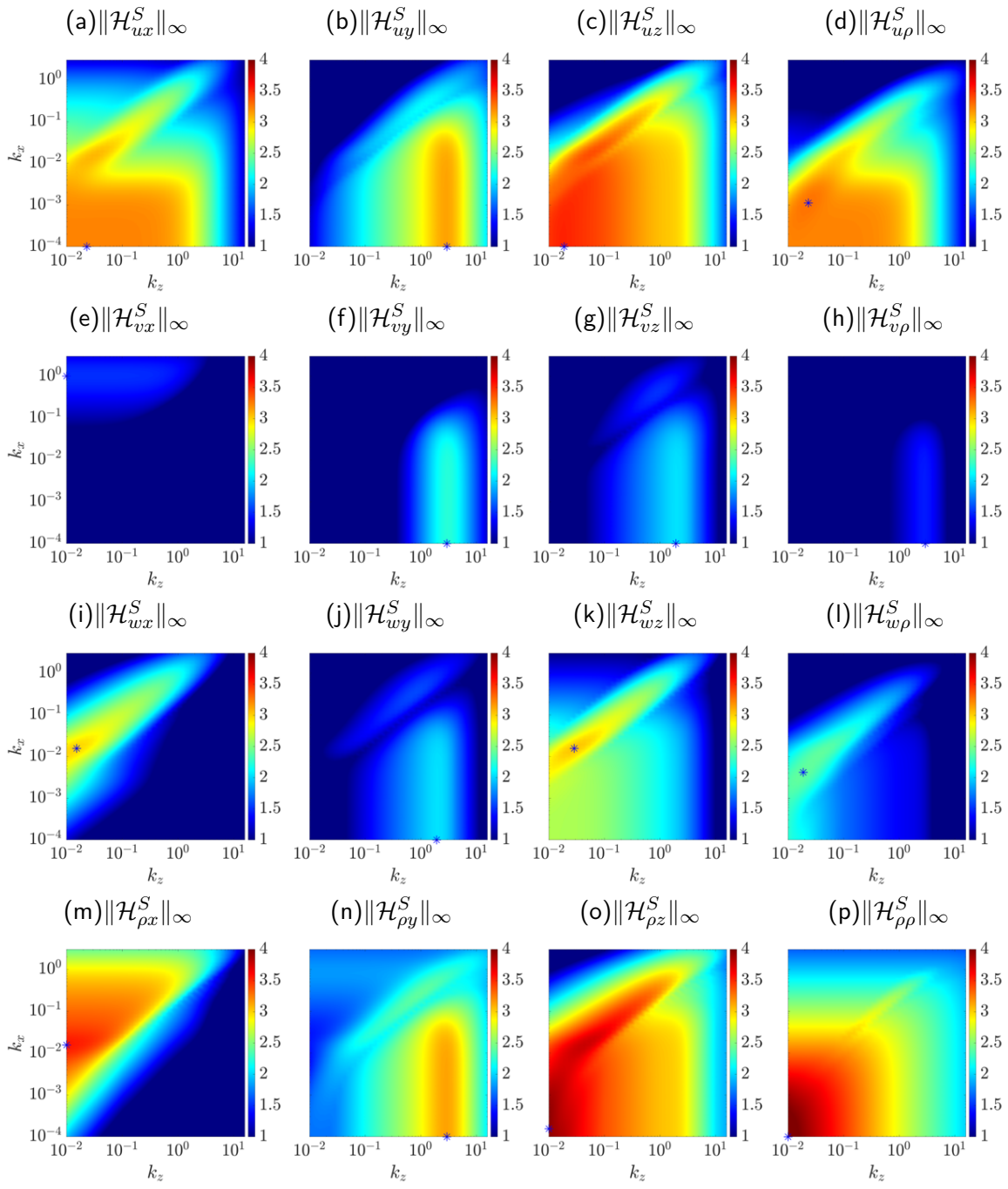

Figure 6.11: Componentwise analysis $\log_{10}[\|\mathcal{H}^S_{ij}\|_\infty](k_x, k_z)$ at $Re = 4250$, $Ri_b = 0.02$, $Pr = 70$ ($i = u, v, w, \rho$ and $j = x, y, z, \rho$). Each column from left to right corresponds to input f_x, f_y, f_z, and f_ρ, and each row from top to bottom corresponds to output u, v, w, and ρ. The symbol (✳, blue) in each panel marks the wavenumber pair (k_x, k_z) that reaches the maximum value of $\|\mathcal{H}^S_{ij}\|_\infty(k_x, k_z)$.

same flow regime in figures 6.4(a) and 6.7(c). This correspondence is due to the fact that the structured feedback interconnections in (6.5)-(6.6) constrain the permissible feedback pathway. In figure 6.11, panel (p) $\|\mathcal{H}^S_{\rho\rho}\|_\infty$ which is associated with input f_ρ and output ρ is significantly larger than other panels at $Pr = 70$ suggesting the strong role of density in the amplification for this parameter range. We can further isolate each component of the frequency response operator $\mathcal{H}^S_\nabla$ by defining:

$$\mathcal{H}^S_{\nabla ij} = \widehat{\boldsymbol{\nabla}}\mathcal{H}^S_{ij}. \tag{6.24}$$

These values, not shown for brevity, show qualitatively similar behavior to $\|\mathcal{H}^S_{ij}\|_\infty$ presented in figures 6.10 and 6.11. This componentwise analysis demonstrates that the quasi-horizontal flow structures appearing at high Pr are associated with the density.

The appearance of this type of quasi-horizontal flow structure associated with density at a high Prandtl number regime is also qualitatively consistent with the observation that the sharpness of the density gradient is observed when increasing Prandtl number (Zhou *et al.*, 2017*b*) and one flow regime prominent of layering (a step-like layers of nearly uniform density separated by thin interface) observed in the literature is high Prandtl number (Taylor & Zhou, 2017).

6.4 Density-associated flow structures at $Pr \gg 1$: analytical scaling

The previous subsection reveals the appearance of quasi-horizontal flow structures associated with density at the $Pr \gg 1$ limit. In this subsection, we further study the analytical scaling of $\|\mathcal{H}^S_\nabla\|_\mu$ over Re and Pr to provide further evidence that such flow structures prefer the $Pr \gg 1$ regime. The analytical scaling over Re and Pr can further provide insight into high Re and Pr regimes beyond the current computation range achievable through numerical simulations.

We start with the streamwise constant ($k_x = 0$) and passive scalar limit ($Ri_b = 0$) to facilitate analytical derivation. The importance of streamwise constant flow structures is suggested

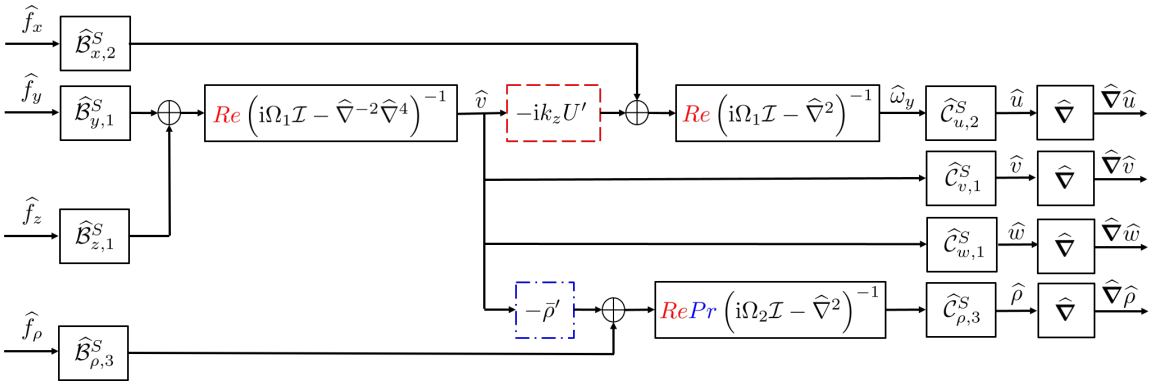

Figure 6.12: Block diagram of the frequency response operator that maps forcing in each momentum and density equation to each velocity and density gradient in streamwise-constant ($k_x = 0$) stratified plane Couette flow at the passive scalar limit $Ri_b = 0$. Here, $\Omega_1 = \omega Re$ and $\Omega_2 = \omega RePr$. The block outlined by (– –, red) contributes to the scaling associated with $\|\mathcal{H}^S_{uy}\|_\infty$, $\|\mathcal{H}^S_{uz}\|_\infty$, while the block outlined by (– · –, blue) contributes to the $\|\mathcal{H}^S_{\rho y}\|_\infty$, and $\|\mathcal{H}^S_{\rho z}\|_\infty$.

by the quasi-horizontal flow structures ($k_x \approx 0$ and $k_z \approx 0$), which are nearly streamwise constant. The independence of the amplification of streamwise constant flow structures $\|\mathcal{H}^S_\nabla\|^{sc}_\mu$ as a function of Ri_b observed in figures 6.6 and 6.8 and the analysis of Langham *et al.* (2020) suggests that the passive scalar limit $Ri_b = 0$ is a reasonable regime to obtain further insight. The analytically derived Re and Pr scalings of each component of $\mathcal{H}^S_{ij}$ in (6.22) and $\mathcal{H}^S_{\nabla ij}$ in (6.24) are presented in theorem 6.2(a) and (b), respectively.

Theorem 6.2 *Given streamwise constant ($k_x = 0$) stratified plane Couette flow at the passive scalar limit $Ri_b = 0$.*

(a) Each component of $\|\mathcal{H}^S_{ij}\|_\infty$ ($i = u, v, w, \rho$ and $j = x, y, z, \rho$) scales as:

$$\begin{bmatrix} \|\mathcal{H}^S_{ux}\|_\infty & \|\mathcal{H}^S_{uy}\|_\infty & \|\mathcal{H}^S_{uz}\|_\infty & \|\mathcal{H}^S_{u\rho}\|_\infty \\ \|\mathcal{H}^S_{vx}\|_\infty & \|\mathcal{H}^S_{vy}\|_\infty & \|\mathcal{H}^S_{vz}\|_\infty & \|\mathcal{H}^S_{v\rho}\|_\infty \\ \|\mathcal{H}^S_{wx}\|_\infty & \|\mathcal{H}^S_{wy}\|_\infty & \|\mathcal{H}^S_{wz}\|_\infty & \|\mathcal{H}^S_{w\rho}\|_\infty \\ \|\mathcal{H}^S_{\rho x}\|_\infty & \|\mathcal{H}^S_{\rho y}\|_\infty & \|\mathcal{H}^S_{\rho z}\|_\infty & \|\mathcal{H}^S_{\rho\rho}\|_\infty \end{bmatrix}$$

$$= \begin{bmatrix} Re\, h^S_{ux}(k_z) & Re^2\, h^S_{uy}(k_z) & Re^2\, h^S_{uz}(k_z) & 0 \\ 0 & Re\, h^S_{vy}(k_z) & Re\, h^S_{vz}(k_z) & 0 \\ 0 & Re\, h^S_{wy}(k_z) & Re\, h^S_{wz}(k_z) & 0 \\ 0 & Re^2 Pr\, h^S_{\rho y}(k_z) & Re^2 Pr\, h^S_{\rho z}(k_z) & RePr\, h^S_{\rho\rho}(k_z) \end{bmatrix}, \tag{6.25}$$

where functions $h^S_{ij}(k_z)$ are independent of the Re and Pr.

(b) Each component of $\|\mathcal{H}^S_{\nabla ij}\|_\infty$ *(*$i = u, v, w, \rho$ *and* $j = x, y, z, \rho$*) scales as:*

$$\begin{bmatrix} \|\mathcal{H}^S_{\nabla ux}\|_\infty & \|\mathcal{H}^S_{\nabla uy}\|_\infty & \|\mathcal{H}^S_{\nabla uz}\|_\infty & \|\mathcal{H}^S_{\nabla u\rho}\|_\infty \\ \|\mathcal{H}^S_{\nabla vx}\|_\infty & \|\mathcal{H}^S_{\nabla vy}\|_\infty & \|\mathcal{H}^S_{\nabla vz}\|_\infty & \|\mathcal{H}^S_{\nabla v\rho}\|_\infty \\ \|\mathcal{H}^S_{\nabla wx}\|_\infty & \|\mathcal{H}^S_{\nabla wy}\|_\infty & \|\mathcal{H}^S_{\nabla wz}\|_\infty & \|\mathcal{H}^S_{\nabla w\rho}\|_\infty \\ \|\mathcal{H}^S_{\nabla \rho x}\|_\infty & \|\mathcal{H}^S_{\nabla \rho y}\|_\infty & \|\mathcal{H}^S_{\nabla \rho z}\|_\infty & \|\mathcal{H}^S_{\nabla \rho\rho}\|_\infty \end{bmatrix}$$

$$= \begin{bmatrix} Re\, h^S_{\nabla ux}(k_z) & Re^2\, h^S_{\nabla uy}(k_z) & Re^2\, h^S_{\nabla uz}(k_z) & 0 \\ 0 & Re\, h^S_{\nabla vy}(k_z) & Re\, h^S_{\nabla vz}(k_z) & 0 \\ 0 & Re\, h^S_{\nabla wy}(k_z) & Re\, h^S_{\nabla wz}(k_z) & 0 \\ 0 & Re^2 Pr\, h^S_{\nabla \rho y}(k_z) & Re^2 Pr\, h^S_{\nabla \rho z}(k_z) & RePr\, h^S_{\nabla \rho\rho}(k_z) \end{bmatrix}, \tag{6.26}$$

where functions $h^S_{\nabla ij}(k_z)$ *are independent of the* Re *and* Pr*.*

The first three columns and three rows presented in theorem 6.2(a) are the same as those derived in Jovanović (2004, theorem 11) for general unstratified wall-bounded shear flows. The proof of theorem 6.2 follows the procedure in unstratified flow (Jovanović, 2004; Jovanović & Bamieh, 2005; Jovanović, 2021) and is outlined as a block diagram in figure 6.12. The key steps entail rescaling the temporal frequency by $\Omega_1 = \omega Re$ and $\Omega_2 = \omega RePr$ and then employing the fact that $\sup_{\omega\in\mathbb{R}}[\cdot] = \sup_{\Omega_1\in\mathbb{R}}[\cdot] = \sup_{\Omega_2\in\mathbb{R}}[\cdot]$. The details of the proof and additional operators employed in figure 6.12 are presented in Appendix C. Figure 6.12 highlights the Reynolds number and Prandtl number that contribute to the scaling for each input-output pair. These results demonstrate that the Prandtl number only contributes to the scaling associated with the density field; i.e., the bottom rows of equations (6.25) and (6.26) corresponding to the density output. We also note that the rightmost columns of equations (6.25) and (6.26) show that the forcing in the density equation f_ρ is not influencing the output corresponding to velocity u, v, w, which is consistent with the passive scalar assumption considered here. Figure 6.12 also shows that adding the gradient operator does not influence the scaling over Re or Pr.

In figure 6.12, the block $-\mathrm{i}k_z U'$ inside of dashed lines (– –, red) contributes to the relatively large scalings of $\|\mathcal{H}^S_{uy}\|_\infty \sim Re^2$, $\|\mathcal{H}^S_{uz}\|_\infty \sim Re^2$ at high Re in theorem 6.2, which has been attributed to the lift-up mechanism; see discussion in Jovanović (2021). Similarly, the block $-\overline{\rho}'$ outlined by (– · –, blue) contributes to the relatively large scalings of $\|\mathcal{H}^S_{\rho y}\|_\infty \sim Re^2 Pr$,

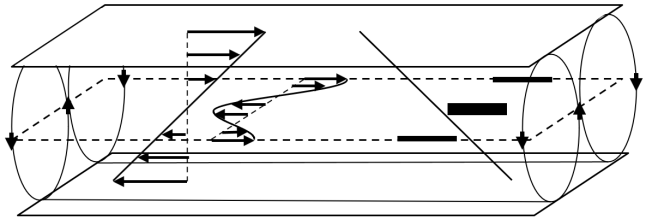

Figure 6.13: An illustration of the lift-up mechanism, where streamwise streaks and density streaks in the channel center are amplified by cross-stream forcing induced by streamwise vortices.

and $\|\mathcal{H}^S_{\rho z}\|_\infty \sim Re^2 Pr$ at high Re or Pr. This amplification can be similarly understood by the lift-up mechanism as sketched in figure 6.13, where cross-stream forcings (e.g., induced by streamwise vortices) redistribute the background velocity and density gradients across the channel height to form streamwise streaks with alternating velocity (shown by the arrow in the horizontal plane at the channel center) and density streaks with high and low-density fluids (thick and thin lines) near the channel center. This similarity between streamwise streaks and density streaks is consistent with the observation that passive scalar streaks can be generated by the same lift-up mechanism as the streamwise streaks (Chernyshenko & Baig, 2005).

The effect of imposing a componentwise structure of nonlinearity within the feedback is analogous to the effect seen in unstratified plane Couette flow (section 5.3.3). The imposed correlation between each component of the modeled forcing $f_{x,\xi}$, $f_{y,\xi}$, $f_{z,\xi}$, $f_{\rho,\xi}$, and the respective velocity and density components u, v, w, ρ constrains the influence of the forcing to its associated component of the velocity or density field. Thus, the overall scaling of $\|\mathcal{H}^S_\nabla\|_\mu$ is related to the worst-case scaling of the diagonal terms in equation (6.26) in theorem 6.2. The concept is formalized in theorem 6.3, which is supported by numerical results of these quantities described in § 6.3. We leave the proof in Appendix C.

Theorem 6.3 *Given wavenumber pair* (k_x, k_z).

$$\|\mathcal{H}^S_\nabla\|_\mu \geq \max[\|\mathcal{H}^S_{\nabla ux}\|_\infty, \|\mathcal{H}^S_{\nabla vy}\|_\infty, \|\mathcal{H}^S_{\nabla wz}\|_\infty, \|\mathcal{H}^S_{\nabla \rho\rho}\|_\infty]. \tag{6.27}$$

We can combine results in theorem 6.2(b) and theorem 6.3 to obtain the scaling of $\|\mathcal{H}^S_\nabla\|_\mu$

in corollary 6.4:

Corollary 6.4 *Given streamwise constant ($k_x = 0$) stratified plane Couette flow at the passive scalar limit $Ri_b = 0$.*

$$\|\mathcal{H}_\nabla^S\|_\mu(0,k_z) \geq max[Re\, h_{\nabla ux}(k_z), Re\, h_{\nabla vy}(k_z), Re\, h_{\nabla wz}(k_z), RePr\, h_{\nabla\rho\rho}(k_z)], \qquad (6.28)$$

where functions $h_{\nabla ij}(k_z)$ with $ij = ux, vy, wz, \rho\rho$ are independent of the Re and Pr.

Although corollary 6.4 provides a lower bound on $\|\mathcal{H}_\nabla^S\|_\mu$, the numerical results suggest that $\|\mathcal{H}_\nabla^S\|_\mu$ follows the same Re and Pr scaling of the right-hand side of (6.28) in corollary 6.4. For example, corollary 6.4 suggests that the lower bound of $\|\mathcal{H}_\nabla^S\|_\mu(0,k_z)$ will scale as $\sim Re$ at a fixed Prandtl number, which is consistent with the dashed lines of figure 6.6(b). At a fixed Reynolds number, corollary 6.4 also suggests that at high Prandtl numbers $Pr \gg 1$, $\|\mathcal{H}_\nabla^S\|_\mu(0,k_z) \sim Pr$ but at low Prandtl numbers $Pr \ll 1$, $\|\mathcal{H}_\nabla^S\|_\mu(0,k_z)$ will become independent of the Prandtl number. This is also consistent with the numerical results shown in the dashed lines of figure 6.8(b) that suggest $\|\mathcal{H}_\nabla^S\|_\mu^{sc} \sim Pr$ when $Pr \gg 1$ and independent of Pr when $Pr \ll 1$. At a high Prandtl number $Pr \gg 1$, theorem 6.3 and corollary 6.4 further suggest that the component $\|\mathcal{H}_{\nabla\rho\rho}^S\|_\infty$ associated with the density will dominate the overall behavior of $\|\mathcal{H}_\nabla^S\|_\mu$, which is consistent with the large amplification of quasi-horizontal flow structures associated with density $\|\mathcal{H}_{\rho\rho}^S\|_\infty$ observed in figure 6.11(p). Corollary 6.4 further supports the notion that the flow structures associated with density prefer the flow regime with $Pr \gg 1$ at the passive scalar limit.

6.5 Summary

This work extends the structured input-output analysis originally developed for unstratified wall-bounded flows (chapter 5) to stratified PCF.

We then apply the structured input–output analysis to characterize highly amplified flow structures in the intermittent regime of stratified plane Couette flow and investigate the behavior

of the flow across a range of Re, Pr, and Ri_b. We first examine how Re and Ri_b affect flow structures with $Pr = 0.7$. This approach predicts the characteristic wavelengths and angle of the oblique turbulent bands observed in very large channel size DNS of the low-Re low-Ri_b intermittent regime of stratified plane Couette flow (Deusebio *et al.*, 2015; Taylor *et al.*, 2016). At the high-Re high-Ri_b intermittent regime, this approach also identifies quasi-horizontal flow structures resembling turbulent-laminar layers (Deusebio *et al.*, 2015) that are associated with amplification close to oblique turbulent bands. We then show that increasing bulk Richardson number is suppressing the amplification of streamwise varying flow structures, which is close to that of streamwise independent flow structures above threshold value $Ri_b > 0.25$. This phenomenon is robust against a wide range of Re and valid at $Pr \approx 1$.

We then examine flow behavior at different Ri_b and Pr. At $Pr \ll 1$, a larger bulk Richardson number is required to suppress streamwise varying flow structures to the same level as streamwise independent ones compared with $Pr \approx 1$. The largest amplification also coincides with the same $PrRi_b$ consistent with the observation of overlapped averaged density profile with the same $PrRi_b$ at the $Pr \ll 1$ regime (Langham *et al.*, 2020). At $Pr \gg 1$, we identify another quasi-horizontal flow structure independent of Ri_b. By decomposing input-output pathways into each velocity and density component, we show that these quasi-horizontal flow structures at $Pr \gg 1$ are associated with density. The importance of this density-associated flow structure at $Pr \gg 1$ is further highlighted by the analytical scaling of amplification over Re and Pr under passive scalar and streamwise constant assumptions. The above observations using structured input-output analysis distinguish two types of quasi-horizontal flow structures, one associated with the high-Re high-Ri_b regime and the other one associated with density that emerges in the high Pr regime.

The results here suggest the promise of this computationally tractable approach in identifying horizontal length scales of prominent flow structures in stratified wall-bounded flows and opens up many directions for future work. For example, this framework may be extended to other stratified wall-bounded flows such as stratified channel flow (Garcia-Villalba & del Alamo, 2011),

stratified open channels (Flores & Riley, 2011; Brethouwer *et al.*, 2012; Donda *et al.*, 2015; He & Basu, 2015, 2016), and the stratified Ekman layer (Deusebio *et al.*, 2014), where the intermittent regimes were also observed. This framework may be also extended to configurations where background density gradient and velocity gradient are orthogonal; e.g., spanwise stratified plane Couette flow (Facchini *et al.*, 2018; Lucas *et al.*, 2019) and spanwise stratified plane Poiseuille flow (Le Gal *et al.*, 2021).

Chapter 7

Plane Couette flow with stabilizing rotation: analogy to stable stratification

> "Prof. G.I. Taylor and Major A. R. Low have both suggested to me that there should be an analogy between the conditions in a layer of liquid heated below and in a liquid between two coaxial cylinders rotating at different rates."
>
> Harold Jeffreys[1], 1928

Rotation is known to share a lot of similarity to stratification in constraining fluid motion (Veronis, 1970). The oblique turbulent bands previously analyzed in plane Couette flow (chapter 5) and stratified plane Couette flow (chapter 6) have also been observed in spanwise rotating plane Couette flow (Tsukahara *et al.*, 2010*a*,*b*; Brethouwer *et al.*, 2012). It is therefore natural to examine the relationship between the role of rotation and its analogy to stratification in wall-bounded shear flows when both of them are stabilizing. This chapter will analyze the effect of stabilizing rotation in plane Couette flow and compare it with that of stable stratification previously studied in chapter 6. This chapter also demonstrates the how to include the effect of a linear body force such as Coriolis force within the structured input-output analysis framework.

[1] (Jeffreys, 1928, p. 202)

7.1 Introduction

The effects of rotation are important in a wide range of engineering devices such as rotating machinery or flow over curved surfaces (Jakirlic *et al.*, 2002; Huang *et al.*, 2019*a*). The Earth's rotation plays a leading role in the large-scale atmospheric and oceanic motion with a length scale on the order of $10^5 - 10^6$ m (Vallis, 2017; Davidson, 2013). Understanding the effect of rotation in modifying fluid motion is important for turbulence modeling and parameterization in both industrial and environmental applications.

Spanwise rotating plane Couette flow (PCF) is a canonical flow configuration that permits the study of the effect of rotation in wall-bounded flows. The rotation axis of this flow is the spanwise direction, which allows us to easily categorize the effect of rotation by comparing its sign with background spanwise vorticity. A small magnitude of rotation is destabilizing when the imposed rotation has the opposite sign of the background vorticity (anti-cyclonic), while the rotation is stabilizing when it is in the same sign as the background vorticity (cyclonic) (Lezius & Johnston, 1976; Hiwatashi *et al.*, 2007; Bech & Andersson, 1996, 1997; Komminaho *et al.*, 1996).

Spanwise rotating PCF is usually connected to another canonical buoyancy-driven (unstably stratified) wall-bounded flow: Rayleigh-Bénard convection (RBC) and their analogy dates back to Rayleigh (1917) and Jeffreys (1928). A type of mathematical equivalence between these two flows can be exploited to study the flow properties. For example, Lezius & Johnston (1976) used the dynamical analogy between the streamwise constant mode in rotating PCF and RBC to derive the marginal stability criteria in rotating PCF using the critical Rayleigh number of RBC predicted by linear stability theory. Nagata (2013, appendix A) showed that there is a mathematical equivalence between two-dimensional three-component (2D/3C) rotating PCF and two-dimensional (2D) RBC. This equivalence was later employed to further study the analogy between heat and momentum transport in these two flows (Eckhardt *et al.*, 2020). Eckhardt *et al.* (2007*a*) derived the exact analogy between Taylor-Couette flow (which is closely related

to spanwise rotating Couette flow (Nagata, 1986; Faisst & Eckhardt, 2000; Brauckmann *et al.*, 2016)) and RBC and used it to extend a unifying scaling theory in RBC (Grossmann & Lohse, 2000) to Taylor-Couette flow.

Observations in direct numerical simulations (DNS) and experiments of spanwise rotating PCF and RBC show some similar flow structures in the full dynamics. In particular, they both share large-scale roll structures that are widely studied in rotating PCF using DNS (Bech & Andersson, 1996, 1997; Gai *et al.*, 2016; Xia *et al.*, 2018, 2019; Huang *et al.*, 2019*b*, 2021), experiments (Tsukahara *et al.*, 2010*b*; Hiwatashi *et al.*, 2007; Suryadi *et al.*, 2014; Kawata & Alfredsson, 2016, 2019), generalized quasilinear approximation (Tobias & Marston, 2017), bifurcation analysis (Nagata *et al.*, 2021; Yang & Xia, 2021), and secondary instability analysis (Daly *et al.*, 2014). Similar flow structures were also observed in RBC, where they are typically referred to as large-scale convection rolls (Bodenschatz *et al.*, 2000).

The above studies mainly focused on the flow regime where the Coriolis force due to rotation and the buoyancy force are both playing a destabilizing role. However, when both of them are stabilizing, the observations within PCF also show some similar phenomena. For example, the stabilizing effect results in transition from laminar to turbulent flow regime to be observed in a higher Reynolds number than PCF; e.g., see experiments of rotating PCF (Tsukahara *et al.*, 2010*b*, figure 2) and DNS of stratified PCF (Deusebio *et al.*, 2015, figure 18). The stabilizing effect also results in the turbulence being highly intermittent, and the associated oblique turbulent bands prevalent in this regime are observed in rotating PCF experiments (Tsukahara *et al.*, 2010*b*,*a*) and DNS (Brethouwer *et al.*, 2012), as well as DNS of stratified PCF (Deusebio *et al.*, 2015; Taylor *et al.*, 2016).

When both rotation and stratification are stabilizing, the flow is typically highly intermittent, which makes it challenging to select an averaging spatial-temporal domain. Moreover, the oblique turbulent bands observed in PCF with stabilizing rotation or stratification require a very large channel size ($\sim O(100)$ times channel half-height) to fully accommodate them (Brethouwer *et al.*, 2012; Deusebio *et al.*, 2015; Taylor *et al.*, 2016), which also imposes computational

challenges. Input-output (resolvent) analysis based on the spatio-temporal frequency response, which has been widely employed in wall-bounded shear flows (Farrell & Ioannou, 1993*a*; Bamieh & Dahleh, 2001; Jovanović & Bamieh, 2005; McKeon & Sharma, 2010; McKeon, 2017) can help overcome these challenges due to its computational tractability and the lack of finite channel effect. For example, resolvent analysis was shown to predict the quantitative effect of varying spanwise rotation rates on coherent structures in rotating turbulent channel flow (Nakashima *et al.*, 2019), as well as to predict coherent structures in stratified turbulent channel flow (Ahmed *et al.*, 2021).

Here we employ the related approach, structured input-output analysis (chapters 5-6). This approach builds upon input-output analysis, but instead adopts a feedback interconnection to represent the nonlinear interactions and uses the structured singular value of this closed loop system to quantify amplification. Structured input-output analysis (chapters 5-6) predicts high amplification under structured forcing associated with the wavelength of oblique turbulent bands in the intermittent regime of both PCF (Prigent *et al.*, 2003) and stratified PCF (Deusebio *et al.*, 2015; Taylor *et al.*, 2016). Here, we show that at a relatively slow rotation rate, the structured input-output captures the wavelength of oblique turbulent bands observed in spanwise rotating PCF (Brethouwer *et al.*, 2012), similar to the observation in the stratified PCF (chapter 6).

The analysis then focuses on a mathematical equivalence between two-dimensional three-component (2D/3C, no streamwise variation) spanwise rotating PCF and two-dimensional (2D, no streamwise variation and no streamwise velocity) vertically stratified PCF. We employ structured input-output analysis (chapters 5-6) to quantify the extent to which this equivalence remains valid (in terms of the most amplified flow structures) under the full three-dimensional and full component flow when both rotation and stratification are stabilizing. The similarity of the most amplified structures within this parameter regime is further quantified by analyzing individual input-output pathways (i.e. each component of body forcing as input and each velocity component as output). This analysis shows that the main difference between these flows is associated with the streamwise velocity and streamwise forcing pair, where rotation suppresses the

amplification of spanwise varying flow structures faster than stratification. The amplification of streamwise dependent flow structures is suppressed faster by stratification than rotation in the regimes where these two flows are equivalent. The largest amplification of streamwise constant (2D/3C) flow structures in rotating PCF is not influenced by rotation number, which suggests additional mathematical equivalence. We then show that there is a mathematical equivalence between 2D/3C rotating PCF with a passive scalar and 2D/3C stratified PCF and demonstrate evidence of this behavior using structured input-output analysis.

The remainder of this chapter is organized as follows. Section 7.2 describes the dynamics of perturbation around laminar rotating PCF and stratified PCF. We then describe the conditions under which they are mathematically equivalent. In section 7.3, we apply structured input-output analysis to rotating PCF. Section 7.4 then analyzes the results obtained from structured input-output analysis for rotating PCF and compares them with stratified PCF. This chapter is summarized in section 7.5.

7.2 Mathematical equivalence between rotating PCF and stratified PCF

In this section, we describe a mathematical equivalence between 2D/3C spanwise rotating PCF and 2D vertically stratified PCF. This idea builds up the existing observation that 2D/3C rotating PCF is mathematically equivalent to 2D Rayleigh-Bénard convection; see e.g., Lezius & Johnston (1976, section 3.1); Nagata (2013, appendix A); Eckhardt *et al.* (2020, table 1). Unstably stratified PCF can also be shown to be mathematically equivalent to Rayleigh-Bénard convection with background shear under a certain rescaling and a change of variables; see e.g., Olvera & Kerswell (2017, appendix B).

We start by considering plane Couette flow between two infinite parallel plates driven by the relative motion between top and bottom counter-moving plates. Here, x, y, and z are, respectively, the streamwise, wall-normal, and spanwise directions, and u, v, and w are corresponding velocity components in these directions. The spatial variables are normalized by the channel

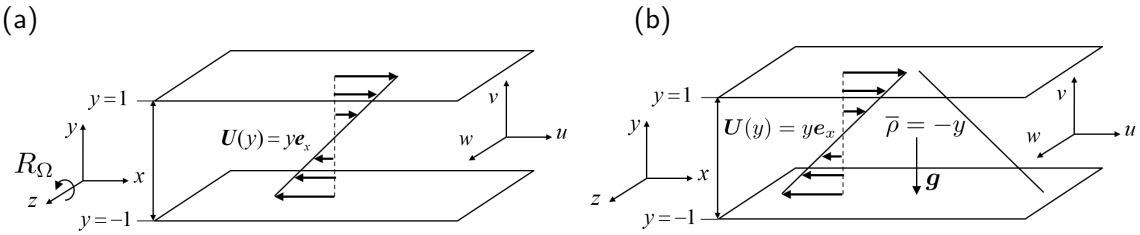

Figure 7.1: Illustration of plane Couette flows and laminar base flow $\boldsymbol{U}(y) = y\boldsymbol{e}_x$ (a) with a spanwise rotation of rotation number R_Ω; (b) with vertical stratification of a linear background density profile $\overline{\rho} = -y$.

half-height h, and the velocity is normalized by half of the velocity difference between the top and bottom walls U_w, where $\pm U_w$ is the velocity at the channel walls. The laminar base flow is $U(y) = y$, and this function is not influenced by spanwise rotation or vertical stratification. Time and pressure are, respectively, normalized by h/U_w, and $\rho_r U_w^2$, where ρ_r is a reference density. The Reynolds number is defined as $Re = U_w h/\nu$, where ν is the kinematic viscosity. We decompose the velocity field $\boldsymbol{u}_{\text{tot}} = \begin{bmatrix} u_{\text{tot}} & v_{\text{tot}} & w_{\text{tot}} \end{bmatrix}^{\mathsf{T}}$, with $^{\mathsf{T}}$ indicating the transpose, into the laminar base flow and fluctuating quantities; i.e., $\boldsymbol{u}_{\text{tot}} = U(y)\boldsymbol{e}_x + \boldsymbol{u}$ with $\boldsymbol{e}_x$ denoting the streamwise unit vector. The pressure field is decomposed similarly: $p_{\text{tot}} = P + p$. We also impose no-slip boundary conditions $\boldsymbol{u}(y = \pm 1) = \boldsymbol{0}$. In what follows, $\boldsymbol{\nabla} := \begin{bmatrix} \partial_x & \partial_y & \partial_z \end{bmatrix}^{\mathsf{T}}$ denotes the gradient operator and $\nabla^2 := \partial_x^2 + \partial_y^2 + \partial_z^2$ denotes the Laplacian operator.

The addition of spanwise rotation or vertical stratification leads to the respective configurations of rotating PCF shown in figure 7.1(a) and stratified PCF shown in figure 7.1(b). The governing equations of fluctuating quantities for both rotating PCF and stratified PCF will be presented in subsections 7.2.1 and 7.2.2, respectively. In subsection 7.2.3, we derive the mathematical equivalence between 2D/3C rotating PCF and 2D stratified PCF.

7.2.1 Spanwise rotating plane Couette flow

Here, we consider the spanwise rotating PCF configuration shown in figure 7.1(a); i.e., the rotation axis is in the spanwise direction. The dynamics of the fluctuations $\boldsymbol{u}$ and p are governed

by:

$$\partial_t \boldsymbol{u} + U\partial_x \boldsymbol{u} + v\,\frac{dU}{dy}\boldsymbol{e}_x - R_\Omega(\boldsymbol{u}\times\boldsymbol{e}_z) + \boldsymbol{\nabla} p - \frac{1}{Re}\nabla^2\boldsymbol{u} = -\boldsymbol{u}\cdot\boldsymbol{\nabla}\boldsymbol{u}, \tag{7.1a}$$

$$\boldsymbol{\nabla}\cdot\boldsymbol{u} = 0. \tag{7.1b}$$

Here, we define the rotation number as $R_\Omega = 2\Omega_z h/U_w$, where Ω_z is the rotation rate. The term in equation (7.1a) associated with R_Ω is the Coriolis acceleration due to the effect of rotation with $\times$ denoting the vector cross product and $\boldsymbol{e}_z$ denoting the unit vector in the spanwise direction. Under the coordinate configuration shown in figure 7.1(a), a positive rotation number R_Ω represents an anti-cyclonic rotation that is destabilizing when $R_\Omega \in (0, 1)$, while a negative R_Ω corresponds to a cyclonic rotation that is stabilizing (Lezius & Johnston, 1976). In this work, we focus on the latter case. The rotation also results in centrifugal force, which can be combined into static pressure, which does not appear in the dynamics of the fluctuations.

7.2.2 Vertically stratified plane Couette flow

Here, we briefly review the governing equations and flow configurations of vertically stratified PCF that were previously provided in chapter 6 as shown in figure 7.1(b) with gravity direction orthogonal to the wall. Here, we also decompose the density $\rho_{\text{tot}} = \rho_r + \overline{\rho} + \rho$, where the background density $\overline{\rho}$ and the density fluctuations ρ are normalized by ρ_0. We use ρ_0 to denote half of density difference between the top and bottom walls, and it is assumed to be much less than the reference density $\rho_0 \ll \rho_r$ so the Boussinesq approximation can be used. The governing equation of fluctuating quantities are:

$$\partial_t \boldsymbol{u} + U\partial_x \boldsymbol{u} + v\,\frac{dU}{dy}\boldsymbol{e}_x + Ri_b\,\rho\,\boldsymbol{e}_y + \boldsymbol{\nabla} p - \frac{1}{Re}\nabla^2\boldsymbol{u} = -\boldsymbol{u}\cdot\boldsymbol{\nabla}\boldsymbol{u}, \tag{7.2a}$$

$$\partial_t \rho + U\partial_x \rho + v\frac{d\overline{\rho}}{dy} - \frac{1}{RePr}\nabla^2\rho = -\boldsymbol{u}\cdot\boldsymbol{\nabla}\rho, \tag{7.2b}$$

$$\boldsymbol{\nabla}\cdot\boldsymbol{u} = 0. \tag{7.2c}$$

Here, the Prandtl number Pr and the bulk Richardson number Ri_b, are defined as:

$$Pr = \frac{\nu}{\kappa}, \quad Ri_b = \frac{g\rho_0 h}{\rho_r U_w^2}, \tag{7.3a,b}$$

where κ is the diffusivity of density and g is the magnitude of gravity. We consider the background density profile $\overline{\rho} = -y$ maintained by static pressure $P = Ri_b y^2/2$. We also consider Dirichlet boundary conditions for density fluctuations $\rho(y = \pm 1) = 0$ that can be maintained by e.g., constant temperatures at the wall with a linear equation of state (with the hotter plate at the top). This background density profile and boundary condition for density fluctuations of stratified PCF were previously studied in Eaves & Caulfield (2015); Deusebio *et al.* (2015); Taylor *et al.* (2016); Zhou *et al.* (2017*a*,*b*); Olvera & Kerswell (2017); Deguchi (2017); Langham *et al.* (2020).

7.2.3 Mathematical equivalence between 2D/3C rotating PCF and 2D stratified PCF

Here, we describe a mathematical equivalence between 2D/3C spanwise rotating PCF and 2D vertically stratified PCF:

Proposition 7.1 (2D/3C-R=2D-S) *Given two-dimensional three-component (2D/3C, no streamwise variation) spanwise rotating plane Couette flow (PCF) associated with Reynolds number Re, background velocity gradient $\frac{dU}{dy}$, and rotation number R_Ω. Given two-dimensional (2D, no streamwise variation and no streamwise velocity) vertically stratified PCF associated with the same Reynolds number Re, Prandtl number Pr, bulk Richardson number Ri_b, background density gradient $\frac{d\overline{\rho}}{dy}$, and Dirichlet boundary conditions of density fluctuation $\rho(y = \pm 1) = 0$. If*

$$R_\Omega \left(\frac{dU}{dy} - R_\Omega \right) = Ri_b \frac{d\overline{\rho}}{dy}, \quad Pr = 1, \quad \text{(2D/3C-R=2D-S)}$$

then these two flows are equivalent in the following sense. The scaled streamwise velocity fluctuation $\tilde{u} := u \left(\frac{d\overline{\rho}}{dy} \right) \Big/ \left(\frac{dU}{dy} - R_\Omega \right)$ in rotating PCF is equivalent to density fluctuations ρ in stratified PCF.

Proof: The 2D/3C (no streamwise variation; i.e., $\partial_x(\cdot) = 0$) version of equation (7.1) directly reduces the governing equation for spanwise rotating PCF of the form:

$$\partial_t u + v\left(\frac{dU}{dy} - R_\Omega\right) - \frac{1}{Re}\nabla_\perp^2 u = -\boldsymbol{u}_\perp \cdot \boldsymbol{\nabla}_\perp u, \tag{7.4a}$$

$$\partial_t \boldsymbol{u}_\perp + R_\Omega u\, \boldsymbol{e}_y + \boldsymbol{\nabla}_\perp p - \frac{1}{Re}\nabla_\perp^2 \boldsymbol{u}_\perp = -\boldsymbol{u}_\perp \cdot \boldsymbol{\nabla}_\perp \boldsymbol{u}_\perp, \tag{7.4b}$$

$$\boldsymbol{\nabla}_\perp \cdot \boldsymbol{u}_\perp = 0, \tag{7.4c}$$

where we denote the cross-stream velocity and derivative as $\boldsymbol{u}_\perp := [v, w]^\mathsf{T}$, $\boldsymbol{u}_\perp \cdot \boldsymbol{\nabla}_\perp(\cdot) := v\partial_y(\cdot) + w\partial_z(\cdot)$, $\nabla_\perp^2 := \partial_y^2 + \partial_z^2$, and $\boldsymbol{\nabla}_\perp := [\partial_y, \partial_z]^\mathsf{T}$. Then, we perform the following change of variable $u = \tilde{u}\left(\frac{dU}{dy} - R_\Omega\right) \Big/ \left(\frac{d\overline{\rho}}{dy}\right)$ to obtain:

$$\partial_t \tilde{u} + v\,\frac{d\overline{\rho}}{dy} - \frac{1}{Re}\nabla_\perp^2 \tilde{u} = -\boldsymbol{u}_\perp \cdot \boldsymbol{\nabla}_\perp \tilde{u}, \tag{7.5a}$$

$$\partial_t \boldsymbol{u}_\perp + R_\Omega\left(\frac{dU}{dy} - R_\Omega\right) \Big/ \left(\frac{d\overline{\rho}}{dy}\right) \tilde{u}\, \boldsymbol{e}_y + \boldsymbol{\nabla}_\perp p - \frac{1}{Re}\nabla_\perp^2 \boldsymbol{u}_\perp = -\boldsymbol{u}_\perp \cdot \boldsymbol{\nabla}_\perp \boldsymbol{u}_\perp, \tag{7.5b}$$

$$\boldsymbol{\nabla}_\perp \cdot \boldsymbol{u}_\perp = 0. \tag{7.5c}$$

The 2D vertically stratified PCF assumes no streamwise variation and does not include a streamwise velocity component; i.e., $\partial_x(\cdot) = 0$ and $u = 0$, which simplifies the governing equation of stratified PCF in equation (7.2) to:

$$\partial_t \rho + v\,\frac{d\overline{\rho}}{dy} - \frac{1}{RePr}\nabla_\perp^2 \rho = -\boldsymbol{u}_\perp \cdot \boldsymbol{\nabla}_\perp \rho, \tag{7.6a}$$

$$\partial_t \boldsymbol{u}_\perp + Ri_b\, \rho\, \boldsymbol{e}_y + \boldsymbol{\nabla}_\perp p - \frac{1}{Re}\nabla_\perp^2 \boldsymbol{u}_\perp = -\boldsymbol{u}_\perp \cdot \boldsymbol{\nabla}_\perp \boldsymbol{u}_\perp, \tag{7.6b}$$

$$\boldsymbol{\nabla}_\perp \cdot \boldsymbol{u}_\perp = 0. \tag{7.6c}$$

Here, we can directly a strong relationship between rescaled streamwise velocity $\tilde{u}$ in rotating PCF and density ρ in stratified PCF, when both have Dirichlet boundary conditions. To have exact mathematical equivalence between 2D/3C rotating PCF and 2D stratified PCF, we also

need to impose the condition $R_\Omega\left(\frac{dU}{dy} - R_\Omega\right) \Big/ \left(\frac{d\overline{\rho}}{dy}\right) = Ri_b$ and $Pr = 1$, which completes the proof. □

Remark 7.1 *The equivalence in proposition 7.1 is independent of the background velocity U in stratified PCF due to its 2D assumption.*

7.3 Structured input-output analysis of rotating plane Couette flow

In this section, we apply the structured input-output analysis (chapter 5) framework to rotating PCF. The Coriolis force imposed by the rotation is linear in the momentum equation (7.1a) and the nonlinearity in rotating PCF can be characterized in the same manner as non-rotating PCF (chapter 5).

Specifically, we follow the procedure in (Chapter 5), and write the nonlinear term in equation (7.1) as

$$\boldsymbol{f} := -\boldsymbol{u}\cdot\boldsymbol{\nabla}\boldsymbol{u} = \begin{bmatrix} -\boldsymbol{u}\cdot\boldsymbol{\nabla}u & -\boldsymbol{u}\cdot\boldsymbol{\nabla}v & -\boldsymbol{u}\cdot\boldsymbol{\nabla}w \end{bmatrix}^{\mathsf{T}} =: \begin{bmatrix} f_x & f_y & f_z \end{bmatrix}^{\mathsf{T}}. \tag{7.7}$$

This expression of the nonlinearity as forcing terms makes (7.1) into a set of forced linear evolution equations. The velocity field $-\boldsymbol{u}$ in (7.7) associated with the forcing components can be viewed as the gain operator, and we model this gain through $-\boldsymbol{u}_\xi$ in each component of nonlinearity:

$$\boldsymbol{f}_\xi := -\boldsymbol{u}_\xi\cdot\boldsymbol{\nabla}\boldsymbol{u} = \begin{bmatrix} -\boldsymbol{u}_\xi\cdot\boldsymbol{\nabla}u & -\boldsymbol{u}_\xi\cdot\boldsymbol{\nabla}v & -\boldsymbol{u}_\xi\cdot\boldsymbol{\nabla}w \end{bmatrix}^{\mathsf{T}} =: \begin{bmatrix} f_{x,\xi} & f_{y,\xi} & f_{z,\xi} \end{bmatrix}^{\mathsf{T}}. \tag{7.8}$$

We now define the spatio-temporal frequency response $\mathcal{H}^R_\nabla(y;k_x,k_z,\omega)$ that will form the basis of the structured input–output response of rotating PCF. We use the superscript ^{R} to distinguish this operator from the non-rotating flow (chapter 5) and stratified PCF (chapter 6). We first perform the standard transformation using the v-ω_y formulation (Schmid & Henningson, 2012) on the velocity field dynamics in (7.1). We also perform the triple Fourier transform

in (x,z,t) domain: $\widehat{\psi}(y;k_x,k_z,\omega) := \int_{-\infty}^{\infty}\int_{-\infty}^{\infty}\int_{-\infty}^{\infty}\psi(x,y,z,t)e^{-\mathrm{i}(k_x x+k_z z+\omega t)}\,dx\,dz\,dt$, where $\mathrm{i}=\sqrt{-1}$ is the imaginary unit and ω is the temporal frequency. $k_x = 2\pi/\lambda_x$ and $k_z = 2\pi/\lambda_z$ are the x and z wavenumbers, respectively.

The resulting system of the transformed linearized equations subject to $\boldsymbol{f}_\xi$ is

$$\mathrm{i}\omega\begin{bmatrix}\widehat{v}\\ \widehat{\omega}_y\end{bmatrix} = \widehat{\mathcal{A}}^R\begin{bmatrix}\widehat{v}\\ \widehat{\omega}_y\end{bmatrix} + \widehat{\mathcal{B}}\begin{bmatrix}\widehat{f}_{x,\xi}\\ \widehat{f}_{y,\xi}\\ \widehat{f}_{z,\xi}\end{bmatrix}, \quad \begin{bmatrix}\widehat{u}\\ \widehat{v}\\ \widehat{w}\end{bmatrix} = \widehat{\mathcal{C}}\begin{bmatrix}\widehat{v}\\ \widehat{\omega}_y\end{bmatrix}. \tag{7.9a,b}$$

The operator $\widehat{\mathcal{A}}^R$ in equation (7.9) is defined as:

$$\widehat{\mathcal{A}}^R(k_x,k_z) := \begin{bmatrix}\widehat{\nabla}^2 & 0\\ 0 & \mathcal{I}\end{bmatrix}^{-1}\begin{bmatrix}-\mathrm{i}k_xU\widehat{\nabla}^2 + \mathrm{i}k_xU'' + \widehat{\nabla}^4/Re & -\mathrm{i}k_zR_\Omega\\ -\mathrm{i}k_zU' + \mathrm{i}k_zR_\Omega & -\mathrm{i}k_xU + \widehat{\nabla}^2/Re\end{bmatrix}, \tag{7.10}$$

where $U' := dU(y)/dy$, $U'' := d^2U(y)/dy^2$, $\widehat{\nabla}^2 := \partial_{yy} - k_x^2 - k_z^2$, $\widehat{\nabla}^4 := \partial_y^{(4)} - 2(k_x^2 + k_z^2)\partial_{yy} + (k_x^2+k_z^2)^2$, and $\mathcal{I}$ is the identity operator. The operator $\widehat{\mathcal{A}}^R$ includes the effect of the Coriolis force as previously reported in; e.g., Wallin *et al.* (2013) and Schmid & Henningson (2012, chapter 6.2.2), and it is the same as the non-rotating equation in ((5.6a) of chapter 5) when $R_\Omega = 0$. The operator $\widehat{\mathcal{B}}$ and $\widehat{\mathcal{C}}$ are the same as equations (5.6b)-(5.6c) and the boundary conditions are the same as (5.7) that previously employed in non-rotating wall-bounded flows in chapter 5).

The spatio-temporal frequency response $\mathcal{H}^R$ of the system in (7.9), which maps the input forcing $\widehat{\boldsymbol{f}}_\xi(y;k_x,k_z,\omega)$ to the velocity vector $\widehat{\boldsymbol{u}}(y;k_x,k_z,\omega)$ at the same spatial-temporal wavenumber-frequency triplet; i.e., $\widehat{\boldsymbol{u}}(y;k_x,k_z,\omega) = \mathcal{H}^R(y;k_x,k_z,\omega)\widehat{\boldsymbol{f}}_\xi(y;k_x,k_z,\omega)$ is given by

$$\mathcal{H}^R(y;k_x,k_z,\omega) := \widehat{\mathcal{C}}\left(\mathrm{i}\omega\,\mathcal{I}_{2\times2} - \widehat{\mathcal{A}}^R\right)^{-1}\widehat{\mathcal{B}}. \tag{7.11}$$

Here $\mathcal{I}_{2\times2} := \mathrm{diag}(\mathcal{I},\mathcal{I})$, where $\mathrm{diag}(\cdot)$ indicates a block diagonal operation.

The linear form of (7.8) allows us to perform the same spatio-temporal Fourier transform as on the velocity field and decompose it as

$$\begin{bmatrix}\widehat{f}_{x,\xi}\\ \widehat{f}_{y,\xi}\\ \widehat{f}_{z,\xi}\end{bmatrix} = \mathrm{diag}\left(-\widehat{\boldsymbol{u}}_\xi^{\mathsf{T}}, -\widehat{\boldsymbol{u}}_\xi^{\mathsf{T}}, -\widehat{\boldsymbol{u}}_\xi^{\mathsf{T}}\right)\mathrm{diag}\left(\widehat{\boldsymbol{\nabla}}, \widehat{\boldsymbol{\nabla}}, \widehat{\boldsymbol{\nabla}}\right)\begin{bmatrix}\widehat{u}\\ \widehat{v}\\ \widehat{w}\end{bmatrix}. \tag{7.12}$$

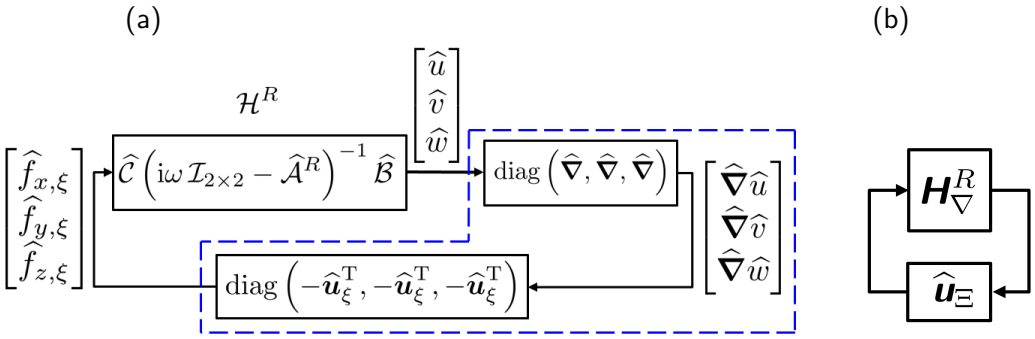

Figure 7.2: Illustration of structured input–output analysis of rotating plane Couette flow: (a) a componentwise description, where blocks inside of (– –, blue) represent the modeled forcing in equation (7.12); (b) a high-level description after discretization.

A block diagram illustrating this model is shown inside the blue dashed line (– –) in figure 7.2(a).

We combine the linear gradient operator with $\mathcal{H}^R$ to isolate the gain $-\boldsymbol{u}_\xi$ that is associated with the response we seek to find. The resulting modified frequency response operator is

$$\mathcal{H}_\nabla^R(y;k_x,k_z,\omega) := \mathrm{diag}\left(\widehat{\boldsymbol{\nabla}},\widehat{\boldsymbol{\nabla}},\widehat{\boldsymbol{\nabla}}\right)\mathcal{H}^R(y;k_x,k_z,\omega). \tag{7.13}$$

The resulting system model is a feedback interconnection between this linear operator and the structured uncertainty

$$\widehat{\boldsymbol{u}}_\Xi := \mathrm{diag}\left(-\widehat{\boldsymbol{u}}_\xi^{\mathsf{T}},-\widehat{\boldsymbol{u}}_\xi^{\mathsf{T}},-\widehat{\boldsymbol{u}}_\xi^{\mathsf{T}}\right). \tag{7.14}$$

The block-diagonal structure in (7.14) leads to a forcing model that retains the componentwise structure of the nonlinearity. Figure 7.2(b) describes the resulting feedback interconnection, where $\boldsymbol{H}_\nabla^R$ and $\widehat{\boldsymbol{u}}_\Xi$ respectively represent the numerical approximations of $\mathcal{H}_\nabla^R$ in (7.13) and $\widehat{\boldsymbol{u}}_\Xi$ in (7.14).

We are interested in characterizing the horizontal length scales of the most amplified flow structures under structured forcing, which can be characterized by the largest structure singular value across all temporal frequencies. The amplification under structured forcing is defined in the same manner described in chapter 5, i.e.,

$$\|\mathcal{H}_\nabla^R\|_\mu(k_x,k_z) := \sup_{\omega\in\mathbb{R}} \mu_{\widehat{\boldsymbol{U}}_\Xi}\left[\boldsymbol{H}_\nabla^R(k_x,k_z,\omega)\right]. \tag{7.15}$$

Here, sup represents the supremum, and $\mu_{\widehat{\boldsymbol{U}}_\Xi}\left[\boldsymbol{H}_\nabla^R\right]$ is the structured singular value (definition

5.1 in chapter 5) associated with $\boldsymbol{H}_{\nabla}^{R}$, and the set $\widehat{\boldsymbol{U}}_{\Xi}$ contains all uncertainties perturbations that have the same block-diagonal structure as $\widehat{\boldsymbol{u}}_{\Xi}$; i.e., $\widehat{\boldsymbol{u}}_{\Xi} \in \widehat{\boldsymbol{U}}_{\Xi}$. This value $\|\mathcal{H}_{\nabla}^{R}\|_{\mu}(k_x, k_z)$ in (7.15) directly quantifies most amplified flow structures (characterized by the associated k_x and k_z pair) under structured forcing.

We employ the Chebyshev differential matrix (Weideman & Reddy, 2000; Trefethen, 2000) to discretize the operators in equation (7.10). The code is validated through comparison of plane Couette and Poiseuille flow results in Jovanović (2004); Jovanović & Bamieh (2005); Schmid (2007). The implementation of spanwise rotation is validated by reproducing the neutral curve in spanwise rotating plane Poiseuille flow (Wallin *et al.*, 2013, figure 2). We use $N_y = 60$ collocation points in the wall-normal direction (excluding the boundary points) along with 48 and 36 logarithmically spaced streamwise and spanwise wavenumbers in the respective spectral ranges $k_x \in [10^{-4}, 10^{0.48}]$ and $k_z \in [10^{-2}, 10^{1.2}]$, unless otherwise mentioned. We also compute results with 1.5 times collocation points in the wall normal direction and verify that the results do not change. The quantity $\|\mathcal{H}_{\nabla}^{R}\|_{\mu}$ in (7.15) for each wavenumber pair (k_x, k_z) is computed using the `mussv` command in the Robust Control Toolbox (Balas *et al.*, 2005) of MATLAB. The arguments of `mussv` employed here include the state-space model of $\boldsymbol{H}_{\nabla}^{R}$ that samples the frequency domain adaptively. The `BlockStructure` argument comprises three full $N_y \times 3N_y$ complex matrices, and we set the `'Uf'` option corresponding to fast algorithm.

7.4 Structured spatio-temporal frequency response under mathematical equivalence (2D/3C-R=2D-S)

In this section, we employ this structured input-output analysis to both spanwise rotating PCF and stratified PCF to characterize the region over which condition required for mathematical equivalence of 2D/3C rotating PCF and 2D stratified PCF lead to similar dominant flow structures within the full systems. The results of structured input-output analysis $\|\mathcal{H}_{\nabla}^{S}\|_{\mu}$ for stratified PCF were computed using the formulation detailed in chapter 6, and the superscript ^{S} highlights that this quantity is associated with stratified PCF. All results $\|\mathcal{H}_{\nabla}^{S}\|_{\mu}$ of stratified PCF here

satisfies condition (2D/3C-R=2D-S); i.e., $Pr = 1$ and $Ri_b = -R_\Omega(1 - R_\Omega)$. § 7.4.1 shows that this condition does indeed provide similar behavior under slow rotation and weak stratification, but this similarity breaks down under rapid rotation and strong stratification as shown in § 7.4.2. Building upon these observations, we then propose a mathematical equivalence between 2D/3C rotating PCF with passive scalar and 2D/3C stratified PCF in § 7.4.3.

7.4.1 Full dynamic analogy between slow rotation and weak stratification

Here, we employ structured input-output analysis for rotating PCF at $Re = 750$ and $R_\Omega = -0.02$. This is the flow regime where oblique turbulent bands are observed in rotating PCF; see e.g., (Brethouwer *et al.*, 2012, figure 4(b)) and (Tsukahara *et al.*, 2010*a*, figure 4).

We first demonstrate the efficacy of our model by comparing the growth rate computed as:

$$R[\widehat{\mathcal{A}}^R(k_x, k_z)] := \max\left\{\mathbb{R}e\left[\text{eig}\left(\widehat{\boldsymbol{A}}^R(k_x, k_z)\right)\right]\right\}, \tag{7.16}$$

where eig$(\cdot)$ is the eigenvalue, $\mathbb{R}e[\cdot]$ represents the real part, max$\{\cdot\}$ is the maximum, and $\widehat{\boldsymbol{A}}^R$ is the discretization of $\widehat{\mathcal{A}}^R$ operator. Figure 7.3 shows the resulting $R[\widehat{\mathcal{A}}^R(k_x, k_z)]$ and it cannot distinguish the preference among a wide range of wavenumbers $k_x \lesssim 1$ and $k_z \lesssim 10$. To further illustrate the relative effect of the feedback interconnection as well as the imposed structure, we compare the results to

$$\|\mathcal{H}^R\|_\infty(k_x, k_z) := \sup_{\omega\in\mathbb{R}} \bar{\sigma}\left[\boldsymbol{H}^R(k_x, k_z, \omega)\right], \tag{7.17}$$

where $\bar{\sigma}$ is the largest singular value of the argument and $\boldsymbol{H}^R$ is the discretization of operator $\mathcal{H}^R$ in (7.11). The $\|\mathcal{H}\|_\infty$ norm for non-rotating plane Couette and plane Poiseuille flows was previously analyzed (Jovanović, 2004; Schmid, 2007; Illingworth, 2020). This quantity in (7.17) describes the maximum singular value of the frequency response operator $\mathcal{H}^R$ over all temporal frequencies. To isolate the effect of the structure imposed on the nonlinearity from the effect of imposing the closed-loop feedback interconnection, we also compute

$$\|\mathcal{H}^R_\nabla\|_\infty(k_x, k_z) := \sup_{\omega\in\mathbb{R}} \bar{\sigma}\left[\boldsymbol{H}^R_\nabla(k_x, k_z, \omega)\right]. \tag{7.18}$$

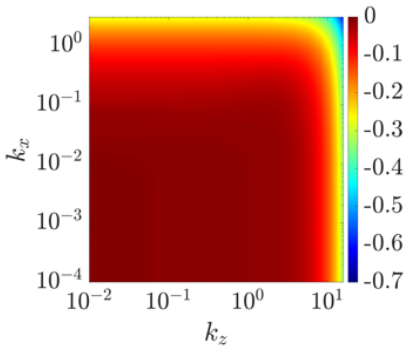

Figure 7.3: $R[\mathcal{A}^R(k_x, k_z)]$ for rotating plane Couette flow at $Re = 750$ and $R_\Omega = -0.02$.

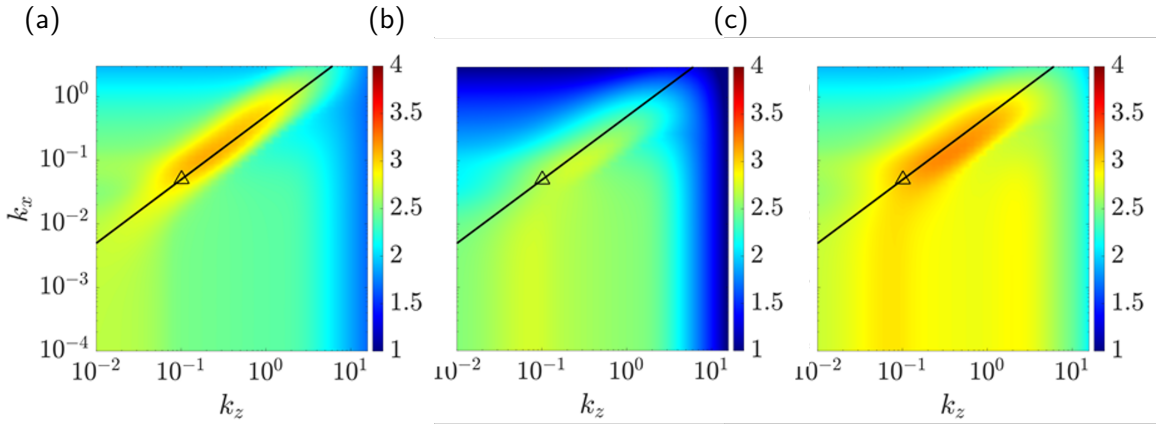

Figure 7.4: (a) $\log_{10}[\|\mathcal{H}_\nabla^R\|_\mu(k_x, k_z)]$, (b) $\log_{10}[\|\mathcal{H}^R\|_\infty(k_x, k_z)]$ and (c) $\log_{10}[\|\mathcal{H}_\nabla^R\|_\infty(k_x, k_z)]$ for rotating plane Couette flow at $Re = 750$ and $R_\Omega = -0.02$. Here symbols are characteristic wavelengths of turbulent band observed in rotating plane Couette flow at $Re = 750$, $R_\Omega = -0.02$; ($\triangle$): $\lambda_x = 125$, $\lambda_z = 62$ from DNS (Brethouwer *et al.*, 2012, figures 4(b) and 17). The black solid line (—) is $\lambda_z = \lambda_x \tan(26^\circ)$ representing a 26° angle of the oblique turbulent bands.

This quantity is the unstructured counterpart of $\|\mathcal{H}_\nabla^R\|_\mu$ that does not specify a particular feedback pathway associated with each component of forcing, which can be obtained by replacing the uncertainty set $\widehat{\boldsymbol{U}}_\Xi$ with the set of full complex matrices $\mathbb{C}^{3N_y \times 9N_y}$.

Figure 7.4 shows quantity (a) $\|\mathcal{H}_\nabla^R\|_\mu$ using structured input-output analysis alongside input-output based approach describing the most amplified flow structures in terms of (b) $\|\mathcal{H}^R\|_\infty$ in equation (7.17) and (c) $\|\mathcal{H}_\nabla^R\|_\infty$ in equation (7.18). The input-output based analyses in figure 7.4 reveal some preference among these wavenumber pairs. In these panels, the symbol ($\triangle$, black) marks $\lambda_x = 125$ and $\lambda_z = 62$, which correspond to the oblique turbulent bands observed in rotating PCF using DNS at $Re = 750$ and $R_\Omega = -0.02$ with channel size $L_x = 250$, $L_z = 125$ (Brethouwer *et al.*, 2012, figures 4(b) and 17). These structures are observed to have

a characteristic inclination angle (measured from the streamwise direction in $x-z$ plane) of $\theta := \tan^{-1}(\lambda_z/\lambda_x) \approx 26^\circ$ represented by the black solid line (—): $\lambda_z = \lambda_x \tan(26^\circ)$.

The results from traditional input-output analysis $\|\mathcal{H}^R\|_\infty$ in figure 7.4(b) leads to a noticeable improvement compared with growth rate analysis $R(\widehat{\mathcal{A}}^R)$ in figure 7.3 as it identifies preferred wavenumber pair in this intermittent regime. Moreover, the inclusion of an unstructured feedback loop for $\|\mathcal{H}^R_\nabla\|_\infty$ in figure 7.4(c) further leads to further improvements and correctly orders the relative of amplification between the oblique turbulent bands and streamwise elongated structures ($k_x \approx 0$). The imposition of the componentwise structure from the nonlinear terms in (7.7) for $\|\mathcal{H}^R_\nabla\|_\mu$ in figure 7.4(a) further improves the prediction of the oblique turbulent bands. While there is some footprint of these structures and this angle in all three panels, the characteristic wavelengths and angle of the oblique turbulent bands reported in DNS (Brethouwer *et al.*, 2012) correspond to the peak value of $\|\mathcal{H}^R_\nabla\|_\mu$ in figure 7.4(a) and the line representing the angle of the structures is quite consistent with the shape of the peak region. This suggests that structured input–output analysis captures both wavelengths and angle of the oblique turbulent bands in the intermittent regime of rotating PCF, and that they are associated with large amplification (sensitivity to disturbances).

The peak region of $\|\mathcal{H}^R_\nabla\|_\mu$ associated with the oblique turbulent bands observed in figure 7.4(a) is very similar to the shape of its counterpart $\|\mathcal{H}^S_\nabla\|_\mu$ in stratified PCF at $Re = 865$, $Pr = 0.7$, and $Ri_b = 0.02$ (figure 6.4(a) in chapter 6) corresponding to the flow regime where oblique turbulent bands are also observed (Deusebio *et al.*, 2015; Taylor *et al.*, 2016). Here, we note that the flow regime of stratified PCF that satisfies the condition in the proposition 7.1 (2D/3C-R=2D-S) will be $Re = 750$, $Pr = 1$, and $Ri_b = 0.0204$ corresponding to $Re = 750$ and $R_\Omega = -0.02$ in rotating PCF. This suggests that a slow rotation and weak stratification plays a similar role in modifying the dynamics of plane Couette flow. The lift-up mechanism (i.e., cross-stream forcing amplifies streamwise elongated streaks) is known to be important for quasi-streamwise ($k_x \ll k_z$) and streamwise elongated ($k_x \approx 0$) flow structures in wall-bounded flows (Ellingsen & Palm, 1975; Landahl, 1975; Brandt, 2014), and it is associated

with both the spanwise variation $k_z \neq 0$ and the wall-normal velocity v; see e.g., coupling term $-\mathrm{i}k_z U' v$ in the evolution equation of wall-normal vorticity; (Jiménez, 2018, equation (6.3)) and (Jovanović, 2021, section 3.1). The spanwise rotation reduces spanwise variation $\partial_z(\cdot)$ and vertical stratification inhibits wall-normal velocity v, and, thus, both of these effects suppress the amplification associated with the lift-up mechanism.

Furthermore, structured input-output analysis shows that the secondary dominant flow structures ($k_x \approx 0$ regimes) of rotating PCF in figure 7.4(a) are associated with a smaller k_z value compared with stratified PCF (figure 6.4(a) in chapter 6). This suggests that spanwise rotation directly reduces the spanwise variation along the rotation axis due to the Taylor-Proudman effect (Taylor, 1917; Proudman, 1916; Davidson, 2013), while the vertical stratification inhibits the vertical motion, which suppresses the amplification of spanwise varying flow structures indirectly. This behavior indicates that spanwise rotation is likely suppressing amplification of spanwise varying flow structures faster than vertical stratification.

We now quantify the similarity and difference between $\|\mathcal{H}_\nabla^R\|_\mu$ of rotating PCF and $\|\mathcal{H}_\nabla^S\|_\mu$ of stratified PCF by isolating the effect of forcing in each component of the momentum equation, i.e. f_x, f_y, f_z in equation (7.7) on the amplification of each velocity component u, v, w. These nine quantities are associated with $\|\mathcal{H}_{ij}^R\|_\infty$, where the spatio-temporal frequency response operator $\mathcal{H}_{ij}^R$ from each forcing component ($j = x, y, z$) to each velocity component ($i = u, v, w$) is

$$\mathcal{H}_{ij}^R = \widehat{\mathcal{C}}_i \left(\mathrm{i}\omega \mathcal{I}_{2\times 2} - \widehat{\mathcal{A}}^R\right)^{-1} \widehat{\mathcal{B}}_j \tag{7.19}$$

with the operators $\widehat{\mathcal{C}}_i$ and $\widehat{\mathcal{B}}_j$ defined in (5.19) in chapter 5.

Figure 7.5 shows $\|\mathcal{H}_{ij}^R\|_\infty$ with $i = u, v, w$ and $j = x, y, z$ and we can see that the diagonal panels resemble the shape of the $\|\mathcal{H}_\nabla^R\|_\mu$ because the structured input-output analysis constrains the permissible feedback pathway as $f_x \to u$, $f_y \to v$, and $f_z \to w$ similar to previous observations (chapters 5-6). We also compare with $\|\mathcal{H}_{ij}^S\|_\infty$ for stratified PCF at $Re = 865$, $Pr = 0.7$, and $Ri_b = 0.02$ (figure 6.10 in chapter 6). The shape of $\|\mathcal{H}_{ux}^R\|_\infty$ of rotating PCF in figure 7.5(a) shows a difference from $\|\mathcal{H}_{ux}^S\|_\infty$ of stratified PCF (figure 6.10(a) in chapter 6), where

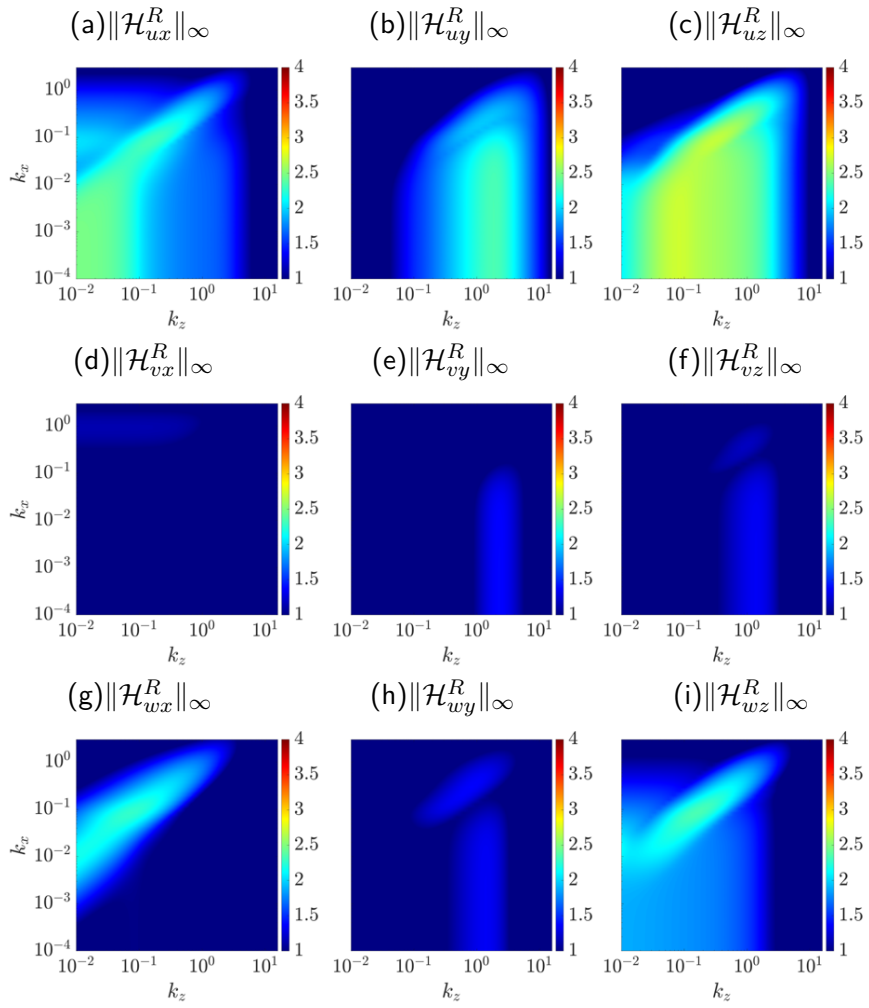

Figure 7.5: Componentwise analysis $\|\mathcal{H}_{ij}\|_\infty$ of rotating PCF at $Re = 750$ and $R_\Omega = -0.02$. Each column from left to right corresponds to input f_x, f_y, f_z, and each row from top to bottom corresponds to output u, v, and w.

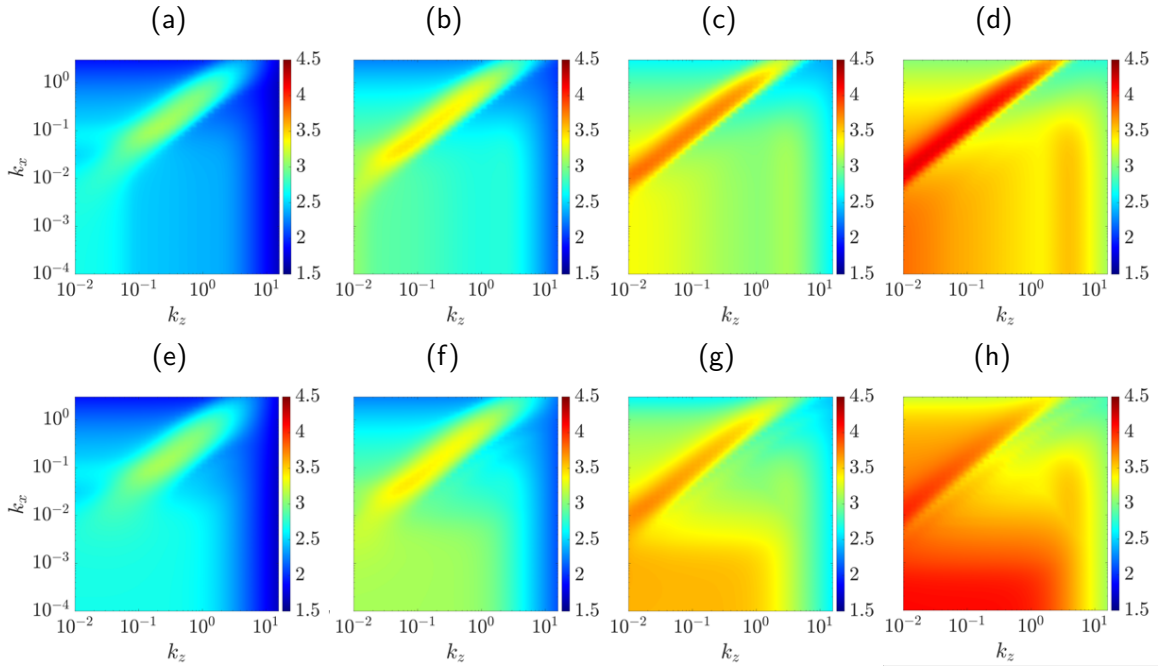

Figure 7.6: Top row: $\log_{10}[\|\mathcal{H}^R_\nabla\|_\mu(k_x,k_z)]$ for rotating PCF at (a) $Re = 750$, $R_\Omega = -0.02$; (b) $Re = 2000$, $R_\Omega = -0.048$; (c) $Re = 6000$, $R_\Omega = -0.116$; (d) $Re = 20000$, $R_\Omega = -0.2$. Bottom row: $\log_{10}[\|\mathcal{H}^S_\nabla\|_\mu(k_x,k_z)]$ for stratified PCF with $Pr = 1$ and (e) $Re = 750$, $Ri_b = 0.0204$; (f) $Re = 2000$, $Ri_b = 0.0503$; (g) $Re = 6000$, $Ri_b = 0.1295$; (h) $Re = 20000$, $Ri_b = 0.24$ based on the condition (2D/3C-R=2D-S).

the rotating PCF constrains the spanwise wavenumber k_z to a smaller value compared with the stratified PCF. This difference is due to the fact that spanwise rotation provide restoring force in streamwise and wall-normal momentum equations, but vertial stratification provide restoring force in wall-normal momentum and density equations; i.e., vertical stratification influence the streamwise velocity and streamwise momentum equation indirectly. This difference between $\|\mathcal{H}^R_{ux}\|_\infty$ and its counterpart $\|\mathcal{H}^S_{ux}\|_\infty$ in stratified PCF also results in the difference between the shape of $\|\mathcal{H}^R_\nabla\|_\mu$ in rotating PCF and $\|\mathcal{H}^S_\nabla\|_\mu$ in stratified PCF at the region $k_x \approx 0$. The amplifications varying over (k_x, k_z) in other panels $\|\mathcal{H}^R_{ij}\|_\infty$ $(ij \neq ux)$ of figure 7.5 are very close to their counterpart $\|\mathcal{H}^S_{ij}\|_\infty$ $(ij \neq ux)$ in stratified PCF (figure 6.10 in chapter 6).

7.4.2 Rapid rotation and strong stratification regime

In this subsection, we then study similarity in the flow structures of rotating PCF and stratified PCF under the conditions (2D/3C-R=2D-S) at rapid rotation and strong stratification. Here, we

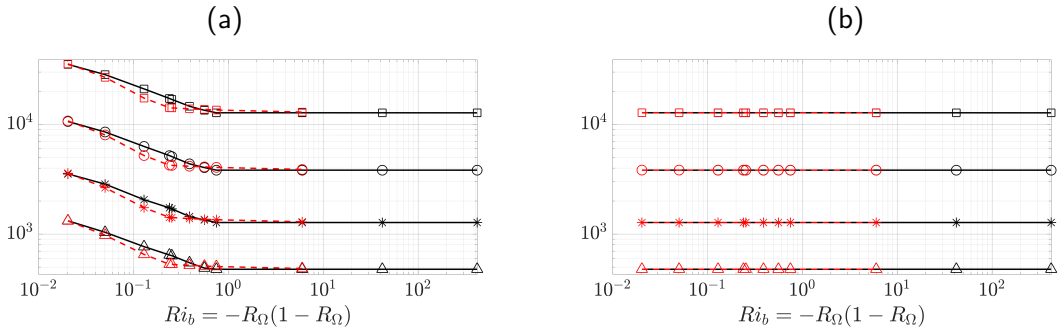

Figure 7.7: (a)The black solid lines are $\|\mathcal{H}_\nabla^R\|_\mu^M$ of rotating PCF at $Re = 750$ (△), $Re = 2000$ (✳), $Re = 6000$ (○), and $Re = 20000$ (□). The red dashed lines are $\|\mathcal{H}_\nabla^S\|_\mu^M$ stratified PCF at $Re = 750$ (△), $Re = 2000$ (✳), $Re = 6000$ (○), and $Re = 20000$ (□). (b) The black solid lines are $\|\mathcal{H}_\nabla^R\|_\mu^{sc}$ of rotating PCF and the red dashed lines are $\|\mathcal{H}_\nabla^S\|_\mu^{sc}$ of stratified PCF. The symbols in panel (b) represent the same Reynolds number as panel (a). Here, all results of stratified PCF are associated with $Pr = 1$.

increase the stabilizing effect of the rotation and stratification as well as the Reynolds number. This is based on the observation that the oblique turbulent bands are prevalent in the intermittent regime are observed at a higher Reynolds number with a stronger stabilizing body force; e.g., see experiments (Tsukahara *et al.*, 2010*b*, figure 2) and DNS (Brethouwer *et al.*, 2012, figure 5) of rotating PCF as well as DNS of stratified PCF (Deusebio *et al.*, 2015, figure 18). The top row of figure 7.6 replots the quantity $\|\mathcal{H}_\nabla^R\|_\mu$ at (a) $Re = 750$, $R_\Omega = -0.02$ (in a different range of color bar) along with results associated with higher Reynolds number and higher magnitudes of rotation number $|R_\Omega|$. These flow regimes are chosen based on the DNS study of the oblique turbulent bands in rotating PCF (Brethouwer *et al.*, 2012, table 1). The bottom row of figure 7.6 shows that the quantity $\|\mathcal{H}_\nabla^S\|_\mu$ with Ri_b and Pr satisfies the condition (2D/3C-R=2D-S). For results at $Re = 20000$ in figures 7.6(d) and (h) the wall-normal grid points are increased to $N_y = 92$. In all of these panels, $\|\mathcal{H}_\nabla^R\|_\mu$ for rotating PCF is constrained to smaller k_z compared with $\|\mathcal{H}_\nabla^S\|_\mu$. In figure 7.6, panels (a)$R_\Omega = -0.02$, (b)$R_\Omega = -0.048$ for rotating PCF and (e)$Ri_b = 0.0204$, (f)$Ri_b = 0.0503$ for stratified PCF show their peaks are close in values and have similar shapes under the condition (2D/3C-R=2D-S), and both of them associated with the oblique turbulent bands. However, the amplification of streamwise varying flow structures such as oblique turbulent bands are suppressed faster in stratified PCF than rotating PCF under the condition (2D/3C-R=2D-S).

We next further compare the efficiency of reducing streamwise variation by rotation and stratification. We aggregate results varying over a range of (k_x, k_z) wavenumber pairs:

$$\|\mathcal{H}_\nabla^R\|_\mu^M := \max_{k_z,\, k_x} \|\mathcal{H}_\nabla^R\|_\mu(k_x, k_z), \tag{7.20}$$

where max represents the maximum value over an enlarged wavenumber domain $k_x \in [10^{-6}, 10^{0.48}]$ and $k_z \in [10^{-6}, 10^{0.48}]$. We then enforce a streamwise constant assumption by restricting the streamwise wavenumber to $k_x = 10^{-6}$:

$$\|\mathcal{H}_\nabla^R\|_\mu^{sc} := \max_{k_z,\, k_x = 10^{-6}} \|\mathcal{H}_\nabla^R\|_\mu(k_x, k_z). \tag{7.21}$$

Comparing the difference between $\|\mathcal{H}_\nabla^R\|_\mu^M$ and $\|\mathcal{H}_\nabla^R\|_\mu^{sc}$ directly shows the efficiency of suppressing the amplification of streamwise varying flow structures by increasing rotation rate. The restriction to streamwise constant mode $\|\mathcal{H}_\nabla^R\|_\mu^{sc}$ is also motivated by this assumption in the mathematical equivalence (2D/3C-R=2D-S).

Figure 7.7(a) plots $\|\mathcal{H}_\nabla^R\|_\mu^M$ for rotating PCF in black solid lines and $\|\mathcal{H}_\nabla^S\|_\mu^M$ for stratified PCF in red dashed lines for four different Reynolds numbers. Figure 7.7(b) then presents the amplification of streamwise constant modes $\|\mathcal{H}_\nabla^R\|_\mu^{sc}$ for rotating PCF and $\|\mathcal{H}_\nabla^S\|_\mu^{sc}$ for stratified PCF with the same markers as panel (a). Here, the horizontal axis is plotted as $Ri_b = -R_\Omega(1 - R_\Omega)$ based on the condition associated with (2D/3C-R=2D-S). We can observe that at $R_\Omega = -0.02$ ($Ri_b = 0.0204$) the amplifications $\|\mathcal{H}_\nabla^R\|_\mu$ of rotating PCF and $\|\mathcal{H}_\nabla^S\|_\mu$ of stratified PCF are very close in value, which also corresponds to the observation in the first columns of figure 7.6. As $|R_\Omega|$ or Ri_b increases, rotating PCF and stratified PCF follow different trends. The stratification is suppressing the amplification of $\|\mathcal{H}_\nabla^S\|_\mu$ in stratified PCF faster than its counterpart $\|\mathcal{H}_\nabla^R\|_\mu$ of rotating PCF. This observation is also consistent with the observation in figure 7.6 for their different feature over (k_x, k_z). Here, we note that suppressing the amplification of streamwise varying flow structures is a secondary effect of either spanwise rotation or vertical stratification, and the quantification using structured input-output analysis reveals their different efficiency in suppressing the amplification of streamwise varying flow structures.

For amplification of streamwise constant flow structures in figure 7.7(b), we observe that increasing $|R_\Omega|$ (the rotation rate of stabilizing rotation) does not influence the $\|\mathcal{H}^R_\nabla\|^{sc}_\mu$ similar to the observation that Ri_b does not influence $\|\mathcal{H}^S_\nabla\|^{sc}_\mu$ in stratified PCF (chapter 6). Thus, both of them are associated with the same quantity of PCF, and the amplification of rotating PCF and stratified PCF overlap with each other over a wide range of $Ri_b = -R_\Omega(1 - R_\Omega)$.

The independence of streamwise constant amplification versus the rotation number can be similarly analyzed as the independence versus bulk Richardson number in stratified PCF (chapter 6). We consider the limit of streamwise and spanwise invariant $k_x = k_z = 0$, which directly results in $\partial_y v = 0$ from the continuity equation. The boundary condition $v(y = \pm 1) = 0$ then directly results in $v = 0$. Using these assumptions, we can then obtain $U\partial_x(\cdot) = 0$, $\boldsymbol{u}\cdot\boldsymbol{\nabla}(\cdot) = 0$, and $vU' = 0$, which can simplify the governing equation of rotating PCF to:

$$\partial_t u = \frac{1}{Re}\partial_y^2 u, \quad \partial_y p = -R_\Omega u, \quad \partial_t w = \frac{1}{Re}\partial_y^2 w, \tag{7.22a-c}$$

Under this limit, the difference of rotation number can be directly balanced by a rescaled pressure without influencing other velocities.

7.4.3 Mathematical equivalence between 2D/3C rotating PCF with a passive scalar and 2D/3C stratified PCF

The overlap between the most amplified structures in 2D/3C rotating PCF and 2D/3C stratified PCF in figure 7.7(b) also suggests that they may have additional mathematical equivalence outside of the conditions in proposition 7.1. 2D/3C stratified PCF has the addition of a density variable compared with 2D/3C rotating PCF. To establish their mathematical equivalence, we propose augmenting the 2D/3C rotating PCF with a passive scalar, where we employ Θ to denote this passive scalar fluctuation associated with background scalar gradient $\frac{d\overline{\Theta}}{dy}$ and Schmidt number $Sc := \frac{\nu}{D}$, where D is the mass diffusivity. The corresponding mathematical equivalence between 2D/3C rotating PCF with a passive scalar and 2D/3C stratified PCF is stated in the next proposition:

Proposition 7.2 (2D/3C-R+P=2D/3C-S) *Given two-dimensional three-component (2D/3C, no streamwise variation) spanwise rotating plane Couette flow (PCF) associated with Reynolds number Re, background velocity gradient $\frac{dU}{dy}$, rotation number R_Ω, a passive scalar with fluctuations Θ, background scalar gradient $\frac{d\overline{\Theta}}{dy}$, and Schmidt number Sc. Given 2D/3C vertically stratified PCF associated with the same Reynolds number Re, background velocity gradient $\frac{dU}{dy}$, Prandtl number Pr, bulk Richardson number Ri_b, background density gradient $\frac{d\overline{\rho}}{dy}$, and Dirichlet boundary conditions of density fluctuation $\rho(y=\pm 1)=0$. If*

$$R_\Omega\left(\frac{dU}{dy}-R_\Omega\right)=Ri_b\frac{d\overline{\rho}}{dy},\ \ Pr=1,\ \ \frac{d\overline{\Theta}}{dy}=\frac{dU}{dy},\ \ Sc=1, \qquad \text{(2D/3C-R+P=2D/3C-S)}$$

then these two flows are equivalent in the following sense. The scaled streamwise velocity fluctuation $\tilde{u}:=u\left(\frac{d\overline{\rho}}{dy}\right)\Big/\left(\frac{dU}{dy}-R_\Omega\right)$ and passive scalar fluctuation Θ in rotating PCF are respectively equivalent to the density fluctuation ρ and streamwise velocity fluctuation u in stratified PCF.

Proof: Compared with proposition 7.1 (2D/3C-R=2D-S), this augments 2D/3C rotating PCF with a passive scalar and adds the streamwise velocity component on 2D stratified PCF to yield 2D/3C velocity field. The governing equation of a passive scalar with a fluctuating component Θ, background scalar gradient $\frac{d\overline{\Theta}}{dy}$ and Schmidt number Sc in 2D/3C rotating PCF is:

$$\partial_t\Theta+v\,\frac{d\overline{\Theta}}{dy}-\frac{1}{ReSc}\nabla_\perp^2\Theta=-\boldsymbol{u}_\perp\cdot\boldsymbol{\nabla}_\perp\Theta. \tag{7.23}$$

The governing equation of streamwise velocity u in 2D/3C stratified PCF is:

$$\partial_t u+v\,\frac{dU}{dy}-\frac{1}{Re}\nabla_\perp^2 u=-\boldsymbol{u}_\perp\cdot\boldsymbol{\nabla}_\perp u. \tag{7.24}$$

When $\frac{d\overline{\Theta}}{dy}=\frac{dU}{dy}$ and $Sc=1$, the scalar fluctuation Θ in 2D/3C rotating PCF is equivalent to the streamwise velocity fluctuation u in 2D/3C stratified PCF. Combining this condition with the condition (2D/3C-R=2D-S), we have that 2D/3C rotating PCF with a passive scalar that is equivalent to 2D/3C stratified PCF under the condition (2D/3C-R+P=2D/3C-S). □

Structured input-output analysis of rotating PCF with a passive scalar is computed by modifying the formulation of stratified PCF (chapter 6) and combining it with the Coriolis force using the procedure of modifying $\widehat{\mathcal{A}}^R$ operator in (7.10). We denote the structured input-output analysis of this system as $\|\mathcal{H}_\nabla^{R+P}\|_\mu$ with the superscript $^{R+P}$ highlighting the fact that it has an additional passive scalar compared with rotating PCF. Figure 7.8 presents the results of $\|\mathcal{H}_\nabla^{R+P}\|_\mu$ at the same Reynolds number and rotation number as figure 7.6 with the condition in the proposition (2D/3C-R+P=2D/3C-S). For the amplification associated with the oblique turbulent band that has streamwise variation, the behavior of $\|\mathcal{H}_\nabla^{R+P}\|_\mu$ in figure 7.8 is close to that of $\|\mathcal{H}_\nabla^{R}\|_\mu$ in figures 7.6(a)-(d).

At the bottom region of (k_x, k_z) in figure 7.8 associated with $k_x \approx 10^{-4}$, results of $\|\mathcal{H}_\nabla^{R+P}\|_\mu$ are very close to $\|\mathcal{H}_\nabla^{S}\|_\mu$ for stratified PCF in figures 7.6(e)-(h). This corresponds to the fact that proposition 7.2 establishes their mathematical equivalence at the 2D/3C ($k_x = 0$) flow configuration. We also recall that the passive scalar fluctuation Θ is equivalent to the streamwise velocity fluctuation in proposition 7.2, which also compensates for the difference between $\|\mathcal{H}_{ux}^{R}\|_\infty$ in figure 7.5(a) and its counterpart $\|\mathcal{H}_{ux}^{S}\|_\infty$ for stratified PCF (figure 6.10(a) in chapter 6). Figure 7.9 shows that $\|\mathcal{H}_\nabla^{R+P}\|_\mu(0, k_z)$ and $\|\mathcal{H}_\nabla^{S}\|_\mu(0, k_z)$ overlap, which further confirms the equivalence in proposition 7.2. The values of $\|\mathcal{H}_\nabla^{R}\|_\mu(0, k_z)$ are instead constrained k_z to a smaller value where $\|\mathcal{H}_\nabla^{R}\|_\mu(0, k_z)$ and $\|\mathcal{H}_\nabla^{S}\|_\mu(0, k_z)$ overlap over each other. This behavior corresponds to the difference between rotating PCF and stratified PCF in figure 7.6 at the 2D/3C ($k_x \approx 0$) limit.

7.5 Summary

In this work, we apply structured input-output analysis to study flow structures in plane Couette flow with a stabilizing spanwise rotation. First, we show that at a relatively slow rotation rate, the structured input-output also captures the wavelength of oblique turbulent bands observed in spanwise rotating PCF (Brethouwer *et al.*, 2012), similar to the observation in the stratified PCF (chapter 6). The analysis then focuses on a mathematical equivalence between two-dimensional

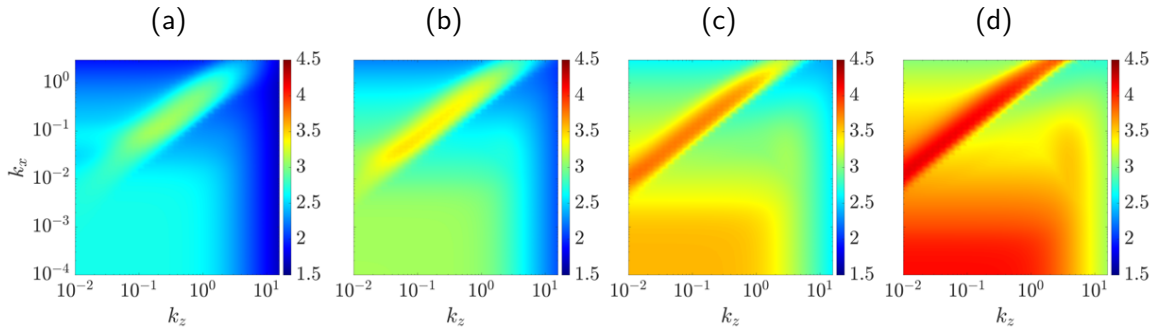

Figure 7.8: $\log_{10}[\|\mathcal{H}_{\nabla}^{R+P}\|_{\mu}(k_x, k_z)]$ for rotating PCF with $\frac{d\overline{\Theta}}{dy} = \frac{dU}{dy}$ and $Sc = 1$ at (a) $Re = 750$, $R_\Omega = -0.02$; (b) $Re = 2000$, $R_\Omega = -0.048$; (c) $Re = 6000$, $R_\Omega = -0.116$; (d) $Re = 20000$, $R_\Omega = -0.2$

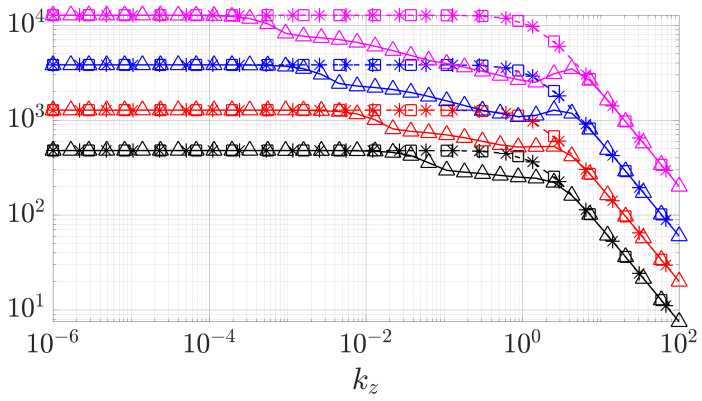

Figure 7.9: Amplification of streamwise constant $k_x = 0$ flow structures of rotating PCF $\|\mathcal{H}_{\nabla}^{R}\|_{\mu}(0, k_z)$ ($\triangle$), rotating PCF with passive scalar $\|\mathcal{H}_{\nabla}^{R+P}\|_{\mu}(0, k_z)$ ($\square$), and stratified PCF $\|\mathcal{H}_{\nabla}^{S}\|_{\mu}(0, k_z)$ ($*$). Four different colors from bottom to top correspond to four different Reynolds number and rotation number: (black): $Re = 750$, $R_\Omega = -0.02$; (red): $Re = 2000$, $R_\Omega = -0.048$; (blue): $Re = 6000$, $R_\Omega = -0.116$; and (magenta): $Re = 20000$, $R_\Omega = -0.2$. Other parameters for rotating PCF with passive scalar and stratified PCF are following the condition (2D/3C-R+P=2D/3C-S).

three-component (2D/3C, no streamwise variation) spanwise rotating PCF and two-dimensional (2D, no streamwise variation and no streamwise velocity) vertically stratified PCF. We employ structured input-output analysis (chapters 5-6) to quantify the extent to which this equivalence remains valid (in terms of the most amplified flow structures) under the full three-dimensional and full component flow when both rotation and stratification are stabilizing. The similarity of the most amplified structures within this parameter regime is further quantified by analyzing individual input-output pathways (i.e. each component of body forcing as input and each velocity component as output). This analysis shows that the main difference between these flows is associated with the streamwise velocity and streamwise forcing pair, where rotation suppresses amplification of spanwise varying flow structures faster than stratification. The amplification of streamwise dependent flow structures is suppressed faster by stratification than rotation in the regimes where these two flows are equivalent. The largest amplification of streamwise constant (2D/3C) flow structures in rotating PCF is not influenced by the rotation number, which suggests additional mathematical equivalence. We then show that there is a mathematical equivalence between 2D/3C rotating PCF with a passive scalar and 2D/3C stratified PCF, and we demonstrate evidence of this behavior using structured input-output analysis.

These results suggest that fuhrer insight could be gained through the study of the flow configuration with both rotation and stratification. This framework may be further extended to quantify the analogy between Coriolis force due to rotation and the Lorentz force due to magnetic field, where the oblique turbulent bands were also observed in channel flow with a stabilizing Lorentz force (Brethouwer *et al.*, 2012).

Chapter 8

Linear matrix inequality based analysis of permissible perturbation amplitude in shear flow models

> "We all know the theorem of Lagrange on the stability of equilibrium in the case where there exists a force-function [potential energy function multiplied by (-1)], as well as the elegant demonstration which has been proposed for it by Lejeune-Dirichlet. This last rests on considerations which can serve for the proof of many other analogous theorems."
>
> Aleksandr M. Lyapunov[1], 1892

Previous chapters 5-7 focus on the wall-parallel length scales of flow structures prevalent in transitional or intermittent regimes of plane Poiseuille flow, plane Couette flow (PCF), stratified PCF, and rotating PCF. Another important question in transitional flow regime is to certify a perturbation amplitude such that flow can sustain while maintaining the laminar state. This chapter will address this question within several low-dimensional shear-flow models.

[1] (Lyapunov, 1992, section 16)

8.1 Introduction

Linear analysis has been widely used to study transition in a range of flows (Drazin & Reid, 2004; Schmid & Henningson, 2012). However, it has been known to fail in predicting the Reynolds number at which transition occurs in wall-bounded shear flows, which are important in a wide range of applications. For example, linear stability analysis indicates that the laminar state of the plane Couette flow is stable against infinitesimal perturbation for any Reynolds number; i.e., $Re_L = \infty$ (Romanov, 1973), while experimental observations indicate that transition occurs at a critical Reynolds number of $Re_C = 360 \pm 10$ (Tillmark & Alfredsson, 1992). This mismatch has been attributed to the fact that the infinitesimal perturbation inherent in linear stability analysis does not capture the true growth of the perturbation either due to nonlinear effects (Waleffe, 1995) as well as to the known algebraic growth (Reddy & Henningson, 1993; Schmid & Henningson, 2012) resulting from the non-normality of the linearized Navier-Stokes (NS) operator (Trefethen *et al.*, 1993; Henningson & Reddy, 1994; Trefethen & Embree, 2005).

Energy methods employ Lyapunov-based analysis of the nonlinear flow field and therefore overcome the limitations to infinitesimal perturbations and linear behavior (Joseph, 2013; Straughan, 2013). Classical energy methods employ the perturbation kinetic energy as a radially unbounded Lyapunov function, which produces a certificate (rigorous proof) of globally asymptotic stability of the base flow at a given Reynolds number. Defining transition to turbulence in terms of loss of this globally asymptotic stability using a quadratic Lyapunov function provides a conservative bound on the transition Reynolds number predicted by the energy method (here denoted Re_E). Thus, Re_E is typically much lower than the critical Reynolds number observed in experiments; e.g., $Re_E \approx 20.7$ for plane Couette flow (See e.g., Figure 5.11(b) in Ref. (Schmid & Henningson, 2012)). Energy methods have recently been expanded to a broader class of polynomial Lyapunov functions, which has led to less conservative bounds for a range of flow configurations (Goulart & Chernyshenko, 2012; Chernyshenko *et al.*, 2014; Huang

et al., 2015; Fuentes *et al.*, 2019). For example, Fuentes *et al.* (2019) employed quartic polynomials as a Lyapunov function to verify the global stability of 2D plane Couette flow at Reynolds numbers below $Re = 252.4$, which is substantially higher than the $Re_E = 177.2$ bound attained through classical energy stability methods. Much of that work has been enabled through the sum of squares (SOS) techniques that provide a computational approach for computing polynomial Lyapunov functions (Prajna *et al.*, 2002; Papachristodoulou *et al.*, 2013). However, both the energy stability method and its generalization provide no information about the flow regime $Re_E < Re < Re_L$, where the base flow is stable against infinitesimal perturbations, but some finite perturbations can lead to transition, for example at the Re_C values observed in experiments.

In general, at a given Re in the flow regime $Re_E < Re < Re_L$, there exists a critical perturbation amplitude above which transition to turbulence is observed for particular forcing shapes and another permissible perturbation amplitude, δ_{p}, below which all perturbations will decay (Baggett & Trefethen, 1997). These perturbation amplitudes are of particular importance in understanding the transition to turbulence and in the design of flow control approaches. However, they are difficult to determine in practice. The most common approach involves extensive numerical simulations (Kreiss *et al.*, 1994; Reddy *et al.*, 1998; Schneider *et al.*, 2007; Eckhardt *et al.*, 2007*b*; Schneider *et al.*, 2010; Chantry & Schneider, 2014) or experiments (Grossmann, 2000; Hof *et al.*, 2003; Peixinho & Mullin, 2007; Mullin, 2011). However, an inherently finite set of experiments or numerical simulations cannot provide a provable bound on either the permissible level of perturbation to maintain a laminar flow state or the critical perturbation that leads to transition. A more rigorous (but likely conservative) bound on the permissible perturbation amplitude can be obtained through computing a region of attraction based on Lyapunov methods; see, e.g., Chapter 8.2 of Ref. (Khalil, 2002). Lyapunov-based methods have been applied in a wide range of stability based analyses for different flow regimes including global stability analysis (Goulart & Chernyshenko, 2012; Chernyshenko *et al.*, 2014; Huang *et al.*, 2015; Fuentes *et al.*, 2019), bounding long time averages (Chernyshenko *et al.*,

2014; Fantuzzi *et al.*, 2016), controller synthesis for laminar wakes (Lasagna *et al.*, 2016; Huang *et al.*, 2017), and finding dynamically important periodic orbits (Lakshmi *et al.*, 2020). However, computation of the Lyapunov function and the associated analysis approaches typically rely on SOS methods, which are known to be computationally expensive when the dimension of the system is large (Zheng *et al.*, 2018).

Alternative approaches to determining permissible perturbations for a given flow condition have combined optimization methods with NS solvers to obtain initial conditions resulting in the largest nonlinear energy growth at a given final time T; i.e., the nonlinear optimal transient growth (Kerswell *et al.*, 2014; Kerswell, 2018). This method has been effective in determining the shape of perturbation that is most efficient in triggering the transition to turbulence (Pringle & Kerswell, 2010; Duguet *et al.*, 2010*a*; Pringle *et al.*, 2012; Rabin *et al.*, 2012; Duguet *et al.*, 2013). However, this method requires an a priori specification of a large enough T to ensure that it captures the full behavior as $T \to \infty$ (Kerswell *et al.*, 2014), which leads to a trade-off between accuracy and computational time.

Low dimensional shear flow models have been used to provide insight into the critical Reynolds number and the permissible perturbation amplitude for a given flow without the full computational burden of the NS equations (Trefethen *et al.*, 1993; Kreiss *et al.*, 1994; Gebhardt & Grossmann, 1994; Waleffe, 1995; Baggett *et al.*, 1995; Baggett & Trefethen, 1997; Moehlis *et al.*, 2004, 2005; Lebovitz & Mariotti, 2013; Joglekar *et al.*, 2015). These models are constructed to capture the transitional behavior of wall-bounded shear flows. In particular, the nine-dimensional shear flow model obtained from a Galerkin projection of NS equations (Moehlis *et al.*, 2004) was designed to reproduce the bifurcations, periodic orbits (Moehlis *et al.*, 2005), and edge of chaos phenomena (Kim & Moehlis, 2008; Joglekar *et al.*, 2015) observed in direct numerical simulations (DNS) of wall-bounded shear flows. This nine-mode model (Moehlis *et al.*, 2004) has been widely studied as a prototype shear flow model, see e.g. (Moehlis *et al.*, 2004, 2005; Kim & Moehlis, 2008; Joglekar *et al.*, 2015; Goulart & Chernyshenko, 2012; Chernyshenko *et al.*, 2014). In particular, the question of transition in this flow has been assessed in terms

of both its global stability (Goulart & Chernyshenko, 2012), bounds on the long-time average of the energy dissipation (Chernyshenko *et al.*, 2014) as well as through exhaustive simulations to determine both permissible and critical perturbations as a function of the Reynolds number (Joglekar *et al.*, 2015). The reduced-order and ability of these models to capture important flow characteristics have led to extensive use of such models to both gain insight into the underlying physics and test analysis tools. However, a number of challenges remain even in characterizing these reduced-order models, including the inability to attain a rigorous bound through simulation and the large computational cost of the prevailing SOS-based analysis tools.

In this work, we address the problem of determining a permissible perturbation amplitude through an alternative view of the stability properties of these nonlinear systems in terms of general input–output properties of the system, see e.g. Bamieh & Dahleh (2001); Ahmadi *et al.* (2019); Jovanović & Bamieh (2005); McKeon & Sharma (2010); Jovanović (2021). A common approach to input–output based analysis involves partitioning the system into a linear system that is forced by the system nonlinearity $h(\cdot)$, as shown in Figure 8.1. This point of view in which the nonlinearity acts as a forcing that mixes the nonlinear modes forms the basis of a number of previous analyses of the system transfer function or resolvent, see e.g. (Bamieh & Dahleh, 2001; Jovanović & Bamieh, 2005; McKeon & Sharma, 2010; Sharma & McKeon, 2013; McKeon *et al.*, 2013; McKeon, 2017; Liu & Gayme, 2019, 2020*a*; Jovanović, 2021). This reformulation of the problem leads to a Luré system (Kalman, 1963; Boyd *et al.*, 1994; Khalil, 2002; Li *et al.*, 2007, 2008) in which a linear time-invariant system is connected to a memoryless nonlinear system. This decomposition enables the use of control theoretic tools to provide insight into the input–output stability of the interconnected system based on the properties of the constitutive linear (transfer function/resolvent) and nonlinear relations $h(\cdot)$ in the two blocks in Figure 8.1 and their interconnection structure Popov (1961); Kalman (1963); Zames (1966); Khalil (2002).

In the context of analyzing the stability and of synthesizing controllers for shear flows, the most widely used theory involves ensuring that the interconnection structure is passive. Passive systems are stable in the sense of Lyapunov (i.e., bounded inputs lead to bounded outputs)

under certain conditions, see e.g., Lemma 6.5-6.7 of Ref. (Khalil, 2002), and, therefore, the concept of passivity is often used for stability analysis and in control design. This concept is useful in terms of analyzing systems of the form in Figure 8.1 because the passivity theorem (e.g., Theorem 6.1 in Ref. (Khalil, 2002)) states that if two systems are passive, the feedback interconnection of these two passive systems remains passive. This property allows one to analyze and control the full nonlinear system through each subsystem; e.g., passivity-based control (van der Schaft, 2000; Ortega *et al.*, 2013). In shear flows, as the nonlinearity is known to be energy-conserving (Joseph, 2013) (lossless), which is a special case of passive, this theory is an appealing analysis tool for these systems. Sharma *et al.* (2011) invoked this theory to synthesize a feedback controller to render the linear system passive in order to stabilize the full nonlinear system governing turbulent channel flow at $Re_\tau = 100$ (i.e. to relaminarize it). Similar approaches have been applied to the Blasius boundary layer (Damaren, 2016, 2018) and for control of channels with sensing and actuation limited to the wall (Heins *et al.*, 2016). The notion of passivity has also been used in recent work to study a wider class of input–output properties Ahmadi *et al.* (2019).

The dynamics of the interconnected system can also be evaluated using the concept of sector bounds (see e.g., Chapter 6 of Ref. (Khalil, 2002)), wherein the nonlinear map of the state $h(\boldsymbol{x})$ mapping the zero state to the origin can be contained within a sector in the $(\boldsymbol{x}, h(\boldsymbol{x}))$ plane. This sector bound on nonlinearity combined with the sector occupying the nonlinear system provides important information about the input–output stability of the interconnected system Zames (1966) and forms the basis of a number of stability analysis tools for nonlinear systems, e.g., Popov and circle criteria (Popov, 1961; Zames, 1966; Khalil, 2002). Passive systems provide a special case of sector bounded systems; see e.g., Definitions 6.1 and 6.2 of Ref. (Khalil, 2002).

Sector bound requirements have proven conservative in problems in which the form of the nonlinearity is known or there are slope restrictions on the sector bound (Park, 1997; Park *et al.*, 2019). Less conservative results can be obtained through relaxing the sector bounds requirement

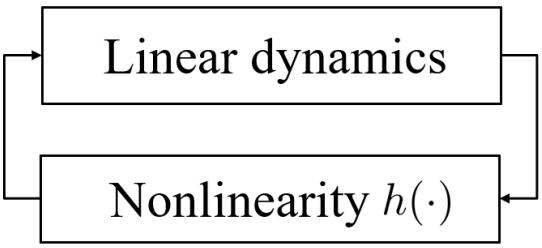

Figure 8.1: Illustration of partitioning the dynamics into a feedback interconnection of linear and nonlinear dynamics; i.e., a Luré system.

and instead imposing local bounds that enable an analysis of the system over a local region rather than by global analysis (Weissenberger, 1968; Hindi & Boyd, 1998; Valmorbida *et al.*, 2018). This approach was used to compute the region of attraction for a dynamical system with logarithmic and fractional nonlinearity by Valmorbida *et al.* (2018). Kalur *et al.* (2020, 2021*b*) similarly employed a local bound on quadratic nonlinearity to perform local stability and energy growth analyses of the four-dimensional Waleffe-Kim-Hamilton (WKH) shear flow model (Waleffe, 1995).

In this work, we employ the notions of passivity and relaxed sector bound constraints to develop a linear matrix inequalities (LMI) based approach to computing a provable bound on the permissible perturbation amplitude δ_{p} for a wide class of shear flow models in which the nonlinearity is passive (in this case energy-conserving) and can be locally sector bounded. We first express known properties of the nonlinearity, e.g. that is energy-conserving (lossless) and has bounded input–output energy in a local region as LMI system constraints. We then formulate the computation of a region of attraction as an LMI, which allows us to analyze systems with quadratic constraints using linear techniques by expressing conditions related to the positive semi-definiteness of symmetric matrices. This approach has been widely applied in analyzing systems using concepts of passivity and sector bounds; see e.g., examples for fluids problem (Ahmadi *et al.*, 2019; Kalur *et al.*, 2021*b*, 2020) and a general formulation (Boyd *et al.*, 1994). The LMI is a natural generalization of linear inequalities where LMI is defined based on the positive semi-definiteness of symmetric matrices. While our approach is similar to the approach taken in analyzing the WKH model in Refs. (Kalur *et al.*, 2020, 2021*b*), we provide a tighter

bound, which is expected to lead to a less conservative estimation of the region of attraction. We also take the further step of computing the permissible perturbation amplitude, i.e. the δ_p below which any perturbation is guaranteed to decay for a full range of shear flow models including the more comprehensive nine-dimensional model Moehlis *et al.* (2004). In particular, we compute the Reynolds number dependent permissible perturbation amplitude δ_p for seven low dimensional shear flow models (Trefethen *et al.*, 1993; Baggett *et al.*, 1995; Waleffe, 1995; Baggett & Trefethen, 1997; Moehlis *et al.*, 2004) and compare it with results obtained from extensive numerical simulation using the same models (Baggett & Trefethen, 1997; Joglekar *et al.*, 2015). The proposed method results in permissible perturbation amplitudes as a function of the Reynolds number for shear flow models (Trefethen *et al.*, 1993; Baggett *et al.*, 1995; Waleffe, 1995; Baggett & Trefethen, 1997; Moehlis *et al.*, 2004) that are conservative, yet consistent with those estimated from simulations with randomly chosen initial conditions (Baggett & Trefethen, 1997; Joglekar *et al.*, 2015). The analysis provides a generalization of both linear analysis and classical energy methods. In addition, this approach overcomes the lack of rigor associated with simulation-based approaches in that our results provide a provable guarantee that the system will converge to the laminar state for any perturbation amplitude below δ_p. The LMI based method is more computationally efficient than SOS programming because we restrict the characteristics of the nonlinearity in order to reduce the search space for candidate Lyapunov functions. We illustrate the computational efficiency of the method through comparisons with the SOS-based approaches for the nine-dimensional shear flow model (Moehlis *et al.*, 2004), which has the largest dimension of the models tested.

The remainder of this chapter is organized as follows. Section 8.2 describes the problem set-up and derivation of the Linear Matrix Inequalities (LMI) based constraints on the nonlinearity, which are then employed to determine permissible perturbation amplitude. In Section 8.3, we apply this framework to shear flow models (Trefethen *et al.*, 1993; Baggett *et al.*, 1995; Waleffe, 1995; Baggett & Trefethen, 1997; Moehlis *et al.*, 2004) and compare the obtained permissible perturbation amplitudes with these obtained from extensive simulations (Baggett & Trefethen,

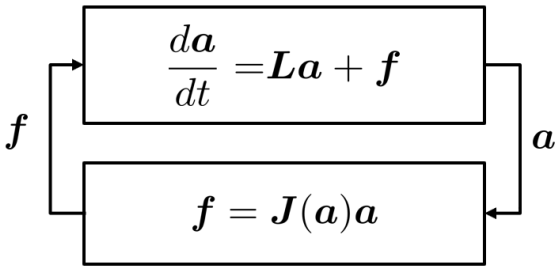

Figure 8.2: Luré partition of dynamics described in equation (8.1).

1997; Joglekar *et al.*, 2015) and SOS programming. Section 8.4 concludes this chapter and discusses future work directions.

8.2 Input–output based analysis framework

The dynamics of a general shear flow can be written in the form,

$$\frac{d\boldsymbol{a}}{dt} = \boldsymbol{L}\boldsymbol{a} + \boldsymbol{f}, \tag{8.1}$$

where $\boldsymbol{a} \in \mathbb{R}^n$ is the state variable, $\boldsymbol{L} \in \mathbb{R}^{n\times n}$ represents the linear operator arising from a linearization about a flow state, and $\boldsymbol{f} \in \mathbb{R}^n$ are the remaining nonlinear terms. This Luré partition of the equations, illustrated in Figure 8.2, views the nonlinearity as feedback forcing to the linear system in the spirit of several previous works using input–output and resolvent analysis, see e.g. Bamieh & Dahleh (2001); Jovanović & Bamieh (2005); McKeon & Sharma (2010); Sharma & McKeon (2013); McKeon *et al.* (2013); McKeon (2017); Liu & Gayme (2019, 2020*a*); Jovanović (2021).

The nonlinear interactions for the class of shear flows of interest here have certain properties that can be exploited in analyzing the block diagram of Figure 8.2. Here we focus our analysis on the spatial discretization of the governing equations, which results in a set of ordinary differential equations that approximate the dynamics in equation (8.1). The nonlinearity is quadratic in the state variable for shear flows and the reduced-order models of interest here. In this setting, such a nonlinearity can be written as $\boldsymbol{f} = \boldsymbol{J}(\boldsymbol{a})\boldsymbol{a}$, where $\boldsymbol{J}(\boldsymbol{a}) \in \mathbb{R}^{n\times n}$ is a state-dependent matrix such that $\boldsymbol{J}(\boldsymbol{0}) = \boldsymbol{0}$, and n denotes the number of points used in the discretization of the state

variable.

In subsection 8.2.1, we use both this quadratic form of the nonlinear interactions and the fact that the nonlinearity is known to be energy-conserving (lossless) (Joseph, 2013; Sharma *et al.*, 2011; Sharma, 2009; Heins *et al.*, 2016; Damaren, 2016, 2018; Ahmadi *et al.*, 2019; Constantin & Doering, 1995) in order to derive constraints that we will later use in our LMI based algorithm in subsection 8.2.2 to evaluate system stability. We take the approach of characterizing the nonlinearity using local rather than (global) sector bounds on two of its properties in order to define an LMI based condition on local stability of the interconnection structure. Our focus on the local rather than global constraints provides relaxation of the strict conditions in classical energy methods in order to understand the behavior of systems whose solutions (laminar states) are stable for finite perturbations but not globally asymptotically stable. In particular, in Lemma 8.1 we provide quadratic bounds on the input–output amplification of the nonlinear term $\boldsymbol{f}$ within a neighborhood. Then in Theorem 8.2, we use these bounds along with a corresponding Lyapunov function to define a region of attraction for the trajectories under the nonlinear mapping. Finally, determining the associated permissible perturbation amplitude to maintain the laminar state is formulated as an LMI constrained optimization problem. Our main theoretical result demonstrates that a feasible solution to this optimization problem provides a permissible perturbation amplitude for the given model.

8.2.1 Characterizing the nonlinear interactions

Prior to presenting the main result, we provide a closed-form expression describing the energy-conserving property using the properties of the operator $\boldsymbol{J}(\boldsymbol{a})$ and a related set of quadratic constraints that capture the properties of the nonlinearity. We then derive an upper bound on the quadratic nonlinearity in a local region, which is presented in Lemma 8.1. These results are used in the proof of Theorem 8.2 that provides an LMI based approach to computing the permissible perturbation amplitude for dynamical systems of the form in equation (8.1).

The nonlinear terms in wall-bounded shear flows (see e.g., employed in Refs. (Joseph, 2013;

Sharma *et al.*, 2011; Sharma, 2009; Heins *et al.*, 2016; Damaren, 2016, 2018; Ahmadi *et al.*, 2019; Constantin & Doering, 1995)) and all of the shear flow models discussed herein (Baggett & Trefethen, 1997; Goulart & Chernyshenko, 2012) are known to be lossless, which is a special case of passivity. We can therefore analyze the dynamics in terms of the partition of the dynamics into feedback interconnection between its constitutive linear and nonlinear parts, as shown in Figure 8.2. In particular, passivity theory allows us to connect the behavior of the nonlinear and linear parts of the system to overall stability within a local region. For the system described in equation (8.1) and Figure 8.2, this lossless property can be expressed as:

$$\boldsymbol{a}^T \boldsymbol{f} = 0, \tag{8.2}$$

i.e., $\boldsymbol{a}^T \boldsymbol{J}(\boldsymbol{a})\boldsymbol{a} = 0$, which implies that $\boldsymbol{J}(\boldsymbol{a})$ is a skew-symmetric matrix. A skew-symmetric matrix $\boldsymbol{J}(\boldsymbol{a})$ of odd dimension is known to have a zero eigenvalue and a corresponding non-trivial nullspace; see e.g., Theorem 5.4.1 in Eves (1980). The non-trivial element in the left null space of $\boldsymbol{J}(\boldsymbol{a})$ is the orthogonal complement of the nonlinear term $\boldsymbol{f}$; i.e. $\boldsymbol{n}$ such that:

$$\boldsymbol{n}^T \boldsymbol{f} = \boldsymbol{n}^T \boldsymbol{J}(\boldsymbol{a})\boldsymbol{a} = 0. \tag{8.3}$$

The energy-conserving property in equation (8.2) and the orthogonal complement in equation (8.3) are associated with two constants of motion $E := \frac{1}{2}\boldsymbol{a}^T\boldsymbol{a}$ and $C := \boldsymbol{n}^T\boldsymbol{a}$ for the dynamical system associated with the nonlinearity: $\frac{d\boldsymbol{a}}{dt} = \boldsymbol{f}$. Such constants of motion are commonly exploited in stability analysis of passive systems, e.g. this notion is employed in the energy-Casimir method that has been widely employed in nonlinear stability analysis of ideal fluids; see e.g., Holm *et al.* (1985); Salmon (1988, Section 7); Morrison (1998, Section VI); Mu & Wu (2001). The feedback interconnection decomposition of the linear and nonlinear dynamics (i.e., a Luré system) allows us to incorporate constraints associated with these constants of motion in the analysis of full nonlinear dynamical system $\frac{d\boldsymbol{a}}{dt} = \boldsymbol{L}\boldsymbol{a} + \boldsymbol{f}$.

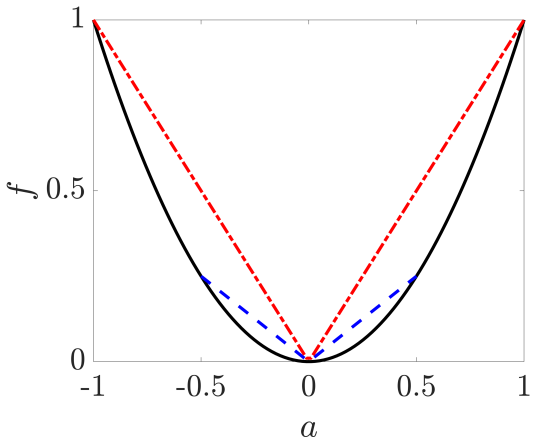

Figure 8.3: Illustration of local sector bounds for a quadratic nonlinear function $f = a^2$ (—) which is bounded by a sector region $f^2 \leq 0.5^2 a^2$ (– –) when $a^2 \leq 0.5^2$ and bounded by another sector region $f^2 \leq a^2$ (– · –) when $a^2 \leq 1$.

We next rewrite the constraints described by equation (8.3) as the following LMI:

$$\boldsymbol{a}^T \boldsymbol{M}_i \boldsymbol{f} = 0, \ i = 1, 2, ..., n, \tag{8.4}$$

$$\boldsymbol{f}^T \boldsymbol{T}_j \boldsymbol{f} = 0, \ j = 1, 2, ..., n, \tag{8.5}$$

where $\boldsymbol{M}_i := \boldsymbol{e}_i \boldsymbol{n}^T$, $\boldsymbol{T}_j := \boldsymbol{e}_j \boldsymbol{n}^T + \boldsymbol{n} \boldsymbol{e}_j^T$ and $\boldsymbol{e}_i$ denotes the standard basis vector, i.e. a column vector with the i^{th} element equal to one, and all other elements equal to zero. We can rewrite equation (8.2) in the form of equation (8.4) by defining $\boldsymbol{M}_0 := \boldsymbol{I}$, which leads to $\boldsymbol{a}^T \boldsymbol{M}_0 \boldsymbol{f} = 0$.

We next provide two sets of local bounds on the nonlinearity that form the relaxed sector bounds that enable us to study the local stability associated with a finite amplitude perturbation, which is of interest in this work. Figure 8.3 illustrates the concept of local sector bounds for a quadratic nonlinear function $f = a^2$ that is bounded by a sector region $f^2 \leq 0.5^2 a^2$ when $a^2 \leq 0.5^2$ and bounded by another sector region $f^2 \leq a^2$ when $a^2 \leq 1$. The first set of local bounds, provided in Lemma 8.1(a), is in terms of a decomposition of the nonlinear term $\boldsymbol{f}$ into components $f_m := \boldsymbol{e}_m^T \boldsymbol{f}$, which enables additional degrees of freedom in characterizing the system properties. Lemma 8.1(b) instead provides an upper bound on the norm of $\boldsymbol{f}$. Both bounds are provided in terms of quadratic forms that are valid in a local region $\|\boldsymbol{a}\|_2 \leq \delta$,

where $\|\boldsymbol{a}\|_2 := \sqrt{\sum_{i=1}^{n} a_i^2} = \sqrt{\boldsymbol{a}^T\boldsymbol{a}}$ denotes the l_2 norm of the state vector $\boldsymbol{a}$. The associated symmetric matrices are independent of the state variable. The bound that is provided in Lemma 8.1(a) is similar to equation (16) of Kalur *et al.* (2020) and equation (15) of Kalur *et al.* (2021*b*), but is shown to be tighter than that proposed in either of these works (see Remark 8.1).

Lemma 8.1 *(a) Given a vector $\boldsymbol{f} \in \mathbb{R}^n$ that can be decomposed into $f_m := \boldsymbol{e}_m^T\boldsymbol{f}$ associated with a quadratic form $f_m = \boldsymbol{a}^T\boldsymbol{R}_m\boldsymbol{a}$ with a symmetric matrix $\boldsymbol{R}_m \in \mathbb{R}^{n\times n}$. In a local region $\|\boldsymbol{a}\|_2^2 \leq \delta^2$, each f_m^2 is bounded as:*

$$f_m^2 \leq \delta^2\boldsymbol{a}^T\boldsymbol{R}_m\boldsymbol{R}_m\boldsymbol{a},\ m = 1, 2, ..., n. \tag{8.6}$$

(b) Given $\boldsymbol{f} = \boldsymbol{J}(\boldsymbol{a})\boldsymbol{a}$ with $\boldsymbol{J}(\boldsymbol{a}) \in \mathbb{R}^{n\times n}$ and a local region $\|\boldsymbol{a}\|_2^2 \leq \delta^2$, $\|\boldsymbol{f}\|_2^2$ is bounded as:

$$\|\boldsymbol{f}\|_2^2 \leq \delta^2\boldsymbol{a}^T\boldsymbol{J}_F\boldsymbol{a}, \tag{8.7}$$

where $\boldsymbol{J}_F \in \mathbb{R}^{n\times n}$ is a symmetric matrix such that $\boldsymbol{a}^T\boldsymbol{J}_F\boldsymbol{a} = \|\boldsymbol{J}(\boldsymbol{a})\|_F^2$ and $\|\boldsymbol{J}(\boldsymbol{a})\|_F := \sqrt{\sum_{i=1}^{n}\sum_{j=1}^{n}|[\boldsymbol{J}(\boldsymbol{a})]_{i,j}|^2}$ denotes the Frobenius norm.

Proof:

Part (a): In a local region $\|\boldsymbol{a}\|_2^2 \leq \delta^2$, we have:

$$f_m^2 = (\boldsymbol{a}^T\boldsymbol{R}_m\boldsymbol{a})(\boldsymbol{a}^T\boldsymbol{R}_m\boldsymbol{a}) \tag{8.8a}$$

$$= \|\boldsymbol{a}\|_2^2\ \|\boldsymbol{R}_m\boldsymbol{a}\|_2^2\ \frac{\boldsymbol{a}^T\boldsymbol{R}_m\boldsymbol{a}}{\|\boldsymbol{a}\|_2\ \|\boldsymbol{R}_m\boldsymbol{a}\|_2}\ \frac{\boldsymbol{a}^T\boldsymbol{R}_m\boldsymbol{a}}{\|\boldsymbol{a}\|_2\ \|\boldsymbol{R}_m\boldsymbol{a}\|_2} \tag{8.8b}$$

$$= \|\boldsymbol{a}\|_2^2\ \|\boldsymbol{R}_m\boldsymbol{a}\|_2^2\ \cos^2\theta_m \tag{8.8c}$$

$$\leq \|\boldsymbol{a}\|_2^2\ \|\boldsymbol{R}_m\boldsymbol{a}\|_2^2 \tag{8.8d}$$

$$\leq \delta^2\boldsymbol{a}^T\boldsymbol{R}_m\boldsymbol{R}_m\boldsymbol{a},\ m = 1, 2, ..., n. \tag{8.8e}$$

Here we used $\frac{\boldsymbol{a}^T\boldsymbol{R}_m\boldsymbol{a}}{\|\boldsymbol{a}\|_2\ \|\boldsymbol{R}_m\boldsymbol{a}\|_2} =: \cos\theta_m$ and $\cos^2\theta_m \leq 1$ with θ_m representing the angle between vectors $\boldsymbol{a}$ and $\boldsymbol{R}_m\boldsymbol{a}$. The last step uses the bound on the local region $\|\boldsymbol{a}\|_2^2 \leq \delta^2$ to attain the

upper bound on f_m^2 in equation (8.6).

Part (b): Using the definition of $\boldsymbol{f}$,

$$\|\boldsymbol{f}\|_2^2 = \|\boldsymbol{J}(\boldsymbol{a})\boldsymbol{a}\|_2^2 \tag{8.9a}$$

$$\leq \|\boldsymbol{a}\|_2^2 \, \|\boldsymbol{J}(\boldsymbol{a})\|_{2,2}^2 \tag{8.9b}$$

$$\leq \|\boldsymbol{a}\|_2^2 \, \|\boldsymbol{J}(\boldsymbol{a})\|_F^2 \tag{8.9c}$$

$$\leq \delta^2 \boldsymbol{a}^T \boldsymbol{J}_F \boldsymbol{a}, \tag{8.9d}$$

where $\|\boldsymbol{J}(\boldsymbol{a})\|_{2,2} := \max_{\boldsymbol{a} \neq \boldsymbol{0}} \frac{\|\boldsymbol{J}(\boldsymbol{a})\boldsymbol{a}\|_2}{\|\boldsymbol{a}\|_2}$ represents the matrix norm induced by the l_2 vector norm and the inequality in equation (8.9b) is directly obtained using the definition of the induced norm. The inequality in equation (8.9c) invokes the matrix norm property $\|\boldsymbol{J}(\boldsymbol{a})\|_{2,2} \leq \|\boldsymbol{J}(\boldsymbol{a})\|_F$; see, e.g., Problem 5.6.P23 in Ref. (Horn & Johnson, 2012). As each element of $\boldsymbol{J}(\boldsymbol{a})$ is a linear function of $\boldsymbol{a}$, the square of the Frobenius norm $\|\boldsymbol{J}(\boldsymbol{a})\|_F^2$ can be written as a quadratic form $\|\boldsymbol{J}(\boldsymbol{a})\|_F^2 = \boldsymbol{a}^T \boldsymbol{J}_F \boldsymbol{a}$ where $\boldsymbol{J}_F$ is independent of $\boldsymbol{a}$. Rewriting the expression in this manner and imposing the bound on the local region $\|\boldsymbol{a}\|_2^2 \leq \delta^2$ lead to the upper bound in equation (8.7). □

Remark 8.1 *We can obtain the bound in equation (16) of Kalur et al. (2020) and equation (15) of Kalur et al. (2021b) from the result (8.6) in Lemma 8.1(a) in the following manner. Starting from (8.6) in Lemma 8.1(a), we further apply the inequalities,*

$$f_m^2 \leq \delta^2 \boldsymbol{a}^T \boldsymbol{R}_m \boldsymbol{R}_m \boldsymbol{a}$$

$$\leq \delta^2 \boldsymbol{a}^T \rho(\boldsymbol{R}_m \boldsymbol{R}_m) \boldsymbol{a} \tag{8.10a}$$

$$\leq \delta^2 \rho(\boldsymbol{R}_m)^2 \boldsymbol{a}^T \boldsymbol{a} \tag{8.10b}$$

with $\rho(\cdot)$ representing the spectral radius and the resulting (8.10b) is the upper bound in Kalur et al. (2021b, 2020). The inequality in equation (8.10a) results from the Rayleigh quotient

theorem (See e.g., Theorem 4.2.2 in Ref. (Horn & Johnson, 2012)) and the definition of the spectral radius, and this inequality achieves equality if and only if all eigenvalues of $\boldsymbol{R}_m\boldsymbol{R}_m$ *are equal to* $\rho(\boldsymbol{R}_m\boldsymbol{R}_m)$*. The inequality in equation (8.10b) results from the Gelfand formula (Corollary 5.6.14 of Ref. (Horn & Johnson, 2012)) and submultiplicativity of the matrix norm (Chapter 5.6 of Ref. (Horn & Johnson, 2012)). Whenever the condition to achieve equality in equation (8.10a) or (8.10b) are violated, our bounds in equation* (8.6) *of Lemma 8.1(a) are tighter than (Kalur* et al., *2021*b, *2020).*

8.2.2 LMI based permissible perturbation amplitude computations

We now present the main theoretical result of this work, in which we pose the problem of determining a permissible perturbation amplitude δ_{p} through testing the feasibility of an LMI constrained optimization problem. The result is presented in the following theorem, which first provides the neighborhood over which perturbations decay. A maximization over said regions is used to determine an estimate of the permissible perturbation amplitude.

Theorem 8.2 *Given the nonlinear dynamical system described in equation (8.1) satisfying the conditions in (8.2) and Lemma 8.1 along with* $\|\boldsymbol{a}\|_2 \leq \delta$*,* $\delta > 0$*.*

If there exists a symmetric matrix $\boldsymbol{P} \in \mathbb{R}^{n\times n}$ *satisfying*

$$\boldsymbol{P} - \epsilon \boldsymbol{I} \succeq 0, \tag{8.11a}$$

$$\epsilon > 0, \tag{8.11b}$$

$$\boldsymbol{G} \preceq 0, \tag{8.11c}$$

$$s_m \geq 0, \quad m = 0, 1, ..., n, \tag{8.11d}$$

where $(\cdot) \succeq 0$ *and* $(\cdot) \preceq 0$*, respectively, represent positive and negative semi-definiteness of the*

associated operator and $\boldsymbol{G}$ *is defined as:*

$$\boldsymbol{G} := \begin{bmatrix} \boldsymbol{L}^T\boldsymbol{P} + \boldsymbol{P}\boldsymbol{L} + \epsilon\boldsymbol{I} + s_0\delta^2\boldsymbol{J}_F + \sum_{m=1}^{n} s_m\delta^2\boldsymbol{R}_m\boldsymbol{R}_m & \boldsymbol{P} + \sum_{i=0}^{n}\lambda_i\boldsymbol{M}_i \\ \boldsymbol{P} + \sum_{i=0}^{n}\lambda_i\boldsymbol{M}_i^T & -s_0\boldsymbol{I} - \sum_{m=1}^{n} s_m\boldsymbol{e}_m\boldsymbol{e}_m^T + \sum_{j=1}^{n}\kappa_j\boldsymbol{T}_j \end{bmatrix},$$

then $\|\boldsymbol{a}(t=0)\|_2 \leq \delta_f \Rightarrow \lim_{t\to\infty}\boldsymbol{a}(t) = 0$, *where* $\delta_f := \delta\sqrt{\frac{\mu_{min}(\boldsymbol{P})}{\mu_{max}(\boldsymbol{P})}}$ *with* $\mu_{min}(\cdot)$ *and* $\mu_{max}(\cdot)$ *denoting the minimal and maximal eigenvalues.*

Proof:

When inequalities in equation (8.11) are feasible, $\boldsymbol{P}$ can be used to define $V := \boldsymbol{a}^T\boldsymbol{P}\boldsymbol{a} \geq \epsilon\boldsymbol{a}^T\boldsymbol{a} > 0, \quad \forall\boldsymbol{a} \neq \boldsymbol{0}$. We now demonstrate that V is a Lyapunov function for the system described in equation (8.1) in the region $\|\boldsymbol{a}\|_2 \leq \delta$. According to Lemma 8.1, we have $\delta^2\boldsymbol{a}^T\boldsymbol{R}_m\boldsymbol{R}_m\boldsymbol{a} - f_m^2 \geq 0,\ m = 1, 2, ..., n$ and $\delta^2\boldsymbol{a}^T\boldsymbol{J}_F\boldsymbol{a} - \boldsymbol{f}^T\boldsymbol{f} \geq 0$, and, therefore, we can further obtain $\forall\boldsymbol{a} \neq \boldsymbol{0}$ in the region $\|\boldsymbol{a}\|_2 \leq \delta$:

$$\begin{aligned} \frac{dV}{dt} \leq & \frac{dV}{dt} + s_0(\delta^2\boldsymbol{a}^T\boldsymbol{J}_F\boldsymbol{a} - \boldsymbol{f}^T\boldsymbol{f}) \\ & + \sum_{m=1}^{n} s_m(\delta^2\boldsymbol{a}^T\boldsymbol{R}_m\boldsymbol{R}_m\boldsymbol{a} - f_m^2) \qquad (8.12a) \\ = & \begin{bmatrix}\boldsymbol{a}\\ \boldsymbol{f}\end{bmatrix}^T \boldsymbol{G} \begin{bmatrix}\boldsymbol{a}\\ \boldsymbol{f}\end{bmatrix} - \epsilon\boldsymbol{a}^T\boldsymbol{a} \qquad (8.12b) \\ \leq & -\epsilon\boldsymbol{a}^T\boldsymbol{a} < 0. \qquad (8.12c) \end{aligned}$$

Thus, by Lyapunov's stability theorem (see e.g., Theorem 4.1 in Ref. (Khalil, 2002)) the origin $\boldsymbol{a} = \boldsymbol{0}$ is asymptotically stable. In addition, a region of attraction of the origin is given by $D_c := \{\boldsymbol{a} | V = \boldsymbol{a}^T\boldsymbol{P}\boldsymbol{a} \leq c\} \subseteq B_\delta := \{\boldsymbol{a} |\ \|\boldsymbol{a}\|_2 \leq \delta\}$, where we select $c > 0$ to define the maximum level set of V contained in B_δ.

Given $\delta_f := \delta\sqrt{\frac{\mu_{\min}(\boldsymbol{P})}{\mu_{\max}(\boldsymbol{P})}}$, the Rayleigh quotient theorem implies that $\mu_{\min}(\boldsymbol{P})\boldsymbol{a}^T\boldsymbol{a} \leq \boldsymbol{a}^T\boldsymbol{P}\boldsymbol{a} \leq \mu_{\max}(\boldsymbol{P})\boldsymbol{a}^T\boldsymbol{a}$ (see e.g., Theorem 4.2.2 in Ref. (Horn & Johnson, 2012)). Therefore $B_{\delta_f} := \{\boldsymbol{a} |\ \|\boldsymbol{a}\|_2 \leq \delta_f\} \subseteq D_c$ and as such, $\|\boldsymbol{a}(t=0)\|_2 \leq \delta_f \Rightarrow \lim_{t\to\infty}\boldsymbol{a}(t) = 0$ as stated in the theorem.

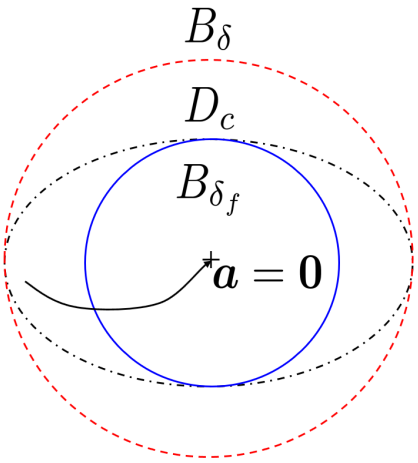

Figure 8.4: A two-dimensional illustration of the set relationship, $B_{\delta_f} \subseteq D_c \subseteq B_\delta$, employed in the proof of Theorem 8.2. B_δ (– –): a local region as a condition to bound the nonlinearity in Lemma 8.1; D_c (– · –): region of attraction of the origin $\boldsymbol{a} = \mathbf{0}$ illustrated with a trajectory (→); B_{δ_f} (—): a circular region contained inside D_c.

□

Figure 8.4 provides a two-dimensional illustration of the set relationship $B_{\delta_f} \subseteq D_c \subseteq B_\delta$ employed in the proof of Theorem 8.2. Theorem 8.2 is essentially trying to find a local Lyapunov function V contained within the B_δ in which the nonlinearity is bounded. The permissible perturbation amplitude is defined as the radius of the largest multidimensional sphere B_{δ_f} contained within the associated region of attraction D_c. The permissible perturbation amplitude can therefore be computed as the solution of the optimization problem:

$$\delta_\mathsf{p} := \max_{\delta} \ \delta_f \tag{8.13}$$

subject to (8.11).

Remark 8.2 *As seen in the depiction of the region of attraction D_c in Figure 8.4, the permissible perturbation amplitude δ_p given in equation (8.13) is conservative in the sense that certain directions can sustain perturbations larger than δ_f. The form of $\boldsymbol{P}$ can be further explored to gain further information regarding the directions that are the most sensitive to perturbations. The notion of perturbation structures that are most likely to lead to transition has been explored*

in other works, see e.g. (Kerswell et al., 2014; Kerswell, 2018; Pringle & Kerswell, 2010; Duguet et al., 2010a; Pringle et al., 2012; Rabin et al., 2012; Duguet et al., 2013; Kim & Moehlis, 2008; Joglekar et al., 2015). Here we focus on providing formal guarantees on the magnitude of the permissible perturbation amplitude, which has been previously studied using extensive simulations (Baggett & Trefethen, 1997; Joglekar et al., 2015).

The formulation and analysis described above provide a means to evaluate both classical energy and linear stability by restricting the form of $\boldsymbol{G}$ in equation (8.11c). In particular, neither classical energy nor linear stability analysis includes the local bounds on the nonlinear terms defined in Lemma 8.1, which take the form of the non-negative multipliers $s_m,\ m = 0, 1, ..., n$ in equation (8.11c). Our formulation further imposes equality constraints in describing the orthogonal complement of the nonlinear term in equation (8.3), which take the form of equations (8.4) and (8.5) that are associated with the multipliers $\lambda_i,\ i = 1, 2, ..., n$ and $\kappa_j,\ j = 1, 2, ..., n$. Classical energy methods do include the constraint associated with energy conservation in equation (8.2), described through the term associated with the multiplier λ_0, which leads to the following simplified form of equation (8.11c) for energy stability analysis

$$\boldsymbol{G}_E := \begin{bmatrix} \boldsymbol{L}^T\boldsymbol{P} + \boldsymbol{P}\boldsymbol{L} + \epsilon\boldsymbol{I} & \boldsymbol{P} + \lambda_0\boldsymbol{I} \\ \boldsymbol{P} + \lambda_0\boldsymbol{I} & \mathbb{O} \end{bmatrix} \preceq 0, \tag{8.14}$$

where $\mathbb{O} \in \mathbb{R}^{n\times n}$ is the zero matrix. By the generalized Schur's complement (See e.g., Theorem 4.3 in Ref. (Gallier, 2010)), the expression in (8.14) is true if and only if both $\boldsymbol{P} + \lambda_0\boldsymbol{I} = \mathbb{O}$ and $\boldsymbol{L}^T\boldsymbol{P} + \boldsymbol{P}\boldsymbol{L} + \epsilon\boldsymbol{I} \preceq 0$. Combining these relations with the condition $\boldsymbol{P} - \epsilon\boldsymbol{I} \succeq 0$ in equation (8.11a) leads to:

$$\boldsymbol{L}^T + \boldsymbol{L} \prec 0, \tag{8.15}$$

where $\prec$ represents negative definiteness. Equation (8.15) is equivalent to the condition for energy stability derived in Ref. (Goulart & Chernyshenko, 2012) with a Lyapunov function of $V = \frac{1}{2}\boldsymbol{a}^T\boldsymbol{a}$. Setting $s_m = 0,\ m = 0, 1, ..., n$ in the LMI formulation removes the local region $\|\boldsymbol{a}\|_2 \leq \delta$ restriction in Lemma 8.1. This means that the Lyapunov function, $V = \frac{1}{2}\boldsymbol{a}^T\boldsymbol{a}$, is

radially unbounded and, therefore, the origin (equilibrium point) of the system in (8.1) with the nonlinearity satisfying (8.2) is globally asymptotically stable ($\delta_{\mathsf{p}} = \infty$), see e.g., Theorem 4.2 in Ref. (Khalil, 2002). Equation (8.14) was used to perform global stability analysis for the WKH model by Kalur *et al.* (2020, 2021*b*).

Linear stability analysis corresponds to a further restriction on $\mathbf{G}_E$ in (8.14), where the off-diagonal elements are replaced by zero matrices (i.e., the nonlinear term $\boldsymbol{f}$ in the model dynamics (8.1) and its energy-conserving constraint in equation (8.2) are removed). In this case, the form of $\boldsymbol{G}$ in equation (8.11c) is

$$\boldsymbol{G}_L := \boldsymbol{L}^T\boldsymbol{P} + \boldsymbol{P}\boldsymbol{L} + \epsilon\boldsymbol{I} \preceq 0, \tag{8.16}$$

and Theorem 8.2 is equivalent to Lyapunov-based linear stability analysis; see e.g., Theorems 4.6 and 4.7 of Ref. (Khalil, 2002).

In the next section, we will employ the proposed framework to compute the permissible perturbation amplitude as a function of the Reynolds number and compare the resulting functions to those obtained from simulations of a range of shear flow models that have been widely used as benchmark problems in the study of transition and low Reynolds number shear flows.

8.3 Numerical results

In this section, we first focus on comparisons of the perturbation as a function of Reynolds numbers for six of the low (2-4) dimensional models studied through extensive numerical simulations in (Baggett & Trefethen, 1997) (subsection 8.3.1). We then perform a more detailed analysis of the nine-dimensional shear flow model (Moehlis *et al.*, 2004) including comparisons of the computational requirements and solutions obtained through SOS-based analysis (subsection 8.3.2).

For all of the results herein, we implement the LMIs in equation (8.11) of Theorem 8.2 in YALMIP (Löfberg, 2004) version R20190425 in MATLAB R2018b and solve the optimization problem in equation (8.13) using the Semi-definite Programming (SDP) solver SeDuMi (Sturm,

1999) version 1.3. We solve the LMI problem and the SOS problem discussed in subsection 8.3.2 by converting it to an SDP, which can be solved using off-the-shelf optimization methods. The feasible region of SDP is the cone of positive semi-definite (PSD) matrices; i.e., a region that is closed under linear combinations of PSD matrices with non-negative coefficients (Vandenberghe & Boyd, 1996; Boyd & Vandenberghe, 2004, Chapter 4.6.2). The dimension of this PSD cone involved in the optimization problem provides a measurement of computational resources required for the solver; e.g., employed in (Zheng *et al.*, 2018). We therefore report this as a benchmark of computational efficiency in subsection 8.3.2. We note that for comparison purposes, all computations are performed on the same computer with a 3.4 GHz Intel Core i7-3770 Central Processing Unit (CPU) and 16GB Random Access Memory (RAM). We set the value of ϵ in equation (8.11b) to 0.01; however, the specific value of ϵ does not alter the results due to the homogeneity of the inequalities in equation (8.11). For each model, we solve the optimization problems in (8.13) over 40 logarithmically spaced Reynolds numbers $Re \in [1, 2000]$. This optimization problem is solved through testing its feasibility over 400 logarithmically spaced $\delta \in [10^{-6}, 1]$ and then selecting the largest δ_f that provides a feasible solution (i.e, satisfies the conditions in equation (8.11)) as δ_{p}, i.e. we find the solution to equation (8.13). The range of $\delta \in [10^{-6}, 1]$ is selected to ensure that we cover the range of permissible perturbation amplitude in the transitional regime (e.g., $Re \geq 100$) observed from simulation results for these shear flow models considered here (Baggett & Trefethen, 1997; Joglekar *et al.*, 2015). We use this approach of solving for particular values δ at each Re as this renders the set of LMI constraints convex, which is more numerically tractable than the alternative bilinear optimization problem. Finally, we use the least-squares fit to find the exponents A and σ in $\delta_{\mathsf{p}}(Re) = 10^{A} Re^{\sigma}$, which is the same functional form used in (Baggett & Trefethen, 1997; Joglekar *et al.*, 2015). We select the same functional form in order to directly compare the scaling exponents σ obtained from extensive simulations with randomly chosen initial conditions computed by Baggett & Trefethen (1997) and Joglekar *et al.* (2015).

For all of the low dimensional shear flow models in section 8.3.1, all of the eigenvalues of

$\boldsymbol{L}$, corresponding to the linearization around the laminar state (origin), have negative real parts for all Reynolds numbers. In other words, the laminar state is linearly stable; i.e., $Re_L = \infty$. However, as is common in linear systems such as these where the linear operator (matrix) is non-normal, i.e., $(\boldsymbol{L}\boldsymbol{L}^T \neq \boldsymbol{L}^T\boldsymbol{L})$, the energy stability requirement $\boldsymbol{L} + \boldsymbol{L}^T \prec 0$ in equation (8.15) is violated at certain Reynolds number $Re_E < Re_L$ for all of the models considered here. The nonlinear terms $\boldsymbol{f}$ for all of these models satisfy the energy-conserving property described by equation (8.2).

8.3.1 Application to shear flow models

We now introduce the set of low dimensional shear flow models and the procedure that is used in applying Theorem 8.2 and equation (8.13). We employ the notation and naming convention (abbreviations based on authors' last names) used in Baggett & Trefethen (1997) for consistency as we compare our results to the simulation results in that work. In particular, we introduce and explain the application of Theorem 8.2 to the two-dimensional TTRD (Trefethen, Trefethen, Reddy, and Driscoll) model proposed in Trefethen *et al.* (1993) and the two variations, TTRD' and TTRD", introduced in (Baggett & Trefethen, 1997). We then provide the details of the three-dimensional BDT (Baggett, Driscoll, and Trefethen) model introduced in Baggett *et al.* (1995) and explain the pertinent values for the application of Theorem 8.2. Finally, we describe the four-dimensional W (Waleffe) proposed by Waleffe (1995) and its three-dimensional variation W' introduced in (Baggett & Trefethen, 1997). For all of the models described in this subsection, we use the same coefficients as (Baggett & Trefethen, 1997) for a direct comparison with their results.

The three variations of the TTRD model are two-dimensional models of the form,

$$\frac{d}{dt}\begin{bmatrix} u \\ v \end{bmatrix} = \begin{bmatrix} -Re^{-1} & 1 \\ 0 & -Re^{-1} \end{bmatrix}\begin{bmatrix} u \\ v \end{bmatrix} + \boldsymbol{f}_{(\cdot)}, \tag{8.17}$$

where the function $\boldsymbol{f}_{(\cdot)}$ describing the nonlinearity for the respective TTRD, TTRD', and TTRD"

variations of the model are given by:

$$\boldsymbol{f}_{\text{TTRD}} := \left\| \begin{bmatrix} u \\ v \end{bmatrix} \right\|_2 \begin{bmatrix} 0 & -1 \\ 1 & 0 \end{bmatrix} \begin{bmatrix} u \\ v \end{bmatrix}, \tag{TTRD}$$

$$\boldsymbol{f}_{\text{TTRD'}} := \begin{bmatrix} 0 & -u \\ u & 0 \end{bmatrix} \begin{bmatrix} u \\ v \end{bmatrix}, \tag{TTRD'}$$

$$\boldsymbol{f}_{\text{TTRD''}} := \begin{bmatrix} 0 & -v \\ v & 0 \end{bmatrix} \begin{bmatrix} u \\ v \end{bmatrix}. \tag{TTRD''}$$

In order to apply the theory in Section 8.2 to the TTRD model, we need to deal with the fact that the nonlinear term (TTRD) involves the l_2 norm of the state variable, and, therefore, Lemma 8.1 is not directly applicable. The following Proposition 8.3 provides corresponding upper bounds on $\boldsymbol{f}_{\text{TTRD}}$ in a form similar to those in Lemma 8.1.

Proposition 8.3 *Given a vector $\boldsymbol{f} \in \mathbb{R}^n$ that can be decomposed into $f_m := \boldsymbol{e}_m^T \boldsymbol{f}$ with expression $f_m = \|\boldsymbol{a}\|_2 \boldsymbol{r}_m^T \boldsymbol{a}$, $m = 1, 2, ..., n$ with $\boldsymbol{r}_m \in \mathbb{R}^n$.*

(a) In a local region $\|\boldsymbol{a}\|_2^2 \leq \delta^2$, each f_m^2 is bounded as

$$f_m^2 = \|\boldsymbol{a}\|_2^2 \boldsymbol{a}^T \boldsymbol{r}_m \boldsymbol{r}_m^T \boldsymbol{a} \leq \delta^2 \boldsymbol{a}^T \boldsymbol{r}_m \boldsymbol{r}_m^T \boldsymbol{a}. \tag{8.18}$$

(b) In a local region $\|\boldsymbol{a}\|_2^2 \leq \delta^2$, $\|\boldsymbol{f}\|_2^2$ is bounded as

$$\|\boldsymbol{f}\|_2^2 \leq \delta^2 \sum_{m=1}^{n} \boldsymbol{a}^T \boldsymbol{r}_m \boldsymbol{r}_m^T \boldsymbol{a}. \tag{8.19}$$

Taking the bounds in Proposition 8.3 and employing the substitution $\boldsymbol{R}_m \boldsymbol{R}_m = \boldsymbol{r}_m \boldsymbol{r}_m^T$ and $\boldsymbol{J}_F = \sum_{m=1}^{n} \boldsymbol{r}_m \boldsymbol{r}_m^T$ enables the direct application of Theorem 8.2. The nonlinearities in equations (TTRD') and (TTRD") are quadratic, so we can directly apply Theorem 8.2. We also note

that for these two-dimensional models, the orthogonal complement satisfying equation (8.3) is trivial, so we set $\boldsymbol{n} = \boldsymbol{0}$ in applying Theorem 8.2.

The results of the application of the optimization procedure described above for solving equation (8.13) over the given parameter ranges followed by the least-squares fit to $\delta_{\mathsf{p}} = 10^{A} Re^{\sigma}$ leads to the parameter values A and α shown in Table 8.1. The table indicates a good agreement between the simulations and the theory for all three models.

Having obtained good results with the two-dimensional TTRD models, we next consider the three-dimensional BDT shear flow model,

$$\frac{d}{dt}\begin{bmatrix} u \\ v \\ w \end{bmatrix} = \begin{bmatrix} -Re^{-1} & Re^{-1/2} & 0 \\ 0 & -Re^{-1} & Re^{-1/2} \\ 0 & 0 & -Re^{-1} \end{bmatrix} \begin{bmatrix} u \\ v \\ w \end{bmatrix} + \left\| \begin{bmatrix} u \\ v \\ w \end{bmatrix} \right\|_2 \begin{bmatrix} 0 & -1 & 1 \\ 1 & 0 & 1 \\ -1 & -1 & 0 \end{bmatrix} \begin{bmatrix} u \\ v \\ w \end{bmatrix}. \qquad \text{(BDT)}$$

The form of the nonlinearity in this model is similar to that in equation (TTRD), and therefore we again use Proposition 8.3 and the previously described substitution in order to apply Theorem 8.2. Since the system is of odd dimension, there is a non-trivial orthogonal complement for the nonlinear term. In particular, we use $\boldsymbol{n}_{\mathsf{BDT}}^{T} = \begin{bmatrix} -1 & 1 & 1 \end{bmatrix}$ in the computation of the $\boldsymbol{M}_i$ and $\boldsymbol{T}_j$ in equation (8.11c). Table 8.1 shows that the values of A and σ obtained through the procedure described above in solving the optimization in equation (8.13) and fitting the function form for $\delta_{\mathsf{p}}(Re)$ agree well with those obtained through extensive simulations.

The final class of low dimensional models that we analyze in this subsection are the four-dimensional W model proposed in Waleffe (1995) and its three-dimensional variation W' provided in (Baggett & Trefethen, 1997). We note here that the four-dimensional W model with the coefficients provided in (Waleffe, 1995) is also referred to as the WKH model, e.g. in (Kalur *et al.*, 2020, 2021*b*) where they perform a related analysis of this particular model. These W and W' models are respectively given by

$$\frac{d}{dt}\begin{bmatrix} u \\ v \\ w \\ n \end{bmatrix} = \begin{bmatrix} -Re^{-1} & 1 & 0 & 0 \\ 0 & -Re^{-1} & 0 & 0 \\ 0 & 0 & -Re^{-1} & 0 \\ 0 & 0 & 0 & -Re^{-1} \end{bmatrix} \begin{bmatrix} u \\ v \\ w \\ n \end{bmatrix} + \begin{bmatrix} 0 & 0 & -w & -v \\ 0 & 0 & w & 0 \\ w & -w & 0 & 0 \\ v & 0 & 0 & 0 \end{bmatrix} \begin{bmatrix} u \\ v \\ w \\ n \end{bmatrix}, \qquad \text{(W)}$$

Model abbreviation	A	σ	σ **in (Baggett & Trefethen, 1997)**
TTRD	-0.03	-3.03	-3
TTRD'	-0.04	-3.07	-3
TTRD"	-0.35	-1.98	-2
BDT	0.03	-3.04	-3
W	-0.45	-1.98	-2
W'	-0.38	-1.94	-2

Table 8.1: A and σ fitting to $\delta_{\mathsf{p}} = 10^{A} Re^{\sigma}$ with δ_{p} obtained from the current framework for each shear flow model. The obtained σ are compared with scaling exponents σ reported in Ref. (Baggett & Trefethen, 1997).

$$\frac{d}{dt}\begin{bmatrix} u \\ v \\ w \end{bmatrix} = \begin{bmatrix} -Re^{-1} & 1 & 0 \\ 0 & -Re^{-1} & 0 \\ 0 & 0 & -Re^{-1} \end{bmatrix}\begin{bmatrix} u \\ v \\ w \end{bmatrix} + \begin{bmatrix} 0 & 0 & -w \\ 0 & 0 & w \\ w & -w & 0 \end{bmatrix}\begin{bmatrix} u \\ v \\ w \end{bmatrix}. \qquad \text{(W')}$$

Both models allow direct application of Lemma 8.1 to bound the nonlinear terms. The analyses for these two models differ in that there exists a non-trivial $\boldsymbol{n}_{\mathsf{W'}}^T = \begin{bmatrix} 1 & 1 & 0 \end{bmatrix}$ for the nonlinear term in the odd-dimensional model (W') but not for the nonlinear term in the even-dimensional model (W). Table 8.1 indicates that the theoretical results and associated optimization problems lead to scalings σ for both the W and W' models that are consistent with those obtained through extensive numerical simulations.

The results in Table 8.1 demonstrate that the scaling exponents σ obtained from the current framework are close to the σ computed from extensive numerical simulations (Baggett & Trefethen, 1997). However, the current framework has the benefit of providing this estimation for the permissible perturbation amplitude without requiring any simulations or experiments. Moreover, the convergence to the origin is guaranteed for *any* perturbation below the obtained permissible perturbation amplitude δ_{p}, whereas numerical simulations and experiments can only test on a finite set of perturbations and, therefore, do not provide provably definitive results. Given the good agreement with simulation studies for commonly studied low-dimensional shear flow models, we next apply the theory to the more comprehensive nine-dimensional model and discuss the computational complexity of this approach versus SOS-based analysis methods.

8.3.2 Application to a 9-D shear flow model and comparison with SOS

In this section, we focus on the nine-dimensional shear flow model (Moehlis *et al.*, 2004). We first compare the permissible perturbation amplitude δ_{p} obtained through the method proposed in Section 8.2 to the values identified using extensive simulations. We then compare our results to the rigorous bounds based on Lyapunov analysis computed through SOS programming. SOS programming (Parrilo, 2000; Prajna *et al.*, 2002; Papachristodoulou & Prajna, 2005*b*) is a widely used tool to search for Lyapunov functions for stability and region of attraction based computations; see e.g., which describe applications in fluid dynamics (Goulart & Chernyshenko, 2012; Chernyshenko *et al.*, 2014; Huang *et al.*, 2015; Lasagna *et al.*, 2016; Huang *et al.*, 2017; Fuentes *et al.*, 2019; Ahmadi *et al.*, 2019; Lakshmi *et al.*, 2020). SOS provides a generalization of the LMI framework that can be used to find higher-order (beyond quadratic) polynomials as the candidate of Lyapunov functions. When the degree of the polynomials in an SOS program is fixed, it is typically solved by converting the SOS constraints to an SDP. Further details of SOS methods and SOS programming can be found in (Parrilo, 2000; Papachristodoulou & Prajna, 2005*b*; Papachristodoulou *et al.*, 2013). The comparison with SOS highlights the computational efficiency of the method and explores the trade-off between the computational efficiency of our LMI based approach and the accuracy that can be obtained through SOS methods, which allow the full representation of the nonlinearity rather than the constraints on its properties detailed in Section 8.2.

The nine-dimensional model is comprised of an eight-dimensional Galerkin model (Waleffe, 1997) describing the self-sustaining process and an additional mode that enables the full model to capture the change in the mean velocity profile as the flow transitions from the laminar to the turbulent state (Moehlis *et al.*, 2004). This model has been widely used as a prototype to study stability and transition in shear flows that have no linear instabilities, see e.g. Moehlis *et al.* (2005); Lakshmi *et al.* (2020); Kim & Moehlis (2008); Goulart & Chernyshenko (2012); Chernyshenko *et al.* (2014); Joglekar *et al.* (2015). The dynamics of the nine-mode model are obtained directly from a Galerkin projection of the NS equations (Moehlis *et al.*, 2004).

Appendix D provides the details of the derivation of the model, which can be written in the form,

$$\frac{d\boldsymbol{a}}{dt} = -\frac{\boldsymbol{\Xi}}{Re}\boldsymbol{a} + \boldsymbol{J}(\boldsymbol{a})\bar{\boldsymbol{a}} + \boldsymbol{J}(\bar{\boldsymbol{a}})\boldsymbol{a} + \boldsymbol{J}(\boldsymbol{a})\boldsymbol{a}, \tag{8.20}$$

where $\bar{\boldsymbol{a}}$ denotes the laminar flow solution. We use the same model coefficients as in (Joglekar *et al.*, 2015), which requires that we use their domain size of $L_x = 1.75\pi$ and $L_z = 1.2\pi$. Here we describe the role of the various terms, but for the sake of brevity, we refer to equation (D.10) in Appendix A for details of each coefficient. The first term on the right-hand side (RHS) of equation (8.20) is the viscous term, and $\boldsymbol{\Xi}$ is a symmetric positive definite matrix. The second term on the RHS of (8.20) $\boldsymbol{J}(\boldsymbol{a})\bar{\boldsymbol{a}}$ is an analog to the mean shear term in the linearized NS equations. The resulting shear production mechanism is critical in maintaining turbulence in wall-bounded shear flows (Kim & Lim, 2000). The following two terms on the RHS of equation (8.20), $\boldsymbol{J}(\bar{\boldsymbol{a}})$ and $\boldsymbol{J}(\boldsymbol{a})$, respectively, correspond to the advection by the laminar mean flow and nonlinear advection. The nonlinear advection term is energy-conserving in analogy to the nonlinear advection term in the NS equations, i.e., $\boldsymbol{a}^T\boldsymbol{J}(\boldsymbol{a})\boldsymbol{a} = 0$. When the Galerkin model is obtained through data (Brunton *et al.*, 2016), this energy-conserving property can be explicitly implemented as a constraint (Loiseau & Brunton, 2018).

In order to apply the theory of Section 8.2, we first express the linear terms as

$$\boldsymbol{L}\boldsymbol{a} := -\frac{\boldsymbol{\Xi}}{Re}\boldsymbol{a} + \boldsymbol{J}(\boldsymbol{a})\bar{\boldsymbol{a}} + \boldsymbol{J}(\bar{\boldsymbol{a}})\boldsymbol{a}, \tag{8.21}$$

which makes it easy to see that the nonlinear form is exactly that in equation (8.1), i.e. $\boldsymbol{f} := \boldsymbol{J}(\boldsymbol{a})\boldsymbol{a}$. The form of the nonlinearity means that we can directly apply the bounds in Lemma 8.1. The nonlinearity is energy-conserving and of odd dimension, therefore there exists a non-trivial element in the left nullspace of $\boldsymbol{J}(\boldsymbol{a})$. The corresponding element $\boldsymbol{n}^T = \begin{bmatrix} 1 & 0 & 0 & 0 & 0 & 0 & 0 & 0 & -1 \end{bmatrix}$ is known and can easily be deduced from equations (D.10a) and (D.10i) in Appendix D.

Having defined the constraint set, we first apply Theorem 8.2 to reproduce results from

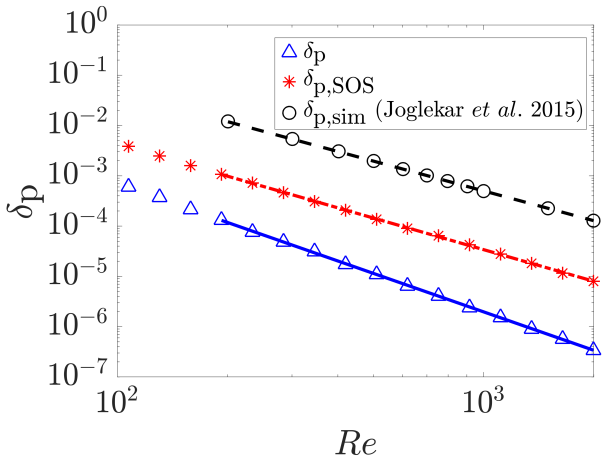

Figure 8.5: Permissible perturbation amplitudes for the nine-dimensional shear flow model (Moehlis *et al.*, 2004) in Section 8.3.2: δ_{p} (△) obtained from Theorem 8.2 and equation (8.13) displaying $\delta_{\mathrm{p}} = 10^{1.92}Re^{-2.54}$ (—); $\delta_{\mathrm{p,SOS}}$ (✳) obtained from the SOS programming in equations (8.22) and (8.23) displaying $\delta_{\mathrm{p,SOS}} = 10^{1.80}Re^{-2.09}$ (– · –); $\delta_{\mathrm{p,sim}}$ (◯) obtained from simulations displaying $\delta_{\mathrm{p,sim}} = 10^{2.61}Re^{-1.97}$ (– –) (Joglekar *et al.*, 2015).

energy stability analysis using the approach described in section 8.2.2. The laminar state of this nine-dimensional shear flow model with a larger domain size ($L_x = 4\pi$ and $L_z = 2\pi$) was shown to be globally asymptotically stable at Reynolds numbers below 7.5 using classical energy methods. Using the proposed method provides a certification that (8.11) is feasible for an arbitrarily large δ resulting in $\delta_{\mathrm{p}} = \infty$ when $Re < Re_E = 7.5$. We note that the energy bound was further improved to $Re_{SOS} = 54.1$ through SOS-based stability analysis using fourth-order polynomial Lyapunov functions (Goulart & Chernyshenko, 2012). However, since the current framework limits the candidate Lyapunov function to a quadratic form (second-order polynomials), this approach cannot recover the results predicted by the SOS programming with fourth-order polynomials. The LMI based method is, however, far more computationally efficient (as discussed later in this section). Methods that can take advantage of these computational benefits while improving accuracy through higher-order Lyapunov functions are a direction of future work.

Figure 8.5 next shows the results of the optimization δ_{p} at each Reynolds number in the range where there is no proof of global asymptotic stability of the laminar state. In particular, we concentrate on $Re \geq 100$ as recent results suggest that the laminar solution of the model is

globally asymptotically stable below $Re < 80.54$ (Lakshmi *et al.*, 2020). We then perform the least-squares fit to the same function $\delta_{\mathsf{p}}(Re) = 10^{A} Re^{\sigma}$ and obtain $\delta_{\mathsf{p}} = 10^{1.92} Re^{-2.54}$ in the range $Re \in (190, 2000)$. These results are plotted alongside the function $\delta_{\mathsf{p,sim}} = 10^{2.61} Re^{-1.97}$ reported in Figure 8 of (Joglekar *et al.*, 2015), which are obtained from 10,000 simulations of the same nine-mode model with randomly chosen initial conditions. The results show that the permissible perturbation amplitude identified using this framework is conservative, however, it has the benefit of providing a rigorous lower bound (Theorem 8.2) on the results obtained from extensive simulations.

In order to illustrate the effects of constraining rather than fully representing the nonlinearity, we now compare our results to those obtained using a quadratic Lyapunov function obtained through SOS programming. SOS-based programs enable the exploration of a larger class of candidate Lyapunov functions; however, these additional degrees of freedom come at the expense of more computational resources; see e.g., (Goulart & Chernyshenko, 2012). The computational complexity increases with the order of the candidate Lyapunov functions. Here, we restrict the candidate Lyapunov functions to quadratic forms $V = \boldsymbol{a}^T \boldsymbol{P} \boldsymbol{a}$ for direct comparison of the accuracy and computational resources associated versus the proposed method based on Theorem 8.2. In particular, we employ Theorem 3.7 in Ref. (Anderson & Papachristodoulou, 2015) to certify local asymptotic stability through checking the conditions,

$$\boldsymbol{P} - \epsilon \boldsymbol{I} \succeq 0, \tag{8.22a}$$

$$\epsilon > 0, \tag{8.22b}$$

$$\frac{dV}{dt} + (\delta^2 - \boldsymbol{a}^T \boldsymbol{a}) \boldsymbol{a}^T \boldsymbol{R} \boldsymbol{a} + \epsilon \boldsymbol{a}^T \boldsymbol{a} \leq 0, \text{ and} \tag{8.22c}$$

$$\boldsymbol{R} \succeq 0. \tag{8.22d}$$

We then define $\delta_{\text{p,SOS}}$ by solving an analogous optimization problem to that in (8.13), specifically,

$$\delta_{\text{p,SOS}} := \max_{\delta} \delta \sqrt{\frac{\mu_{\text{min}}(\boldsymbol{P})}{\mu_{\text{max}}(\boldsymbol{P})}} \tag{8.23}$$

subject to (8.22).

Note that the term $(\delta^2 - \boldsymbol{a}^T\boldsymbol{a})\boldsymbol{a}^T\boldsymbol{R}\boldsymbol{a}$ in equation (8.22c) involves a fourth-order polynomial in $\boldsymbol{a}$ and it is this constraint that prevents us from directly formulating the problem as an LMI, which adds to the additional computational complexity. We employ SOSTOOLS version 3.03 (Papachristodoulou *et al.*, 2013) to implement the inequalities in equation (8.22) and test the feasibility of equation (8.23). SOSTOOLS converts the SOS programming problem into an SDP (Prajna *et al.*, 2002; Papachristodoulou *et al.*, 2013). For comparison purposes, we use the same SDP solver, SeDuMi v1.3, as before.

The resulting $\delta_{\text{p,SOS}}$ values at each Reynolds number and function $\delta_{\text{p,SOS}} = 10^{1.80}Re^{-2.09}$ are provided in Figure 8.5 alongside the LMI and simulation results. Clearly, the results obtained from the SOS are closer to the simulation results than those obtained from LMI based method in equation (8.13). In particular, the permissible perturbation amplitude $\delta_{\text{p,SOS}}$ shows a scaling exponent σ of -2.09, which is closer to the -1.97 observed in the simulation results in Ref. (Joglekar *et al.*, 2015). However, this improved accuracy is achieved at the expense of high computational resources as highlighted in Table 8.2. The results indicate that incorporating more properties of nonlinearity, e.g. those that are captured by the SOS formulation, could improve the performance of the LMI approach. Further analysis of the perturbation structures associated with the lowest permissible perturbations, as discussed in Remark 8.2, may provide additional insights into the results to provide an understanding of the system stability. This incorporation and analysis require some additional theory and computational tools for efficient implementation, so we leave this as a topic of future work.

Table 8.2 compares each of the computational steps contributing to the total computational time of the proposed LMI method to the SOS-based solution. We divide the computation time

Method	LMI	SOS
Preprocessing time (s)	197	657837
SDP Solver time (s)	667	17209
Size of the largest PSD cone	18	54
Number of constraints	74	795

Table 8.2: Comparison of the proposed LMI framework in Theorem 8.2 and (8.13) with SOS programming in equations (8.22) and (8.23) for the same nine-dimensional model of sinusoidal shear flow (Moehlis *et al.*, 2004) in Section 8.3.2.

into the following steps. The 'Preprocessing time' describes the time to convert the problems into an SDP (which is the method of solution in both cases). The computation time used to solve the SDP is reported as the 'SDP solver time'. We also report the size of the largest positive semi-definite cone and the number of constraints (for every fixed given δ and Re) to further explain where the differences in the computational times arise.

The values in Table 8.2 clearly indicate that the LMI based framework in Theorem 8.2 uses substantially less computational time compared with the SOS programming. Here, we also note that the proposed LMI framework can effectively reduce the size of the largest PSD cone and the number of constraints, resulting in a more efficient estimation for permissible perturbation amplitude. This computational efficiency is achieved through constraining the nonlinearity rather than directly including it, which directly contributes to smaller problem inputs to the SDP solver. This reduction in the number of inputs to the SDP solver suggests that the LMI framework may also have the benefit of saving the memory, which is another computational bottleneck of SOS (Zheng *et al.*, 2018). However, as also indicated in Theorem 8.2, the LMI formulation is currently limited to quadratic Lyapunov functions, which constraints the results that can be obtained. Further analysis of this trade-off between accuracy and computation along with adapting the method to increase accuracy with less additional computational burden are directions of ongoing work.

8.4 Summary

This work proposes an input–output inspired approach to determining the permissible level of perturbation amplitude to maintain a laminar flow state. The proposed framework partitions the dynamics into a feedback interconnection of the linear and nonlinear dynamics; i.e., a Luré system in which nonlinearity is static feedback. We construct quadratic constraints of the nonlinear term that are restricted by system physics to be energy-conserving (lossless) and to have bounded input–output energy in a local region. These constraints allow us to formulate computation of the region of attraction of the laminar state (a set of safe perturbations) and permissible perturbation amplitude as Linear Matrix Inequalities (LMI), which are solved efficiently through available toolboxes. The proposed framework provides a generalization of both linear analysis and classical energy methods. We apply our approach to a wide class of low dimensional nonlinear shear flow models (Trefethen *et al.*, 1993; Baggett *et al.*, 1995; Waleffe, 1995; Baggett & Trefethen, 1997; Moehlis *et al.*, 2004) for a range of Reynolds numbers. The results from our analytically derived bounds on the permissible perturbation amplitude are consistent with the bounds identified through exhaustive simulations (Baggett & Trefethen, 1997; Joglekar *et al.*, 2015). However, our results are obtained at a much lower computational cost and have the benefit of providing a provable guarantee that a certain level of perturbation is permissible.

We perform a more detailed analysis of the nine-mode model of shear flows, which shows that the framework provides more conservative but provably correct results as the model complexity increases. A comparison to SOS-based Lyapunov analysis of the full nonlinear system shows that the inherent restriction of the candidate Lyapunov function to a smaller set capturing nonlinearity through constraints on its properties rather than direct description provides improved computational efficiency. However, this increased efficiency comes at the cost of reduced accuracy, which future work aims to further characterize and mitigate through extensions to the proposed approach.

The accuracy of the approach could potentially be improved through tightening the bounds

in Lemma 8.1. One approach that is promising is the direct use of a quadratic form of $\boldsymbol{a}$ to represent $\|\boldsymbol{J}(\boldsymbol{a})\|_{2,2}$, which will render the approach less conservative but require some additional theory and computational tools for efficient implementation. Other forms of nonlinearity are also interesting directions for future work. In particular, the extension to systems with a nonlinearity involving the l_2 norm of state variables in Proposition 8.3 here demonstrates its applicability to problems that are not typically straightforward using SOS programming; e.g., a change of variables and additional constraints are required to describe such a nonlinearity as polynomial (Papachristodoulou & Prajna, 2005*a*). Generalizing the current framework to a wider class of nonlinear systems (Valmorbida *et al.*, 2018) involving these and other constraints less amenable to polynomial analysis may be a promising direction.

Other directions for future work involve a more detailed analysis of the shape of the region of attraction and extensions to partial differential equations based models as a step toward analysis of the full NS equations; see e.g., (Ahmadi *et al.*, 2019).

Chapter 9

Conclusions and future directions

9.1 Conclusions

This work investigates the characteristic length, time, and velocity scales in a wide range of canonical wall-bounded shear flows through the application of input-output analysis based techniques. A range of approaches based on the traditional open-loop spatio-temporal frequency response of the linearized dynamics and extensions that capture nonlinear interactions through a novel feedback structure are applied to analyze plane Poiseuille flow along with plane Couette flow in cannonical, stably stratified and spanwise rotating configurations.

In chapter 2, we introduce the input-output and feedback interconnection based analyses and the associated spatio-temportal response operators. This chapter also employs low-dimensional toy models to illustrate these analysis tools.

Chapter 3 describes the application of traditional (open-loop) input-output analysis to the determination and analysis of convective velocity across a range of flow scales in turbulent channel flows, with particular emphasis on the mechanism underlying the breakdown of Taylor's hypothesis in the near-wall region. The convective velocity for a fluctuating quantity associated with streamwise–spanwise wavelength pairs at each wall-normal location is obtained through the maximization of the power spectral density associated with the spatio-temporal response operator associated with the linear part of the Navier-Stokes equations with a turbulent mean

profile. Delta-correlated Gaussian forcing that provides the input forcing and the outputs corresponding to each velocity and vorticity component are analyzed. We first demonstrate that the mean convective velocities computed in this manner agrees well with those reported previously in the literature. We then exploit the analytical framework to probe the underlying mechanisms contributing to the local convective velocity at different wall-normal locations by isolating the contributions of each streamwise–spanwise wavelength pair (wall-parallel flow scale). The resulting analysis suggests that the behavior of the convective velocity in the near-wall region is influenced by large-scale structures further away from the wall. We then investigate the role of each linear term in the momentum equation to isolate the contribution of the pressure, mean shear, and viscous effects to the deviation of the convective velocity from the mean at each flow scale. Our analysis highlights the role of the viscous effects, particularly in regards to large channel spanning structures whose influence extends to the near-wall region. We leverage these findings to provide a viscous correction to Taylor's hypothesis that greatly improves its accuracy in predicting the convective velocity of both the velocity and vorticity components in the near wall region.

Chapter 4 employs the recently proposed one-way spatial integration technique (Towne & Colonius, 2015) to perform describes the spatial input-output analysis, which is used to investigate the streamwise propagation of large-scale structures in an actuated turbulent boundary layer. The transformation of the dynamics to reflect the spatial rather than temporal evolution of the flow field eliminates the ambiguity associated with the need to specify a particular streamwise wavenumber in input–output (resolvent) analysis. This downstream marching also embeds a wall-normal dependent convective velocity for flow structures associated with a dominant temporal frequency. The application of interest is a turbulent boundary layer with a fixed frequency actuation signal applied in the outer layer to generate synthetic large scale structures. The effect of the actuator on the flow is modeled as a body force associated with a dominant temporal frequency comprised of a Dirac delta function in the streamwise direction and, a Gaussian function in the wall-normal direction that is uniform in the spanwise direction. The results are compared

with the evolution of large-scale structures experimentally generated through a dielectric barrier discharge plasma actuator attached to a plate mounted in the outer region of the flow. Large-scale structures obtained from this spatial input–output analysis show qualitative agreements with measurements from hot-wire measurements and a phase-locked analysis. These differences in convective velocity as a function of wall normal height lead to increasing inclination angle as the induced structures travel downstream. The ability of the framework to capture this behavior demonstrates its benefit over the use of the traditional input-output response as that type of analysis has been shown to produce a single convective velocity over all wall-normal heights given a single streamwise wavenumber and actuation frequency pair. The detailed velocity field produced through the analysis enables us to perform a quadrant trajectory analysis to assess the similarity between these actuated large-scale structures and the large-scale structures naturally occurring in a canonical wall-bounded turbulent flow. The similarities observed highlight the promise of a spatial framework in modeling and analyzing large-scale structures in turbulent boundary layers through a spatially localized perturbation with a dominant temporal frequency.

Chapter 5 introduces structured input-output analysis and its application to improve the prediction of the most amplified transition-inducing flow structures (optimal perturbation) in transitional plane Couette and plane Poiseuille flows. This framework employs a *structured* singular value-based approach that preserves certain input–output properties of the nonlinear forcing function in an effort to recover the larger range of key flow features identified through nonlinear analysis, experiments, and direct numerical simulation (DNS). Application of this method to transitional plane Couette and plane Poiseuille flows leads to the identification of not only the streamwise coherent structures predicted through traditional input–output approaches but also characterization of the oblique flow structures as those requiring the least energy to induce transition in agreement with DNS studies, and nonlinear optimal perturbation analysis. The proposed approach also captures the recently observed oblique turbulent bands that have been linked to transition in experiments and DNS with very large channel size. The ability to identify the larger amplification of the streamwise varying structures predicted from DNS and

nonlinear analysis in both flow regimes suggests that the structured approach allows one to maintain the nonlinear effects associated with the weakening of the lift-up mechanism, which is known to dominate the linear operator. Capturing this key nonlinear mechanism enables the prediction of the wider range of known transitional flow structures within the analytical input–output modeling paradigm.

Chapter 6 extends structured input-output analysis to include density stratification and employs it to analyze the characteristic length scales of flow structures in stratified plane Couette flow. This approach predicts high amplification associated with the wavelengths of oblique turbulent bands observed in a very large channel with extents $\sim O(100)$ times of channel half-height in the low-Reynolds number (Re) low-bulk Richardson number (Ri_b) intermittent regime. In the high-Re high-Ri_b intermittent regime, this approach highlights quasi-horizontal flow structures resembling turbulent-laminar layers that are associated with amplification close to oblique turbulent bands. This approach further suggests the threshold value of the Miles-Howard theorem ($Ri_b > 0.25$) is associated with suppressing the amplification of streamwise dependent flow structures at Prandtl number close to one ($Pr \approx 1$) and this behavior is robust across a wide range of Re. At $Pr \ll 1$, the amplification is determined by $PrRi_b$, and a larger Ri_b is required to suppress the prevalence of streamwise dependent flow structures. At $Pr \gg 1$, this approach identifies another quasi-horizontal flow structure independent of Ri_b. By decomposing input-output pathways into each velocity and density component, we show these quasi-horizontal flow structures at $Pr \gg 1$ are associated with density. The importance of this density-associated flow structure at $Pr \gg 1$ is further demonstrated through analytically derived scaling of amplification over Re and Pr under the passive scalar and streamwise constant assumptions.

Chapter 7 then employs structured input-output analysis to examine a mathematical analogy between rotating plane Couette flow and stratified plane Couette flow. In particular, we focuses on a mathematical equivalence between two-dimensional three-component (2D/3C, no streamwise variation) spanwise rotating PCF and two-dimensional (2D, no streamwise variation and no streamwise velocity) vertically stratified PCF. At relatively slow rotation, the structured

input-output analysis captures the streamwise and spanwise wavelengths of the oblique turbulent bands in rotating PCF similar to the observation in the stratified PCF. Increasing the stabilizing effect of rotation and stratification associated with the mathematical equivalence, this approach quantifies that stratification is suppressing the amplification of streamwise dependent flow structures faster than rotation. The largest amplification of streamwise constant (2D/3C) flow structures in rotating PCF is not influenced by the rotation number, which suggests additional mathematical equivalence. We then extend (2D/3C-R=2D-S) to a mathematical equivalence between stratified and rotating PCF 2D/3C rotating PCF. We illustrate one additional mathematical equivalence between 2D/3C rotating PCF with passive scalar and 2D/3C stratified PCF and demonstrate the validity of this theoretical behavior using structured input-output analysis.

Chapter 8 proposes a linear matrix inequality based method to provide a provable Reynolds number-dependent bound on the amplitude of perturbations a flow can sustain while maintaining the laminar state. We construct quadratic constraints on the nonlinear term based on the fact that the system physics are energy-conserving (lossless) and have bounded input–output energy. Computing the region of attraction of the laminar state (set of safe perturbations) and permissible perturbation amplitude are then reformulated as Linear Matrix Inequalities (LMI). Solving this LMI problem is more computationally efficient than prevailing nonlinear approaches based on sum of squares programming. We apply our approach to low-dimensional nonlinear shear flow models for a range of Reynolds numbers. The results from our analytically derived bounds are consistent with the bounds identified through exhaustive simulations. However, they have the added benefits of being achieved at a much lower computational cost and providing a provable guarantee that a certain level of perturbation is permissible.

9.2 Future directions

The traditional input-output analysis in chapter 3 are relatively well-developed, and thus, we will focus on directions of future work involving structural input-output approach proposed in this thesis. One important direction is the extension of the structured input-output frameworks to

flow configurations of increasing complexity. For example, the current development focuses on flow defined using a Cartesian coordinate frame. An natural question is whether the nonlinearity can be treated similarly in cylindrical and, spherical coordinate frames as well as in more general complex flow geometries. In particular, oblique turbulent bands have been observed in a wider range of wall-bounded flows such as annual pipe flow, duct flow, Taylor-Couette flow, and Torsional Couette flow; see a recent review (Tuckerman *et al.*, 2020). Extension to these coordinate frames would enable us to explore whether their wavelengths can be similarly predicted by structured input-output analysis. Flows with the two-dimensional base flow and flow over an airfoil or riblet have been analyzed with the closely related resolvent-based analysis; see e.g., (Yeh & Taira, 2019; Chavarin & Luhar, 2020). It is therefore natural to ask whether structured input-output analysis can be extended to these configurations and whether or not this approach can provide additional physical insight.

Another direction for future exploration is the extension of the structured input-output analysis to spatially developing flows by e.g., combining the feedback interconnection structure within a spatial input-output paradigm like that studied in in chapter 4. Combining the structured input-output analysis approach in chapter 5 with Lyapunov-based arguments such as those used in chapter 8 to certify a permissible perturbation amplitude in canonical wall-bounded shear flows may also provide additional insight into the subcritical transition within a linear and computational tractable framework. It is also interesting to further develop the current structured input-output analysis to provide additional insight into the nonlinear saturation for supercritical transition observed in a wider flow regime of wall-bounded shear flows; e.g., with destabilizing rotation or stratification,

The structured input-output analysis can be also viewed as a reduced-order model the of nonlinearity. Here we use the simplest form of the structured uncertainty that captures the input-output pathways of interest. However, some further refinement may provide additional insight into the underlying physics, e.g., constraining the uncertain velocity $-\boldsymbol{u}_\xi$ as divergence-free and enforcing its discretization $-\widehat{\boldsymbol{u}}_\xi^{\mathsf{T}}$ in (5.14) with a diagonal structure for each of the

sub-blocks of. It may be also interesting to incorporate more properties of nonlinearity such as triadic interaction employing the harmonic balance method, see e.g., (Rigas *et al.*, 2021). Further insight may also be gained by extending the singular value decomposition (that also has left and right singular vectors) to perform a 'structured singular value decomposition' may also provide additional insight into the shape of underlying flow structures. This information may be extracted from the scaling matrix D in § 2.3.2.

The structured input-output analysis in chapters 5-7 can be also interpreted as 'structured robust stability' analysis and it may be further augmented with additional user-defined input-output pathways, e.g., with an input that models a particular type of actuation and output that models some sensor measurement. Then an interesting question is certifying certain system performance including controllability, observability, and bounded input-output gain within the structured feedback interconnection; i.e., structured robust performance (Zhou *et al.*, 1996, chapter 11). For flow control and drag reduction application, we can also add another feedback interconnection to synthesize a feedback controller (μ synthesis) (Zhou *et al.*, 1996, chapter 11).

The extension of these analysis tools in this thesis to increased flow configuration complexity relies on further development to increase computational efficiency. The main computational bottleneck of traditional input-output analysis and structured input-output analysis within this dissertation is memory. The analysis based on LMI and SOS in chapter 8 also require large memory when the dimension of the dynamical system is relatively large. There is a significant amount of progress in increasing the computational speed and reducing the memory bottleneck of input-output and resolvent-based analysis (e.g., randomized algorithm (Ribeiro *et al.*, 2020)). It is interesting to explore whether similar techniques can be employed to further increase the computational efficiency of structured singular value-based computations. There is also significant progress in semi-definite programming that forms the core solver in LMI and SOS based optimization problems (e.g., (Zheng *et al.*, 2018)). Understanding whether these new techniques can be employed in fluid dynamics problems to provide additional insight is an open question.

Appendix A

Asymptotic consistent turbulent boundary layer profile

Here, we describe the asymptotic consistent turbulent boundary layer profile developed by Monkewitz *et al.* (2007), which was also previously used; e.g., in Cossu *et al.* (2009). The mean profile is provided by:

$$U = u_\tau[U_i^+(y^+) - U_{log}^+(y^+) + U_e^+(Re_{\delta_*}) - U_w^+(\eta)]. \tag{A.1}$$

u_τ is the wall friction velocity, $y^+ = yu_\tau/\nu$ is the wall-normal location in the inner units $U_e^+ = U_e/u_\tau$ is the free stream velocity U_e scaled with u_τ. $Re_{\delta_*} = U_e\delta_*/\nu$ is the Reynolds number scaled on the displacement thickness length scale, and $\eta = y/\Delta$ is the wall-normal coordinate scaled with the Rotta-Clauser outer length scale $\Delta = \delta_* U_e^+$. The inner and the outer coordinates are related by $y^+ = Re_{\delta_*}\eta$. Then we have the explicit formula for these mean

velocity from Monkewitz *et al.* (2007):

$$
\begin{aligned}
U_i^+(y^+) =& 0.68285472\ \ln(y^{+2} + 4.7673096y^+ + 9545.9963) \\
&+ 1.2408249\ \arctan(0.010238083y^+ + 0.024404056) \\
&+ 1.2384572\ \ln(y^+ + 95.232690) - 11.930683 \\
&- 0.50435126\ \ln(y^{+2} - 7.8796955y^+ + 78.389178) \\
&+ 4.7413546\ \arctan(0.12612158y^+ - 0.49689982) \\
&- 2.7768771\ \ln(y^{+2} + 16.209175y^+ + 933.16587) \\
&+ 0.37625729\ \arctan(0.033952353y^+ + 0.27516982) \\
&+ 6.5624567\ \ln(y^+ + 13.670520) + 6.1128254, \qquad \text{(A.2a)}
\end{aligned}
$$

$$
U_{log}^+(y^+) = \frac{1}{\kappa}\ln(y^+) + B, \qquad \text{(A.2b)}
$$

$$
U_e^+(Re_{\delta_*}) = \frac{1}{\kappa}\ln(Re_{\delta_*}) + C, \qquad \text{(A.2c)}
$$

$$
U_w^+(\eta) = [\frac{1}{\kappa}E_1(\eta) + w_0]\frac{1}{2}[1 - \tanh(\frac{w_{-1}}{\eta} + w_2\eta^2 + w_8\eta^8)], \qquad \text{(A.2d)}
$$

where $\kappa = 0.384$, $B = 4.17$, $C = 3.3$, $w_0 = 0.6332$, $w_{-1} = -0.096$, $w_2 = 28.5$, $w_8 = 33000$, and $E_1(\eta) = \int_\eta^\infty \frac{e^{-t}}{t}dt$. These analytical expressions are validated to be the same as the mean profile at $Re_\tau = 690$ obtained from direct numerical simulations (Simens *et al.*, 2009; Jiménez *et al.*, 2010) (`https://torroja.dmt.upm.es/turbdata/blayers/low_re/profiles/`).

Appendix B

Proof of theorems 5.3-5.4

B.1 Proof of theorem 5.3

Proof: We define the following sets of uncertainty:

$$\widehat{\boldsymbol{U}}_{\Xi,ux} := \left\{ \text{diag}\left(-\widehat{\boldsymbol{u}}_{\xi}^{\mathsf{T}}, \boldsymbol{0}, \boldsymbol{0}\right) : -\widehat{\boldsymbol{u}}_{\xi}^{\mathsf{T}} \in \mathbb{C}^{N_y \times 3N_y} \right\}, \tag{B.1a}$$

$$\widehat{\boldsymbol{U}}_{\Xi,vy} := \left\{ \text{diag}\left(\boldsymbol{0}, -\widehat{\boldsymbol{u}}_{\xi}^{\mathsf{T}}, \boldsymbol{0}\right) : -\widehat{\boldsymbol{u}}_{\xi}^{\mathsf{T}} \in \mathbb{C}^{N_y \times 3N_y} \right\}, \tag{B.1b}$$

$$\widehat{\boldsymbol{U}}_{\Xi,wz} := \left\{ \text{diag}\left(\boldsymbol{0}, \boldsymbol{0}, -\widehat{\boldsymbol{u}}_{\xi}^{\mathsf{T}}\right) : -\widehat{\boldsymbol{u}}_{\xi}^{\mathsf{T}} \in \mathbb{C}^{N_y \times 3N_y} \right\}. \tag{B.1c}$$

Here, $\boldsymbol{0} \in \mathbb{C}^{N_y \times 3N_y}$ is a zero matrix with the size $N_y \times 3N_y$. Then, using the definition of the structured singular value in definition 5.1, we have:

$$\begin{aligned}
&\mu_{\widehat{\boldsymbol{U}}_{\Xi,ux}}\left[\boldsymbol{H}_{\nabla}(k_x,k_z,\omega)\right] \\
=&\frac{1}{\min\{\bar{\sigma}[\widehat{\boldsymbol{u}}_{\Xi,ux}] \,:\, \widehat{\boldsymbol{u}}_{\Xi,ux} \in \widehat{\boldsymbol{U}}_{\Xi,ux},\, \det[\boldsymbol{I} - \boldsymbol{H}_{\nabla}(k_x,k_z,\omega)\widehat{\boldsymbol{u}}_{\Xi,ux}] = 0\}} && \text{(B.2a)} \\
=&\frac{1}{\min\{\bar{\sigma}[-\widehat{\boldsymbol{u}}_{\xi}^{\mathsf{T}}] \,:\, -\widehat{\boldsymbol{u}}_{\xi}^{\mathsf{T}} \in \mathbb{C}^{N_y \times 3N_y},\, \det[\boldsymbol{I}_{3N_y} - \boldsymbol{H}_{\nabla ux}(k_x,k_z,\omega)(-\widehat{\boldsymbol{u}}_{\xi}^{\mathsf{T}})] = 0\}} && \text{(B.2b)} \\
=&\bar{\sigma}[\boldsymbol{H}_{\nabla ux}(k_x,k_z,\omega)]. && \text{(B.2c)}
\end{aligned}$$

Here, the equality (B.2a) is obtained by substituting the uncertainty set in (B.1a) into definition 5.1. The equality (B.2b) is obtained by performing block diagonal partition of terms inside

of $\det[\cdot]$ and employing zeros in the uncertainty set in equation (B.1a). Here, $\boldsymbol{H}_{\nabla ux}$ is the discretization of $\mathcal{H}_{\nabla ux}$ and $\boldsymbol{I}_{3N_y} \in \mathbb{C}^{3N_y \times 3N_y}$ in (B.2b) is an identity matrix with matching size $(3N_y \times 3N_y)$, whereas $\boldsymbol{I} \in \mathbb{C}^{9N_y \times 9N_y}$ in (B.2a). The equality (B.2c) is using the definition of unstructured singular value; see e.g., (Zhou *et al.*, 1996, equation (11.1)).

Similarly, we have:

$$\mu_{\widehat{\boldsymbol{U}}_{\Xi,vy}}\left[\boldsymbol{H}_{\nabla}(k_x,k_z,\omega)\right] = \bar{\sigma}[\boldsymbol{H}_{\nabla vy}(k_x,k_z,\omega)], \tag{B.3a}$$

$$\mu_{\widehat{\boldsymbol{U}}_{\Xi,wz}}\left[\boldsymbol{H}_{\nabla}(k_x,k_z,\omega)\right] = \bar{\sigma}[\boldsymbol{H}_{\nabla wz}(k_x,k_z,\omega)]. \tag{B.3b}$$

Using the fact that $\widehat{\boldsymbol{U}}_{\Xi} \supseteq \widehat{\boldsymbol{U}}_{\Xi,ij}$ with $ij = ux, vy, wz$ and equalities in (B.2)-(B.3), we have:

$$\mu_{\widehat{\boldsymbol{U}}_{\Xi}}\left[\boldsymbol{H}_{\nabla}(k_x,k_z,\omega)\right] \geq \mu_{\widehat{\boldsymbol{U}}_{\Xi,ij}}\left[\boldsymbol{H}_{\nabla}(k_x,k_z,\omega)\right] = \bar{\sigma}[\boldsymbol{H}_{\nabla ij}(k_x,k_z,\omega)]. \tag{B.4}$$

Applying the supreme operation $\sup_{\omega\in\mathbb{R}}[\cdot]$ on (B.4) and using definitions of $\|\cdot\|_\mu$ and $\|\cdot\|_\infty$ we have:

$$\|\mathcal{H}_{\nabla}\|_\mu \geq \|\mathcal{H}_{\nabla ux}\|_\infty, \quad \|\mathcal{H}_{\nabla}\|_\mu \geq \|\mathcal{H}_{\nabla vy}\|_\infty, \quad \|\mathcal{H}_{\nabla}\|_\mu \geq \|\mathcal{H}_{\nabla wz}\|_\infty. \tag{B.5a-c}$$

This directly results in inequality (5.21) of theorem 5.3. □

B.2 Proof of theorem 5.4

Proof: Under the assumptions of streamwise constant $k_x = 0$ for plane Couette flow or plane Poiseuille flow in theorem 5.4, the operator $\widehat{\mathcal{A}}$, $\widehat{\mathcal{B}}$, and $\widehat{\mathcal{C}}$ can be simplified and decomposed as:

$$\widehat{\mathcal{A}}(k_x,k_z) = \begin{bmatrix} \frac{\widehat{\nabla}^{-2}\widehat{\nabla}^4}{Re} & 0 \\ -\mathrm{i}k_z U' & \frac{\widehat{\nabla}^2}{Re} \end{bmatrix}, \tag{B.6a}$$

$$\widehat{\mathcal{B}}(k_x,k_z) = \begin{bmatrix} 0 & -k_z^2\widehat{\nabla}^{-2} & -\mathrm{i}k_z\widehat{\nabla}^{-2}\partial_y \\ \mathrm{i}k_z & 0 & 0 \end{bmatrix} =: \begin{bmatrix} 0 & \widehat{\mathcal{B}}_{y,1} & \widehat{\mathcal{B}}_{z,1} \\ \mathcal{B}_{x,2} & 0 & 0 \end{bmatrix}, \tag{B.6b}$$

$$\widehat{\mathcal{C}}(k_x,k_z) = \begin{bmatrix} 0 & -\mathrm{i}/k_z \\ \mathcal{I} & 0 \\ \mathrm{i}\partial_y/k_z & 0 \end{bmatrix} =: \begin{bmatrix} 0 & \widehat{\mathcal{C}}_{u,2} \\ \widehat{\mathcal{C}}_{v,1} & 0 \\ \widehat{\mathcal{C}}_{w,1} & 0 \end{bmatrix}. \tag{B.6c}$$

Here, we employ a matrix inverse formula for the lower triangle block matrix:

$$\begin{bmatrix} L_{11} & 0 \\ L_{21} & L_{22} \end{bmatrix}^{-1} = \begin{bmatrix} L_{11}^{-1} & 0 \\ -L_{22}^{-1} L_{21} L_{11}^{-1} & L_{22}^{-1} \end{bmatrix} \tag{B.7}$$

to compute $\left(\mathrm{i}\omega\mathcal{I}_{2\times 2} - \widehat{\mathcal{A}}\right)^{-1}$. Then, we employ a change of variable $\Omega = \omega Re$ similar to (Jovanović, 2004; Jovanović & Bamieh, 2005; Jovanović, 2021) to obtain $\mathcal{H}_{\nabla ij}$ with $i = u, v, w$, and $j = x, y, z$ as:

$$\mathcal{H}_{\nabla ux} = \widehat{\boldsymbol{\nabla}}\widehat{\mathcal{C}}_{u,2} Re \left(\mathrm{i}\Omega\mathcal{I} - \widehat{\nabla}^2\right)^{-1} \widehat{\mathcal{B}}_{x,2}, \tag{B.8a}$$

$$\mathcal{H}_{\nabla uy} = \widehat{\boldsymbol{\nabla}}\widehat{\mathcal{C}}_{u,2} Re \left(\mathrm{i}\Omega\mathcal{I} - \widehat{\nabla}^2\right)^{-1} (-\mathrm{i}k_z U') Re \left(\mathrm{i}\Omega\mathcal{I} - \widehat{\nabla}^{-2}\widehat{\nabla}^4\right)^{-1} \widehat{\mathcal{B}}_{y,1}, \tag{B.8b}$$

$$\mathcal{H}_{\nabla uz} = \widehat{\boldsymbol{\nabla}}\widehat{\mathcal{C}}_{u,2} Re \left(\mathrm{i}\Omega\mathcal{I} - \widehat{\nabla}^2\right)^{-1} (-\mathrm{i}k_z U') Re \left(\mathrm{i}\Omega\mathcal{I} - \widehat{\nabla}^{-2}\widehat{\nabla}^4\right)^{-1} \widehat{\mathcal{B}}_{z,1}, \tag{B.8c}$$

$$\mathcal{H}_{\nabla vx} = 0, \tag{B.8d}$$

$$\mathcal{H}_{\nabla vy} = \widehat{\boldsymbol{\nabla}}\widehat{\mathcal{C}}_{v,1} Re \left(\mathrm{i}\Omega\mathcal{I} - \widehat{\nabla}^{-2}\widehat{\nabla}^4\right)^{-1} \widehat{\mathcal{B}}_{y,1}, \tag{B.8e}$$

$$\mathcal{H}_{\nabla vz} = \widehat{\boldsymbol{\nabla}}\widehat{\mathcal{C}}_{v,1} Re \left(\mathrm{i}\Omega\mathcal{I} - \widehat{\nabla}^{-2}\widehat{\nabla}^4\right)^{-1} \widehat{\mathcal{B}}_{z,1}, \tag{B.8f}$$

$$\mathcal{H}_{\nabla wx} = 0, \tag{B.8g}$$

$$\mathcal{H}_{\nabla wy} = \widehat{\boldsymbol{\nabla}}\widehat{\mathcal{C}}_{w,1} Re \left(\mathrm{i}\Omega\mathcal{I} - \widehat{\nabla}^{-2}\widehat{\nabla}^4\right)^{-1} \widehat{\mathcal{B}}_{y,1}, \tag{B.8h}$$

$$\mathcal{H}_{\nabla wz} = \widehat{\boldsymbol{\nabla}}\widehat{\mathcal{C}}_{w,1} Re \left(\mathrm{i}\Omega\mathcal{I} - \widehat{\nabla}^{-2}\widehat{\nabla}^4\right)^{-1} \widehat{\mathcal{B}}_{z,1}. \tag{B.8i}$$

Taking the operation that $\|\cdot\|_\infty = \sup_{\omega\in\mathbb{R}} \bar{\sigma}[\cdot] = \sup_{\Omega\in\mathbb{R}} \bar{\sigma}[\cdot]$, we have the scaling relation in theorem 5.4. □

Appendix C

Proof of theorems 6.2-6.3

C.1 Proof of theorem 6.2

Proof: Under the assumptions of streamwise constant $k_x = 0$ and passive scalar limit $Ri_b = 0$ for stratified plane Couette flow in theorem 6.2, the operator $\widehat{\mathcal{A}}^S$, $\widehat{\mathcal{B}}^S$, and $\widehat{\mathcal{C}}^S$ can be simplified and decomposed as:

$$\widehat{\mathcal{A}}^S(k_x,k_z) = \begin{bmatrix} \frac{\widehat{\nabla}^{-2}\widehat{\nabla}^4}{Re} & 0 & 0 \\ -\mathrm{i}k_z U' & \frac{\widehat{\nabla}^2}{Re} & 0 \\ -\overline{\rho}' & 0 & \frac{\widehat{\nabla}^2}{RePr} \end{bmatrix}, \tag{C.1a}$$

$$\widehat{\mathcal{B}}^S(k_x,k_z) = \begin{bmatrix} 0 & -k_z^2\widehat{\nabla}^{-2} & -\mathrm{i}k_z\widehat{\nabla}^{-2}\partial_y & 0 \\ \mathrm{i}k_z & 0 & 0 & 0 \\ 0 & 0 & 0 & \mathcal{I} \end{bmatrix} =: \begin{bmatrix} 0 & \widehat{\mathcal{B}}^S_{y,1} & \widehat{\mathcal{B}}^S_{z,1} & 0 \\ \mathcal{B}^S_{x,2} & 0 & 0 & 0 \\ 0 & 0 & 0 & \widehat{\mathcal{B}}^S_{\rho,3} \end{bmatrix} \tag{C.1b}$$

$$\widehat{\mathcal{C}}^S(k_x,k_z) = \begin{bmatrix} 0 & -\mathrm{i}/k_z & 0 \\ \mathcal{I} & 0 & 0 \\ \mathrm{i}\partial_y/k_z & 0 & 0 \\ 0 & 0 & \mathcal{I} \end{bmatrix} =: \begin{bmatrix} 0 & \widehat{\mathcal{C}}^S_{u,2} & 0 \\ \widehat{\mathcal{C}}^S_{v,1} & 0 & 0 \\ \widehat{\mathcal{C}}^S_{w,1} & 0 & 0 \\ 0 & 0 & \widehat{\mathcal{C}}^S_{\rho,3} \end{bmatrix} \tag{C.1c}$$

Here, we employ a matrix inverse formula for the lower triangle block matrix:

$$\begin{bmatrix} L_{11} & 0 & 0 \\ L_{21} & L_{22} & 0 \\ L_{31} & 0 & L_{33} \end{bmatrix}^{-1} = \begin{bmatrix} L_{11}^{-1} & 0 & 0 \\ -L_{22}^{-1}L_{21}L_{11}^{-1} & L_{22}^{-1} & 0 \\ -L_{33}^{-1}L_{31}L_{11}^{-1} & 0 & L_{33}^{-1} \end{bmatrix} \tag{C.2}$$

to compute $\left(\mathrm{i}\omega\mathcal{I}_{3\times 3} - \widehat{\mathcal{A}}^S\right)^{-1}$. Then, we employ a change of variable $\Omega_1 = \omega Re$ and $\Omega_2 = \omega RePr$ to obtain componentwise frequency response operator $\mathcal{H}^S_{ij}$ with $i = u, v, w, \rho$, and

$j = x, y, z, \rho$ as:

$$\mathcal{H}^S_{ux} = \widehat{\mathcal{C}}^S_{u,2} Re \left(\mathsf{i}\Omega_1 \mathcal{I} - \widehat{\nabla}^2\right)^{-1} \widehat{\mathcal{B}}^S_{x,2}, \tag{C.3a}$$

$$\mathcal{H}^S_{uy} = \widehat{\mathcal{C}}^S_{u,2} Re \left(\mathsf{i}\Omega_1 \mathcal{I} - \widehat{\nabla}^2\right)^{-1} (-\mathsf{i}k_z U') Re \left(\mathsf{i}\Omega_1 \mathcal{I} - \widehat{\nabla}^{-2}\widehat{\nabla}^4\right)^{-1} \widehat{\mathcal{B}}^S_{y,1}, \tag{C.3b}$$

$$\mathcal{H}^S_{uz} = \widehat{\mathcal{C}}^S_{u,2} Re \left(\mathsf{i}\Omega_1 \mathcal{I} - \widehat{\nabla}^2\right)^{-1} (-\mathsf{i}k_z U') Re \left(\mathsf{i}\Omega_1 \mathcal{I} - \widehat{\nabla}^{-2}\widehat{\nabla}^4\right)^{-1} \widehat{\mathcal{B}}^S_{z,1}, \tag{C.3c}$$

$$\mathcal{H}^S_{u\rho} = 0, \tag{C.3d}$$

$$\mathcal{H}^S_{vx} = 0, \tag{C.3e}$$

$$\mathcal{H}^S_{vy} = \widehat{\mathcal{C}}^S_{v,1} Re \left(\mathsf{i}\Omega_1 \mathcal{I} - \widehat{\nabla}^{-2}\widehat{\nabla}^4\right)^{-1} \widehat{\mathcal{B}}^S_{y,1}, \tag{C.3f}$$

$$\mathcal{H}^S_{vz} = \widehat{\mathcal{C}}^S_{v,1} Re \left(\mathsf{i}\Omega_1 \mathcal{I} - \widehat{\nabla}^{-2}\widehat{\nabla}^4\right)^{-1} \widehat{\mathcal{B}}^S_{z,1}, \tag{C.3g}$$

$$\mathcal{H}^S_{v\rho} = 0, \tag{C.3h}$$

$$\mathcal{H}^S_{wx} = 0, \tag{C.3i}$$

$$\mathcal{H}^S_{wy} = \widehat{\mathcal{C}}^S_{w,1} Re \left(\mathsf{i}\Omega_1 \mathcal{I} - \widehat{\nabla}^{-2}\widehat{\nabla}^4\right)^{-1} \widehat{\mathcal{B}}^S_{y,1}, \tag{C.3j}$$

$$\mathcal{H}^S_{wz} = \widehat{\mathcal{C}}^S_{w,1} Re \left(\mathsf{i}\Omega_1 \mathcal{I} - \widehat{\nabla}^{-2}\widehat{\nabla}^4\right)^{-1} \widehat{\mathcal{B}}^S_{z,1}, \tag{C.3k}$$

$$\mathcal{H}^S_{w\rho} = 0, \tag{C.3l}$$

$$\mathcal{H}^S_{\rho x} = 0, \tag{C.3m}$$

$$\mathcal{H}^S_{\rho y} = \widehat{\mathcal{C}}^S_{\rho,3} RePr \left(\mathsf{i}\Omega_2 \mathcal{I} - \widehat{\nabla}^2\right)^{-1} (-\bar{\rho}') Re \left(\mathsf{i}\Omega_1 \mathcal{I} - \widehat{\nabla}^{-2}\widehat{\nabla}^4\right)^{-1} \widehat{\mathcal{B}}^S_{y,1}, \tag{C.3n}$$

$$\mathcal{H}^S_{\rho z} = \widehat{\mathcal{C}}^S_{\rho,3} RePr \left(\mathsf{i}\Omega_2 \mathcal{I} - \widehat{\nabla}^2\right)^{-1} (-\bar{\rho}') Re \left(\mathsf{i}\Omega_1 \mathcal{I} - \widehat{\nabla}^{-2}\widehat{\nabla}^4\right)^{-1} \widehat{\mathcal{B}}^S_{z,1}, \tag{C.3o}$$

$$\mathcal{H}^S_{\rho\rho} = \widehat{\mathcal{C}}^S_{\rho,3} RePr \left(\mathsf{i}\Omega_2 \mathcal{I} - \widehat{\nabla}^2\right)^{-1} \widehat{\mathcal{B}}^S_{\rho,3}. \tag{C.3p}$$

Taking the operation that $\|\cdot\|_\infty = \sup_{\omega\in\mathbb{R}}\bar{\sigma}[\cdot] = \sup_{\Omega_1\in\mathbb{R}}\bar{\sigma}[\cdot] = \sup_{\Omega_2\in\mathbb{R}}\bar{\sigma}[\cdot]$, we have a scaling relation in theorem 6.2(a).

Using the relation that $\mathcal{H}^S_{\nabla ij} = \widehat{\boldsymbol{\nabla}}\mathcal{H}^S_{ij}$ in equation (6.24) with $i = u, v, w, \rho$, and $j = x, y, z, \rho$, and similarly employ the notion of $\|\cdot\|_\infty$, we have the scaling relation in theorem 6.2(b). □

C.2 Proof of theorem 6.3

Proof: We define the set of uncertainties:

$$\widehat{\boldsymbol{U}}^S_{\Xi,ux} := \left\{\text{diag}\left(-\widehat{\boldsymbol{u}}^{\mathsf{T}}_\xi, \boldsymbol{0}, \boldsymbol{0}, \boldsymbol{0}\right) : -\widehat{\boldsymbol{u}}^{\mathsf{T}}_\xi \in \mathbb{C}^{N_y\times 3N_y}\right\}, \tag{C.4a}$$

$$\widehat{\boldsymbol{U}}^S_{\Xi,vy} := \left\{\text{diag}\left(\boldsymbol{0}, -\widehat{\boldsymbol{u}}^{\mathsf{T}}_\xi, \boldsymbol{0}, \boldsymbol{0}\right) : -\widehat{\boldsymbol{u}}^{\mathsf{T}}_\xi \in \mathbb{C}^{N_y\times 3N_y}\right\}, \tag{C.4b}$$

$$\widehat{\boldsymbol{U}}^S_{\Xi,wz} := \left\{\text{diag}\left(\boldsymbol{0}, \boldsymbol{0}, -\widehat{\boldsymbol{u}}^{\mathsf{T}}_\xi, \boldsymbol{0}\right) : -\widehat{\boldsymbol{u}}^{\mathsf{T}}_\xi \in \mathbb{C}^{N_y\times 3N_y}\right\}, \tag{C.4c}$$

$$\widehat{\boldsymbol{U}}^S_{\Xi,\rho\rho} := \left\{\text{diag}\left(\boldsymbol{0}, \boldsymbol{0}, \boldsymbol{0}, -\widehat{\boldsymbol{u}}^{\mathsf{T}}_\xi\right) : -\widehat{\boldsymbol{u}}^{\mathsf{T}}_\xi \in \mathbb{C}^{N_y\times 3N_y}\right\}, \tag{C.4d}$$

Here, $\boldsymbol{0} \in \mathbb{C}^{N_y\times 3N_y}$ is a zero matrix with the size $N_y \times 3N_y$. Then, using the definition of structured singular value in definition 6.1, we have:

$$\begin{aligned}
&\mu_{\widehat{\boldsymbol{U}}^S_{\Xi,ux}}\left[\boldsymbol{H}^S_\nabla(k_x,k_z,\omega)\right]\\
=&\frac{1}{\min\{\bar{\sigma}[\widehat{\boldsymbol{u}}^S_{\Xi,ux}] \,:\, \widehat{\boldsymbol{u}}^S_{\Xi,ux}\in\widehat{\boldsymbol{U}}^S_{\Xi,ux},\, \det[\boldsymbol{I}-\boldsymbol{H}^S_\nabla(k_x,k_z,\omega)\widehat{\boldsymbol{u}}^S_{\Xi,ux}]=0\}} &\text{(C.5a)}\\
=&\frac{1}{\min\{\bar{\sigma}[-\widehat{\boldsymbol{u}}^{\mathsf{T}}_\xi] \,:\, -\widehat{\boldsymbol{u}}^{\mathsf{T}}_\xi\in\mathbb{C}^{N_y\times 3N_y},\, \det[\boldsymbol{I}_{3N_y}-\boldsymbol{H}^S_{\nabla ux}(k_x,k_z,\omega)(-\widehat{\boldsymbol{u}}^{\mathsf{T}}_\xi)]=0\}} &\text{(C.5b)}\\
=&\bar{\sigma}[\boldsymbol{H}^S_{\nabla ux}(k_x,k_z,\omega)] &\text{(C.5c)}
\end{aligned}$$

Here, the equality (C.5a) is obtained by substituting the uncertainty set in (C.4a) into definition 6.1. The equality (C.5b) is obtained by performing block diagonal partition of terms inside of $\det[\cdot]$ and employing zeros in the uncertainty set in equation (C.4a). Here, $\boldsymbol{H}^S_{\nabla ux}$ is the

discretization of $\mathcal{H}^S_{\nabla ux}$ and $\boldsymbol{I}_{3N_y} \in \mathbb{C}^{3N_y \times 3N_y}$ in (C.5b) is an identity matrix with matching size $(3N_y \times 3N_y)$ to distinguish $\boldsymbol{I} \in \mathbb{C}^{12N_y \times 12N_y}$ in (C.5a). The equality (C.5c) is using the definition of unstructured singular value; see e.g., (Zhou *et al.*, 1996, equation (11.1)).

Similarly, we have:

$$\mu_{\widehat{\boldsymbol{U}}^S_{\Xi,vy}} \left[\boldsymbol{H}^S_\nabla(k_x,k_z,\omega)\right] = \bar{\sigma}[\boldsymbol{H}^S_{\nabla vy}(k_x,k_z,\omega)], \tag{C.6a}$$

$$\mu_{\widehat{\boldsymbol{U}}^S_{\Xi,wz}} \left[\boldsymbol{H}^S_\nabla(k_x,k_z,\omega)\right] = \bar{\sigma}[\boldsymbol{H}^S_{\nabla wz}(k_x,k_z,\omega)], \tag{C.6b}$$

$$\mu_{\widehat{\boldsymbol{U}}^S_{\Xi,\rho\rho}} \left[\boldsymbol{H}^S_\nabla(k_x,k_z,\omega)\right] = \bar{\sigma}[\boldsymbol{H}^S_{\nabla\rho\rho}(k_x,k_z,\omega)]. \tag{C.6c}$$

Using the fact that $\widehat{\boldsymbol{U}}^S_\Xi \supseteq \widehat{\boldsymbol{U}}^S_{\Xi,ij}$ with $ij = ux, vy, wz, \rho\rho$ and equalities in (C.5)-(C.6), we have:

$$\mu_{\widehat{\boldsymbol{U}}^S_\Xi} \left[\boldsymbol{H}^S_\nabla(k_x,k_z,\omega)\right] \geq \mu_{\widehat{\boldsymbol{U}}^S_{\Xi,ij}} \left[\boldsymbol{H}^S_\nabla(k_x,k_z,\omega)\right] = \bar{\sigma}[\boldsymbol{H}^S_{\nabla ij}(k_x,k_z,\omega)]. \tag{C.7}$$

Applying the supreme operation $\sup_{\omega\in\mathbb{R}}[\cdot]$ on (C.7) and using definitions of $\|\cdot\|_\mu$ and $\|\cdot\|_\infty$ we have:

$$\|\mathcal{H}^S_\nabla\|_\mu \geq \|\mathcal{H}^S_{\nabla ux}\|_\infty, \quad \|\mathcal{H}^S_\nabla\|_\mu \geq \|\mathcal{H}^S_{\nabla vy}\|_\infty, \tag{C.8a,b}$$

$$\|\mathcal{H}^S_\nabla\|_\mu \geq \|\mathcal{H}^S_{\nabla wz}\|_\infty, \quad \|\mathcal{H}^S_\nabla\|_\mu \geq \|\mathcal{H}^S_{\nabla\rho\rho}\|_\infty. \tag{C.8c,d}$$

This directly results in inequality (6.27) of theorem 6.3. □

Appendix D

Dynamics for the 9D shear flow model in Section 8.3.2

The nine-dimensional shear flow model (Moehlis *et al.*, 2004) considers the incompressible flow between two parallel flat plates under a sinusoidal body force. Figure D.1 illustrates this configuration, where x, y, and z represent the streamwise, wall-normal, and spanwise directions, respectively. The length is non-dimensionalized by h, where h is the channel half height. The characteristic velocity U_0 is taken to be the laminar velocity resulting from the sinusoidal body force at a distance $h/2$ from the top wall. The time and pressure are, respectively, in units of h/U_0 and $U_0^2\rho$, where ρ is the fluid density. The governing equations of the fluid between these two parallel flat plates are described by the incompressible NS equations:

$$\frac{\partial \boldsymbol{u}}{\partial t} = -(\boldsymbol{u}\cdot\nabla)\boldsymbol{u} - \nabla p + \frac{1}{Re}\nabla^2\boldsymbol{u} + \boldsymbol{F}_S(y), \tag{D.1a}$$

$$\nabla\cdot\boldsymbol{u} = 0 \tag{D.1b}$$

with the Reynolds number defined as $Re = \frac{U_0 h}{\nu}$, where ν is the kinematic viscosity.

The boundary conditions are set up as free-slip boundaries at the walls $y = \pm 1$; i.e.,

$$u_y|_{y=\pm 1} = 0, \tag{D.2a}$$

$$\left.\frac{\partial u_x}{\partial y}\right|_{y=\pm 1} = \left.\frac{\partial u_z}{\partial y}\right|_{y=\pm 1} = 0, \tag{D.2b}$$

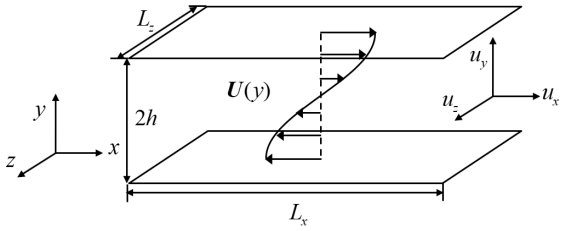

Figure D.1: The illustration of sinusoidal shear flow as Refs. (Moehlis *et al.*, 2004, 2005).

where u_x, u_y, and u_z represent the streamwise, wall-normal, and spanwise velocity, respectively. These free-slip boundary conditions make it easy to construct the Galerkin basis based on physical observations, and the underlying self-sustaining process is demonstrated to be robust no matter whether the boundary is free-slip or no-slip (Waleffe, 1997). Following Waleffe (Waleffe, 1997), the non-dimensionalized sinusoidal body force $\boldsymbol{F}_S(y) = \frac{\sqrt{2}\pi^2}{4Re}\sin(\pi y/2)\boldsymbol{e}_x$ results in the laminar profile $\boldsymbol{U}(y) = \sqrt{2}\sin(\pi y/2)\boldsymbol{e}_x$ with $\boldsymbol{e}_x$ denoting the unit vector in the streamwise direction. This shear flow with free-slip boundary conditions and sinusoidal body force is also fully resolved to study the large-scale feature of transitional turbulence (Chantry *et al.*, 2016, 2017; Tuckerman *et al.*, 2020). In the following, we denote the flow domain $0 \leq x \leq L_x$, $-1 \leq y \leq 1$, and $0 \leq z \leq L_z$ as Ω.

Then, we project the NS equations in (D.1a) to Galerkin modes $\boldsymbol{u}_i, i = 1, 2, ..., 9$ that are orthogonal and normalized as:

$$\int_\Omega \boldsymbol{u}_n \cdot \boldsymbol{u}_m d\Omega = 2L_x L_z \delta_{mn}, \tag{D.3}$$

where δ_{mn} is the Kronecker delta function. These modes satisfy the divergence-free constraint and boundary conditions at the wall. The detail of these modes are reported in the following equation (D.4), which can be also seen in equations (7)-(17) in Ref. (Moehlis *et al.*, 2004) and Appendix C in Ref. (Goulart & Chernyshenko, 2012):

$$\boldsymbol{u}_1 := \begin{bmatrix} \sqrt{2}\sin(\pi y/2) \\ 0 \\ 0 \end{bmatrix}, \tag{D.4a}$$

$$\boldsymbol{u}_2 := \begin{bmatrix} \cos^2(\pi y/2)\cos(\gamma z) \\ 0 \\ 0 \end{bmatrix} \cdot \frac{4}{\sqrt{3}}, \tag{D.4b}$$

$$\boldsymbol{u}_3 := \begin{bmatrix} 0 \\ 2\gamma\cos(\pi y/2)\cos(\gamma z) \\ \pi\sin(\pi y/2)\sin(\gamma z) \end{bmatrix} \cdot \frac{2}{\sqrt{4\gamma^2+\pi^2}}, \tag{D.4c}$$

$$\boldsymbol{u}_4 := \begin{bmatrix} 0 \\ 0 \\ \cos(\alpha x)\cos^2(\pi y/2) \end{bmatrix} \cdot \frac{4}{\sqrt{3}}, \tag{D.4d}$$

$$\boldsymbol{u}_5 := \begin{bmatrix} 0 \\ 0 \\ 2\sin(\alpha x)\sin(\pi y/2) \end{bmatrix}, \tag{D.4e}$$

$$\boldsymbol{u}_6 := \begin{bmatrix} -\gamma\cos(\alpha x)\cos^2(\frac{\pi y}{2})\sin(\gamma z) \\ 0 \\ \alpha\sin(\alpha x)\cos^2(\frac{\pi y}{2})\cos(\gamma z) \end{bmatrix} \cdot \frac{4\sqrt{2}}{\sqrt{3}\,\kappa_{\alpha\gamma}}, \tag{D.4f}$$

$$\boldsymbol{u}_7 := \begin{bmatrix} \gamma\sin(\alpha x)\sin(\pi y/2)\sin(\gamma z) \\ 0 \\ \alpha\cos(\alpha x)\sin(\pi y/2)\cos(\gamma z) \end{bmatrix} \cdot \frac{2\sqrt{2}}{\kappa_{\alpha\gamma}}, \tag{D.4g}$$

$$\boldsymbol{u}_8 := \begin{bmatrix} \pi\alpha\sin(\alpha x)\sin(\frac{\pi y}{2})\sin(\gamma z) \\ 2(\alpha^2+\gamma^2)\cos(\alpha x)\cos(\frac{\pi y}{2})\sin(\gamma z) \\ -\pi\gamma\cos(\alpha x)\sin(\frac{\pi y}{2})\cos(\gamma z) \end{bmatrix} \cdot N_8, \tag{D.4h}$$

$$\boldsymbol{u}_9 := \begin{bmatrix} \sqrt{2}\sin(3\pi y/2) \\ 0 \\ 0 \end{bmatrix}, \tag{D.4i}$$

where $\alpha := 2\pi/L_x$, $\beta := \pi/2$, $\gamma := 2\pi/L_z$, $\kappa_{\alpha\gamma} := \sqrt{\alpha^2+\gamma^2}$, and

$$N_8 := \frac{2\sqrt{2}}{\sqrt{(\alpha^2+\gamma^2)(4\alpha^2+4\gamma^2+\pi^2)}}. \tag{D.5}$$

Through expanding the velocity under these Galerkin modes $\boldsymbol{u} = \sum_{i=1}^{9} \tilde{a}_i \boldsymbol{u}_i$, substituting this expansion into the momentum equation (D.1a) and enforcing the residue to be orthogonal to each Galerkin mode, we obtain the Galerkin projection of the original governing equations as

a nine-dimensional dynamical system:

$$\frac{d\tilde{a}_i}{dt} = -\frac{\xi_{ij}}{Re}\tilde{a}_j + N_{ijk}\tilde{a}_j\tilde{a}_k + F_i, \tag{D.6}$$

where each coefficient is obtained through:

$$\xi_{ij} := \frac{\int_\Omega (-\nabla^2 \boldsymbol{u}_j)\cdot \boldsymbol{u}_i d\Omega}{\int_\Omega \boldsymbol{u}_i \cdot \boldsymbol{u}_i d\Omega}, \tag{D.7a}$$

$$N_{ijk} := \frac{-\int_\Omega [\boldsymbol{u}_j \cdot \nabla \boldsymbol{u}_k]\cdot \boldsymbol{u}_i d\Omega}{\int_\Omega \boldsymbol{u}_i \cdot \boldsymbol{u}_i d\Omega}, \text{ and} \tag{D.7b}$$

$$F_i := \frac{\int_\Omega \boldsymbol{F}_S \cdot \boldsymbol{u}_i d\Omega}{\int_\Omega \boldsymbol{u}_i \cdot \boldsymbol{u}_i d\Omega}. \tag{D.7c}$$

The pressure term in equation (D.1a) has no contribution to the Galerkin projection results as these modes are divergence-free, vanish at the wall, and satisfy periodic boundary conditions in wall parallel directions. Here, we rewrite equation (D.6) as:

$$\frac{d\tilde{\boldsymbol{a}}}{dt} = -\frac{\boldsymbol{\Xi}}{Re}\tilde{\boldsymbol{a}} + \boldsymbol{J}(\tilde{\boldsymbol{a}})\tilde{\boldsymbol{a}} + \boldsymbol{F}, \tag{D.8}$$

where we define entries of a positive definite matrix as $[\boldsymbol{\Xi}]_{i,j} := \xi_{ij}$, entries of the state-dependent matrix as $[\boldsymbol{J}(\tilde{\boldsymbol{a}})]_{i,j} := N_{ijk}\tilde{a}_k$, and entries of the forcing vectors as $[\boldsymbol{F}]_i := F_i$.

For completeness of this paper, we also document the details of $\boldsymbol{\Xi}$ and $\boldsymbol{J}(\tilde{\boldsymbol{a}})$ of this Galerkin model in the following equations (D.9) and (D.10), which were also reported in (21)-(32) of Ref. (Moehlis *et al.*, 2004) and Appendix C in Ref. (Goulart & Chernyshenko, 2012):

$$\begin{aligned}\boldsymbol{\Xi} =& \text{diag}(\beta^2, \frac{4\beta^2}{3}+\gamma^2, \kappa^2_{\beta\gamma}, \frac{3\alpha^2+4\beta^2}{3}, \kappa^2_{\alpha\beta},\\ & \frac{3\alpha^2+4\beta^2+3\gamma^2}{3}, \kappa^2_{\alpha\beta\gamma}, \kappa^2_{\alpha\beta\gamma}, 9\beta^2),\end{aligned} \tag{D.9}$$

and

$$[\boldsymbol{J}(\tilde{\boldsymbol{a}})\tilde{\boldsymbol{a}}]_1 = \sqrt{\frac{3}{2}}\frac{\beta\gamma}{\kappa_{\beta\gamma}}\tilde{a}_2\tilde{a}_3 - \sqrt{\frac{3}{2}}\frac{\beta\gamma}{\kappa_{\alpha\beta\gamma}}\tilde{a}_6\tilde{a}_8, \tag{D.10a}$$

$$[\boldsymbol{J}(\tilde{\boldsymbol{a}})\tilde{\boldsymbol{a}}]_2 = \frac{10}{3\sqrt{6}}\frac{\gamma^2}{\kappa_{\alpha\gamma}}\tilde{a}_4\tilde{a}_6 - \frac{\gamma^2}{\sqrt{6}\kappa_{\alpha\gamma}}\tilde{a}_5\tilde{a}_7$$

$$
\begin{aligned}
&- \frac{\alpha\beta\gamma}{\sqrt{6}\kappa_{\alpha\gamma}\kappa_{\alpha\beta\gamma}}\tilde{a}_5\tilde{a}_8 \\
&- \sqrt{\frac{3}{2}}\frac{\beta\gamma}{\kappa_{\beta\gamma}}(\tilde{a}_1\tilde{a}_3 + \tilde{a}_3\tilde{a}_9), \qquad \text{(D.10b)}
\end{aligned}
$$

$$
\begin{aligned}
[\boldsymbol{J}(\tilde{\boldsymbol{a}})\tilde{\boldsymbol{a}}]_3 =& \sqrt{\frac{2}{3}}\frac{\alpha\beta\gamma}{\kappa_{\alpha\gamma}\kappa_{\beta\gamma}}(\tilde{a}_5\tilde{a}_6 + \tilde{a}_4\tilde{a}_7) \\
&+ \frac{\beta^2(3\alpha^2+\gamma^2) - 3\gamma^2\kappa_{\alpha\gamma}^2}{\sqrt{6}\kappa_{\alpha\gamma}\kappa_{\beta\gamma}\kappa_{\alpha\beta\gamma}}\tilde{a}_4\tilde{a}_8, \qquad \text{(D.10c)}
\end{aligned}
$$

$$
\begin{aligned}
[\boldsymbol{J}(\tilde{\boldsymbol{a}})\tilde{\boldsymbol{a}}]_4 =& -\frac{\alpha}{\sqrt{6}}(\tilde{a}_1\tilde{a}_5 + \tilde{a}_5\tilde{a}_9) - \frac{10}{3\sqrt{6}}\frac{\alpha^2}{\kappa_{\alpha\gamma}}\tilde{a}_2\tilde{a}_6 \\
&- \sqrt{\frac{3}{2}}\frac{\alpha\beta\gamma}{\kappa_{\alpha\gamma}\kappa_{\beta\gamma}}\tilde{a}_3\tilde{a}_7 \\
&- \sqrt{\frac{3}{2}}\frac{\alpha^2\beta^2}{\kappa_{\alpha\gamma}\kappa_{\beta\gamma}\kappa_{\alpha\beta\gamma}}\tilde{a}_3\tilde{a}_8, \qquad \text{(D.10d)}
\end{aligned}
$$

$$
\begin{aligned}
[\boldsymbol{J}(\tilde{\boldsymbol{a}})\tilde{\boldsymbol{a}}]_5 =& \frac{\alpha}{\sqrt{6}}(\tilde{a}_1\tilde{a}_4 + \tilde{a}_4\tilde{a}_9) + \sqrt{\frac{2}{3}}\frac{\alpha\beta\gamma}{\kappa_{\alpha\gamma}\kappa_{\beta\gamma}}\tilde{a}_3\tilde{a}_6 \\
&+ \frac{\alpha^2}{\sqrt{6}\kappa_{\alpha\gamma}}\tilde{a}_2\tilde{a}_7 - \frac{\alpha\beta\gamma}{\sqrt{6}\kappa_{\alpha\gamma}\kappa_{\alpha\beta\gamma}}\tilde{a}_2\tilde{a}_8, \qquad \text{(D.10e)}
\end{aligned}
$$

$$
\begin{aligned}
[\boldsymbol{J}(\tilde{\boldsymbol{a}})\tilde{\boldsymbol{a}}]_6 =& \frac{10}{3\sqrt{6}}\frac{\alpha^2-\gamma^2}{\kappa_{\alpha\gamma}}\tilde{a}_2\tilde{a}_4 - \sqrt{\frac{2}{3}}\frac{2\alpha\beta\gamma}{\kappa_{\alpha\gamma}\kappa_{\beta\gamma}}\tilde{a}_3\tilde{a}_5 \\
&+ \frac{\alpha}{\sqrt{6}}(\tilde{a}_1\tilde{a}_7 + \tilde{a}_7\tilde{a}_9) \\
&+ \sqrt{\frac{3}{2}}\frac{\beta\gamma}{\kappa_{\alpha\beta\gamma}}(\tilde{a}_1\tilde{a}_8 + \tilde{a}_8\tilde{a}_9), \qquad \text{(D.10f)}
\end{aligned}
$$

$$
\begin{aligned}
[\boldsymbol{J}(\tilde{\boldsymbol{a}})\tilde{\boldsymbol{a}}]_7 =& \frac{\alpha\beta\gamma}{\sqrt{6}\kappa_{\alpha\gamma}\kappa_{\beta\gamma}}\tilde{a}_3\tilde{a}_4 + \frac{-\alpha^2+\gamma^2}{\sqrt{6}\kappa_{\alpha\gamma}}\tilde{a}_2\tilde{a}_5 \\
&- \frac{\alpha}{\sqrt{6}}(\tilde{a}_1\tilde{a}_6 + \tilde{a}_6\tilde{a}_9), \qquad \text{(D.10g)}
\end{aligned}
$$

$$
[\boldsymbol{J}(\tilde{\boldsymbol{a}})\tilde{\boldsymbol{a}}]_8 = \frac{\gamma^2(3\alpha^2-\beta^2+3\gamma^2)}{\sqrt{6}\kappa_{\alpha\gamma}\kappa_{\beta\gamma}\kappa_{\alpha\beta\gamma}}\tilde{a}_3\tilde{a}_4
$$

$$+\sqrt{\frac{2}{3}}\frac{\alpha\beta\gamma}{\kappa_{\alpha\gamma}\kappa_{\alpha\beta\gamma}}\tilde{a}_2\tilde{a}_5, \tag{D.10h}$$

$$[\boldsymbol{J}(\tilde{\boldsymbol{a}})\tilde{\boldsymbol{a}}]_9 = \sqrt{\frac{3}{2}}\frac{\beta\gamma}{\kappa_{\beta\gamma}}\tilde{a}_2\tilde{a}_3 - \sqrt{\frac{3}{2}}\frac{\beta\gamma}{\kappa_{\alpha\beta\gamma}}\tilde{a}_6\tilde{a}_8, \tag{D.10i}$$

where $[\boldsymbol{J}(\tilde{\boldsymbol{a}})\tilde{\boldsymbol{a}}]_m := \boldsymbol{e}_m^T\boldsymbol{J}(\tilde{\boldsymbol{a}})\tilde{\boldsymbol{a}},\ m = 1, 2, ..., 9$ is the m^{th} component of $\boldsymbol{J}(\tilde{\boldsymbol{a}})\tilde{\boldsymbol{a}}$, and $\kappa_{\alpha\beta} := \sqrt{\alpha^2+\beta^2}$, $\kappa_{\beta\gamma} := \sqrt{\beta^2+\gamma^2}$ and $\kappa_{\alpha\beta\gamma} := \sqrt{\alpha^2+\beta^2+\gamma^2}$.

The laminar profile $\boldsymbol{U}(y)$ in this model corresponds to a fixed point $\bar{\boldsymbol{a}} = \begin{bmatrix}1 & 0 & 0 & 0 & 0 & 0 & 0 & 0 & 0\end{bmatrix}^T$, and it satisfies:

$$-\frac{\boldsymbol{\Xi}}{Re}\bar{\boldsymbol{a}} + \boldsymbol{J}(\bar{\boldsymbol{a}})\bar{\boldsymbol{a}} + \boldsymbol{F} = \boldsymbol{0}. \tag{D.11}$$

We can perform a decomposition of Galerkin coefficients similar to Reynolds decomposition:

$$\tilde{\boldsymbol{a}} = \bar{\boldsymbol{a}} + \boldsymbol{a}, \tag{D.12}$$

so as to shift the laminar state to the origin of fluctuating coefficients $\boldsymbol{a}$. The resulting dynamical system for these fluctuating coefficients is

$$\frac{d\boldsymbol{a}}{dt} = -\frac{\boldsymbol{\Xi}}{Re}\boldsymbol{a} + \boldsymbol{J}(\boldsymbol{a})\bar{\boldsymbol{a}} + \boldsymbol{J}(\bar{\boldsymbol{a}})\boldsymbol{a} + \boldsymbol{J}(\boldsymbol{a})\boldsymbol{a}, \tag{D.13}$$

which gives equation (8.20) in section 8.3.2.

Bibliography

Abbassi, M., Baars, W., Hutchins, N. & Marusic, I. 2017 Skin-friction drag reduction in a high-Reynolds-number turbulent boundary layer via real-time control of large-scale structures. *Int. J. Heat Fluid Flow* **67**, 30–41.

Adrian, R. J. 2007 Hairpin vortex organization in wall turbulence. *Phys. Fluids* **19** (4), 041301.

Adrian, R. J., Meinhart, C. D. & Tomkins, C. D. 2000 Vortex organization in the outer region of the turbulent boundary layer. *J. Fluid Mech.* **422**, 1–54.

Ahmadi, M., Valmorbida, G., Gayme, D. & Papachristodoulou, A. 2019 A framework for input–output analysis of wall-bounded shear flows. *J. Fluid Mech.* **873**, 742–785.

Ahmed, M. A., Bae, H. J., Thompson, A. F. & McKeon, B. 2021 Resolvent analysis of stratification effects on wall-bounded shear flows. *arXiv preprint arXiv:2101.11771* .

Alves, L. D. B., Hirata, S. C., Schuabb, M. & Barletta, A. 2019 Identifying linear absolute instabilities from differential eigenvalue problems using sensitivity analysis. *J. Fluid Mech.* **870**, 941–969.

Anderson, J. & Papachristodoulou, A. 2015 Advances in computational Lyapunov analysis using sum-of-squares programming. *Discrete Cont. Dyn.-B* **20** (8), 2361–2381.

Andreas, E. L. 2002 Parameterizing scalar transfer over snow and ice: A review. *J. Hydrometeorol.* **3** (4), 417–432.

Artham, S., Zhang, Z. & Gnanamanickam, E. P. 2021 Inner–outer interactions in a forced plane wall jet. *Exp. Fluids* **62** (2), 1–20.

Ashpis, D. E. & Reshotko, E. 1990 The vibrating ribbon problem revisited. *J. Fluid Mech.* **213**, 531–547.

Baars, W. J., Hutchins, N. & Marusic, I. 2016 Spectral stochastic estimation of high-Reynolds-number wall-bounded turbulence for a refined inner-outer interaction model. *Phys. Rev. Fluids* **1** (5), 054406.

Baars, W. J., Hutchins, N. & Marusic, I. 2017 Self-similarity of wall-attached turbulence in boundary layers. *J. Fluid Mech.* **823**, R2.

Baggett, J. S., Driscoll, T. A. & Trefethen, L. N. 1995 A mostly linear model of transition to turbulence. *Phys. Fluids* **7** (4), 833–838.

Baggett, J. S. & Trefethen, L. N. 1997 Low-dimensional models of subcritical transition to turbulence. *Phys. Fluids* **9** (4), 1043–1053.

Balakumar, B. & Adrian, R. 2007 Large- and very-large-scale motions in channel and boundary-layer flows. *Philos. Trans. R. Soc. London A Math. Phys. Eng. Sci.* **365** (1852), 665–681.

Balas, G., Chiang, R., Packard, A. & Safonov, M. 2005 Robust control toolbox. *For Use with Matlab. Users Guide, Version* **3**.

Bamieh, B. & Dahleh, M. 2001 Energy amplification in channel flows with stochastic excitation. *Phys. Fluids* **13** (11), 3258–3269.

Barkley, D. 2016 Theoretical perspective on the route to turbulence in a pipe. *J. Fluid Mech.* **803**, P1.

Barkley, D. & Tuckerman, L. S. 2007 Mean flow of turbulent-laminar patterns in plane Couette flow. *J. Fluid Mech.* **576**, 109–137.

Bech, K. H. & Andersson, H. I. 1996 Secondary flow in weakly rotating turbulent plane Couette flow. *J. Fluid Mech.* **317**, 195–214.

Bech, K. H. & Andersson, H. I. 1997 Turbulent plane Couette flow subject to strong system rotation. *J. Fluid Mech.* **347**, 289–314.

Bergstresser, R. Unknown *Comments from the inventor of purple harmony plates*. https://www.bibliotecapleyades.net/ciencia/esp_ciencia_universalenergy02.htm.

Bertolotti, F. P., Herbert, T. & Spalart, P. R. 1992 Linear and nonlinear stability of the Blasius boundary layer. *J. Fluid Mech.* **242**, 441–474.

Bhatt, S. & Gnanamanickam, E. 2020 Linear and nonlinear mechanisms within a forced plane wall jet. *Phys. Rev. Fluids* **5** (7), 074604.

Bodenschatz, E., Pesch, W. & Ahlers, G. 2000 Recent developments in Rayleigh-Bénard convection. *Annu. Rev. Fluid Mech.* **32** (1), 709–778.

Bottin, S., Dauchot, O., Daviaud, F. & Manneville, P. 1998 Experimental evidence of streamwise vortices as finite amplitude solutions in transitional plane Couette flow. *Phys. Fluids* **10** (10), 2597–2607.

Boyd, S., El Ghaoui, L., Feron, E. & Balakrishnan, V. 1994 *Linear matrix inequalities in system and control theory*. SIAM.

Boyd, S. & Vandenberghe, L. 2004 *Convex optimization*. Cambridge university press.

Bradshaw, P. 1967 'Inactive' motion and pressure fluctuations in turbulent boundary layers. *J. Fluid Mech.* **30** (2), 241–258.

Brandt, L. 2014 The lift-up effect: The linear mechanism behind transition and turbulence in shear flows. *Eur. J. Mech. B-Fluid* **47**, 80–96.

Brauckmann, H. J., Salewski, M. & Eckhardt, B. 2016 Momentum transport in Taylor–Couette flow with vanishing curvature. *J. Fluid Mech.* **790**, 419–452.

Bretthouwer, G., Duguet, Y. & Schlatter, P. 2012 Turbulent-laminar coexistence in wall flows with Coriolis, buoyancy or Lorentz forces. *J. Fluid Mech.* **704**, 137–172.

Briggs, R. J. 1964 *Electron-stream interaction with plasmas*. MIT.

Brown, G. L. & Thomas, A. S. W. 1977 Large structure in a turbulent boundary layer. *Phys. Fluids* **20** (10), S243–S252.

Brunton, S. L., Proctor, J. L. & Kutz, J. N. 2016 Discovering governing equations from data by sparse identification of nonlinear dynamical systems. *Proc. Natl. Acad. Sci.* **113** (15), 3932–3937.

Bullock, K. J., Cooper, R. E. & Abernathy, F. H. 1978 Structural similarity in radial correlations and spectra of longitudinal velocity fluctuations in pipe flow. *J. Fluid Mech.* **88** (3), 585–608.

Butler, K. M. & Farrell, B. F. 1992 Three-dimensional optimal perturbations in viscous shear flow. *Phys. Fluids A* **4** (8), 1637–1650.

Butler, K. M. & Farrell, B. F. 1993 Optimal perturbations and streak spacing in wall-bounded turbulent shear flow. *Phys. Fluids A* **5** (3), 774–777.

Carper, M. & Porté-Agel, F. 2004 The role of coherent structures in subfilter-scale dissipation of turbulence measured in the atmospheric surface layer. *J. Turbul.* **5**, 1–24.

Caulfield, C. P. 2020 Open questions in turbulent stratified mixing: Do we even know what we do not know? *Phys. Rev. Fluids* **5** (11), 110518.

Caulfield, C. P. 2021 Layering, instabilities, and mixing in turbulent stratified flows. *Annu. Rev. Fluid Mech.* **53** (1), 113–145.

Chandran, D., Baidya, R., Monty, J. P. & Marusic, I. 2016 Measurement of two-dimensional energy spectra in a turbulent boundary layer. In *Proceedings of the 20th Australasian Fluid Mechanics Conference*. Perth, Australia.

Chandran, D., Baidya, R., Monty, J. P. & Marusic, I. 2017 Two-dimensional energy spectra in high-Reynolds-number turbulent boundary layers. *J. Fluid Mech.* **826**, R1.

Chantry, M. & Schneider, T. M. 2014 Studying edge geometry in transiently turbulent shear flows. *J. Fluid Mech.* **747** (2), 506–517.

Chantry, M., Tuckerman, L. S. & Barkley, D. 2016 Turbulent–laminar patterns in shear flows without walls. *J. Fluid Mech.* **791**, R8.

Chantry, M., Tuckerman, L. S. & Barkley, D. 2017 Universal continuous transition to turbulence in a planar shear flow. *J. Fluid Mech.* **824**, R1.

Chapman, S. J. 2002 Subcritical transition in channel flows. *J. Fluid Mech.* **451**, 35–97.

Chavarin, A. & Luhar, M. 2020 Resolvent analysis for turbulent channel flow with riblets. *AIAA J.* **58** (2), 589–599.

Chernyshenko, S. & Baig, M. 2005 The mechanism of streak formation in near-wall turbulence. *J. Fluid Mech.* **544**, 99–131.

Chernyshenko, S. I., Goulart, P., Huang, D. & Papachristodoulou, A. 2014 Polynomial sum of squares in fluid dynamics: a review with a look ahead. *Phil. Trans. R. Soc. A* **372** (2020), 20130350.

Cherubini, S. & De Palma, P. 2013 Nonlinear optimal perturbations in a Couette flow: bursting and transition. *J. Fluid Mech.* **716**, 251–279.

Cherubini, S. & De Palma, P. 2015 Minimal-energy perturbations rapidly approaching the edge state in Couette flow. *J. Fluid Mech.* **764**, 572–598.

Chevalier, M., Hœpffner, J., Bewley, T. R. & Henningson, D. S. 2006 State estimation in wall-bounded flow systems. Part 2. Turbulent flows. *J. Fluid Mech.* **552**, 167–187.

Chung, D. & McKeon, B. J. 2010 Large-eddy simulation of large-scale structures in long channel flow. *J. Fluid Mech.* **661**, 341–364.

Constantin, P. & Doering, C. R. 1995 Variational bounds on energy dissipation in incompressible flows. II. Channel flow. *Phys. Rev. E* **51** (4), 3192–3198.

Corke, T. C. & Thomas, F. O. 2018 Active and passive turbulent boundary-layer drag reduction. *AIAA J.* **56** (10), 3835–3847.

Cossu, C., Pujals, G. & Depardon, S. 2009 Optimal transient growth and very large-scale structures in turbulent boundary layers. *J. Fluid Mech.* **619**, 79–94.

Cushman-Roisin, B. & Beckers, J. M. 2011 *Introduction to geophysical fluid dynamics: physical and numerical aspects*. Academic press.

Daly, C., Schneider, T. M., Schlatter, P. & Peake, N. 2014 Secondary instability and tertiary states in rotating plane Couette flow. *J. Fluid Mech.* **761**, 27–61.

Damaren, C. J. 2016 Laminar-turbulent transition control using passivity analysis of the OrrSommerfeld equation. *J. Guid. Control Dyn.* **39** (7), 1602–1613.

Damaren, C. J. 2018 Transition control of the Blasius boundary layer using passivity. *Aerosp. Syst.* **2** (1), 21–31.

Davey, A. & Reid, W. 1977 On the stability of stratified viscous plane Couette flow. Part 1. Constant buoyancy frequency. *J. Fluid Mech.* **80** (3), 509–525.

Davidson, P. A. 2013 *Turbulence in rotating, stratified and electrically conducting fluids*. Cambridge University Press.

De Souza, D., Bergier, T. & Monchaux, R. 2020 Transient states in plane Couette flow. *J. Fluid Mech.* **903**, A33.

Deguchi, K. 2017 Scaling of small vortices in stably stratified shear flows. *J. Fluid Mech.* **821**, 582–594.

Deguchi, K. & Hall, P. 2015 Asymptotic descriptions of oblique coherent structures in shear flows. *J. Fluid Mech.* **782**, 356–367.

del Álamo, J. C. & Jiménez, J. 2003 Spectra of the very large anisotropic scales in turbulent channels. *Phys. Fluids* **15** (6), L41.

del Álamo, J. C. & Jiménez, J. 2006 Linear energy amplification in turbulent channels. *J. Fluid Mech.* **559**, 205–213.

del Álamo, J. C. & Jiménez, J. 2009 Estimation of turbulent convection velocities and corrections to Taylor's approximation. *J. Fluid Mech.* **640**, 5–26.

del Álamo, J. C., Jiménez, J., Zandonade, P. & Moser, R. D. 2004 Scaling of the energy spectra of turbulent channels. *J. Fluid Mech.* **500**, 135–144.

Dennis, D. J. C. & Nickels, T. B. 2008 On the limitations of Taylor's hypothesis in constructing long structures in a turbulent boundary layer. *J. Fluid Mech.* **614**, 197–206.

D'Errico, J. 2020 Eigenshuffle (https://www.mathworks.com/matlabcentral/fileexchange/22885-eigenshuffle). *MATLAB Central File Exchange*. .

Deusebio, E., Brethouwer, G., Schlatter, P. & Lindborg, E. 2014 A numerical study of the unstratified and stratified Ekman layer. *J. Fluid Mech.* **755**, 672–704.

Deusebio, E., Caulfield, C. & Taylor, J. R. 2015 The intermittency boundary in stratified plane Couette flow. *J. Fluid Mech.* **781**, 298–329.

Dinkelacker, A., Hessel, M., Meier, G. E. A. & Schewe, G. 1977 Investigation of pressure fluctuations beneath a turbulent boundary layer by means of an optical method. *Phys. Fluids* **20** (10), S216–S224.

Donda, J., Van Hooijdonk, I., Moene, A., Jonker, H., van Heijst, G., Clercx, H. & van de Wiel, B. 2015 Collapse of turbulence in stably stratified channel flow: a transient phenomenon. *Q. J. R. Meteorolog. Soc.* **141** (691), 2137–2147.

Doyle, J. 1982 Analysis of feedback systems with structured uncertainties. *IEE Proceedings D-Control Theory and Applications* **129** (6), 242–250.

Drazin, P. G. & Reid, W. H. 2004 *Hydrodynamic stability*. Cambridge university press.

Duguet, Y., Brandt, L. & Larsson, B. R. J. 2010*a* Towards minimal perturbations in transitional plane Couette flow. *Phys. Rev. E* **82** (2), 026316.

Duguet, Y., Monokrousos, A., Brandt, L. & Henningson, D. S. 2013 Minimal transition thresholds in plane Couette flow. *Phys. Fluids* **25** (8), 084103.

Duguet, Y. & Schlatter, P. 2013 Oblique laminar-turbulent interfaces in plane shear flows. *Phys. Rev. Lett.* **110** (3), 034502.

Duguet, Y., Schlatter, P. & Henningson, D. S. 2010*b* Formation of turbulent patterns near the onset of transition in plane Couette flow. *J. Fluid Mech.* **650**, 119–129.

Duvvuri, S. & McKeon, B. 2016 Nonlinear interactions isolated through scale synthesis in experimental wall turbulence. *Phy. Rev. Fluids* **1** (3), 032401.

Duvvuri, S. & McKeon, B. 2017 Phase relations in a forced turbulent boundary layer: implications for modelling of high Reynolds number wall turbulence. *Proc. R. Soc. London A Math. Phys. Eng. Sci.* **375** (2089), 20160080.

Duvvuri, S. & McKeon, B. J. 2015 Triadic scale interactions in a turbulent boundary layer. *J. Fluid Mech.* **767**, R4.

Eaves, T. & Caulfield, C. P. 2017 Multiple instability of layered stratified plane Couette flow. *J. Fluid Mech.* **813**, 250–278.

Eaves, T. S. & Caulfield, C. P. 2015 Disruption of SSP/VWI states by a stable stratification. *J. Fluid Mech.* **784**, 548–564.

Eckhardt, B., Doering, C. R. & Whitehead, J. P. 2020 Exact relations between Rayleigh–Bénard and rotating plane Couette flow in two dimensions. *J. Fluid Mech.* **903**, R4.

Eckhardt, B., Grossmann, S. & Lohse, D. 2007*a* Torque scaling in turbulent Taylor-Couette flow between independently rotating cylinders. *J. Fluid Mech.* **581**, 221–250.

Eckhardt, B., Schneider, T. M., Hof, B. & Westerweel, J. 2007*b* Turbulence transition in pipe flow. *Annu. Rev. Fluid Mech.* **39**, 447–468.

Ellingsen, T. & Palm, E. 1975 Stability of linear flow. *Phys. Fluids* **18** (4), 487–488.

Elofsson, P. A. & Alfredsson, P. H. 1998 An experimental study of oblique transition in plane Poiseuille flow. *J. Fluid Mech.* **358**, 177–202.

Eves, H. W. 1980 *Elementary matrix theory*. Courier Corporation.

Facchini, G., Favier, B., Le Gal, P., Wang, M. & Le Bars, M. 2018 The linear instability of the stratified plane Couette flow. *J. Fluid Mech.* **853**, 205–234.

Faisst, H. & Eckhardt, B. 2000 Transition from the Couette-Taylor system to the plane Couette system. *Phys. Rev. E* **61** (6), 7227.

Fantuzzi, G., Goluskin, D., Huang, D. & Chernyshenko, S. I. 2016 Bounds for deterministic and stochastic dynamical systems using sum-of-squares optimization. *SIAM J. Appl. Dyn. Syst.* **15** (4), 1962–1988.

Farabee, T. M. & Casarella, M. J. 1991 Spectral features of wall pressure fluctuations beneath turbulent boundary layers. *Phys. Fluids A-Fluid* **3** (10), 2410–2420.

Farano, M., Cherubini, S., Robinet, J. C. & De Palma, P. 2015 Hairpin-like optimal perturbations in plane Poiseuille flow. *J. Fluid Mech.* **775**, R2.

Farano, M., Cherubini, S., Robinet, J. C. & De Palma, P. 2016 Subcritical transition scenarios via linear and nonlinear localized optimal perturbations in plane Poiseuille flow. *Fluid Dyn. Res.* **48** (6), 061409.

Farrell, B. F. 1987 Developing disturbances in shear. *J. Atmos. Sci.* **44** (16), 2191–2199.

Farrell, B. F. & Ioannou, P. J. 1993*a* Stochastic forcing of the linearized Navier-Stokes equations. *Phys. Fluids A* **5** (11), 2600–2609.

Farrell, B. F. & Ioannou, P. J. 1993*b* Transient development of perturbations in stratified shear flow. *J. Atmos. Sci.* **50** (14), 2201–2214.

Favre, A., Gaviglio, J. & Dumas, R. 1967 Structure of velocity space-time correlations in a boundary layer. *Phys. Fluids* **10** (9), S138–S145.

Fisher, M. J. & Davies, P. O. A. L. 1964 Correlation measurements in a non-frozen pattern of turbulence. *J. Fluid Mech.* **18** (1), 97–116.

Flores, O. & Riley, J. 2011 Analysis of turbulence collapse in the stably stratified surface layer using direct numerical simulation. *Boundary Layer Meteorol.* **139** (2), 241–259.

Frisch, U. & Kolmogorov, A. N. 1995 *Turbulence the legacy of A.N. Kolmogorov*. Cambridge University Press.

Fuentes, F., Goluskin, D. & Chernyshenko, S. 2019 Global stability of fluid flows despite transient growth of energy. *arXiv preprint arXiv:1911.09079* .

Gai, J., Xia, Z., Cai, Q. & Chen, S. 2016 Turbulent statistics and flow structures in spanwise-rotating turbulent plane Couette flows. *Phys. Rev. Fluids* **1** (5), 054401.

Gallier, J. 2010 The Schur complement and symmetric positive semidefinite (and definite) matrices. *Penn Engineering* .

Galperin, B., Sukoriansky, S. & Anderson, P. S. 2007 On the critical Richardson number in stably stratified turbulence. *Atmos. Sci. Lett.* **8** (3), 65–69.

Ganapathisubramani, B., Hutchins, N., Monty, J. P., Chung, D. & Marusic, I. 2012 Amplitude and frequency modulation in wall turbulence. *J. Fluid Mech.* **712**, 61–91.

Garaud, P. 2021 Journey to the center of stars: The realm of low Prandtl number fluid dynamics. *Phys. Rev. Fluids* **6** (3), 030501.

Garaud, P., Gagnier, D. & Verhoeven, J. 2017 Turbulent transport by diffusive stratified shear flows: from local to global models. I. Numerical simulations of a stratified plane Couette flow. *Astrophys. J.* **837** (2), 133.

Garaud, P., Gallet, B. & Bischoff, T. 2015 The stability of stratified spatially periodic shear flows at low Péclet number. *Phys. Fluids* **27** (8), 084104.

Garcia-Villalba, M. & del Alamo, J. C. 2011 Turbulence modification by stable stratification in channel flow. *Phys. Fluids* **23** (4), 045104.

Gebhardt, T. & Grossmann, S. 1994 Chaos transition despite linear stability. *Phys. Rev. E* **50** (5), 3705.

Geng, C., He, G., Wang, Y., Xu, C., Lozano-Durán, A. & Wallace, J. M. 2015 Taylor's hypothesis in turbulent channel flow considered using a transport equation analysis. *Phys. Fluids* **27** (2), 025111.

Goldstein, S. 1931 On the stability of superposed streams of fluids of different densities. *Proc. R. Soc. London, Ser. A* **132** (820), 524–548.

Goodstein, D. L. 1989 Richard P. Feynman, teacher. *Physics Today* **42** (2), 70.

Goulart, P. J. & Chernyshenko, S. 2012 Global stability analysis of fluid flows using sum-of-squares. *Physica D* **241** (6), 692–704.

Grachev, A. A., Fairall, C. W., Persson, P. O. G., Andreas, E. L. & Guest, P. S. 2005 Stable boundary-layer scaling regimes: The SHEBA data. *Boundary Layer Meteorol.* **116** (2), 201–235.

Grant, H. L. 1958 The large eddies of turbulent motion. *J. Fluid Mech.* **4** (2), 149–190.

Grossmann, S. 2000 The onset of shear flow turbulence. *Rev. Mod. Phys.* **72** (2), 603.

Grossmann, S. & Lohse, D. 2000 Scaling in thermal convection: a unifying theory. *J. Fluid Mech.* **407**, 27–56.

Guala, M., Hommema, S. E. & Adrian, R. J. 2006 Large-scale and very-large-scale motions in turbulent pipe flow. *J. Fluid Mech.* **554**, 521–542.

Gustavsson, L. H. 1991 Energy growth of three-dimensional disturbances in plane Poiseuille flow. *J. Fluid Mech.* **224**, 241–260.

Harris, S. R. & Hack, P. 2020 Well-posed spatial marching of high-amplitude perturbations in viscous shear flows. In *AIAA Scitech 2020 Forum*, p. 0829.

He, P. & Basu, S. 2015 Direct numerical simulation of intermittent turbulence under stably stratified conditions. *Nonlinear Processes Geophys.* **22**, 447–471.

He, P. & Basu, S. 2016 Development of similarity relationships for energy dissipation rate and temperature structure parameter in stably stratified flows: A direct numerical simulation approach. *Environ. Fluid Mech.* **16** (2), 373–399.

Heins, P. H., Jones, B. L. & Sharma, A. S. 2016 Passivity-based output-feedback control of turbulent channel flow. *Automatica* **69**, 348–355.

Henningson, D. S. & Reddy, S. C. 1994 On the role of linear mechanisms in transition to turbulence. *Phys. Fluids* **6** (3), 1396–1398.

Hindi, H. & Boyd, S. 1998 Analysis of linear systems with saturation using convex optimization. In *Proceedings of the 37th IEEE Conference on Decision and Control*, pp. 903–908. IEEE.

Hiwatashi, K., Alfredsson, P. H., Tillmark, N. & Nagata, M. 2007 Experimental observations of instabilities in rotating plane Couette flow. *Phys. Fluids* **19** (4), 048103.

Hœpffner, J., Chevalier, M., Bewley, T. R. & Henningson, D. S. 2005 State estimation in wall-bounded flow systems. Part 1. Perturbed laminar flows. *J. Fluid Mech.* **534**, 263–294.

Hof, B., Juel, A. & Mullin, T. 2003 Scaling of the turbulence transition threshold in a pipe. *Phys. Rev. Lett.* **91** (24), 244502.

Holm, D. D., Marsden, J. E., Ratiu, T. & Weinstein, A. 1985 Nonlinear stability of fluid and plasma equilibria. *Phys. Rep.* **123** (1-2), 1–116.

Horn, R. A. & Johnson, C. R. 1991 Topics in matrix analysis, 1991. *Cambridge University Presss, Cambridge* .

Horn, R. A. & Johnson, C. R. 2012 *Matrix analysis*. Cambridge university press.

Howard, L. N. 1961 Note on a paper of John W. Miles. *J. Fluid Mech.* **10** (4), 509–512.

Huang, D., Chernyshenko, S., Goulart, P., Lasagna, D., Tutty, O. & Fuentes, F. 2015 Sum-of-squares of polynomials approach to nonlinear stability of fluid flows: an example of application. *Proc. R. Soc. A* **471** (2183), 20150622.

Huang, D., Jin, B., Lasagna, D., Chernyshenko, S. & Tutty, O. 2017 Expensive control of long-time averages using sum of squares and its application to a laminar wake flow. *IEEE Trans. Control Syst. Technol.* **25** (6), 2073–2086.

Huang, X., Yang, W., Li, Y., Qiu, B., Guo, Q. & Zhuqing, L. 2019*a* Review on the sensitization of turbulence models to rotation/curvature and the application to rotating machinery. *Appl. Math. Comput.* **341**, 46–69.

Huang, Y., Xia, Z. & Chen, S. 2021 Hysteresis behaviour in spanwise rotating plane Couette flow at Re_w= 2600. *J. Turbul.* **22**, 254–266.

Huang, Y., Xia, Z., Wan, M., Shi, Y. & Chen, S. 2019*b* Hysteresis behavior in spanwise rotating plane Couette flow with varying rotation rates. *Phys. Rev. Fluids* **4** (5), 052401.

Huerre, P., Batchelor, G. K., Moffatt, H. K. & Worster, M. G. 2000 Open shear flow instabilities. *Perspectives in fluid dynamics* pp. 159–229.

Huerre, P. & Monkewitz, P. A. 1985 Absolute and convective instabilities in free shear layers. *J. Fluid Mech.* **159**, 151–168.

Huerre, P. & Monkewitz, P. A. 1990 Local and global instabilities in spatially developing flows. *Annu. Rev. Fluid Mech.* **22** (1), 473–537.

Hussain, A. K. M. F. & Reynolds, W. C. 1970 The mechanics of an organized wave in turbulent shear flow. *J. Fluid Mech.* **41** (2), 241–258.

Hussain, A. K. M. F. & Reynolds, W. C. 1972 The mechanics of an organized wave in turbulent shear flow. Part 2. Experimental results. *J. Fluid Mech.* **54** (2), 241–261.

Hutchins, N. & Marusic, I. 2007 Evidence of very long meandering features in the logarithmic region of turbulent boundary layers. *J. Fluid Mech.* **579**, 1–28.

Hutchins, N., Monty, J. P., Ganapathisubramani, B., Ng, H. C. H. & Marusic, I. 2011 Three-dimensional conditional structure of a high-Reynolds-number turbulent boundary layer. *J. Fluid Mech.* **673**, 255–285.

Huynh, D. & McKeon, B. 2020*a* Characterization of the spatio-temporal response of a turbulent boundary layer to dynamic roughness. *Flow Turbul. Combust.* **104** (2), 293–316.

Huynh, D. & McKeon, B. 2020*b* Measurements of a turbulent boundary layer-compliant surface system in response to targeted, dynamic roughness forcing. *Exp. Fluids* **61** (4), 1–15.

Hwang, J. & Sung, H. J. 2017 Influence of large-scale motions on the frictional drag in a turbulent boundary layer. *J. Fluid Mech.* **829**, 751–779.

Hwang, Y. & Cossu, C. 2010*a* Amplification of coherent streaks in the turbulent Couette flow an input–output analysis at low Reynolds number. *J. Fluid Mech.* **643**, 333–348.

Hwang, Y. & Cossu, C. 2010*b* Linear non-normal energy amplification of harmonic and stochastic forcing in the turbulent channel flow. *J. Fluid Mech.* **664**, 51–73.

Illingworth, S. J. 2020 Streamwise-constant large-scale structures in Couette and Poiseuille flows. *J. Fluid Mech.* **889**, A13.

Illingworth, S. J., Monty, J. P. & Marusic, I. 2018 Estimating large-scale structures in wall turbulence using linear models. *J. Fluid Mech.* **842**, 146–162.

Jacobi, I. & McKeon, B. J. 2011*a* Dynamic roughness perturbation of a turbulent boundary layer. *J. Fluid Mech.* **688**, 258–296.

Jacobi, I. & McKeon, B. J. 2011*b* New perspectives on the impulsive roughness-perturbation of a turbulent boundary layer. *J. Fluid Mech.* **677**, 179–203.

Jacobi, I. & McKeon, B. J. 2013 Phase relationships between large and small scales in the turbulent boundary layer. *Exp. Fluids* **54** (3), 1481.

Jakirlic, S., Hanjalic, K. & Tropea, C. 2002 Modeling rotating and swirling turbulent flows: a perpetual challenge. *AIAA J.* **40** (10), 1984–1996.

Jeffreys, H. 1928 Some cases of instability in fluid motion. *Proc. R. Soc. London, Ser. A* **118** (779), 195–208.

Jiménez, J. 2013 How linear is wall-bounded turbulence. *Phys. Fluids* **25** (11), 110814.

Jiménez, J. 2018 Coherent structures in wall-bounded turbulence. *J. Fluid Mech.* **842**, P1.

Jiménez, J., del Álamo, J. C. & Flores, O. 2004 The large-scale dynamics of near-wall turbulence. *J. Fluid Mech.* **505**, 179–199.

Jiménez, J., Hoyas, S., Simens, M. P. & Mizuno, Y. 2010 Turbulent boundary layers and channels at moderate Reynolds numbers. *J. Fluid Mech.* **657**, 335–360.

Joglekar, M., Feudel, U. & Yorke, J. A. 2015 Geometry of the edge of chaos in a low-dimensional turbulent shear flow model. *Phys. Rev. E* **91** (5), 052903.

Jose, S., Roy, A., Bale, R. & Govindarajan, R. 2015 Analytical solutions for algebraic growth of disturbances in a stably stratified shear flow. *Proc. R. Soc. A* **471** (2181), 20150267.

Jose, S., Roy, A., Bale, R., Iyer, K. & Govindarajan, R. 2018 Optimal energy growth in a stably stratified shear flow. *Fluid Dyn. Res.* **50** (1), 011421.

Joseph, D. D. 2013 *Stability of fluid motions I*. Springer Science & Business Media.

Jovanović, M. & Bamieh, B. 2001 Modeling flow statistics using the linearized Navier-Stokes equations. In *Proceedings of the 40th IEEE Conference on Decision and Control*, pp. 4944–4949. IEEE.

Jovanovic, M. & Bamieh, B. 2001 The spatio-temporal impulse response of the linearized navier-stokes equations. In *Proceedings of the 2001 American Control Conference*, pp. 1948–1953. IEEE.

Jovanović, M. R. 2004 Modeling, analysis, and control of spatially distributed systems. PhD thesis, University of California at Santa Barbara.

Jovanović, M. R. 2021 From bypass transition to flow control and data-driven turbulence modeling: An input-output viewpoint. *Annu. Rev. Fluid Mech.* **53** (1), 311–345.

Jovanović, M. R. & Bamieh, B. 2004 Unstable modes versus non-normal modes in supercritical channel flows. In *Proceedings of the 2004 American Control Conference*, pp. 2245–2250. IEEE.

Jovanović, M. R. & Bamieh, B. 2005 Componentwise energy amplification in channel flows. *J. Fluid Mech.* **534**, 145–183.

Kalman, R. E. 1963 Lyapunov functions for the problem of Lur'e in automatic control. *Proc. Natl. Acad. Sci.* **49** (2), 201.

Kalur, A., Mushtaq, T., Seiler, P. & Hemati, M. S. 2021*a* Estimating regions of attraction for transitional flows using quadratic constraints. *IEEE Control Syst. Lett.* **6**, 482–487.

Kalur, A., Seiler, P. & Hemati, M. S. 2020 Stability and Performance Analysis of Nonlinear and Non-Normal Systems using Quadratic Constraints. In *AIAA Scitech 2020 Forum*, p. 0833.

Kalur, A., Seiler, P. & Hemati, M. S. 2021*b* Nonlinear Stability Analysis of Transitional Flows using Quadratic Constraints. *Phys. Rev. Fluids* **6** (4), 044401.

Kanazawa, T. 2018 Lifetime and growing process of localized turbulence in plane channel flow. PhD thesis, Osaka University.

de Kat, R. & Ganapathisubramani, B. 2015 Frequency-wavenumber mapping in turbulent shear flows. *J. Fluid Mech.* **783**, 166–190.

Kawata, T. & Alfredsson, P. H. 2016 Experiments in rotating plane Couette flow–momentum transport by coherent roll-cell structure and zero-absolute-vorticity state. *J. Fluid Mech.* **791**, 191–213.

Kawata, T. & Alfredsson, P. H. 2019 Scale interactions in turbulent rotating planar Couette flow: insight through the Reynolds stress transport. *J. Fluid Mech.* **879**, 255–295.

Kerswell, R. R. 2018 Nonlinear nonmodal stability theory. *Annu. Rev. Fluid Mech.* **50** (1), 319–345.

Kerswell, R. R., Pringle, C. C. & Willis, A. P. 2014 An optimization approach for analysing nonlinear stability with transition to turbulence in fluids as an exemplar. *Rep. Prog. Phys.* **77** (8).

Khalil, H. K. 2002 *Nonlinear systems*. Upper Saddle River.

Kim, J. 2011 Physics and control of wall turbulence for drag reduction. *Philos. Trans. Royal Soc. A* **369** (1940), 1396–1411.

Kim, J. & Hussain, F. 1993 Propagation velocity of perturbations in turbulent channel flow. *Phys. Fluids A* **5** (3), 695–706.

Kim, J. & Lim, J. 2000 A linear process in wall-bounded turbulent shear flows. *Phys. Fluids* **12** (8), 1885–1888.

Kim, J., Moin, P. & Moser, R. 1987 Turbulence statistics in fully developed channel flow at low Reynolds number. *J. Fluid Mech.* **177**, 133–166.

Kim, L. & Moehlis, J. 2008 Characterizing the edge of chaos for a shear flow model. *Phys. Rev. E* **78** (3), 1–9.

Komminaho, J., Lundbladh, A. & Johansson, A. V. 1996 Very large structures in plane turbulent Couette flow. *J. Fluid Mech.* **320**, 259–285.

Kreiss, G., Lundbladh, A. & Henningson, D. S. 1994 Bounds for threshold amplitudes in subcritical shear flows. *J. Fluid Mech.* **270**, 175–198.

Kreiss, H. O. 1970 Initial boundary value problems for hyperbolic systems. *Commun. Pure Appl. Math.* **23** (3), 277–298.

Kreplin, H. & Eckelmann, H. 1979 Propagation of perturbations in the viscous sublayer and adjacent wall region. *J. Fluid Mech.* **95** (2), 305–322.

Krogstad, P., Kaspersen, J. H. & Rimestad, S. 1998 Convection velocities in a turbulent boundary layer. *Phys. Fluids* **10** (4), 949–957.

Kundu, P. K. & Beardsley, R. C. 1991 Evidence of a critical Richardson number in moored measurements during the upwelling season off northern California. *J. Geophys. Res.: Oceans* **96** (C3), 4855–4868.

Lakshmi, M. V., Fantuzzi, G., Fernández-Caballero, J. D., Hwang, Y. & Chernyshenko, S. I. 2020 Finding extremal periodic orbits with polynomial optimization, with application to a nine-mode model of shear flow. *SIAM J. Appl. Dyn. Syst.* **19** (2), 763–787.

Landahl, M. T. 1975 Wave breakdown and turbulence. *SIAM J. Appl. Math.* **28** (4), 735–756.

Langham, J., Eaves, T. S. & Kerswell, R. R. 2020 Stably stratified exact coherent structures in shear flow: the effect of Prandtl number. *J. Fluid Mech.* **882**, A10.

Lasagna, D., Huang, D., Tutty, O. R. & Chernyshenko, S. 2016 Sum-of-squares approach to feedback control of laminar wake flows. *J. Fluid Mech.* **809**, 628–663.

Le Gal, P., Harlander, U., Borcia, I., Le Dizès, S., Chen, J. & Favier, B. 2021 The instability of the vertically-stratified horizontal plane Poiseuille flow. *J. Fluid Mech.* **907**, R1.

Lebovitz, N. & Mariotti, G. 2013 Edges in models of shear flow. *J. Fluid Mech.* **721**, 386–402.

Lee, M. & Moser, R. D. 2015 Direct numerical simulation of turbulent channel flow up to $Re_\tau = 5200$. *J. Fluid Mech.* **774**, 395–415.

LeHew, J., Guala, M. & McKeon, B. J. 2010 A study of convection velocities in a zero pressure gradient turbulent boundary layer. In *Proceedings of the 40th Fluid Dynamics Conference and Exhibit*, p. 4474. Chicago, Illinois.

LeHew, J., Guala, M. & McKeon, B. J. 2011 A study of the three-dimensional spectral energy distribution in a zero pressure gradient turbulent boundary layer. *Exp. Fluids* **51** (4), 997–1012.

Lezius, D. K. & Johnston, J. P. 1976 Roll-cell instabilities in rotating laminar and trubulent channel flows. *J. Fluid Mech.* **77** (1), 153–174.

Li, F. & Malik, M. R. 1996 On the nature of PSE approximation. *Theor. Comput. Fluid Dyn.* **8** (4), 253–273.

Li, G., Heath, W. P. & Lennox, B. 2007 An improved stability criterion for a class of Lure systems. In *2007 46th IEEE Conference on Decision and Control*, pp. 4483–4488. IEEE.

Li, G., Heath, W. P. & Lennox, B. 2008 Concise stability conditions for systems with static nonlinear feedback expressed by a quadratic program. *IET Control Theory Appl.* **2** (7), 554–563.

Lien, R. C. & Sanford, T. B. 2004 Turbulence spectra and local similarity scaling in a strongly stratified oceanic bottom boundary layer. *Cont. Shelf Res.* **24** (3), 375–392.

Lignieres, F. 1999 The small-Péclet-number approximation in stellar radiative zones. *Astron. Astrophys.* **348**, 933–939.

Lin, C. C. 1953 On Taylor's hypothesis and the acceleration terms in the Navier-Stokes equations. *Q. Appl. Math.* **10** (4), 295–306.

Liu, C. & Gayme, D. F. 2018 Input-output based analysis of convective velocity in turbulent channels. *Bull. Am. Phys. Soc., Atlanta, GA,* **63** (13).

Liu, C. & Gayme, D. F. 2019 Convective velocities of vorticity fluctuations in turbulent channel flows an input-output approach. In *Proceedings of the Eleventh International Symposium on Turbulence and Shear Flow Phenomenon*. Southampton, UK.

Liu, C. & Gayme, D. F. 2020*a* An input-output based analysis of convective velocity in turbulent channels. *J. Fluid Mech.* **888**, A32.

Liu, C. & Gayme, D. F. 2020*b* Input-output inspired method for permissible perturbation amplitude of transitional wall-bounded shear flows. *Phys. Rev. E* **102** (6), 063108.

Liu, C. & Gayme, D. F. 2020*c* A linear matrix inequality based approach for efficient approximation of permissible perturbation amplitude in wall-bounded shear flows at transitional Reynolds numbers. *Bull. Am. Phys. Soc., Chicago, IL (Virtual),* **65** (13).

Liu, C. & Gayme, D. F. 2021*a* Structured input–output analysis of transitional wall-bounded flows. *arXiv preprint arXiv:2104.00062* .

Liu, C. & Gayme, D. F. 2021*b* Structured input–output analysis of wall-parallel length scales in transitional plane Couette flow. In *AIAA Aviation 2021 Forum*.

Liu, C., Gluzman, I., Lozier, M., Midya, S., Gordeyev, S., Thomas, F. O. & Gayme, D. F. 2021 Spatial input-output based modeling of large-scale structures in actuated turbulent boundary layers. In *AIAA Aviation 2021 Forum*, p. 2873.

Löfberg, J. 2004 YALMIP: A toolbox for modeling and optimization in MATLAB. In *Proceedings of the CACSD Conference*. Taipei, Taiwan.

Loiseau, J. C. & Brunton, S. L. 2018 Constrained sparse Galerkin regression. *J. Fluid Mech.* **838**, 42–67.

Lozano-Durán, A. & Jiménez, J. 2014 Time-resolved evolution of coherent structures in turbulent channels characterization of eddies and cascades. *J. Fluid Mech.* **759**, 432–471.

Lozier, M., Midya, S., Thomas, F. O. & Gordeyev, S. 2019 Experimental studies of boundary layer dynamics using active flow control of large-scale structures. In *Proceedings of the Eleventh International Symposium on Turbulence and Shear Flow Phenomenon*. Southampton, UK.

Lozier, M. E., Thomas, F. O. & Gordeyev, S. 2020 Streamwise evolution of turbulent boundary layer response to active control actuator. In *AIAA Scitech 2020 Forum*, p. 0097.

Lozier, M. E., Thomas, F. O. & Gordeyev, S. 2021 Turbulent Boundary Layer Response to Active Control Actuator. In *AIAA Scitech 2021 Forum*, p. 1455.

Lucas, D., Caulfield, C. & Kerswell, R. R. 2019 Layer formation and relaminarisation in plane Couette flow with spanwise stratification. *J. Fluid Mech.* **868**, 97–118.

Luhar, M., Sharma, A. S. & McKeon, B. J. 2014 On the structure and origin of pressure fluctuations in wall turbulence predictions based on the resolvent analysis. *J. Fluid Mech.* **751**, 38–70.

Lumley, J. L. 1965 Interpretation of time spectra measured in high-intensity shear flows. *Phys. Fluids* **8** (6), 1056–1062.

Lundbladh, A., Henningson, D. S. & Reddy, S. C. 1994 Threshold amplitudes for transition in channel flows. In *Transition, turbulence and combustion*, pp. 309–318. Springer.

Lyapunov, A. M. 1992 The general problem of the stability of motion. *Int. J. Control* **55** (3), 531–534.

Lyons, R., Panofsky, H. & Wollaston, S. 1964 The critical Richardson number and its implications for forecast problems. *J. Appl. Meteorol.* **3** (2), 136–142.

Madhusudanan, A., Illingworth, S. J. & Marusic, I. 2019 Coherent large-scale structures from the linearized Navier-Stokes equations. *J. Fluid Mech.* **873**, 89–109.

Mahrt, L. 1999 Stratified atmospheric boundary layers. *Boundary Layer Meteorol.* **90** (3), 375–396.

Mahrt, L. 2014 Stably stratified atmospheric boundary layers. *Annu. Rev. Fluid Mech.* **46**, 23–45.

Marusic, I. & Heuer, W. D. C. 2007 Reynolds number invariance of the structure inclination angle in wall turbulence. *Phys. Rev. Lett.* **99** (11), 114504.

Marusic, I., McKeon, B. J., Monkewitz, P. A., Nagib, H. M., Smits, A. J. & Sreenivasan, K. R. 2010 Wall-bounded turbulent flows at high Reynolds numbers: Recent advances and key issues. *Phys. Fluids* **22** (6), 065103.

Marusic, I. & Monty, J. P. 2019 Attached eddy model of wall turbulence. *Annu. Rev. Fluid Mech.* **51**, 49–74.

Mathis, R., Hutchins, N. & Marusic, I. 2009*a* Large-scale amplitude modulation of the small-scale structures in turbulent boundary layers. *J. Fluid Mech.* **628**, 311–337.

Mathis, R., Monty, J. P., Hutchins, N. & Marusic, I. 2009*b* Comparison of large-scale amplitude modulation in turbulent boundary layers, pipes, and channel flows. *Phys. Fluids* **21** (11), 111703.

McKeon, B. J. 2010 Controlling turbulence. *Science* **327** (5972), 1462–1463.

McKeon, B. J. 2017 The engine behind (wall) turbulence perspectives on scale interactions. *J. Fluid Mech.* **817**, P1.

McKeon, B. J., Jacobi, I. & Duvvuri, S. 2018 Dynamic roughness for manipulation and control of turbulent boundary layers: an overview. *AIAA J.* **56** (6), 2178–2193.

McKeon, B. J. & Sharma, A. S. 2010 A critical-layer framework for turbulent pipe flow. *J. Fluid Mech.* **658**, 336–382.

McKeon, B. J., Sharma, A. S. & Jacobi, I. 2013 Experimental manipulation of wall turbulence: a systems approach. *Phys. Fluids* **25** (3), 031301.

Mellibovsky, F. & Meseguer, A. 2009 Critical threshold in pipe flow transition. *Philos. Trans. R. Soc. A Math. Phys. Eng. Sci.* **367** (1888), 545–560.

Miles, J. W. 1961 On the stability of heterogeneous shear flows. *J. Fluid Mech.* **10** (4), 496–508.

Moarref, R., Jovanović, M. R., Tropp, J. A., Sharma, A. S. & McKeon, B. J. 2014 A low-order decomposition of turbulent channel flow via resolvent analysis and convex optimization. *Phys. Fluids* **26** (5), 051701.

Moarref, R., Sharma, A. S., Tropp, J. A. & McKeon, B. J. 2013 Model-based scaling of the streamwise energy density in high-Reynolds-number turbulent channels. *J. Fluid Mech.* **734**, 275–316.

Moehlis, J., Faisst, H. & Eckhardt, B. 2004 A low-dimensional model for turbulent shear flows. *New J. Phys.* **6**, 1–17.

Moehlis, J., Faisst, H. & Eckhardt, B. 2005 Periodic orbits and chaotic sets in a low-dimensional model for shear flows. *SIAM J. Appl. Dyn. Syst.* **4** (2), 352–376.

Monkewitz, P. A., Chauhan, K. A. & Nagib, H. M. 2007 Self-consistent high-Reynolds-number asymptotics for zero-pressure-gradient turbulent boundary layers. *Phys. Fluids* **19** (11), 115101.

Monokrousos, A., Bottaro, A., Brandt, L., Di Vita, A. & Henningson, D. S. 2011 Nonequilibrium thermodynamics and the optimal path to turbulence in shear flows. *Phys. Rev. Lett.* **106** (13), 1–4.

Monty, J. P., Stewart, J. A., Williams, R. C. & Chong, M. S. 2007 Large-scale features in turbulent pipe and channel flows. *J. Fluid Mech.* **589**, 147–156.

Morra, P., Nogueira, P. A. S., Cavalieri, A. V. G. & Henningson, D. S. 2021 The colour of forcing statistics in resolvent analyses of turbulent channel flows. *J. Fluid Mech.* **907**, A24.

Morra, P., Semeraro, O., Henningson, D. S. & Cossu, C. 2019 On the relevance of Reynolds stresses in resolvent analyses of turbulent wall-bounded flows. *J. Fluid Mech.* **867**, 969–984.

Morrison, P. J. 1998 Hamiltonian description of the ideal fluid. *Rev. Mod. Phys.* **70** (2), 467.

Mu, M. & Wu, Y. H. 2001 Arnol'd nonlinear stability theorems and their application to the atmosphere and oceans. *Surv. Geophys.* **22** (4), 383–426.

Mullin, T. 2011 Experimental studies of transition to turbulence in a pipe. *Annu. Rev. Fluid Mech.* **43**, 1–24.

Naderi, A., Bhattacharjee, N. & Folch, A. 2019 Digital manufacturing for microfluidics. *Annu. Rev. Biomed. Eng.* **21**, 325–364.

Nagano, Y. & Tagawa, M. 1995 Coherent motions and heat transfer in a wall turbulent shear flow. *J. Fluid Mech.* **305**, 127–157.

Nagata, M. 1986 Bifurcations in Couette flow between almost corotating cylinders. *J. Fluid Mech.* **169**, 229–250.

Nagata, M. 2013 A note on the mirror-symmetric coherent structure in plane Couette flow. *J. Fluid Mech.* **727**, R1.

Nagata, M., Song, B. & Wall, D. P. 2021 Onset of vortex structures in rotating plane Couette flow. *J. Fluid Mech.* **918**, A2.

Nakashima, S., Luhar, M. & Fukagata, K. 2019 Reconsideration of spanwise rotating turbulent channel flows via resolvent analysis. *J. Fluid Mech.* **861**, 200–222.

Nieuwstadt, F. T. 1984 The turbulent structure of the stable, nocturnal boundary layer. *J. Atmos. Sci.* **41** (14), 2202–2216.

Nogueira, P. A. S., Morra, P., Martini, E., Cavalieri, A. V. G. & Henningson, D. S. 2021 Forcing statistics in resolvent analysis: application in minimal turbulent Couette flow. *J. Fluid Mech.* **908**, A32.

Olvera, D. & Kerswell, R. 2017 Exact coherent structures in stably stratified plane Couette flow. *J. Fluid Mech.* **826**, 583–614.

Orszag, S. A. 1971 Accurate solution of the Orr–Sommerfeld stability equation. *J. Fluid Mech.* **50** (4), 689–703.

Ortega, R., Perez, J. A. L., Nicklasson, P. J. & Sira-Ramirez, H. J. 2013 *Passivity-based control of Euler-Lagrange systems: mechanical, electrical and electromechanical applications*. Springer.

Packard, A. & Doyle, J. 1993 The complex structured singular value. *Automatica* **29** (1), 71–109.

Panton, R. L. & Linebarger, J. H. 1974 Wall pressure spectra calculations for equilibrium boundary layers. *J. Fluid Mech.* **65** (2), 261–287.

Papachristodoulou, A., Anderson, J., Valmorbida, G., Prajna, S., Seiler, P. & Parrilo, P. 2013 SOSTOOLS version 3.00 sum of squares optimization toolbox for MATLAB. *arXiv preprint arXiv:1310.4716* .

Papachristodoulou, A. & Prajna, S. 2005*a* Analysis of non-polynomial systems using the sum of squares decomposition. In *Positive polynomials in control*, pp. 23–43. Springer.

Papachristodoulou, A. & Prajna, S. 2005*b* A tutorial on sum of squares techniques for systems analysis. In *Proceedings of the 2005, American Control Conference, 2005.*, pp. 2686–2700. IEEE.

Paranjape, C. 2019 Onset of turbulence in plane Poiseuille flow. PhD thesis, Institute of Science and Technology Austria.

Paranjape, C. S., Duguet, Y. & Hof, B. 2020 Oblique stripe solutions of channel flow. *J. Fluid Mech.* **897**, A7.

Park, J., Lee, S. Y. & Park, P. 2019 A less conservative stability criterion for discrete-time Lur'e systems with sector and slope restrictions. *IEEE Trans. Autom. Control* **64** (10), 4391–4395.

Park, P. 1997 A revisited Popov criterion for nonlinear Lur'e systems with sector-restrictions. *Int. J. Control* **68** (3), 461–470.

Parrilo, P. A. 2000 Structured semidefinite programs and semialgebraic geometry methods in robustness and optimization. PhD thesis, California Institute of Technology.

Pedlosky, J. 2013 *Geophysical fluid dynamics*. Springer Science & Business Media.

Peixinho, J. & Mullin, T. 2007 Finite-amplitude thresholds for transition in pipe flow. *J. Fluid Mech.* **582**, 169–178.

Perry, A. E. & Chong, M. S. 1982 On the mechanism of wall turbulence. *J. Fluid Mech.* **119**, 173–217.

Perry, A. E., Henbest, S. & Chong, M. S. 1986 A theoretical and experimental study of wall turbulence. *J. Fluid Mech.* **165**, 163–199.

Philip, J., Svizher, A. & Cohen, J. 2007 Scaling law for a subcritical transition in plane Poiseuille flow. *Phys. Rev. Lett.* **98** (15), 154502.

Pope, S. B. 2000 *Turbulent flows*. Cambridge, England: Cambridge university press.

Popov, V. M. 1961 Absolute stability of nonlinear systems of automatic control. *Autom. Remote Control* **22** (8), 857–875.

Prajna, S., Papachristodoulou, A. & Parrilo, P. A. 2002 Introducing SOSTOOLS: A general purpose sum of squares programming solver. In *Proceedings of the 41st IEEE Conference on Decision and Control, 2002.*, pp. 741–746. IEEE.

Prigent, A., Grégoire, G., Chaté, H. & Dauchot, O. 2003 Long-wavelength modulation of turbulent shear flows. *Physica D* **174** (1-4), 100–113.

Prigent, A., Grégoire, G., Chaté, H., Dauchot, O. & van Saarloos, W. 2002 Large-scale finite-wavelength modulation within turbulent shear flows. *Phys. Rev. Lett.* **89** (1), 014501.

Pringle, C. C. T. & Kerswell, R. R. 2010 Using nonlinear transient growth to construct the minimal seed for shear flow turbulence. *Phys. Rev. Lett.* **105** (15), 1–4.

Pringle, C. C. T., Willis, A. P. & Kerswell, R. R. 2012 Minimal seeds for shear flow turbulence: using nonlinear transient growth to touch the edge of chaos. *J. Fluid Mech.* **702**, 415–443.

Proudman, J. 1916 On the motion of solids in a liquid possessing vorticity. *Proc. R. Soc. London, Ser. A* **92** (642), 408–424.

Pujals, G., García-Villalba, M., Cossu, C. & Depardon, S. 2009 A note on optimal transient growth in turbulent channel flows. *Phys. Fluids* **21** (1), 015109.

Rabin, S. M. E., Caulfield, C. P. & Kerswell, R. R. 2012 Triggering turbulence efficiently in plane Couette flow. *J. Fluid Mech.* **712**, 244–272.

Ran, W., Zare, A., Hack, M. P. & Jovanović, M. R. 2019 Stochastic receptivity analysis of boundary layer flow. *Phys. Rev. Fluids* **4** (9), 093901.

Ranade, P., Duvvuri, S., McKeon, B., Gordeyev, S., Christensen, K. & Jumper, E. J. 2019 Turbulence amplitude amplification in an externally forced, subsonic turbulent boundary layer. *AIAA J.* **57** (9), 3838–3850.

Rantzer, A. 1996 On the KalmanYakubovichPopov lemma. *Syst. Control Lett.* **28** (1), 7–10.

Rayleigh, L. 1917 On the dynamics of revolving fluids. *Proc. R. Soc. London, Ser. A* **93** (648), 148–154.

Reddy, S. C. & Henningson, D. S. 1993 Energy growth in viscous channel flows. *J. Fluid Mech.* **252**, 209–238.

Reddy, S. C., Schmid, P. J., Baggett, J. S. & Henningson, D. S. 1998 On stability of streamwise streaks and transition thresholds in plane channel flows. *J. Fluid Mech.* **365**, 269–303.

Reetz, F., Kreilos, T. & Schneider, T. M. 2019 Exact invariant solution reveals the origin of self-organized oblique turbulent-laminar stripes. *Nat. Commun.* **10** (1), 1–6.

Renard, N. & Deck, S. 2015 On the scale-dependent turbulent convection velocity in a spatially developing flat plate turbulent boundary layer at Reynolds number $Re_\theta = 13000$. *J. Fluid Mech.* **775**, 105–148.

Reynolds, O. 1883 XXIX. An experimental investigation of the circumstances which determine whether the motion of water shall be direct or sinuous, and of the law of resistance in parallel channels. *Philos. Trans. R. Soc. London.* **174**, 935–982.

Reynolds, W. C. & Hussain, A. K. M. F. 1972 The mechanics of an organized wave in turbulent shear flow. Part 3. Theoretical models and comparisons with experiments. *J. Fluid Mech.* **54** (2), 263–288.

Ribeiro, J. H. M., Yeh, C.-A. & Taira, K. 2020 Randomized resolvent analysis. *Phys. Rev. Fluids* **5** (3), 033902.

Richardson, L. F. 2007 *Weather prediction by numerical process*. Cambridge university press.

Rigas, G., Sipp, D. & Colonius, T. 2021 Nonlinear input/output analysis: application to boundary layer transition. *J. Fluid Mech.* **911**, A15.

Robinson, S. K. 1991 Coherent motions in the turbulent boundary layer. *Annu. Rev. Fluid Mech.* **23** (1), 601–639.

Rohr, J., Itsweire, E., Helland, K. & Van Atta, C. 1988 Growth and decay of turbulence in a stably stratified shear flow. *J. Fluid Mech.* **195**, 77–111.

Romanov, V. A. 1973 Stability of plane-parallel Couette flow. *Funct. Anal. Appl.* **7** (2), 137–146.

Safonov, M. G. 1982 Stability margins of diagonally perturbed multivariable feedback systems. *IEE Proceedings D (Control Theory and Applications)* **129** (6), 251–256.

Salehipour, H., Peltier, W. & Caulfield, C. 2018 Self-organized criticality of turbulence in strongly stratified mixing layers. *J. Fluid Mech.* **856**, 228–256.

Salmon, R. 1988 Hamiltonian fluid mechanics. *Annu. Rev. Fluid Mech.* **20** (1), 225–256.

van der Schaft, A. J. 2000 *L_2-gain and passivity techniques in nonlinear control*. Springer.

Schmid, P. & Henningson, D. 1992 A new mechanism for rapid transition involving a pair of oblique waves. *Phys. Fluids A* **4** (9), 1986–1989.

Schmid, P. J. 2007 Nonmodal stability theory. *Annu. Rev. Fluid Mech.* **39**, 129–162.

Schmid, P. J. & Henningson, D. S. 2012 *Stability and transition in shear flows*. Springer Science & Business Media.

Schneider, T. M., Eckhardt, B. & Yorke, J. A. 2007 Turbulence transition and the edge of chaos in pipe flow. *Phys. Rev. Lett.* **99** (3), 1–4.

Schneider, T. M., Marinc, D. & Eckhardt, B. 2010 Localized edge states nucleate turbulence in extended plane Couette cells. *J. Fluid Mech.* **646**, 441–451.

Sharma, A., Morrison, J., McKeon, B., Limebeer, D., Koberg, W. & Sherwin, S. 2011 Relaminarisation of $\mathrm{Re}_\tau = 100$ channel flow with globally stabilising linear feedback control. *Phys. Fluids* **23** (12), 125105.

Sharma, A. S. 2009 Model reduction of turbulent fluid flows using the supply rate. *Int. J. Bifurc. Chaos* **19** (04), 1267–1278.

Sharma, A. S. & McKeon, B. J. 2013 On coherent structure in wall turbulence. *J. Fluid Mech.* **728**, 196–238.

Sharma, A. S., Moarref, R. & McKeon, B. J. 2017 Scaling and interaction of self-similar modes in models of high Reynolds number wall turbulence. *Phil. Trans. R. Soc. A* **375** (2089), 20160089.

Shimizu, M. & Manneville, P. 2019 Bifurcations to turbulence in transitional channel flow. *Phys. Rev. Fluids* **4** (11), 113903.

Simens, M. P., Jiménez, J., Hoyas, S. & Mizuno, Y. 2009 A high-resolution code for turbulent boundary layers. *J. Comput. Phys.* **228** (11), 4218–4231.

Smits, A. J., McKeon, B. J. & Marusic, I. 2011 High-Reynolds number wall turbulence. *Annu. Rev. Fluid Mech.* **43** (1), 353–375.

Smyth, W. & Moum, J. 2013 Marginal instability and deep cycle turbulence in the eastern equatorial Pacific Ocean. *Geophys. Res. Lett.* **40** (23), 6181–6185.

Smyth, W., Nash, J. & Moum, J. 2019 Self-organized criticality in geophysical turbulence. *Sci. Rep.* **9** (1), 1–8.

Smyth, W. D. & Carpenter, J. R. 2019 *Instability in geophysical flows*. Cambridge University Press.

Song, B. & Xiao, X. 2020 Trigger turbulent bands directly at low Reynolds numbers in channel flow using a moving-force technique. *J. Fluid Mech.* **903**, A43.

Squire, D. T., Hutchins, N., Morrill-Winter, C., Schultz, M. P., Klewicki, J. C. & Marusic, I. 2017 Applicability of Taylor's hypothesis in rough-and smooth-wall boundary layers. *J. Fluid Mech.* **812**, 398–417.

Straughan, B. 2013 *The energy method, stability, and nonlinear convection*. Springer Science & Business Media.

Sturm, J. F. 1999 Using SeDuMi 1.02, a MATLAB toolbox for optimization over symmetric cones. *Optim. Methods Softw.* **11** (1-4), 625–653.

Suryadi, A., Segalini, A. & Alfredsson, P. H. 2014 Zero absolute vorticity: insight from experiments in rotating laminar plane Couette flow. *Phys. Rev. E* **89** (3), 033003.

Symon, S., Illingworth, S. J. & Marusic, I. 2021 Energy transfer in turbulent channel flows and implications for resolvent modelling. *J. Fluid Mech.* **911**, A3.

Tang, Z. & Jiang, N. 2020 The effect of a synthetic input on small-scale intermittent bursting events in near-wall turbulence. *Phys. Fluids* **32** (1), 015110.

Tang, Z., Jiang, N., Zheng, X. & Wu, Y. 2019 Local dynamic perturbation effects on amplitude modulation in turbulent boundary layer flow based on triple decomposition. *Phys. Fluids* **31** (2), 025120.

Tang, Z., Ma, X., Jiang, N., Cui, X. & Zheng, X. 2021 Local dynamic perturbation effects on the scale interactions in wall turbulence. *J. Turbul.* **22** (3), 208–230.

Tao, J., Eckhardt, B. & Xiong, X. 2018 Extended localized structures and the onset of turbulence in channel flow. *Phys. Rev. Fluids* **3** (1), 011902.

Taylor, C. A. & Draney, M. T. 2004 Experimental and computational methods in cardiovascular fluid mechanics. *Annu. Rev. Fluid Mech.* **36**, 197–231.

Taylor, G. I. 1917 Motion of solids in fluids when the flow is not irrotational. *Proc. R. Soc. London, Ser. A* **93** (648), 99–113.

Taylor, G. I. 1931 Effect of variation in density on the stability of superposed streams of fluid. *Proc. R. Soc. London, Ser. A* **132** (820), 499–523.

Taylor, G. I. 1938 The spectrum of turbulence. *Proc. R. Soc. London A Math. Phys. Eng. Sci.* **164** (919), 476–490.

Taylor, J. & Zhou, Q. 2017 A multi-parameter criterion for layer formation in a stratified shear flow using sorted buoyancy coordinates. *J. Fluid Mech.* **823**, R5.

Taylor, J. R., Deusebio, E., Caulfield, C. P. & Kerswell, R. R. 2016 A new method for isolating turbulent states in transitional stratified plane Couette flow. *J. Fluid Mech.* **808**, R1.

Thomas, F. O., Corke, T. C., Iqbal, M., Kozlov, A. & Schatzman, D. 2009 Optimization of dielectric barrier discharge plasma actuators for active aerodynamic flow control. *AIAA J.* **47** (9), 2169–2178.

Tillmark, N. & Alfredsson, P. H. 1992 Experiments on transition in plane Couette flow. *J. Fluid Mech.* **235**, 89–102.

Tobias, S. & Marston, J. 2017 Three-dimensional rotating Couette flow via the generalised quasilinear approximation. *J. Fluid Mech.* **810**, 412–428.

Towne, A. & Colonius, T. 2015 One-way spatial integration of hyperbolic equations. *J. Comput. Phys.* **300**, 844–861.

Towne, A., Rigas, G. & Colonius, T. 2019 A critical assessment of the parabolized stability equations. *Theor. Comput. Fluid Dyn.* **33** (3-4), 359–382.

Townsend, A. A. 1961 Equilibrium layers and wall turbulence. *J. Fluid Mech.* **11** (1), 97–120.

Townsend, A. A. 1976 *The structure of turbulent shear flow*. Cambridge, England: Cambridge University Press.

Trefethen, L. N. 2000 *Spectral methods in MATLAB*. Society for Industrial and Applied Mathematics (SIAM).

Trefethen, L. N. & Embree, M. 2005 *Spectra and pseudospectra: the behavior of nonnormal matrices and operators*. Princeton University Press.

Trefethen, L. N. & Halpern, L. 1986 Well-posedness of one-way wave equations and absorbing boundary conditions. *Math. Comput.* **47** (176), 421–435.

Trefethen, L. N., Trefethen, A. E., Reddy, S. C. & Driscoll, T. A. 1993 Hydrodynamic stability without eigenvalues. *Science* **261** (5121), 578.

Tsukahara, T., Kawaguchi, Y. & Kawamura, H. 2014 An experimental study on turbulent-stripe structure in transitional channel flow. *arXiv preprint arXiv:1406.1378* .

Tsukahara, T., Kawaguchi, Y., Kawamura, H., Tillmark, N. & Alfredsson, P. H. 2010*a* Turbulence stripe in transitional channel flow with/without system rotation. In *Seventh IUTAM Symposium on Laminar-Turbulent Transition*, pp. 421–426. Springer.

Tsukahara, T., Seki, Y., Kawamura, H. & Tochio, D. 2005 DNS of turbulent channel flow at very low Reynolds numbers. In *Proceedings of the Fourth International Symposium on Turbulence and Shear Flow Phenomena*. Williamsburg, USA.

Tsukahara, T., Tillmark, N. & Alfredsson, P. 2010*b* Flow regimes in a plane Couette flow with system rotation. *J. Fluid Mech.* **648**, 5–33.

Tuckerman, L. S. & Barkley, D. 2011 Patterns and dynamics in transitional plane Couette flow. *Phys. Fluids* **23** (4), 041301.

Tuckerman, L. S., Chantry, M. & Barkley, D. 2020 Patterns in wall-bounded shear flows. *Annu. Rev. Fluid Mech.* **52** (1), 343–367.

Tuckerman, L. S., Kreilos, T., Schrobsdorff, H., Schneider, T. M. & Gibson, J. F. 2014 Turbulent-laminar patterns in plane Poiseuille flow. *Phys. Fluids* **26** (11), 114103.

Turner, J. S. 1979 *Buoyancy effects in fluids*. Cambridge University Press.

Vadarevu, S. B., Symon, S., Illingworth, S. J. & Marusic, I. 2019 Coherent structures in the linearized impulse response of turbulent channel flow. *J. Fluid Mech.* **863**, 1190–1203.

Vallis, G. K. 2017 *Atmospheric and oceanic fluid dynamics*. Cambridge University Press.

Valmorbida, G., Drummond, R. & Duncan, S. R. 2018 Regional analysis of slope-restricted Lurie systems. *IEEE Trans. Autom. Control* **64** (3), 1201–1208.

Vandenberghe, L. & Boyd, S. 1996 Semidefinite programming. *SIAM Rev.* **38** (1), 49–95.

Veers, P., Dykes, K., Lantz, E., Barth, S., Bottasso, C. L., Carlson, O., Clifton, A., Green, J., Green, P., Holttinen, H. & others 2019 Grand challenges in the science of wind energy. *Science* **366** (6464).

Veronis, G. 1970 The analogy between rotating and stratified fluids. *Annu. Rev. Fluid Mech.* **2** (1), 37–66.

Waleffe, F. 1995 Transition in shear flows. Nonlinear normality versus non-normal linearity. *Phys. Fluids* **7** (12), 3060–3066.

Waleffe, F. 1997 On a self-sustaining process in shear flows. *Phys. Fluids* **9** (4), 883–900.

Wallace, J. M. 2016 Quadrant analysis in turbulence research: History and evolution. *Annu. Rev. Fluid Mech.* **4**, 131–158.

Wallace, J. M., Eckelmann, H. & Brodkey, R. S. 1972 The wall region in turbulent shear flow. *J. Fluid Mech.* **54** (1), 39–48.

Wallin, S., Grundestam, O. & Johansson, A. V. 2013 Laminarization mechanisms and extreme-amplitude states in rapidly rotating plane channel flow. *J. Fluid Mech.* **730**, 193–219.

Weatherly, G. L. & Martin, P. J. 1978 On the structure and dynamics of the oceanic bottom boundary layer. *J. Phys. Oceanogr.* **8** (4), 557–570.

Weideman, J. A. C. & Reddy, S. C. 2000 A MATLAB differentiation matrix suite. *ACM Trans. Math. Softw.* **26** (4), 465–519.

Weissenberger, S. 1968 Application of results from the absolute stability problem to the computation of finite stability domains. *IEEE Trans. Autom. Control* **13** (1), 124–125.

Willmarth, W. W. & Wooldridge, C. E. 1962 Measurements of the fluctuating pressure at the wall beneath a thick turbulent boundary layer. *J. Fluid Mech.* **14** (2), 187–210.

Wills, J. A. B. 1964 On convection velocities in turbulent shear flows. *J. Fluid Mech.* **20** (3), 417–432.

Xia, Z., Shi, Y., Cai, Q., Wan, M. & Chen, S. 2018 Multiple states in turbulent plane Couette flow with spanwise rotation. *J. Fluid Mech.* **837**, 477–490.

Xia, Z., Shi, Y., Wan, M., Sun, C., Cai, Q. & Chen, S. 2019 Role of the large-scale structures in spanwise rotating plane Couette flow with multiple states. *Phys. Rev. Fluids* **4** (10), 104606.

Xiao, X. & Song, B. 2020 The growth mechanism of turbulent bands in channel flow at low Reynolds numbers. *J. Fluid Mech.* **883**, R1.

Xiong, X., Tao, J., Chen, S. & Brandt, L. 2015 Turbulent bands in plane-Poiseuille flow at moderate Reynolds numbers. *Phys. Fluids* **27** (4), 041702.

Yang, X. I. A. & Howland, M. F. 2018 Implication of Taylor's hypothesis on measuring flow modulation. *J. Fluid Mech.* **836**, 222–237.

Yang, X. I. A. & Xia, Z. 2021 Bifurcation and multiple states in plane Couette flow with spanwise rotation. *J. Fluid Mech.* **913**, A49.

Yeh, C.-A. & Taira, K. 2019 Resolvent-analysis-based design of airfoil separation control. *J. Fluid Mech.* **867**, 572–610.

Zaman, K. B. M. Q. & Hussain, A. K. M. F. 1981 Taylor hypothesis and large-scale coherent structures. *J. Fluid Mech.* **112**, 379–396.

Zames, G. 1966 On the input-output stability of time-varying nonlinear feedback systems–Part II: Conditions involving circles in the frequency plane and sector nonlinearities. *IEEE Trans. Autom. Control* **11** (3), 465–476.

Zare, A., Jovanović, M. R. & Georgiou, T. T. 2017 Colour of turbulence. *J. Fluid Mech.* **812**, 636–680.

Zhao, S. & Duncan, S. 2013 Passivity of plane Poiseuille flow. In *2013 European Control Conference (ECC)*, pp. 1077–1082. IEEE.

Zheng, Y., Fantuzzi, G. & Papachristodoulou, A. 2018 Fast ADMM for sum-of-squares programs using partial orthogonality. *IEEE Trans. Autom. Control* **64** (9), 3869–3876.

Zhou, K., Doyle, J. C. & Glover, K. 1996 *Robust and optimal control*. Prentice hall.

Zhou, Q., Taylor, J. R. & Caulfield, C. P. 2017*a* Self-similar mixing in stratified plane Couette flow for varying Prandtl number. *J. Fluid Mech.* **820**, 86–120.

Zhou, Q., Taylor, J. R., Caulfield, C. P. & Linden, P. 2017*b* Diapycnal mixing in layered stratified plane Couette flow quantified in a tracer-based coordinate. *J. Fluid Mech.* **823**, 198–229.

Zonta, F. & Soldati, A. 2018 Stably stratified wall-bounded turbulence. *Appl. Mech. Rev.* **70** (4), 040801.